COSMIC RAY PROPAGATION IN TURBULENT GALACTIC MAGNETIC FIELDS

AMIT SETA

Thesis submitted for the degree of
Doctor of Philosophy

School of Mathematics, Statistics and Physics
Newcastle University, Newcastle upon Tyne, UK

July 2019

Abstract

Cosmic rays and magnetic fields are important non-thermal components of the interstellar medium in galaxies. This thesis explores the intermittent structure of the magnetic field generated by a fluctuation dynamo and the interaction of cosmic rays with small-scale random magnetic fields.

First, the nonlinear state of fluctuation dynamo is described in terms of the statistical and structural properties of magnetic and velocity fields. Using three-dimensional fluctuation dynamo simulations, we study their properties in the kinematic and saturated stages. The alignment of the magnetic field, electric current density, and velocity field are analyzed to suggest a possible saturation mechanism for the fluctuation dynamo. Furthermore, we also study the change in the diffusion of magnetic fields by calculating local magnetic Reynolds number in the kinematic and saturated stages. We show that both the amplification and diffusion of magnetic fields are affected by nonlinearity. The dynamo-generated magnetic field is intermittent, i.e., concentrated in filaments, ribbons, and sheets. Minkowski functionals are used to characterize the shape of the magnetic structures and study its dependence on magnetic Reynolds number. We find that all three length scales of magnetic structures decreases on saturation. We also propose that observing magnetic fields in elliptical galaxies, via a grid of the Faraday rotation measures from background polarized sources, would serve as a probe of the fluctuation dynamo action in a galactic environment.

Next, the effect of magnetic field intermittency on cosmic ray propagation is studied. Using test-particle simulations, it is shown that the diffusivity of low energy cosmic rays is enhanced when the magnetic field is intermittent. It is demonstrated that the cosmic ray diffusion in any random magnetic field (Gaussian or intermittent) can be better described as a correlated random walk rather the usual Brownian motion. Then, the energy equipartition between magnetic fields and cosmic rays usually assumed to infer magnetic field strength from synchrotron intensity observations is discussed. Using test-particle and magnetohydrodynamic simulations, it is shown that the cosmic ray and magnetic field energy densities are not correlated on scales less than the driving scale of the turbulence. Even when the cosmic ray and magnetic field energy densities are uncorrelated, small-scale structures are seen in the spatial distribution of cosmic rays as they are trapped between random magnetic mirrors. These results exclude the possibility of local energy equipartition between cosmic rays and magnetic fields.

Acknowledgements

With this thesis, a journey has reached its destination. I was extremely fortunate to meet and interact with various people on the way, who have made this journey enriching and enjoyable. Here, I would try to acknowledge their contribution.

First and foremost, I am deeply grateful to my advisors, Prof. Anvar Shukurov, Dr. Paul J. Bushby and Dr. Toby S. Wood, for their continuous guidance, support, and enthusiasm. I have learned a lot from them and am inspired by their passion for science. They have always been willing to take on extra workload in order to help me. Their role during the journey was a perfect combination of being an advisor, a colleague, and a friend. When I am having trouble, they help me find the right way, thus being my advisor. They gave me the freedom to lead my own research and were always interested in my work, thus being my colleague. They provided a very friendly environment where I can discuss anything with them, thus being my friend. I am lucky to have them. Also, special thanks to Prof. Anvar Shukurov for sharing his life experiences which made my life easier.

The astrophysics group at Newcastle University is an outstanding place to be as a graduate student. Everyone is interested in all three aspects (theoretical, numerical and observational) of the subject. I thank all the members of the group for very useful discussions about our respective research topics. The atmosphere within the group is perfect for scientific growth. I would take this opportunity to thank the following people. Dr. Andrew P. Snodin for being a wonderful collaborator and for long discussions over emails. Dr. Andrew Fletcher for being the supervisor of my first reading project on radio astronomy and explaining me the intricacies of magnetic field observations. Dr. Christopher A. Hales for guiding my second reading project on radio astronomy and being supportive of my research. Dr. Luiz Santiago Rodrigues for discussions on cosmic rays, magnetic fields, Python, the Pencil code, and many other topics. Dr. Graeme R. Sarson for discussing with me about the Pencil code and also for providing a very encouraging yearly review of my research. Dr. Tamara Rogers for helping me teach the advanced astrophysics course and our friendly conversations. All my students for their helpful feedback and for a wonderful teaching experience.

I have also learned a lot from my interactions with the visitors to the school, especially from Prof. Alexander A. Schekochihin, Prof. Luke Drury, Dr. Jörg P. Rachen, Dr. Andrey Beresnyak, Dr. Luke Chamandy, and Dr. Frederick A. Gent. I would like to thank Dr. Michael Beaty and others for help with computing-related problems and everyone at the school office for support with the administrative work. I am grateful to all the graduate

students and postdoctoral fellows at the school for their support and help throughout the entire period.

Newcastle as a city has been very welcoming. I thank everyone at the Hindu temple for organizing and celebrating almost all the Indian festivals, especially Navratri. I thank friends outside the university for their immense support throughout the past four years. I am also thankful to Dr. Sunanda Roy Mahapatra, Boudi and Prisha for their support during a tough time in my final year. I am inspired by Dr. Mahapatra's humble and helpful nature.

I was lucky to interact with various experts in the field who are outside Newcastle. In particular, I have benefited a lot from continuous discussions with the following three astrophysicists. I am extremely fortunate to have a father figure, Prof. Kandaswamy Subramanian, in my journey from very early on. I thank him for introducing me to the wonderful field of astrophysical magnetic fields and for always supporting me. I enjoy discussing astrophysics with him and have learned a lot from him. I am grateful to Prof. Ellen G. Zweibel for hosting me at her department and very useful discussions on various topics including cosmic ray streaming, cosmic ray hydrodynamics, the multiphase ISM and magnetic field observations. It is an absolute pleasure to discuss astrophysics with her and I got to learn so much from her. I also thank her for helping me find a postdoctoral position. I thank Dr. Sui Ann Mao for teaching me Miriad (a radio interferometry data reduction package) and for very useful discussions on a number of topics related to magnetic field observations. I really appreciate her support and care.

During my PhD, I also got opportunities to visit other research institutes. I have learned a lot from each of my visits and would like to thank all my hosts (in chronological order): Prof. Prateek Sharma (Indian Institute of Science, Bangalore, India), Prof. Ralf Klessen (University of Heidelberg, Heidelberg, Germany), Prof. Ellen G. Zweibel (University of Wisconsin, Madison, USA), Prof. Kandaswamy Subramanian (Inter University Centre for Astronomy and Astrophysics, Pune, India) and Dr. Sui Ann Mao (Max Planck Institute for Radio Astronomy, Bonn, Germany). From my US trip, I also thank Dr. Paolo Desiati, Chad Bustard, Dr. Josh Wiener, Gandhari Wattal, Harsha Gurram, Dr. Luca Comisso, Dr. Arijit Bose and especially Dr. Pallavi Bhat for various discussions and making my visit more enjoyable. I would also like to thank my friends at Bonn, Dr. Rainer Beck, Dr. Marita Krause, Dr. Aritra Basu, Maja Kierdorf and Yik Ki (Jackie) Ma for a number of useful discussions on observations of magnetic fields in galaxies. I would like to thank the members of the IMAGINE Consortium, especially Prof. François Boulanger, Prof. Torsten Enßlin, Dr. Philipp Girichidis, Prof. Marijke Haverkorn, Prof. Silvia Mollerach, Prof. Christoph Pfrommer, Dr. Jörg P. Rachen, Prof. Günter Sigl and Dr. Arjen van Vliet, for interesting

discussions during the meeting at the Lorentz Centre, Leiden in March 2017.

Many thanks to everyone at the UM-DAE CBS, Mumbai. The faculty at CBS nurtured me in my undergraduate days. I owe a lot of my interest in physics and mathematics to them. I am also grateful to many friends at CBS, especially Quanta II, III and IV, for being an integral part of my life. They have taught me various things about life in general. I also thank the friends I made during those days while visiting the National Centre for Radio Astrophysics and the Inter University Centre for Astronomy and Astrophysics.

I would also like to thank my examiners, Dr. Graeme R. Sarson and especially Prof. Torsten Enßlin, for thoroughly going through the thesis, very useful suggestions and an enjoyable viva experience.

At this important stage of my life, I would like to remember my friend Abhijit Varma. He was a very jovial person and his passion for science, arts and sports was inspiring. I thank Rajiv Uncle and Aparna Aunty for visiting me at Newcastle and giving me memories for the lifetime. I am so lucky to meet them, know them and be a small part of their life. They gave me a much better perspective on life and beyond. I wish them health and happiness.

Last but surely not least, I would like to thank my parents, Rajesh Seta and Kiran Seta, and my brother, Dr. Tanvir Seta, for their love, support, and everything. My father has always been very supportive of me. He has given me enough freedom and has encouraged me in all my endeavours. I am inspired by my brother's excellent academic record and dedication towards his challenging profession. My mother is my hero. We chat about anything and everything and in that process, she subtly teaches me a lot about life. I think this thesis indirectly completes her dream of pursuing higher studies.

I am quite overwhelmed with this fantastic journey and hope the destination paves the way for a new beginning.

Declaration

This dissertation is based on the research conducted at the School of Mathematics, Statistics and Physics, Newcastle University from September 2014 to June 2018. The material presented is original except where reference is made to the work of others in the text. The chapter-wise details are given below.

- Chapter 2 is based on the paper in preparation:
  Amit Seta, Paul J. Bushby, Anvar Shukurov, Toby S. Wood
  "Saturation mechanism of the nonlinear fluctuation dynamo".

- Chapter 3 (except Section 3.1, Section 3.5 and Section 3.7) is largely based on the published paper:
  Anvar Shukurov, Andrew P. Snodin, **Amit Seta**, Paul J. Bushby, Toby S. Wood
  "Cosmic rays in intermittent magnetic fields",
  The Astrophysical Journal Letters, 839, L16, 2017,
  where I developed a parallel code to generate intermittent magnetic fields using the single scale flow, developed a parallel code for particle propagation in intermittent and randomized magnetic fields, confirmed the cosmic ray random walk model numerically, and contributed to writing the paper.

- Chapter 4 (except Section 4.1, Section 4.2, Section 4.4, Section 4.9 and Section 4.11) is based on the published paper:
  Amit Seta, Anvar Shukurov, Toby S. Wood, Paul J. Bushby, Andrew P. Snodin
  "Relative distribution of cosmic rays and magnetic fields",
  Monthly Notices of the Royal Astronomical Society, 473, 4544, 2018.

- Chapter 5 is based on the paper in preparation:
  Amit Seta, Christopher A. Hales
  "Magnetic fields in elliptical galaxies: an observational probe for the fluctuation dynamo action".

Amit Seta
Newcastle Upon Tyne
July 2019

List of Symbols

Symbol	Description
ψ	polarization angle
$\mathcal{P}$	fractional polarization
RM	rotation measure
DM	dispersion measure
ν	kinematic viscosity
η	magnetic diffusivity
Re	Reynolds number
Re_{M}	magnetic Reynolds number
$\mathrm{Re}_{\mathrm{M}}^{(\mathrm{crit})}$	critial magnetic Reynolds number
Pr_{M}	magnetic Prandtl number
$\mathbf{u}$	turbulent velocity field
k_{F}	forcing wavenumber for driven flow
$\mathbf{b}$	small-scale or random magnetic field
$\mathbf{B}_0$	large-scale or mean magnetic field
$\mathbf{B}$	total magnetic field
r_{L}	Larmor radius of a cosmic ray particle
l_u	correlation length of turbulent velocity field
l_b	correlation length of small-scale magnetic field
l_0	driving scale of turbulence
ω_0	Larmor frequency of a cosmic ray particle
v_{A}	Alfvén speed
v_0	cosmic ray particle speed
c	speed of light
t_{d}	diffusion time for cosmic rays
κ	cosmic ray diffusivity
μ	cosmic ray pitch angle
n_{e}	thermal electron number density
n_{cr}	cosmic ray number density
n_{crp}	cosmic ray proton number density
n_{cre}	cosmic ray electron number density

List of Figures

1.1 High resolution magnetogram of a solar active region taken using Solar and Heliospheric Observatory - Michelson Doppler Imager (Krivova & Solanki, 2004). The dark and white patches show magnetic fields of opposite polarity and grey shows zero magnetic flux. The random distribution of strong magnetic field regions surrounded by very high magnetic field is a sign of spatial intermittency on the surface of the Sun. 6

1.2 Magnetic field from the first numerical simulation of fluctuation dynamo (Meneguzzi et al., 1981). The shaded regions show the magnetic field (within less than 5% of its maximum value). The magnetic field is concentrated in small regions, which confirms spatial intermittency of the amplified magnetic fields. 7

1.3 Slices of gas density from a three dimensional simulation of supersonic turbulence driven by solenoidal (left panel) and compressible (right panel) forcing (Federrath, 2013). The gas density is stronger in filaments and the field is more intermittent (higher kurtosis) when the turbulence is driven by a compressible forcing. 7

1.4 Snapshots of water flow past a circular cylinder for (a) Re $= 0.16$, (b) Re $= 9.6$, (c) Re $= 26$ and (d) Re $= 2000$ (van Dyke, 1982). Streamlines are seen by aluminium dust in water for (a),(b) and (c), and by air bubbles in water for (d). For low Re the flow is laminar but as Re increases the flow past the cylinder becomes more and more turbulent. 9

1.5 Initially laminar smoke streams becomes turbulent on passing through a plate with perforations (van Dyke, 1982). Based on the mesh size, Re $= 1500$. . . . 10

1.6 Turbulence produced by sweeping grid of bars at uniform velocity through a still water tank (Sreenivasan, 1999). Unlike Fig. 1.4 and Fig. 1.5, the turbulence here is homogenous and isotropic. The distribution is clearly intermittent with many small-scale structures. 11

1.7 Energy spectrum obtained from a series of experiments: turbulence generated by boundary layers, wakes, grids, pipes, ducts, jets, and tides in the ocean (Pope, 2000). On scaling both axis with properties of the system, all curves lie along same the line. Thus, the viscosity or the large-scale properties of a turbulent system, doesn't affect the spectra in the inertial range and the Kolmogorov scaling is universal. 13

1.8 Energy spectra normalized with Kolmogorov scaling obtained from direct numerical simulations by solving Navier-Stokes equation (Gotoh et al., 2002). The horizontal line shows 1.64. The curves lie on top of each other independent of R_λ, which is the Reynolds number. This confirms Kolmogorov scaling. 14

1.9 The PDFs of a single velocity field component obtained from numerical simulations for various Reynolds numbers, here given by R_λ (Gotoh et al., 2002). The PDFs are non-Gaussian with heavy tails confirming that the velocity field is intermittent. Also, as Reynolds number increases, intermittency increases. . 14

1.10 Power spectrum of fluctuations in electron density in the ISM obtained from variety of observations (Armstrong et al., 1995). The power law spectrum confirms that the ISM is turbulent and the slope approximately agrees with the Kolmogorov theory. 15

1.11 Illustration of the α (left) and ω (right) effect (Ruzmaikin et al., 1988). The left panel shows poloidal magnetic field is generated by twisting loops of toroidal magnetic field in a galaxy and the right panel shows the conversion poloidal magnetic field into toroidal magnetic field by differential rotation. . . 22

1.12 The cosmic ray spectrum for different particle types obtained from a number of experiments (Zweibel, 2013). It is a power law spectrum (with energy spectral index $\delta = 2.7$ above $10\,\mathrm{GeV}$) across a huge range of energy scales. . 26

1.13 Figure taken from ACE News #83 - Oct 6, 2004. Relative abundance of various elements in solar system (blue) and galactic cosmic rays (black) measured using the Advanced Composition Explorer (ACE) spacecraft managed by National Aeronautics and Space Administration (NASA). Except lighter elements, galactic cosmic ray composition is very similar to the solar abundances. The excess of certain elements (Be is in excess by six orders of magnitude) in galactic cosmic rays is due to interaction of galactic cosmic rays with the interstellar gas. 28

1.14 Distribution of isotopes of Be in low energy (few GeV) galactic cosmic rays (a) and in laboratory (b) (Garcia-Munoz et al., 1977). The isotopes Be^9 and Be^{10} have much less counts as compared to other isotopes because of the radioactive decay. 29

1.15 Combined cosmic ray anisotropy $\delta_{\rm cr}$ derived from data from Tibet-AS and IceCube experiments (Ahlers & Mertsch, 2017). Even at relatively high energy (10^3 times higher than the average cosmic ray energy of GeV), the level of anisotropy is quite small ($\sim 10^{-3}$) and cosmic ray distribution can be considered almost isotropic. 30

1.16 Figure taken from Planck's webpage. It shows the dust emission at 353 GHz where the color shows the total intensity (blue minimum, intense red maximum) and the striations show the direction of the Milky Way magnetic field projected on the plane of the sky. 38

1.17 Gradient of observed linear polarization for patch of the Milky Way (Gaensler et al., 2011). By comparing statistics of the gradient with that obtained from the numerical simulations, it can be shown that the ISM is turbulent with Mach number approximately equal to 2. 39

1.18 Contours of total synchrotron intensity overlaid on the top of the optical image and lines shows the magnetic field vectors obtained from polarized intensity in M51 (Fletcher et al., 2011). The polarized synchrotron intensity traces the ordered magnetic field (field generated by the large-scale dynamo and anisotropic turbulent field). 40

1.19 (a) A statistical study to detect magnetic field in high redshift galaxies (Bernet et al., 2008). Cumulative histogram showing number of RM measurements with value less than that on the x axis for systems with no MgII absorber (red), one of more MgII absorbers (blue) and two MgII absorbers (black). The systems with MgII absorbers statistically shows higher values of RM. This can be used to study properties of magnetic fields in high redshift galaxies. (b) An observational study to detect magnetic field in an individual high redshift galaxy (Mao et al., 2017). Faraday depth spectra (fractional polarization versus Faraday depth) of two gravitationally lensed images (blue and red) with lensing galaxy at a redshift of 0.439. The difference in the mean and standard deviation of two components is used to infer the magnetic field in the lensing galaxy. 41

1.20 Flowchart showing interactions between cosmic rays and magnetic fields in the ISM which leads to cosmic ray diffusion. 43

2.1 The stretch-twist-fold-merge mechanism (image credits: Anvar Shukurov). S and B are the cross section and magnetic field strength of the initial flux tube. $\phi = SB$ is the magnetic flux associated with the tube. 48

2.2 Log-log plots of kinetic (E_k, dashed) with a well-defined inertial range and magnetic (M_k, solid) energy spectra for the fluctuation dynamo at $\mathrm{Pr_M} \gg 1, l_\eta \ll l_\nu$ (a) and $\mathrm{Pr_M} \ll 1, l_\eta \gg l_\nu$ (b). 50

2.3 The evolution of the magnetic field obtained in the Roberts flows in a periodic box of non-dimensional size $(2\pi)^3$ with 128^3 mesh points for various $\mathrm{Re_M}$ with $k_\mathrm{F} = 5$ (a) and for various forcing wave numbers k_F with $\mathrm{Re_M} = 1250$ (b). $t_0 = 1/\,u_\mathrm{rms} k_\mathrm{F}$ is the eddy turnover time. 52

2.4 (a) The 2D cut in the xy-plane of the velocity field through the middle of the domain with vectors $(u_x/\,u_\mathrm{rms}, u_y/\,u_\mathrm{rms})$ and colours showing the magnitude of $u_z/\,u_\mathrm{rms}$ for the Roberts flow with $k_\mathrm{F} = 1$ and $\mathrm{Re_M} = 1250$ in a 128^3 simulation. (b) As (a) but for the exponentially growing magnetic field. . . . 53

2.5 Isosurfaces of $b^2/\,b^2_\mathrm{rms} = 2$ (blue) and $b^2/\,b^2_\mathrm{rms} = 3$ (yellow) for the magnetic field generated by using the Roberts flow with $k_\mathrm{F} = 1$ and $\mathrm{Re_M} = 1250$ in a 128^3 simulation. 54

2.6 As in Fig. 2.4 but for $k_\mathrm{F} = 5$. 55

2.7 As in Fig. 2.4 but for the ABC flow with $A = B = C = 1$, $k_{\mathrm{F}x} = k_{\mathrm{F}y} = k_{\mathrm{F}z} = 1$ and $\mathrm{Re_M} = 1250$. 57

2.8 Isosurfaces of $b^2/\,b^2_\mathrm{rms} = 3$ (blue) and $b^2/\,b^2_\mathrm{rms} = 4$ (yellow) for the magnetic field generated by the ABC flow with $A = B = C = 1$, $k_{\mathrm{F}x} = k_{\mathrm{F}y} = k_{\mathrm{F}z} = 1$ and $\mathrm{Re_M} = 1250$ in a 128^3 simulation. The magnetic structures are of various sizes and are randomly oriented. 58

2.9 As in Fig. 2.4 but for the Galloway–Proctor flow with $k_{\mathrm{F}y} = k_{\mathrm{F}z} = 1, \omega = 1$, $A = C = \sqrt{3/2}$ and $\mathrm{Re_M} = 1250$. 59

2.10 Isosurfaces of $b^2/\,b^2_\mathrm{rms} = 3$ (blue) and $b^2/\,b^2_\mathrm{rms} = 4$ (yellow) for the magnetic field generated by using the Galloway–Proctor flow with $k_{\mathrm{F}y} = k_{\mathrm{F}z} = 1$, $\omega = 1$, $A = C = \sqrt{3/2}$ and $\mathrm{Re_M} = 1250$ in a 128^3 simulation. The magnetic structures are of a fixed shape and are equidistant. 60

2.11 A 2D cut in the xy-plane through the middle of the domain with vectors $(b_x/\,b_\mathrm{rms}, b_y/\,b_\mathrm{rms})$ and colours showing the magnitude of $b_z/\,b_\mathrm{rms}$ for the W flow with $\mathrm{Re_M} = 314$ in a periodic box of non-dimensional size $(2\pi)^3$ with 256^3 points. 60

2.12 A 2D cut in the xy-plane through the middle of the domain with vectors $(b_x/\,b_{\mathrm{rms}}, b_y/\,b_{\mathrm{rms}})$ and colours showing the magnitude of $b_z/\,b_{\mathrm{rms}}$ for the KS flow with $\mathrm{Re_M} = 4800$ in a periodic box of a non-dimensional size 2π with 512^3 mesh points 61

2.13 Isosurfaces of $b^2/\,b^2_{\mathrm{rms}} = 3$ (blue) and $b^2/\,b^2_{\mathrm{rms}} = 4$ (yellow) for the magnetic field generated by the KS flow with $\mathrm{Re_M} = 4800$ in a periodic box of a non-dimensional size $(2\pi)^3$ with 512^3 mesh points. The magnetic filaments are of various shapes and sizes. 62

2.14 The probability density function of the single magnetic field component $b_x/\,b_{\mathrm{rms}}$ generated by the KS flow for various values of magnetic Reynolds number $\mathrm{Re_M}$ as specified in the legend. The dashed curve shows a Gaussian distribution. The distribution is strongly non-Gaussian with long tails. 62

2.15 The magnetic field spectra M_k for various magnetic Reynolds numbers $\mathrm{Re_M}$ (specified in the legend) in the KS flow. The spectrum at smaller wave numbers follows the Kazantsev spectrum, $M_k \propto k^{3/2}$ (dashed) and the resistive scale increases with $\mathrm{Re_M}$. 63

2.16 Root mean square (rms) of the velocity field u_{rms} and magnetic field b_{rms} as functions of normalized time t/t_0 (where $t_0 = 1/\,u_{\mathrm{rms}}k_{\mathrm{F}}$, the eddy turnover time) for $\mathrm{Re_M} = 1122$. The randomly initialized magnetic field first decreases till it evolves into an eigenfunction of the induction equation and then increases exponentially with time (black-dashed) during the kinematic stage (area shaded in light red). As magnetic field grows, its feedback on the flow slows down the exponential increase (the transition stage, area shaded in light green). Finally, the magnetic field reaches a statistically steady state in the saturated stage (area shaded in light blue). 66

2.17 The shell-averaged (one-dimensional) kinetic E_k (dashed) and magnetic M_k (solid) energy spectra in the kinematic (red), transition (green) and saturated (blue) stages for $\mathrm{Re_M} = 1122$. The kinetic energy spectrum roughly follows the Kolmogorov spectrum, $E_k \propto k^{-5/3}$ (dotted, black). The magnetic spectra are initially peaked at large wave numbers with $M_k \propto k^{3/2}$ (dashed, black) at smaller wave numbers (Kazantsev, 1968). As the magnetic field saturates, the power shifts to smaller wave numbers and the magnetic spectrum flattens. 67

2.18 The PDF of the normalized velocity field component $u_x/u_{\rm rms}$ for $\rm Re_M = 1122$ and $\rm Re_M = 2244$ in the kinematic (dashed) and saturated (solid) stages for the value of $\rm Re_M$ given in the legend. The velocity field is roughly Gaussian (dashed, black) in both the stages for both $\rm Re_M$. 68

2.19 A 2D cut in the xy-plane with vectors $(u_x/u_{\rm rms}, u_y/u_{\rm rms})$ and colour showing the magnitude of $u_z/u_{\rm rms}$ in the kinematic (a) and saturated (b) stages with $\rm Re_M = 2244$. The velocity field in both the stages looks qualitatively the same. The structures are of the size of half of the domain. 69

2.20 The PDF of the normalized magnetic field component $b_x/b_{\rm rms}$ for $\rm Re_M = 1122$ and $\rm Re_M = 2244$ in the kinematic (dashed) and saturated (solid) stages for the values of $\rm Re_M$ given in the legend. The magnetic field for both $\rm Re_M$ in both stages is far from a Gaussian (dashed, black). It has heavy tails which is a sign of intermittency. 70

2.21 The PDF of the normalized magnetic field strength $b/b_{\rm rms}$ for $\rm Re_M = 1122$ and $\rm Re_M = 2244$ in the kinematic (dashed) and saturated (solid) stages for the values of $\rm Re_M$ given in the legend. The PDF of the magnetic field in the kinematic state follows a lognormal distribution (dashed, black). The magnetic field is more intermittent in the kinematic stage than in the saturated stage. 71

2.22 As Fig. 2.19 but for the magnetic field. The magnetic field in the kinematic stage is intermittent with random magnetic structures. In the saturated stage, the field remains intermittent but the structures are larger. 72

2.23 Schematic of the folded structure of the magnetic field. The field is amplified by turbulent velocity via its stretching $\mathbf{u_s}$ and compressive $\mathbf{u_c}$ components. The field reverses several times within a magnetic structure. The field direction changes along the smaller length scale which is comparable to the resistive scale l_η and the length of the folds are the order of the viscous scale l_ν. 76

2.24 A 2D cut in the xy-plane with vectors $(b_x/b_{\rm rms}, b_y/b_{\rm rms})$ and colours showing the magnitude of $b_z/b_{\rm rms}$ in the saturated stage with $\rm Pr_M = 50$. The red circle shows a magnetic structure where the field reverses and the blue circle shows a strong magnetic structure where such a reversal is not observed. At high $\rm Pr_M$, magnetic structures with both the presence and absence of field reversals within them are observed (and are also seen in previous studies, e.g. Brandenburg & Subramanian, 2005). 77

2.25 Two dimensional correlation of $\mathbf{u} \cdot \nabla \mathbf{u}$ and $\mathbf{b} \cdot \nabla \mathbf{b}$ for a run with $\mathrm{Pr_M} = 50$. Both quantities are approximately equal in magnitude and uncorrelated. . . . 78

2.26 The total and conditional probability distribution functions of the cosines of the angles between $\mathbf{u}$ and $\mathbf{b}$, $\cos(\theta)_{\mathbf{u},\mathbf{b}}$ (a) and between $\mathbf{j}$ and $\mathbf{b}$, $\cos(\theta)_{\mathbf{j},\mathbf{b}}$ (b) for $\mathrm{Re_M} = 1122$ in the kinematic (red) and saturated (blue) states. The magnetic field in the saturated stage is more aligned with velocity field (reducing the induction effects) as compared to kinematic stage. The magnetic field also become better aligned with the electric current density, reducing the back reaction on the velocity field. 81

2.27 As Fig. 2.26 but for $\mathrm{Re_M} = 1496$. 82

2.28 The cross correlation of $\cos(\theta)_{\mathbf{u},\mathbf{b}}$ and $\cos(\theta)_{\mathbf{j},\mathbf{b}}$ in the kinematic (a,c) and saturated (b,d) stages for $\mathrm{Re_M} = 1122$. Panels (a) and (b) refers to the whole domain and the difference between them is not significant. Panels (c) and (d) refers to only the strong field regions ($b/\,b_{\mathrm{rms}} \geq 1.5$). The yellow patch close to low $\cos(\theta)_{\mathbf{j},\mathbf{b}}$ and high $\cos(\theta)_{\mathbf{u},\mathbf{b}}$ in the kinematic stage vanishes for the saturated stage. The peak in the count is always at high $\cos(\theta)_{\mathbf{u},\mathbf{b}}$ and high $\cos(\theta)_{\mathbf{j},\mathbf{b}}$, which implies significant alignment between magnetic field, velocity field and current density. 83

2.29 The total and conditional PDFs of the cosine of the angle between the direction of local compression and the magnetic field $\cos(\theta)_{\mathbf{e}_1,\mathbf{b}}$ (a) and between the direction of local stretching and the magnetic field $\cos(\theta)_{\mathbf{e}_3,\mathbf{b}}$ (b) for $\mathrm{Re_M} = 1796$ in the kinematic (red) and saturated (blue) stages. 85

2.30 The total and conditional PDFs of the local growth term $\lambda_1 \mathbf{b}_1^2 + \lambda_2 \mathbf{b}_2^2 + \lambda_3 \mathbf{b}_3^2$ (a) and the local dissipation term $\mathbf{j}^2$ (b) in the kinematic (red) and saturated (blue) stages for $\mathrm{Re_M} = 1122$. When the local growth term is negative, its magnitude is plotted and this denoted by '$-$' in the legend. Both the local growth and dissipation terms over the entire volume decreases on saturation. This is true same in both the weak and strong field regions, except for the local dissipation term, which increases in the weak field regions. 87

2.31 As Fig. 2.30 but for $\mathrm{Re_M} = 1796$. 88

2.32 The total and conditional PDFs of the local magnetic Reynolds number $(\mathrm{Re_M})_{\mathrm{loc}}$ in the kinematic (red) and saturated (blue) stages with $\mathrm{Re_M} = 1122$. The purple dashed line shows the critical magnetic Reynolds number $\mathrm{Re_M^{(crit)}} = 220$ and the black dashed line shows $\mathrm{Re_M}$ for this run. 89

2.33 As Fig. 2.32 but for $\mathrm{Re_M} = 1796$. 90

2.34 (a)The iso-surfaces of simple structures, showing the transition from a sphere to a filament. Planarity and filamentarity (p, f) for these shapes are: sphere $(2\times10^{-4}, 3\times10^{-5})$, pancake $(0.92, 0.12)$, thick filament $(0.47, 0.75)$ and thin filament $(0.07, 0.92)$. (b) The (p, f) plane showing the transition between various shapes as α and β are varied in Eq. (2.37) (the Blaschke diagram). Solid line: $\alpha = 1$ constant, β increasing, the transition from a sphere to a pancake. Dashed line: α increasing, $\beta \gg 1$ constant, the transition from a pancake to a filament. Dotted line: $\alpha \gg 1$ decreasing to $\alpha = 1$, $\beta \gg 1$ decreasing to $\beta = 1$, transition from a filament to a sphere. 93

2.35 Isosurfaces of $b/b_{\text{rms}} = 2$ (blue) and $b/b_{\text{rms}} = 3$ (yellow) for the magnetic field generated by using the W flow (Eq. (2.5)) with $\text{Re}_{\text{M}} = 314$ in a periodic box of non-dimensional size $(2\pi)^3$ with 256^3 grid points. 94

2.36 (a) Thickness T, width W and length L of magnetic structures obtained using the W flow as a function of the level of magnetic field $\alpha = b/b_{\text{rms}}$. All three dimensions decrease as magnetic field strength (α) increases and at approximately the same rate. (b) Planarity p and filamentarity f for those structures as a function of the magnetic field strength level α. $f > p$, so the structures are filamentary. Also, p roughly remains constant as α increases but f increases. This can be confirmed in qualitative terms by a visual inspection of Fig. 2.35. 95

2.37 Average length (L), thickness (T) and width (W) of magnetic structures generated by a kinematic fluctuation dynamo with the KS flow as functions of Re_{M}. The average is calculated over 30 magnetic field levels between $\alpha = b/b_{\text{rms}} = 2.5$ and $\alpha = b/b_{\text{rms}} = 4.5$. The length roughly remains constant as Re_{M} changes. The other two length scales, T and W, decrease as Re_{M} increases, approximately as $\text{Re}_{\text{M}}^{-0.4}$. 96

2.38 (a) Average length (L), thickness (T) and width (W) of magnetic structures in the kinematic (dashed, color) and saturated stages (solid, color) of the non-linear fluctuation dynamo as functions of $\mathrm{Re_M}$. The length of the structures L roughly remains the same with $\mathrm{Re_M}$. The slight increase in the length after $\mathrm{Re_M} \approx 600$ is because of the decrease in Re (see Table 2.4). The width and thickness of the magnetic structures both decrease as $\mathrm{Re_M^{-0.5}}$. The $\mathrm{Re_M}$ dependence of the size of the structures is approximately the same in both the kinematic and saturated stages. (b) Planarity (p) and filamentarity (f) of the magnetic structures functions of $\mathrm{Re_M}$ for the kinematic (dashed, color) and saturated (solid, color) stages. As $\mathrm{Re_M}$ increases, the filamentarity increases and the planarity decreases but they seem to approach an asymptotic value after $\mathrm{Re_M} \approx 1200$. The trend with respect to $\mathrm{Re_M}$ is the same for both the kinematic and saturated stages. 99

3.1 Trajectories of a low-energy particle in a turbulent magnetic field. a) Particle following a field line giving rise to Field Line Random Walk (FLRW) limit for an ensemble of particles over a long time. b) Particle following the field line initially but is then backscattered, eventually giving rise to diffusion along the magnetic field line for an ensemble of particles over a long time. c) Particle after following field line for some time, jumps to another field line, which over a long time for an ensemble of particles gives rise to diffusion perpendicular to the magnetic field line. 103

3.2 Isosurfaces of $b^2/b^2_{\mathrm{rms}} = 2.5$ (blue) and $b^2/b^2_{\mathrm{rms}} = 5$ (yellow) for the intermittent magnetic field at $\mathrm{Re_M} = 314$ generated by the W flow (a) and for the same magnetic field after randomizing phases (b). Intermittent field shows filaments of fixed shape (a specific consequence of this choice of flow) whereas randomized field lacks such elongated structures. 107

3.3 As Fig. 3.2 but now for the KS flow with $\mathrm{Re_M} = 3182$. Intermittent field (a) shows filaments of various width, length, and thickness, whereas randomized (b) field lacks such structures. 108

3.4 2D cut in the yz–plane through the middle of the domain with vectors for $(b_y/\,b_{\rm rms}, b_z/\,b_{\rm rms})$ and colours showing the magnitude of $b_x/\,b_{\rm rms}$ for intermittent (a) and randomized (b) magnetic field generated using the W flow for $\mathrm{Re_M} = 314$. For intermittent magnetic field the colours are saturated for both positive and negative values to match the scale of the randomized field. The intermittent magnetic field is more ordered and stronger in the filaments, whereas the randomized field lacks such structures. 109

3.5 A Fig. 3.4 but now for the KS flow for $\mathrm{Re_M} = 3182$. For intermittent magnetic field (a) the colours are saturated for both positive and negative values to match the scale of the randomized field (b) (see the x-axis of Fig. 3.7 for the actual difference in numbers). The randomized field lacks structures seen in the intermittent field. 110

3.6 Spectra of intermittent NR (red, magneta) and randomized R (blue dashed, green dashed) magnetic fields generated using W flow ($\mathrm{Re_M} = 314$) and KS flow ($\mathrm{Re_M} = 1082$) respectively. For both flows, the spectra of intermittent and randomized magnetic fields is identical. For KS flow, the spectra agrees with the Kazantsev scaling (Kazantsev, 1968) $k^{3/2}$ (black dotted) power law spectrum at small wavenumbers. The scaling holds only for flows which are δ-correlated in time and only the KS flow is time dependent. 111

3.7 PDFs of $b_x/\,b_{\rm rms}$ for intermittent (blue) and randomized (red) magnetic field generated using the KS flow for $\mathrm{Re_M} = 3182$. Both have zero mean but the intermittent magnetic field has long tails, whereas the randomized field (obtained by Fourier phase randomization) has a Gaussian PDF (dashed). . . 111

3.8 Single particle trajectories for $r_{\rm L}/l_b = 0.45$ (a) and 13 (b) in the intermittent magnetic field of Fig. 3.5a. Colours shows the strength of the magnetic field along the trajectory normalized to its maximum value along the part of trajectory shown. For $r_{\rm L}/l_b = 0.45$, the particle path is more tangled than for $r_{\rm L}/l_b = 13$ where the particle motion is almost ballistic between rare scattering events. Also note different spatial scales. 113

3.9 Same as Fig. 3.8 but for the randomized magnetic field. More scattering events are seen in these trajectories in comparison to the particle trajectories in the intermittent magnetic field. 114

3.10 The cosmic ray diffusion coefficient for the W flow, $\mathrm{Re_M} = 314$ (red) and the KS flow, $\mathrm{Re_M} = 3182$ (blue) as a function of $r_{\rm L}/l_0$. For $r_{\rm L} \gg l_0$, the diffusion coefficient follows the high-energy scaling $\kappa \propto r_{\rm L}^2$ (dashed black). . 116

3.11 The ratio of diffusion coefficients from intermittent, κ, and randomized, κ_{R}, magnetic fields for the KS flow, $\mathrm{Re}_{\mathrm{M}} = 1082$ (red), 3182 (blue). The dashed lines of same colour show the corresponding CRW model, Eq. (3.15). 117

3.12 The ratio of perpendicular, $\kappa_{\perp}$, to parallel, $\kappa_{\parallel}$, diffusion coefficients for intermittent (solid lines) and randomized (dashed lines) magnetic fields in the presence of a mean magnetic field $b_{\mathrm{rms}}/B_0 = 1$ (magenta), 2 (blue) for the KS flow. The red dash–dotted line shows the ratio obtained using Eq. (3.13) for each case. 120

3.13 The ratio of diffusion coefficients from intermittent, κ, and randomized, κ_{R} magnetic fields in the presence of a mean magnetic field $b_{\mathrm{rms}}/B_0 = 1$ (magenta), 2 (blue) for the KS flow, $\mathrm{Re}_{\mathrm{M}} = 3182$; $\kappa_{\parallel}$ and $\kappa_{\perp}$ are shown solid and dashed, respectively. 120

3.14 A charged particle with the pitch angle β is deflected by an angle θ in a magnetic structure of a thickness d. The dashed-line represents the particle moving out of the paper and going back in again to represent the gyration of the particle around the magnetic field shown in red, which is assumed to be in the plane of the paper. 122

3.15 The dependence of cosmic ray diffusivity in intermittent and randomized magnetic fields on $\langle\cos\theta\rangle$ (solid lines) for W (a) and KS (b) flow. The corresponding CRW approximations (Eq. (3.15) with $\langle\cos\theta\rangle$ calculated from the simulated particle trajectories) are shown with dashed lines. The different data points refer to different values of r_{L}/l_0. These results are obtained for $B_0 = 0$. 123

3.16 Figure taken from Tautz & Lerche (2016). Isotropic cosmic ray intensity f as a function of time t obtained by solving the diffusion equation (blue dashed), by solving the telegraph equation (black) and that obtained from test-particle simulations (red). Initially, the telegraph equation better captures the ballistic behaviour of the particles but over long time, both the diffusion equation and the telegraph equation give similar solutions. Both f and t are given in arbitrary units. 126

4.1 Normalized cosmic ray diffusivity $\kappa/v_0 l_0$ as a function of normalized time $\omega_0 t$ for $r_\mathrm{L}/l_0 = 0.016, 0.159, 1.592$ for the intermittent (a) and randomized (b) magnetic fields shown in Fig. 3.5. The dashed lines of the corresponding colours show the time t_d after which the propagation becomes diffusive: $\kappa(t) \approx \kappa$ at $t > t_\mathrm{d}$. For low energy particles ($r_\mathrm{L} \leq l_b$), the diffusivity in the intermittent magnetic field is larger than in the randomized (Gaussian) field of identical power spectrum as discussed in Section 3.4. 134

4.2 Cosmic ray (velocity direction shown by blue arrow) interacting with a localized magnetic fluctuation of magnitude δB with mean field along the z-axis. . 135

4.3 Pitch angle μ calculated from the trajectory of a single particle obtained numerically as a function of normalized time $\omega_0 t$ for the case where the gyroresonance condition holds (a) and doesn't hold (b). When gyroresonance condition is satisfied, the particle is scattered and its pitch angle changes. Also for such a scattering $\delta\mu \propto \delta B/B_0$ as shown in (a). When the gyroresonance condition doesn't hold, the particle's pitch angle varies across the magnetic fluctuation but returns back to its initial pitch angle once the particle crosses the fluctuation. Thus, $\delta\mu = 0$ for the case (b). To avoid overlap in (b), the time axis for case $\delta B/B_0 = 0.01$ and $\delta B/B_0 = 0.1$ are shifted by $+50$ and -50 normalized time units respectively. 138

4.4 Sketch of the power spectrum of the random magnetic field showing the energy cascade from a larger scale (l_max, usually the driving scale of turbulence) to the Larmor radius (r_L) of the particle. The field is isotropic up to a transition scale (l_t) and then it becomes anisotropic (Goldreich & Sridhar, 1995). When the turbulence is anisotropic, the power spectrum for parallel fluctuations is steeper than that for the perpendicular case. However, for the gyroresonance condition (Eq. (4.7)) only the fluctuations parallel to the field are important and thus we only consider that for our estimate. 143

4.5 Normalized parallel $\kappa_\parallel/v_0 l_0$ (a) and perpendicular $\kappa_\perp/v_0 l_0$ (b) cosmic ray diffusivity as a function of normalized time $\omega_0 t$ for particles propagating in a uniform magnetic field but with pitch angle scattering (PAS) model included. Initially, the particle gyrates around magnetic field and thus $\kappa_\parallel$ varies linearly with time and because of gyration the $\kappa_\perp$ oscillates. After sufficient scattering, the diffusion sets in both in the direction parallel and perpendicular to the imposed uniform magnetic field. The red dotted line shows the diffusion time t_d. 145

4.6 Time correlation function of pitch angle μ as a function of normalized time $\omega_0 t$ for particles propagating in a uniform magnetic field with PAS included. The correlation gradually decreases and drops to ≈ 0 once the diffusion sets in. This can also be used to determine the diffusion time t_d (shown by the red dotted line). 146

4.7 Probability density function (PDF) of the relative number density of cosmic ray particles, $n_\mathrm{cr}/\langle n_\mathrm{cr}\rangle$, where $\langle n_\mathrm{cr}\rangle$ is the mean cosmic ray number density over the numerical domain, for various r_L/l_0 in intermittent (a) and randomized (Gaussian) magnetic fields (b), with no mean-field and no pitch angle scattering (PAS). Long tails are a signature of intermittent structures in the cosmic ray distribution. For high-energy particles, the distribution is nearly Gaussian (with width increasing as energy decreases) in both intermittent and Gaussian magnetic fields, but below a certain energy ($r_\mathrm{L} \lesssim l_b$) long tails develop. A black dashed line shows the PDF of a random variable drawn from a Gaussian distribution with unit mean value and standard deviation of 0.07 (obtained by fitting the Gaussian). 147

4.8 PDF of $n_\mathrm{cr}/\langle n_\mathrm{cr}\rangle$ for $r_\mathrm{L}/l_0 = 0.0016$ in the intermittent field with an imposed mean field of various magnitudes B_0 (a) and with the pitch angle scattering further included (b). Intermittency in the cosmic ray distribution increases as the mean field becomes stronger, especially for $B_0/\,b_\mathrm{rms} \geq 1$, manifested in heavier tails at larger $n_\mathrm{cr}/\langle n_\mathrm{cr}\rangle$. The pitch angle scattering enhances diffusion and thus decreases the level of intermittency. 148

4.9 (a) Isosurfaces of the number density of cosmic rays in the intermittent magnetic field at $n_\mathrm{cr}/\langle n_\mathrm{cr}\rangle = 3.5$ for $r_\mathrm{L}/l_0 = 0.0016$. A number of small-scale cosmic ray structures are seen confirming an intermittent cosmic ray distribution. (b) The variation of the relative number density of the particles along the straight line $(x, z) = (\pi, 3.97)$, characterized by rare, strong maxima against a weakly fluctuating background. 149

4.10 Isosurfaces of the number density of cosmic rays at $n_\mathrm{cr}/\langle n_\mathrm{cr}\rangle = 3.5$ for $r_\mathrm{L}/l_0 = 0.0016$ in an intermittent magnetic field with an imposed mean field of a strength $B_0/\,b_\mathrm{rms} = 1$ aligned with the x-axis (a) and with PAS further added (b). 150

4.11 The fractional volume of cosmic ray structures with $n_{\mathrm{cr}}/\langle n_{\mathrm{cr}}\rangle \geq \nu$ for Models A–E of Table 4.1. A black dashed line shows the fractional volume for a random variable drawn from a Gaussian distribution with unit mean value and standard deviation of 0.07. 152

4.12 PDF of intermittent magnetic field energy density normalized to its rms value, $b^2/\,b_{\mathrm{rms}}^2$, and the number density of cosmic rays normalized to its mean, $n_{\mathrm{cr}}/\langle n_{\mathrm{cr}}\rangle$, for $r_{\mathrm{L}}/l_0 = 0.0016, 0.0032$. All three of them have power-law tails and the same exponent. Statistical errors are considerable at probability densities below about 5×10^{-5}. 152

4.13 The scatter plot of cosmic ray number density, $n_{\mathrm{cr}}/\langle n_{\mathrm{cr}}\rangle$ and magnetic energy density, $b^2/\,b_{\mathrm{rms}}^2$, in an intermittent magnetic field for $r_{\mathrm{L}}/l_0 = 0.0016$. If they are correlated, we would expect a straight line with unit gradient but instead we see a cloud of points. 153

4.14 (a) The joint probability density function (PDF) $p(n_{\mathrm{cr}}, b^2)$ of $b^2/\,b_{\mathrm{rms}}^2$ and $n_{\mathrm{cr}}/\langle n_{\mathrm{cr}}\rangle$ in the intermittent magnetic field for $0 \leq b^2/\,b_{\mathrm{rms}}^2 \leq 0.5$ and $0.25 \leq n_{\mathrm{cr}}/\langle n_{\mathrm{cr}}\rangle \leq 1.75$. (b) The joint PDF $p(n_{\mathrm{cr}}, b^2)$ as a function of $n_{\mathrm{cr}}/\langle n_{\mathrm{cr}}\rangle$ alone for various values of $b^2/\,b_{\mathrm{rms}}^2$ together with least-square fits of the form $p(n_{\mathrm{cr}}, b^2) = A(b^2)\mathrm{e}^{-(n_{\mathrm{cr}}/\langle n_{\mathrm{cr}}\rangle-1.0)^2/0.18}$ (smooth dashed curves). 155

4.15 (a) The height of the curve's peak in Fig. 4.14b A as a function of $b^2/\,b_{\mathrm{rms}}^2$ fitted with an exponential (red, dashed). (b) Scatter plot of the computed and fitted values of $p(n_{\mathrm{cr}}, b^2)$, with a line corresponding to the perfect agreement shown (dashed, blue). Most points lie close to the dashed blue line confirming that the accuracy of the fit is reasonable. 156

4.16 As in Fig. 4.14 but for the randomized (Gaussian) magnetic field for $0 \leq b^2/\,b_{\mathrm{rms}}^2 \leq 3.0$ and $0.25 \leq n_{\mathrm{cr}}/\langle n_{\mathrm{cr}}\rangle \leq 1.75$. 157

4.17 As in Fig. 4.15 but for the randomized (Gaussian) magnetic field for $0 \leq b^2/\,b_{\mathrm{rms}}^2 \leq 3.0$ and $0.25 \leq n_{\mathrm{cr}}/\langle n_{\mathrm{cr}}\rangle \leq 1.75$. 158

4.18 (a) The cosine of the particle pitch angle μ calculated from its trajectory as a function of normalized time $\omega_0 t$ for a single particle reflection. The fact that $\mu_{\mathrm{final}} = -\mu_{\mathrm{initial}}$ confirms that the particle is reflected back along the arrival direction, i.e. oscillates between the magnetic mirrors. (b) The cosine of the pitch angle μ as a function of kx, where k is the wavenumber of the wave and x is the displacement along the x-axis. For particles with the same energy but different initial pitch angles (before they enter the trap). When the initial pitch angle is less than a critical value, the particles are trapped. 160

4.19 (a) A particle trajectory near a maximum of $n_{\rm cr}$ at $(3.15, 2.55, 5.975)$ with magnetic field strength along the trajectory shown with colour. The dark grey lines show magnetic field lines near the trajectory. The particle moves forward and backward between two magnetic mirrors. (b) The particle pitch angle μ as a function of z with magnetic field strength colour coded. The particle turns around (μ changes sign) at the magnetic mirrors, regions where magnetic field is stronger. 162

4.20 The PDFs of cosmic ray number density on increasing the averaging time (a) and decreasing number of particles from 8192 (Fig. 4.7a) to 1024 (b) for $r_{\rm L}/l_0 = 0.0016$ in the intermittent magnetic field. The distribution tends to be less intermittent (weaker tail in the distribution) as the averaging time increases or the number of particles increases. As the averaging time or number of particles increases even further, we expect that the distribution would tend to a Gaussian distribution and would eventually become a delta function at $n_{\rm cr} = \langle n_{\rm cr}\rangle$ for a very large averaging time or equivalently a large number of particles. 166

4.21 Time evolution of the rms velocity field $u_{\rm rms}$ (red) , rms magnetic field $b_{\rm rms}$ (blue) and mean cosmic ray energy density $\langle e_{\rm cr}\rangle$ (magenta) as a function of normalized time t/t_0, where t_0 is the eddy turnover time, for the case where $\langle e_{\rm cr}\rangle > b^2_{\rm rms}$. The magnetic field decreases till it becomes an eigenfunction of the induction equation and then it grows exponentially (kinematic stage, light pink). The magnetic field finally saturates (saturated stage, light blue) due to the back reaction on the velocity flow by Lorentz forces. The cosmic ray energy density saturates faster than the magnetic field. 168

4.22 (a) 2D cut in the xy-plane through the middle of the domain with vectors for $(b_x/\,b_{\rm rms}, b_y/\,b_{\rm rms})$ and colours showing the magnitude of $b_z/\,b_{\rm rms}$ for magnetic field in the kinematic stage. (b) Similar 2D cut at the same time for the normalized energy density of cosmic rays $e_{\rm cr}/\langle e_{\rm cr}\rangle$ in the kinematic stage. This is for the case where $\langle e_{\rm cr}\rangle > b^2_{\rm rms}$. 169

4.23 As in Fig. 4.22 but for the saturated stage. 170

4.24 The scatter plot for the normalized energy densities of cosmic rays $e_{\rm cr}/\langle e_{\rm cr}\rangle$ and magnetic fields $b^2/\langle b^2\rangle$ for the case with $\langle e_{\rm cr}\rangle \approx \langle b^2\rangle$ at the box scale. Even though both energy densities are equal when averaged over the size of the domain, locally they are not correlated. 171

5.1 Two dimensional histogram of the redshift of the sources z and the calculated magnetic field of host galaxies $b_{\rm rms}(\,\mu{\rm G}\,)$. There is no clear trend of magnetic fields with redshift. 183

5.2 (a) PDFs of RM for the cases where the electron number density $n_{\rm e}$ is not correlated to the magnetic field strength: $n_{\rm e}$ constant (red) and $n_{\rm e}$ following the King distribution (blue) with $a = 1.25l_0$, where l_0 is the driving scale of turbulence. Both distributions are roughly Gaussian with mean $\mu \approx 0$ (since a mean magnetic field is absent). The standard deviation σ is lower for the King profile. (b) PDF of RM for the case where $n_{\rm e}$ is related to magnetic field strength b via the flux freezing condition, i.e., $n_{\rm e} \propto b^{3/2}$. The distribution is non-Gaussian and can be approximated by a product of a Cauchy–Lorentz distribution and an exponential function. The parameters of the resulting function are as follows: the location parameter $x_0 = 0$, the width at half-maximum $w = 3.6$ and the standard deviation of the exponential function $\sigma = 15.81$. 186

5.3 95th percentile deviation from the combined σ of the elliptical galaxy and the Milky Way foreground versus the number of sources. We have assumed that the standard deviation of rotation measures due to the elliptical galaxy and foreground are $300\,{\rm rad\,m^{-2}}$ and $100\,{\rm rad\,m^{-2}}$ respectively. When the number of sources $n_{\rm obs}$ is greater than 9 (red dotted line), the error in the observed σ is less than half of σ_e in 95% of cases. Thus, we need at least 10 sources to differentiate between the elliptical galaxy and the Milky Way foreground. . . 188

5.4 Properties of $1.4\,{\rm GHz}$ extragalactic sources of radio intensity up to $1\,\mu{\rm Jy}$ (Hales, 2013). The total and linearly polarized intensity normalized by the differential source counts (top panel), the total number of source counts (middle panel) and the average spacing between the sources (bottom panel) are shown as functions of the intensity. The dotted lines shows the fitted models. Knowing the number of sources required per square degree, we can use the middle panel to obtain the minimum intensity we must achieve to observe that many sources. 189

A.1 Time evolution of the density ρ (a), pressure p (b), temperature T (c) and velocity in x direction v_x (d) for solution of Sod shock tube test using the Pencil (solid line) and FLASH (dotted line) codes. For profiles from FLASH, the number of dots increases closer to the shock since it use adaptive mesh refinement. The agreement between two solutions is quite good. 201

List of Tables

1.1 The exponent μ in $\langle r^2\rangle \propto t^\mu$ characterizes the nature of population evolution. 25

2.1 Parameters of various nonlinear fluctuation dynamo simulations in a numerical domain of size $(2\pi)^3$ with 256^3 mesh points. In all cases, the forcing scale k_F is approximately equal to 1.5 (flow driven at $k = 1$ and $k = 2$), the forcing amplitude $F_0 = 0.02$, the magnetic Prandtl number $\mathrm{Pr_M} = 1$ and the rms velocity in the saturated state is $u_\mathrm{rms} \approx 0.11$. The Reynolds number, the magnetic Reynolds number, both based on the forcing scale $2\pi/k_\mathrm{F}$, the rms magnetic field in the saturated state b_rms, the ratio of magnetic to kinetic energy in the saturated state $\varepsilon_\mathrm{M}/\varepsilon_\mathrm{K} = b^2_\mathrm{rms}/\,u^2_\mathrm{rms}$, the correlation length of the velocity field in the kinematic stage $l_{u\mathrm{kin}}$, the correlation length of the magnetic field in the kinematic stage $l_{b\mathrm{kin}}$, the correlation length of the velocity field in the saturated stage $l_{u\mathrm{sat}}$ and the correlation length of the magnetic field in the saturated stage $l_{b\mathrm{sat}}$ are also given. 65

2.2 Four Minkowski functions V_0, V_1, V_2, V_3, their geometrical interpretation and definitions for a three dimensional structure. $\mathrm{d}V$ is the volume element, $\mathrm{d}S$ is the surface element, and κ_1 and κ_2 are the principle curvatures of the surface of a structure. 91

2.3 Minkowski functionals V_0, V_1, V_2, V_3, their analytical expression (Schmalzing et al., 1999) and values calculated using analytical expression and obtained numerically, for a sphere with the centre at (π, π, π) of radius $r = \pi$ in a periodic box of size $(2\pi)^3$ with 128^3 grid points. 92

2.4 Parameters of various runs for the nonlinear fluctuation dynamo in a numerical domain of $(2\pi)^3$ in size with 512^3 mesh points. In all cases, the forcing scale is $k_\mathrm{F} \approx 5$, the forcing amplitude is $F_0 \approx 0.02$ and the hydrodynamic viscosity is $\nu = 4 \times 10^{-4}$. The magnetic diffusivity η, the rms velocity in the saturated stage u_rms, the Reynolds number Re, the magnetic Reynolds number $\mathrm{Re_M}$, the magnetic Prandtl number $\mathrm{Pr_M}$ and the critical magnetic Reynolds number $\mathrm{Re_M^{(crit)}}(\approx 220\mathrm{Pr_M^{-1/2}})$ are given. 98

4.1 The volume filling factor $f = \langle n_\mathrm{cr}\rangle^2/\langle n^2_\mathrm{cr}\rangle$ in a representative selection of simulations, summarising the effects of particle energy, magnetic field structure and pitch angle scattering (PAS). 151

4.2 Non-dimensional parameters used to solve the MHD and cosmic ray fluid equations (Eq. (4.26) - Eq. (4.30)) and their corresponding ISM values. 167

5.1 List of sources, their redshifts z, the depolarization fraction for jets $\mathrm{DP_j}$ and counter jets $\mathrm{DP_{cj}}$ (Garrington et al., 1991). The calculated standard deviation of the rotation measure in jets $\sigma_{\mathrm{RM_j}}(\,\mathrm{rad\,m^{-2}})$, counter jets $\sigma_{\mathrm{RM_{cj}}}(\,\mathrm{rad\,m^{-2}})$, elliptical hosts $\sigma_{\mathrm{RM_{ellip}}}(\,\mathrm{rad\,m^{-2}})$ and the rms magnetic field $b_{\mathrm{rms}}(\,\mu\mathrm{G}\,)$ in ellipticals are also given. 181

Contents

Abstract **i**

Acknowledgements **v**

Declaration **vi**

List of Symbols **vi**

List of Figures **vii**

List of Tables **xxiv**

Contents **xxviii**

1 Introduction and overview **1**

- 1.1 Introduction . . . 2
- 1.2 Gaussian and intermittent random fields . . . 3
- 1.3 Turbulence . . . 5
- 1.4 Magnetohydrodynamics . . . 12
- 1.5 Dynamo theory . . . 18
  - 1.5.1 Mean-field dynamos . . . 20
  - 1.5.2 Fluctuation dynamos . . . 23
- 1.6 MHD turbulence . . . 23
- 1.7 Diffusion . . . 24
- 1.8 Cosmic rays . . . 25
- 1.9 Tracers of galactic magnetic fields . . . 32
- 1.10 Observations of magnetic fields in galaxies . . . 38
- 1.11 Aim and structure of the thesis . . . 42

2 Fluctuation dynamo and its nonlinear states **44**

- 2.1 Random magnetic fields in the ISM . . . 45
- 2.2 Introduction to fluctuation dynamos . . . 47
- 2.3 Kinematic dynamos . . . 51
- 2.4 Non-linear fluctuation dynamo . . . 61
  - 2.4.1 Basic equations and numerical modelling . . . 61

2.4.2 Spatially intermittent nature of the dynamo generated magnetic fields 67
2.4.3 Saturation of the fluctuation dynamo 73
2.5 Magnetic field morphology 91
2.5.1 Minkowski functionals 91
2.5.2 Structures in kinematic dynamos 94
2.5.3 Structures in nonlinear dynamos 98
2.6 Discussion and conclusions 100

3 Cosmic ray diffusion in intermittent magnetic fields 101
3.1 Introduction 102
3.2 Intermittent and non-intermittent magnetic fields 105
3.3 Cosmic ray propagation 106
3.4 Effect of magnetic intermittency on cosmic ray diffusion 115
3.5 Mean field and classical scattering results 118
3.6 Cosmic ray propagation as a correlated random walk 121
3.7 Diffusion or telegraph equation? 124
3.8 Discussion and conclusions 127

4 Correlation between cosmic rays and magnetic fields 129
4.1 Introduction 130
4.2 Energy equipartition argument: previous tests and our approach 131
4.3 Construction of cosmic ray number density from test-particle simulations . . 133
4.4 Pitch angle scattering 133
4.5 Magnetic field at the Larmor scale 139
4.5.1 Intrinsic turbulence: self-generated waves 139
4.5.2 Extrinsic turbulence: MHD turbulence cascade 141
4.6 Spatial intermittency of cosmic ray distribution 144
4.7 Statistical relation between magnetic fields and cosmic rays 151
4.8 Random magnetic traps 159
4.9 Magnetic traps and cosmic ray diffusion 164
4.10 Cosmic ray distribution and the Liouville's theorem 164
4.11 Coupling of cosmic rays and thermal gas 165
4.12 Discussion and conclusions 172

5 Magnetic fields in elliptical galaxies 174
5.1 Motivation 175

5.2 Magnetic fields in elliptical galaxies 176
5.3 Simulated Faraday rotation measure in elliptical galaxies 184
  5.3.1 Theoretical predictions of rotation measure fluctuations 184
  5.3.2 Numerical simulations 185
5.4 Specific observational target: Maffei 1 188
5.5 Discussion and conclusions 190

6 Final discussion and outlook **191**

Appendix A Shock Tube Test **200**

Bibliography **202**

Chapter 1

Introduction and overview

"We cannot make bricks without straw; that is a common enough saying. It is equally true that we cannot construct a rational astrophysical theory without an adequate base of physical knowledge."

– Subrahmanyan Chandrasekhar

"What we observe is not nature itself, but nature exposed to our method of questioning."

– Werner Heisenberg

1.1 Introduction

The gas density, temperature and magnetic fields in the observable universe range from 10^{-27} (hot intracluster medium) to $10^{15}\,\mathrm{g\,cm^{-3}}$ (neutron stars), 3 (cosmic microwave background) to $10^{12}\,\mathrm{K}$ (supernova explosions) and 10^{-6} (interstellar and intergalactic medium) to $10^{15}\,\mathrm{G}$ (magnetars), respectively. A special place in this range is occupied by galaxies, the most readily identifiable structures in the extragalactic sky. A galaxy is a gravitationally bound, evolving system of stars, gas, dust, dark matter, magnetic fields and relativistic particles. Galaxies are characterized by their morphology (spiral, elliptical, lenticular, barred, irregular and dwarf), luminosity (ranging from 10^3 to $10^{12} L_\odot$, where $L_\odot$ is the solar luminosity), amount of cold gas (a measure of star formation activity: low in ellipticals, higher in spirals), color (related to the age and metallicity of stars: ellipticals are redder than spirals), nuclear activity (might have active galactic nuclei (AGN) at the centre) and redshift (high-redshift galaxies statistically represents 'younger' stages of a present-day galaxy).

Elliptical galaxies are ellipsoidal in shape, have little gas and star formation. Most of the elliptical galaxies have negligible rotation and many of them have an AGN at the centre. Spiral galaxies have a spherical central bulge, a thin disc, and halo surrounding it. They have approximately flat rotation curves which implies that they rotate differentially with angular velocity highest close to the centre and decreasing as the galactocentric radius increases.

The space between stars is filled with the interstellar medium (ISM) and it contains roughly 10% of a galaxy's visible mass. The ISM gas spans a wide range in both number density (10^{-4}–$10^{4}\,\mathrm{cm^{-3}}$) and temperature (10–$10^{6}\,\mathrm{K}$). Based on density and temperature, the ISM can be divided into several phases: cold, warm and hot (Cox, 2005). Dense molecular clouds (the cold phase) occupy small volume as compared to the other phases but contain significant mass and are a seat of star formation. Supernova explosions heat up the ISM, drive turbulence, accelerate particles to relativistic energies and generate galactic outflows. The ISM turbulence in turn amplifies magnetic fields.

Cosmic rays are relativistic charged particles which are accelerated in supernova shocks and permeate the ISM of galaxies. The energy density of cosmic rays ($\sim 1\,\mathrm{eV\,cm^{-3}}$ near the Sun) in spiral galaxies is comparable to the thermal, magnetic and gravitational energy densities. Cosmic rays provide pressure support against gravitational field via their interaction with the galactic magnetic field. Thus, they play an important role in the dynamics and energetics of the ISM. The primary aim of this thesis is to study the cosmic ray-magnetic field interaction and properties of turbulent magnetic fields in the ISM. In this chapter, the basic facts and concepts relevant to galactic magnetic fields and cosmic rays are introduced.

1.2 Gaussian and intermittent random fields

Because of the rigorous driving by supernova and other energy sources, the ISM is turbulent and its studies involves the theory of random fields. In probability theory, a random variable is a quantity whose value is a possible outcome of a random phenomenon. They are used to model stochastic processes, where the value of the variable varies randomly over possible values in the domain of the physical variable. The values of random variables are not fixed but are either measured from an experiment (which is a representation of a random phenomena) or drawn from a distribution function (decided based on the underlying physics). For example, the outcome of rolling a dice is a random variable in the domain $\{1, 2, 3, 4, 5, 6\}$. The probability distribution function of particle speeds in a classical ideal gas is given by a Maxwell–Boltzmann distribution. A random field is a collection of random variables.

The random field usually has power on various scales and the contribution from each scale can be characterized by a power spectrum, which can be computed using Fourier transforms. Here, for simplicity, the quantities are defined for a one dimensional field but can be extended to higher dimensions. The Fourier transform, $f(k)$, and power spectrum, p_k, of a one dimensional function $f(x)$ is given by

$$f(k) = \frac{1}{2\pi}\int_{-\infty}^{\infty} f(x) e^{-\mathrm{i}k\,x}\,\mathrm{d}x, \tag{1.1}$$

$$p_k = \frac{1}{\sqrt{2\pi}}|f_k|^2, \tag{1.2}$$

where k is the wave number. A power law spectrum $p_k \propto k^n$, where n is constant, is a common class of spectrum in physics. Another useful quantity to study random fields is the autocorrelation function

$$C(r) = \langle f(x) f(x^{'})\rangle = \langle f(x) f(x+r)\rangle, \tag{1.3}$$

where $\langle\cdots\rangle$ denote an average over possible combinations of x and $x+r$. The autocorrelation function and the one-dimensional shell-averaged power spectrum are related by the following equation (Monin & Yaglom, 1971; Davidson, 2004)

$$C(r) = 2\int_{0}^{\infty} p_k \frac{\sin(kr)}{kr}\,\mathrm{d}k. \tag{1.4}$$

For an isotropic random field, the distance along any direction from any point in the random field after which the correlation becomes negligible is known as the ‘correlation length’.

Using the correlation function, the correlation length l_{c} is defined as

$$l_{\mathrm{c}} = \int_0^\infty C(r)\,\mathrm{d}r. \tag{1.5}$$

Since the autocorrelation function and power spectrum are related, the correlation length can also be expressed in terms of its power spectrum as follows

$$l_{\mathrm{c}} = \frac{\pi}{2}\frac{\int_0^\infty 2\pi k^{-1} p_k\,\mathrm{d}k}{\int_0^\infty p_k\,\mathrm{d}k}. \tag{1.6}$$

One of the most common distributions in physics is the Gaussian distribution. The distribution of possible sums of a large number of independent random variables gives a Gaussian distribution by the central limit theorem. The Gaussian distribution f in one dimension is given by

$$f(x,\mu,\sigma) = \frac{1}{\sqrt{2\pi\sigma^2}} e^{-\frac{(x-\mu)^2}{2\sigma^2}}, \tag{1.7}$$

where μ is the mean of the distribution and σ is the standard deviation. In three dimension, the Gaussian function will be a product of Gaussian functions in three dimensions $f(x,\mu_x,\sigma_x)f(y,\mu_y,\sigma_y)f(z,\mu_z,\sigma_z)$. A Gaussian function is completely characterized by its power spectrum or autocorrelation function.

In qualitative terms, an intermittent field is a random field with rare high peaks. The series of random numbers

$$0.1, 0.6, 0, 0, 0.3, 0.9, 10^2, 0.3, 0, 10^1, 0.2, 0.1, 0, 0.6, 0, 0, 0, 0.1, 0, \cdots, \tag{1.8}$$

is an example of an intermittent random field in one dimension. The probability distribution function of an intermittent random field develops long tails as compared to a Gaussian distribution due to such rare but strong events. Thus, an intermittent field is also sometimes referred to as a non-Gaussian field. A Gaussian field arises from a sum of large number of independent random quantities and an intermittent field arises from a product of large number of independent quantities (Zel'dovich et al., 1987). Here we provide a simple example of an intermittent field to illustrate the idea. Consider $p_n = r_1 r_2 \cdots r_i \cdots r_n$ as a product of independently random quantities r_i, where each r_i can take value 0 or 2 with probability $1/2$. For large enough n, one of the r_i will be equal to 0 and then p_n will also be 0. However, for every finite n, there is one non-zero p_n which is equal to 2^n and the probability of that happening is

2^{-n}. This non-zero value contributes to the mean and higher order statistical moments of the distribution. For instance the mean (first order moment) of the distribution is

$$\langle p_n \rangle = 0(1-2^{-n}) + 2^n 2^{-n} = 1. \tag{1.9}$$

The root mean square (second order moment) value is

$$\langle p_n^2 \rangle = 0^2(1-2^{-n}) + 2^{2n} 2^{-n} = 2^n. \tag{1.10}$$

The higher order statistical moments grows exponentially as n increases. This is another feature of an intermittent random field. The degree of intermittency can be characterized by the kurtosis (a measure of how strong tail the distribution has), which is given by

$$\mathrm{Kurt}(f) = \frac{\langle (f - \langle f \rangle)^4 \rangle}{\langle (f - \langle f \rangle)^2 \rangle^2}, \tag{1.11}$$

where $\langle \cdots \rangle$ denotes average over the domain. Kurtosis helps to compare different intermittent fields, i.e., higher the kurtosis, higher the intermittency. The kurtosis of a Gaussian distribution is 3 and thus an intermittent random field usually have kurtosis higher than 3. Fig. 1.1 shows the presence of spatially intermittent magnetic fields on the surface of the Sun. Fig. 1.2 and Fig. 1.3 shows the intermittency in magnetic fields and gas density in numerical simulations. Unlike a Gaussian field, higher order moments are required to describe an intermittent field. In fact, a Gaussian and an intermittent field can have exactly same power spectra (and autocorrelation function). This is done via phase randomization as described in Section 3.2 of Chapter 3.

1.3 Turbulence

Fluid flows are described by the Navier-Stokes (NS) equation. For incompressible flows $(\nabla \cdot \mathbf{u} = 0)$,

$$\frac{\partial \mathbf{u}}{\partial t} + (\mathbf{u} \cdot \nabla)\mathbf{u} = -\frac{\nabla P}{\rho} + \frac{\mathbf{F}}{\rho} + \nu \nabla^2 \mathbf{u}, \tag{1.12}$$

where ρ is the density of the fluid, $\mathbf{u}$ is the velocity of the flow, P is the pressure, F represents the body forces (gravity, Coriolis force, friction, etc.) acting on the fluid and ν (assumed to be constant in space) is the kinematic viscosity. The ratio of inertial to viscous term is defined

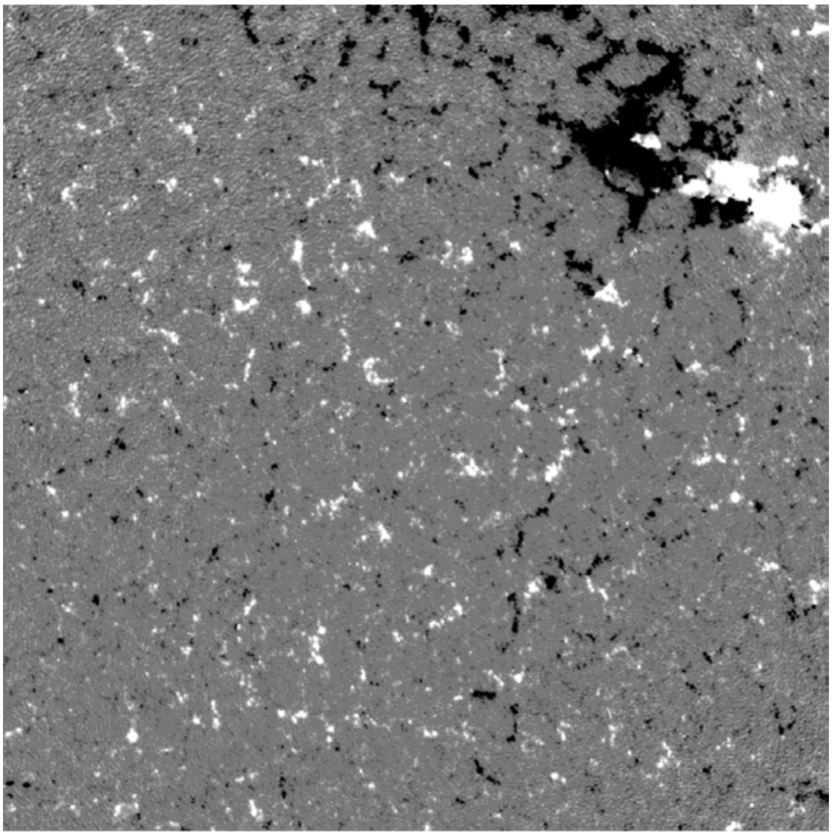

Figure 1.1: High resolution magnetogram of a solar active region taken using Solar and Heliospheric Observatory - Michelson Doppler Imager (Krivova & Solanki, 2004). The dark and white patches show magnetic fields of opposite polarity and grey shows zero magnetic flux. The random distribution of strong magnetic field regions surrounded by very high magnetic field is a sign of spatial intermittency on the surface of the Sun.

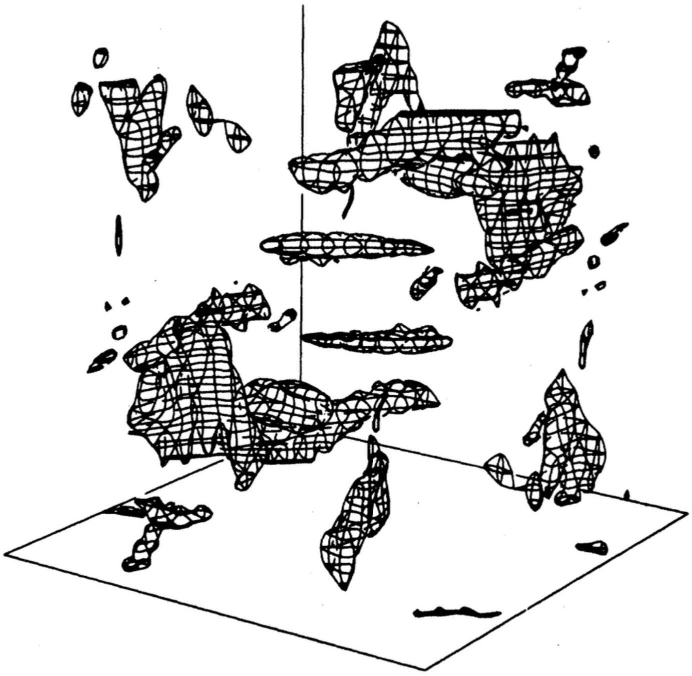

Figure 1.2: Magnetic field from the first numerical simulation of fluctuation dynamo (Meneguzzi et al., 1981). The shaded regions show the magnetic field (within less than 5% of its maximum value). The magnetic field is concentrated in small regions, which confirms spatial intermittency of the amplified magnetic fields.

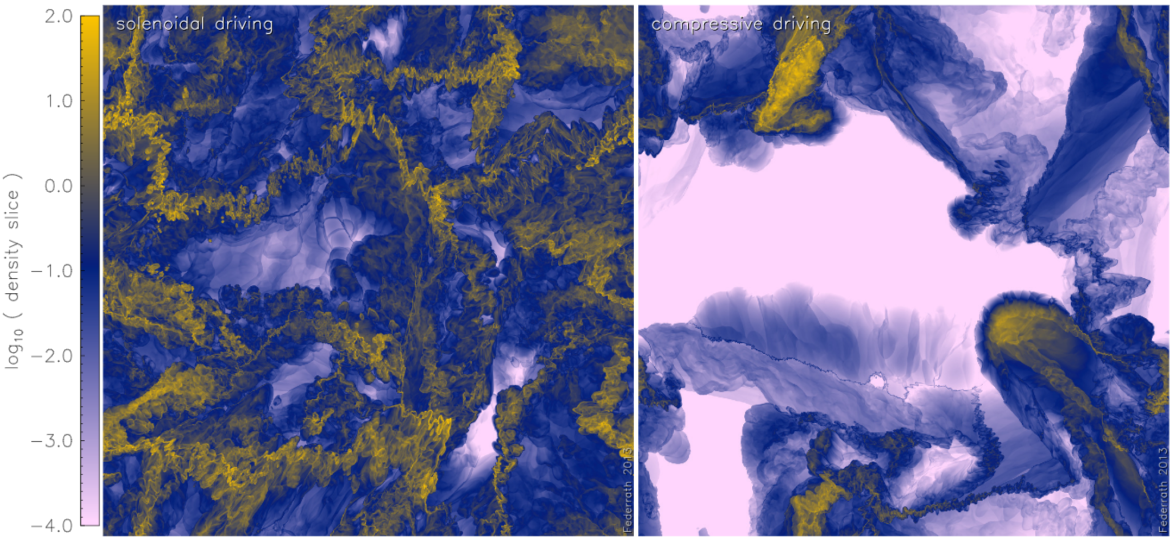

Figure 1.3: Slices of gas density from a three dimensional simulation of supersonic turbulence driven by solenoidal (left panel) and compressible (right panel) forcing (Federrath, 2013). The gas density is stronger in filaments and the field is more intermittent (higher kurtosis) when the turbulence is driven by a compressible forcing.

as the Reynolds number

$$\mathrm{Re} = UL/\nu, \tag{1.13}$$

where U is the characteristic speed of the flow and L is its typical length scale. At low enough values of Re the flow is laminar (smooth streamlines) and becomes turbulent when Re increases. For example consider streamlines of a flow past a circular cylinder as shown in Fig. 1.4. For Re < 1, the flow passes the cylinder preserving the symmetry of the flow and its original pattern is preserved past the cylinder as shown in Fig. 1.4a. As Re increases, the eddies form (Fig. 1.4b and Fig. 1.4c) at the rear but the flow is still laminar and regains its original pattern downstream. Finally, at high Re (Fig. 1.4d), the flow becomes turbulent. Another example is shown in Fig. 1.5, where the laminar smoke streams on passing through a perforated plate becomes turbulent. Fig. 1.6 shows hydrodynamic turbulence in a water tank which is isotropic and homogenous.

Turbulence is ubiquitous in nature, from the convection in a room to astrophysical scales. There is no rigorous definition of turbulence but it is usually characterized by following attributes.

- Randomness – Turbulent flows are random in nature. If two tracer particles have a small separation initially, they would quickly diverge in a turbulent flow. The turbulent flow is irregular or random and thus statistical theories are used to describe it.

- Presence of multiple scales – As seen in Fig. 1.4d, Fig. 1.5 and Fig. 1.6, there are multiple scales presents in a turbulent flow. Turbulence can be thought of as interaction of eddies of various sizes. Though there are smaller scales in turbulence, the size of the smallest eddies is still much larger than the molecular size and thus the continuum approximation required for the fluid description still holds.

- Large Reynolds number – The onset of turbulence is usually characterized by large Reynolds number, i.e., the dominance of inertial over viscous forces. There exists a critical Reynolds number beyond which the flow becomes turbulent and that depends on the properties of the fluid and driving scale of turbulence.

- Diffusive – Turbulence increases the flow or exchange of momentum as fluid particles move randomly and thus the diffusivity increases in turbulent flows.

- Cascade and dissipation – The energy passes from the large-scale eddies to the smaller ones without much dissipation of energy during the process. This process of transfer-

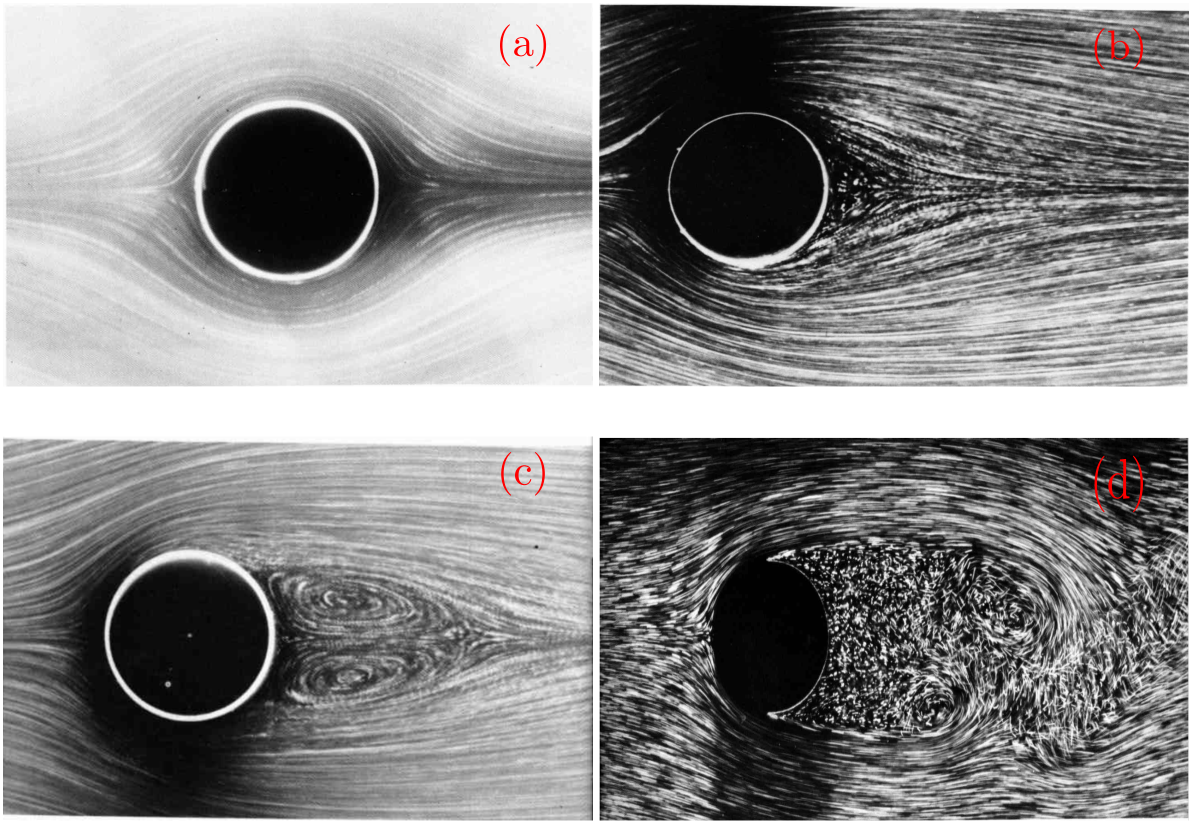

Figure 1.4: Snapshots of water flow past a circular cylinder for (a) Re $= 0.16$, (b) Re $= 9.6$, (c) Re $= 26$ and (d) Re $= 2000$ (van Dyke, 1982). Streamlines are seen by aluminium dust in water for (a),(b) and (c), and by air bubbles in water for (d). For low Re the flow is laminar but as Re increases the flow past the cylinder becomes more and more turbulent.

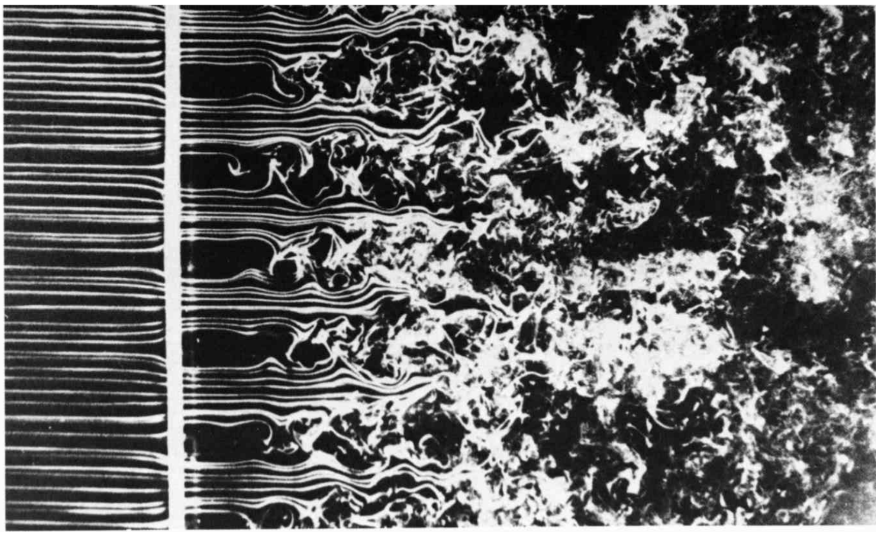

Figure 1.5: Initially laminar smoke streams becomes turbulent on passing through a plate with perforations (van Dyke, 1982). Based on the mesh size, Re $= 1500$.

ring energy from largest possible eddies (where practically there is no dissipation) to smallest scale is referred to as an energy cascade. Next, this energy is dissipated at the scale of the smallest eddies, where the kinetic energy is converted to heat. For steady state to be maintained, externally energy has to be continually injected at large scales which follows to smaller scales via cascade and then is finally dissipated at the viscous scale. However, in shock wave turbulence, both cascade and dissipation occurs at all scales.

- Time-dependent – Turbulent flow is time-dependent and irreversible. The statistical properties of turbulence may not change much with time but the instantaneous flow pattern continuously changes.

The velocity in a turbulent medium is an example of a random field which has power over a range of scales. It is thus customary to define energy at each scale using Fourier transforms. The range of scales smaller than the driving scale of turbulence and greater than viscous scale, where negligible dissipation occurs, is referred to as the ‘inertial range’. Kolmogorov studied the statistical laws of turbulent fields at high Reynolds numbers and suggested the following two hypotheses: at small scales, local isotropy and homogeneity exist and in the inertial range, the turbulent energy spectrum is independent of the viscosity and the large-scale properties of the system (Kolmogorov, 1941). In the inertial range, the interaction between close-by scales are most important and there are no special scales. Thus, the energy

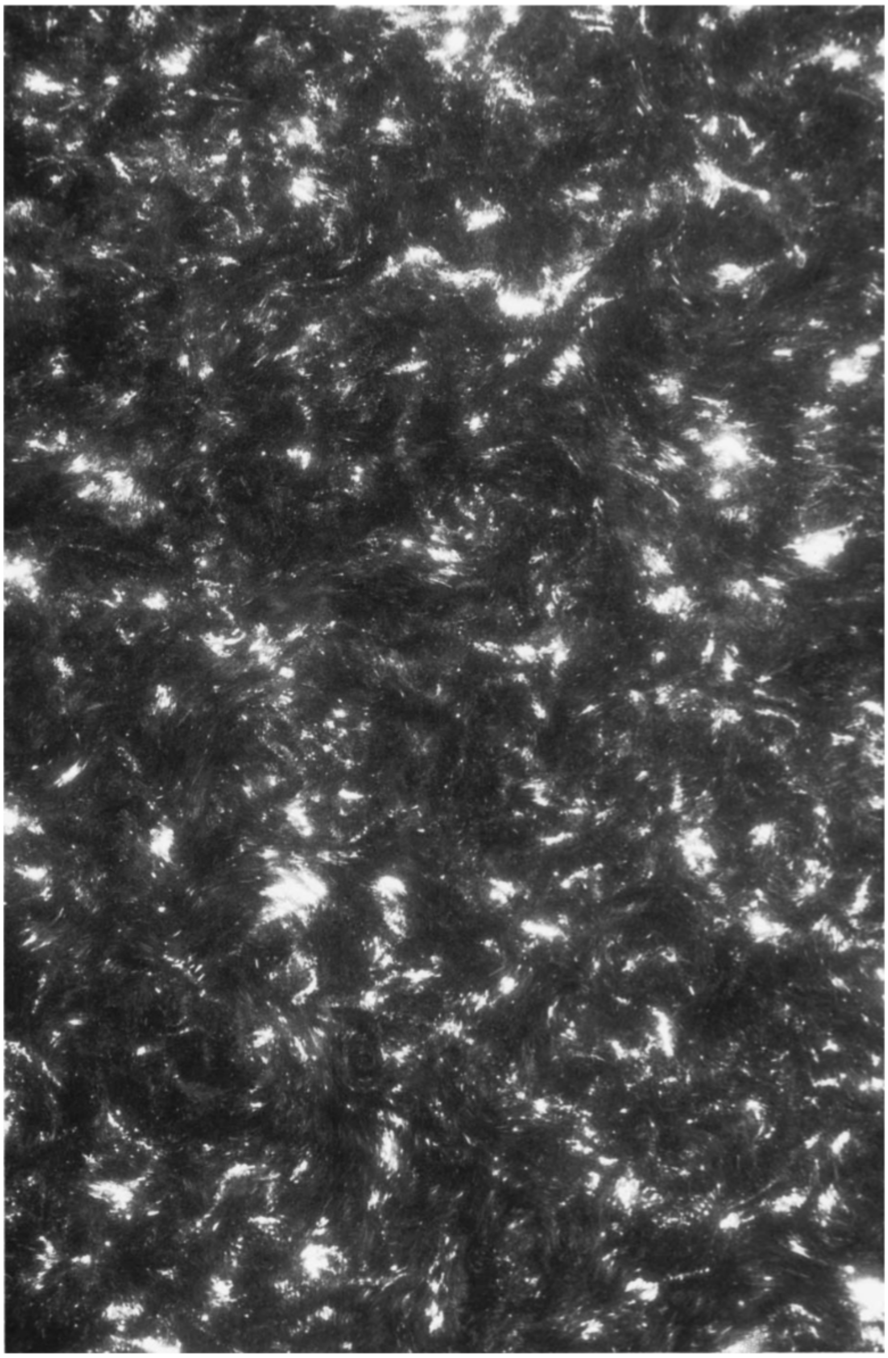

Figure 1.6: Turbulence produced by sweeping grid of bars at uniform velocity through a still water tank (Sreenivasan, 1999). Unlike Fig. 1.4 and Fig. 1.5, the turbulence here is homogenous and isotropic. The distribution is clearly intermittent with many small-scale structures.

spectrum E_k, defined via

$$\int_0^\infty E_k \mathrm{d}k = \frac{1}{2}\langle \mathbf{u}^2 \rangle, \tag{1.14}$$

where E_k represents kinetic energy per wavenumber per unit mass and $\mathbf{u}$ is the turbulent velocity, depends only on the wavenumber k and the rate of energy transfer ε. Using dimensional arguments, we obtain

$$E_k = c\varepsilon^{2/3}k^{-5/3}, \tag{1.15}$$

where c is a constant independent of k. The energy spectrum $E_k \propto k^{-5/3}$ is known as Kolmogorov's spectrum of turbulence. This spectrum is confirmed in a series of experiments as shown in Fig. 1.7 and also in high-resolution direct numerical simulations (Fig. 1.8). The velocity field in these numerical simulations is intermittent as illustrated by PDFs of a single velocity component in Fig. 1.9. The ISM of galaxies is also turbulent as confirmed by the power law spectrum of electron density obtained with various radio observations. The slope roughly agrees with the Kolmogorov spectrum (Fig. 1.10).

1.4 Magnetohydrodynamics

Magnetohydrodynamics (MHD) is the study of electrically conducting fluids. It is applicable to plasma too when the plasma is sufficiently collisional (to be treated as a continuum) and is overall charge neutral (no net charge). The electric currents in the plasma generate magnetic fields, which in turn react back on the plasma via the Lorentz force. Thus, Maxwell's equation and fluid equations (Navier-Stokes and continuity equation) with the Lorentz force included are used to describe plasma when MHD is applicable.

Maxwell's equations in the CGS units are

$$\nabla \cdot \mathbf{E} = 4\pi\rho_\mathrm{c} \quad \text{(Gauss's law)}, \tag{1.16}$$

$$\nabla \cdot \mathbf{B} = 0 \quad \text{(no magnetic monopoles)}, \tag{1.17}$$

$$\frac{1}{c}\frac{\partial \mathbf{E}}{\partial t} = \nabla \times \mathbf{B} - \frac{4\pi}{c}\mathbf{J} \quad \text{(Ampere's law with Maxwell's displacement current)}, \tag{1.18}$$

$$\frac{1}{c}\frac{\partial \mathbf{B}}{\partial t} = -\nabla \times \mathbf{E} \quad \text{(Faraday's law)}, \tag{1.19}$$

where $\mathbf{E}$ is the electric field, $\mathbf{B}$ is the magnetic field, $\mathbf{J}$ is the electric current density, ρ_c is the

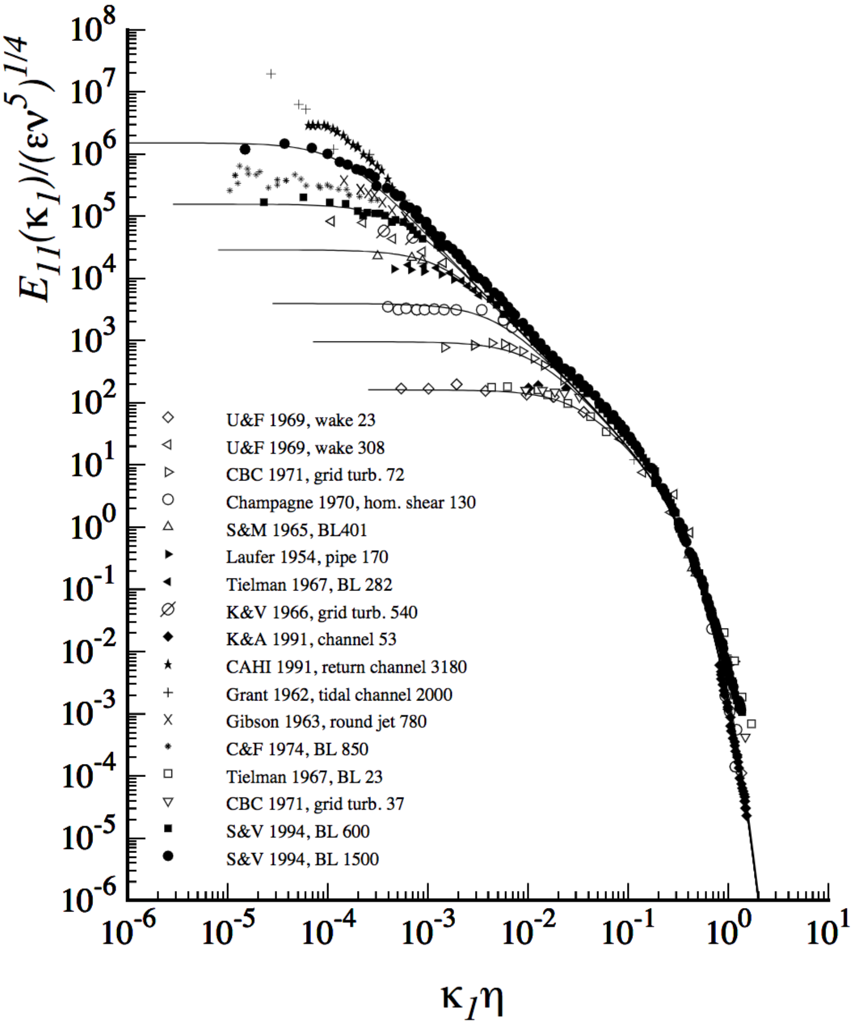

Figure 1.7: Energy spectrum obtained from a series of experiments: turbulence generated by boundary layers, wakes, grids, pipes, ducts, jets, and tides in the ocean (Pope, 2000). On scaling both axis with properties of the system, all curves lie along same the line. Thus, the viscosity or the large-scale properties of a turbulent system, doesn't affect the spectra in the inertial range and the Kolmogorov scaling is universal.

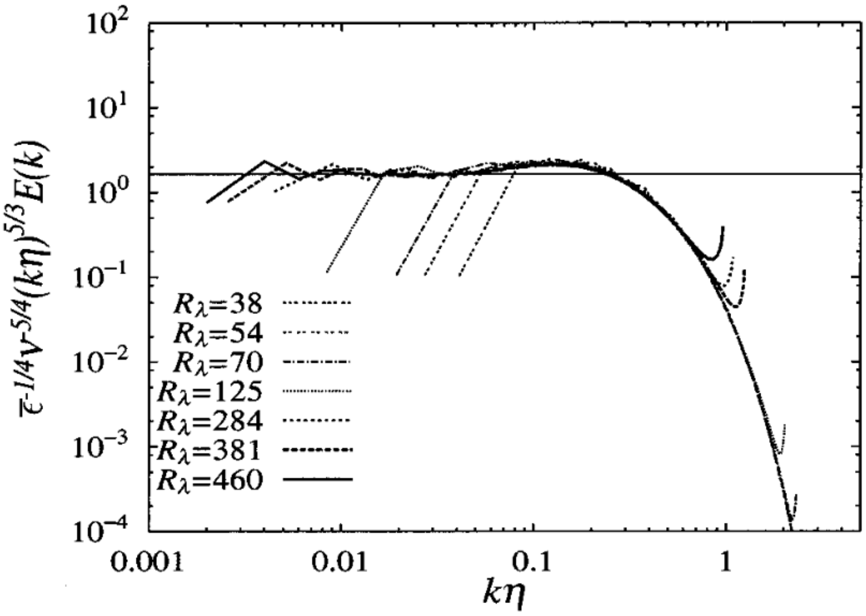

Figure 1.8: Energy spectra normalized with Kolmogorov scaling obtained from direct numerical simulations by solving Navier-Stokes equation (Gotoh et al., 2002). The horizontal line shows 1.64. The curves lie on top of each other independent of R_λ, which is the Reynolds number. This confirms Kolmogorov scaling.

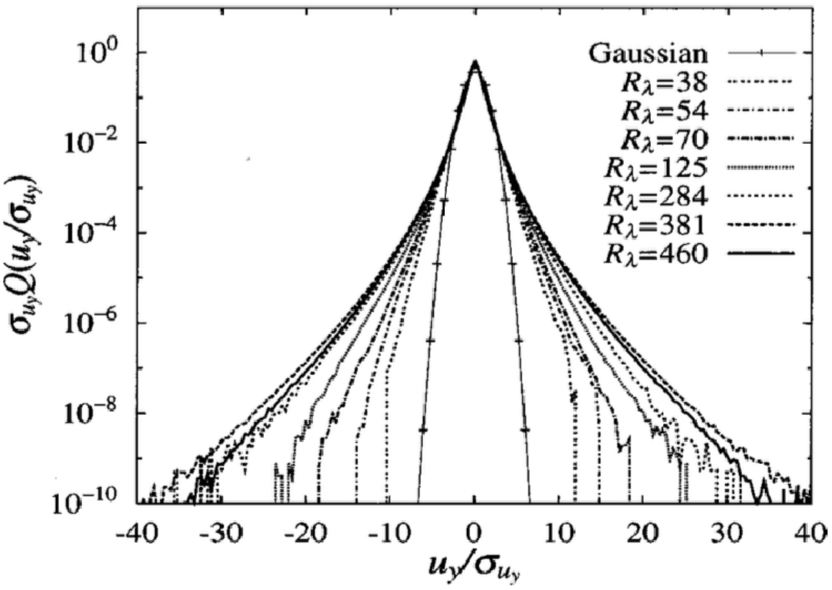

Figure 1.9: The PDFs of a single velocity field component obtained from numerical simulations for various Reynolds numbers, here given by R_λ (Gotoh et al., 2002). The PDFs are non-Gaussian with heavy tails confirming that the velocity field is intermittent. Also, as Reynolds number increases, intermittency increases.

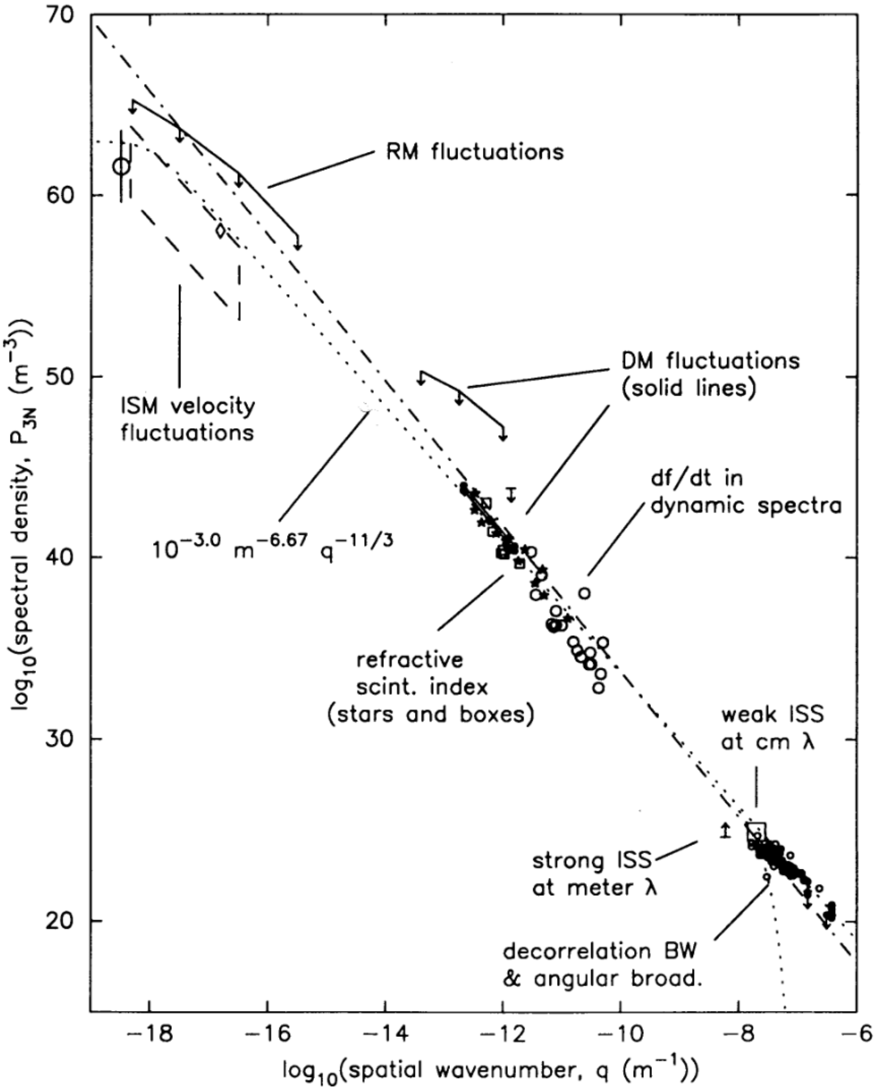

Figure 1.10: Power spectrum of fluctuations in electron density in the ISM obtained from variety of observations (Armstrong et al., 1995). The power law spectrum confirms that the ISM is turbulent and the slope approximately agrees with the Kolmogorov theory.

charge density and c is the speed of light. The time evolution of magnetic fields in a plasma is described quantitatively by the induction equation, which can be derived using Maxwell's equation and Ohm's law. For non-relativistic plasma, the term $\left(c^{-1}\frac{\partial \mathbf{E}}{\partial t}\right)$ in Eq. (1.18) can be neglected. Let L be the typical length scale of the system and T be the typical time over which $\mathbf{B}$ and $\mathbf{E}$ vary, then from Eq. (1.19) we get

$$\frac{1}{c}\frac{|\mathbf{B}|}{T} \sim \frac{|\mathbf{E}|}{L}. \tag{1.20}$$

Then, comparing terms $\frac{1}{c}\frac{\partial \mathbf{E}}{\partial t}$ and $\nabla \times \mathbf{B}$ in Eq. (1.18) gives

$$\frac{\left|\frac{1}{c}\frac{\partial \mathbf{E}}{\partial t}\right|}{|\nabla \times \mathbf{B}|} \sim \frac{\frac{1}{c}\frac{|\mathbf{E}|}{T}}{\frac{|\mathbf{B}|}{L}} \sim \frac{L^2}{T^2 c^2}. \tag{1.21}$$

Thus, the displacement term can be neglected when $L^2/T^2 \ll c^2$ or equivalently when the time scale over which over $\mathbf{B}$ varies is larger than the light crossing time of the system. For a typical spiral galaxy of a size $30\,\mathrm{kpc}$, the light crossing time is $\sim 10^4$ years, whereas the magnetic field in such systems varies over few times the rotation period, which is approximately 10^8 years (Beck et al., 1996; Brandenburg & Subramanian, 2005). Thus, the displacement term can be safely neglected. This is also true for most astrophysical plasmas (except in jets of active galactic nuclei, gamma-ray bursts, pulsar winds and magnetospheres of magnetars where relativistic effects of magnetized plasma might be important - Beskin (2010)). Neglecting the displacement current, the Eq. (1.18) reduces to

$$\nabla \times \mathbf{B} = \frac{4\pi}{c}\mathbf{J}. \tag{1.22}$$

The standard Ohm's law in a fixed frame of reference is

$$\mathbf{J} = \sigma\left(\mathbf{E} + \frac{\mathbf{u} \times \mathbf{B}}{c}\right), \tag{1.23}$$

where σ is the electrical conductivity and $\mathbf{u}$ is the fluid velocity. Substituting Eq. (1.23) to Eq. (1.22), we get

$$\nabla \times \mathbf{B} = \frac{4\pi\sigma}{c}\left(\mathbf{E} + \frac{\mathbf{u} \times \mathbf{B}}{c}\right). \tag{1.24}$$

Taking curl of Eq. (1.24), defining magnetic diffusivity $\eta = c^2/4\pi\sigma$ and using Eq. (1.19) we obtain the induction equation as

$$\frac{\partial \mathbf{B}}{\partial t} = \nabla \times (\mathbf{u} \times \mathbf{B} - \eta \nabla \times \mathbf{B}). \tag{1.25}$$

If magnetic diffusivity η is constant in space, Eq. (1.25) reduces to

$$\frac{\partial \mathbf{B}}{\partial t} = \nabla \times (\mathbf{u} \times \mathbf{B}) + \eta \nabla^2 \mathbf{B}. \tag{1.26}$$

Since the induction equation is linear in magnetic field, $\mathbf{B} = \mathbf{0}$ is always a solution. Thus, to amplify magnetic field a seed magnetic field is required. The first term on the right-hand side of the Eq. (1.26) is the induction term which represents the amplification of magnetic field due to interaction with the fluid flow. The second term represents magnetic field diffusion. The ratio of induction to diffusion term is known as the magnetic Reynolds number $\mathrm{Re_M}$, which is defined as

$$\mathrm{Re_M} = UL/\eta, \tag{1.27}$$

where U is the typical speed and L is the typical length scale of the system. For $\mathbf{u} = \mathbf{0}$, the magnetic field would decay. Thus, for the magnetic field to grow, $\mathbf{u}$ must be non-zero and the inductive effects must win over the magnetic field diffusion. Usually, in astrophysical plasmas, the diffusion term is much smaller than the inductive term. For example, $\mathrm{Re_M}$ for spiral galaxies is of the order of 10^{18} and for galaxy clusters is of the order of 10^{29} (Brandenburg & Subramanian, 2005). The magnetic field might also be amplified when magnetic diffusivity varies with space (Pétrélis et al., 2016; Rogers & McElwaine, 2017), then Eq. (1.25) is used. For $\eta = 0$, the magnetic field is frozen into the fluid (Alfvén's theorem) and this is referred to as flux freezing. For turbulent systems with spatially 'rough' velocities, the flux can be frozen but in a statistical sense (Eyink, 2011).

Magnetic fields also react back on the plasma by exerting the Lorentz force on the charged particles. The Lorentz force $\mathbf{F}_L$ on a single charged particle with a charge q propagating with a velocity $\mathbf{v}$ in presence of a magnetic field $\mathbf{B}$ and an electric field $\mathbf{E}$ is

$$\mathbf{F}_L = q\left(\mathbf{E} + \frac{\mathbf{v} \times \mathbf{B}}{c}\right). \tag{1.28}$$

Let n_p be the number density of positive charges with charge q_p and velocity $\mathbf{v}_\mathrm{p}$ and n_n be the number density of negative charges with charge q_n and velocity $\mathbf{v}_\mathrm{n}$. Then the Lorentz force per unit volume $\mathbf{f}_L$ is

$$\mathbf{f}_L = \rho_c \mathbf{E} + \frac{\mathbf{J} \times \mathbf{B}}{c}, \tag{1.29}$$

where $\rho_\mathrm{c} = q_\mathrm{p} n_\mathrm{p} - q_\mathrm{n} n_\mathrm{n}$ is the effective net charge and $\mathbf{J} = q_\mathrm{p} n_\mathrm{p} \mathbf{v}_\mathrm{p} - q_\mathrm{n} n_\mathrm{n} \mathbf{v}_\mathrm{n}$ is the current density. For a non-relativistic plasma, the term with electric field in Eq. (1.29) can be neglected in comparision with the term with magnetic field. Using Eq. (1.16), Eq. (1.20) and Eq. (1.22), the ratio of the two terms in Eq. (1.29) is

$$\frac{|\rho_c \mathbf{E}|}{|\frac{\mathbf{J} \times \mathbf{B}}{c}|} \sim \frac{|\mathbf{E}|^2}{|\mathbf{B}|^2} \sim \frac{L^2}{T^2 c^2} \ll 1, \tag{1.30}$$

where L is the typical length scale of the system and T is the typical time over which $\mathbf{B}$ and $\mathbf{E}$ vary. Thus, the effect of an electric field can safely be ignored. When the Lorentz force is included, the Navier-Stokes equation Eq. (1.12) for an incompressible fluid is

$$\frac{\partial \mathbf{u}}{\partial t} + (\mathbf{u} \cdot \nabla)\mathbf{u} = -\frac{\nabla P}{\rho} + \frac{1}{\rho}\frac{\mathbf{J} \times \mathbf{B}}{c} + \frac{\mathbf{F}}{\rho} + \nu \nabla^2 \mathbf{u}. \tag{1.31}$$

Using Eq. (1.22) the Lorentz force can be further decomposed into two components

$$\frac{\mathbf{J} \times \mathbf{B}}{c} = \frac{1}{c}\frac{c}{4\pi}(\nabla \times \mathbf{B}) \times \mathbf{B} = \frac{1}{4\pi}(\mathbf{B} \cdot \nabla)\mathbf{B} - \frac{1}{8\pi}\nabla \mathbf{B}^2. \tag{1.32}$$

The first term is the derivative of magnetic field along itself and physically represents the magnetic tension. The second term represents magnetic pressure.

1.5 Dynamo theory

The evolution and maintenance of magnetic field is generally explained by a dynamo theory, which is the conversion of kinetic energy (usually due to turbulence) to magnetic energy. Turbulence is common in most astrophysical objects and is usually maintained by a regularly occurring physical mechanism: convection in stars, supernovae blowing off in galaxies, and motion and mergers of galaxies in galaxy clusters. The dynamo process taps this turbulent kinetic energy to amplify an initially weak seed magnetic field.

Based on scales, the magnetic fields in these systems can be divided into two types: the large-scale or the mean field, which are coherent over scales comparable to the size of the system and the small-scale or the fluctuating field, whose correlation length is the order of the driving scale of turbulence. Usually for galaxies, the root mean square (rms) magnitude of both the fields is comparable and thus both kinds of fields are equally important for the ISM dynamics. As with magnetic fields, the dynamos are also divided into two categories: mean-field (or large-scale) and fluctuation (or small-scale) dynamo, for generating each type of field. The magnetic field in spiral galaxies can also be amplified by compression in spiral arms or shear in interarm regions. These fields seems to be ordered over galaxy scales in the observational probes and are referred to as 'anisotropic turbulent' fields (Beck, 2016).

Necessity of dynamo action in spiral galaxies

Since Re_{M} in spiral galaxies is quite high ($\sim 10^{18}$), magnetic field doesn't decay much due to ohmic diffusion. However, due to small-scale velocity fluctuations in a turbulent plasma, magnetic field decays via turbulent diffusion. The decay time scale τ_{decay} based on turbulent diffusivity is

$$\tau_{\mathrm{decay}} = \frac{L^2}{\eta_t}, \tag{1.33}$$

where L is the characteristic length scale of the magnetic field and η_t is the turbulent diffusivity. The turbulent diffusivity is given by

$$\eta_t \approx \frac{1}{3} l_0 v_0, \tag{1.34}$$

where l_0 is the driving scale of the turbulence and v_0 is the typical turbulent velocity. In spiral galaxies, the turbulence is driven by supernova explosions and the maximum size of supernova (after it has reached a steady state with the surrounding medium) is 100–$500\,\mathrm{pc}$. The turbulent velocity can be estimated by considering that a small fraction of total energy emitted by supernova is converted into the kinetic energy of the turbulence (Shukurov, 2004). The rate $\dot{e}_{\mathrm{turb}}$ at which supernova supplies kinetic energy to medium is

$$\dot{e}_{\mathrm{turb}} = f \nu_{\mathrm{SN}} E_{\mathrm{SN}} M_{\mathrm{gas}}^{-1}, \tag{1.35}$$

where f is the fraction of total supernova energy that is fed into the medium, ν_{SN} is the rate at which supernova explodes, E_{SN} is the energy released in a single explosion event and M_{gas}^{-1} is the total galaxy mass. $\dot{e}_{\mathrm{turb}}$ can also be expressed as rate of gain in turbulent kinetic energy of the medium per unit mass, i.e., $v_0^2(v_0/l_0)$. For Milky Way, using $l_0 = 100\,\mathrm{pc}$, $f = 0.07$, $\nu_{\mathrm{SN}} = (30\,\mathrm{yr})^{-1}$, $E_{\mathrm{SN}} = 10^{51}\,\mathrm{erg}$ and $M_{\mathrm{gas}} = 4 \times 10^9\,\mathrm{M}_\odot$ ($\mathrm{M}_\odot$ being the solar mass), we obtain $v_0 \approx 10\,\mathrm{km\,s^{-1}}$. Using Eq. (1.34), we get $\eta_t \approx 10^{26}\,\mathrm{cm^2\,s^{-1}}$. Since the large-scale magnetic field varies over a few kiloparsecs in a spiral galaxy, using $L = 1\,\mathrm{kpc}$ and $\eta_t = 10^{26}\,\mathrm{cm^2\,s^{-1}}$ in Eq. (1.33), we get $\tau_{\mathrm{decay}} \approx 10^8\,\mathrm{yr}$. However, the lifetime of a galaxy is the order of $10^{10}\,\mathrm{yr}$. Thus, any initial magnetic field must have decayed by now by turbulent diffusivity. Since we still observe magnetic fields in number of spiral galaxies (Beck, 2016), magnetic fields in spiral galaxies must be amplified and maintained by a dynamo mechanism. This also confirms that the observed galactic magnetic field cannot be of a primordial origin.

In the absence of a dynamo, the magnetic energy in a differentially rotating system is also lost via the flux expulsion (removal of the magnetic flux) (Weiss, 1966; Moffatt, 1978). However, the galactic magnetic field in this process is expelled quite slowly over a time scale of the order $t_0\mathrm{Re}_{\mathrm{M}}^{1/3}$, where t_0 is the eddy turnover time of the flow and Re_{M} is the magnetic Reynolds number (Weiss, 1966; Gilbert et al., 2016). For galaxies, $t_0 = l_0/v_0 = 100\,\mathrm{pc}/10\,\mathrm{km\,s^{-1}} \approx 10^7\,\mathrm{yr}$ and $\mathrm{Re}_{\mathrm{M}} \sim 10^{18}$ (Brandenburg & Subramanian, 2005). The field is lost via the flux expulsion over the time scale of the order of $10^{13}\,\mathrm{yr}$ and thus the turbulent diffusion is a much more efficient process for the removal of magnetic energy from galaxies. So, the flux expulsion mechanism cannot justify the need for a dynamo action in galaxies.

Another magnetic energy loss mechanism in spiral galaxies is via advection of magnetic flux by galactic winds. We follow arguments given in Shukurov et al. (2006) to calculate the time scale for the magnetic energy loss by this mechanism. Supernova explosions produce hot gas which leaves the galactic disk in the form of a wind. The vertical velocity of the hot gas through the surface of the disk u_z is approximately within the range 100–$200\,\mathrm{km\,s^{-1}}$. The volume filling factor of the hot gas f is within the range 0.2–0.3. Assuming number density of $0.1\,\mathrm{cm^{-3}}$ for the gas, the relative density of the hot gas is $\rho_h/\rho \simeq 10^{-27}/10^{-25} = 10^{-2}$. The effective mass averaged advection speed is $U_0 = f u_z \rho_h/\rho \simeq 1$–$2\,\mathrm{km\,s^{-1}}$. The time scale for magnetic flux removal via advection is of the order of h/U_0, where h is the scale height of the warm gas layer. Using $h = 0.5\,\mathrm{kpc}$, we obtain the time scale to be of the order of $10^8\,\mathrm{yr}$, which is comparable to the decay time scale via turbulent magnetic diffusivity. Thus, the removal of magnetic flux via winds is also an efficient mechanism to decrease magnetic energy, which further justifies a need for a dynamo action in galaxies.

1.5.1 Mean-field dynamos

The turbulent (mean-field) dynamo theory has been successful in explaining the large-scale magnetic fields in planets, stars and galaxies. Magnetic field, being divergence free, can be decomposed into toroidal and poloidal components. The mean-field dynamo is a process in which toroidal and poloidal components of magnetic fields are continuously generated from each other. Turbulent motions in galaxies (mainly stellar winds, supernovae explosions and superbubbles) push loops of the toroidal magnetic field out of the plane of the disk (density stratification is important). They are then twisted by Coriolis effect generating the poloidal field. This is known as the α-effect and is illustrated in the left-hand panel Fig. 1.11. The poloidal field is further stretched by differential rotation regenerating the toroidal magnetic field. This is known as the ω-effect and is shown in the right-hand panel of Fig. 1.11. Thus, the closed toroidal-poloidal cycle leads to an exponential growth of the mean field. The $\alpha\omega$-dynamo can occur in physical systems with turbulence, density stratification, and differential rotation.

In the mean-field theory, the velocity and magnetic fields are split into a mean or large-scale component and a turbulent or small-scale fluctuating components by averaging over an appropriate length scale (for more about details on averaging see Gent et al., 2013b). Two separate equation for the evolution of mean and fluctuating magnetic fields are obtained from the induction equation. In the equation for the mean magnetic field, a 'mean electromotive force' emerges which depends on the statistical properties of the fluctuating velocity and magnetic fields. To solve the equation for the mean magnetic field, the mean electromotive force needs to be expressed in terms of mean quantities and their derivatives (the 'closure problem') (Krause & Rädler, 1980; Moffatt, 1978). The constants in the expansion are referred to as turbulent transport coefficients. Assuming a particular form of the mean electromotive force and transport coefficients, exponentially growing solutions of the mean field, i.e., a dynamo solution, can be obtained. As the mean magnetic field grows, it reacts back on the mean and fluctuating components. This leads to the saturation of the mean magnetic field. The nonlinearity in mean-field dynamo theory is usually modelled by varying transport coefficients based on the magnetic field strength (Chamandy et al., 2014).

There have been various criticism of the mean-field galactic dynamo theory in its present form. Particularly important problems are the poor understanding of the nonlinear form and physics of turbulent diffusion, uncertainty in the description of removal of magnetic flux from the disc, the effects of the multiphase structure of the ISM on the magnetic field, and the effect of rapidly growing strong fluctuating field on the mean field (Kulsrud, 1999; Shukurov, 2004). Most of the uncertainties are related to the α-effect, since the role of the ω-effect is simpler both physically and mathematically. An alternative model for the α-effect is magnetic loops rising up from the disk due to magnetic buoyancy instability, which is further enhanced by cosmic rays, and subsequently reconnecting loops (the 'Parker instability') (Parker, 1992). The numerical simulation of the instability agrees with the analytical results (Rodrigues et al.,

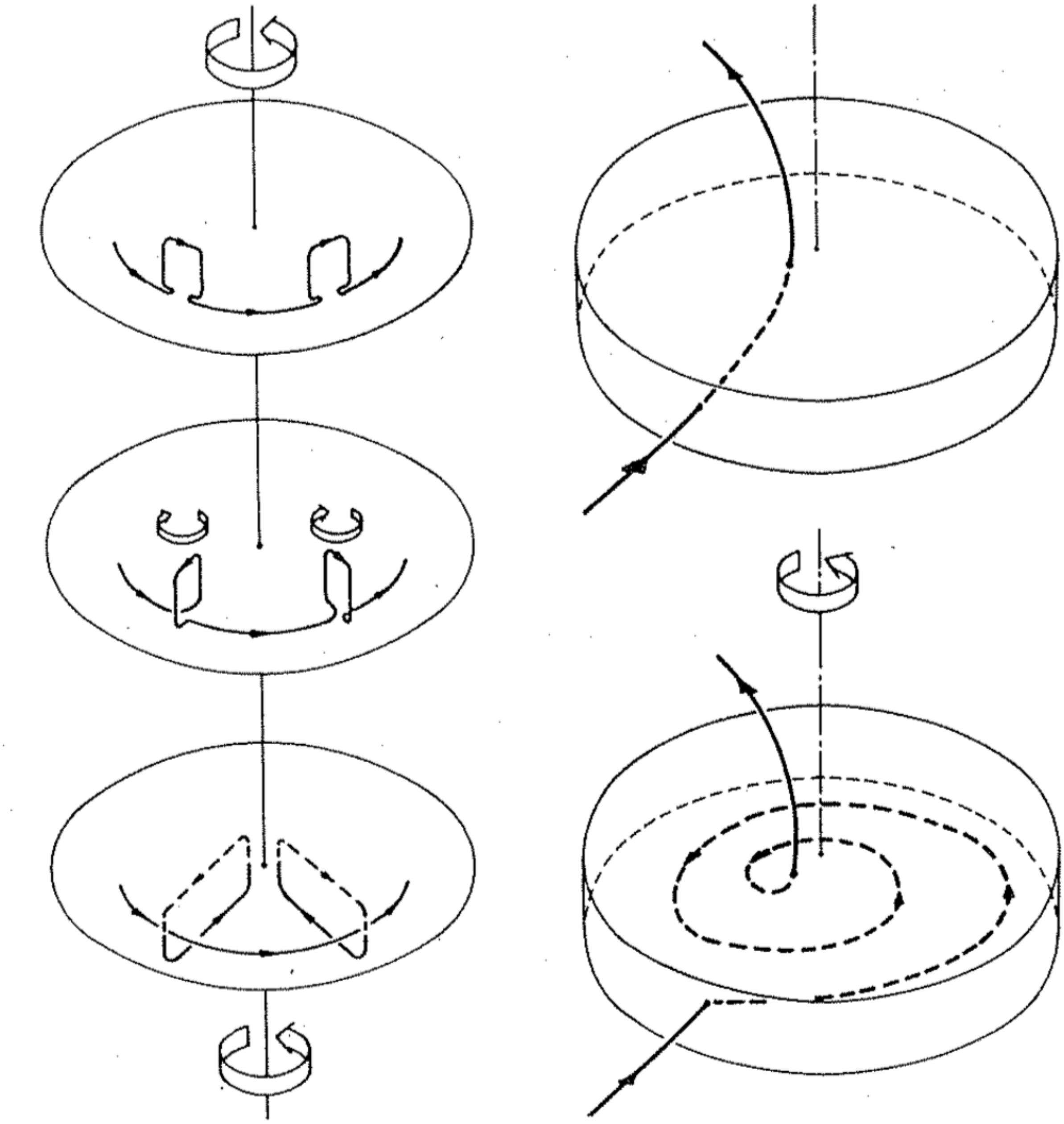

Figure 1.11: Illustration of the α (left) and ω (right) effect (Ruzmaikin et al., 1988). The left panel shows poloidal magnetic field is generated by twisting loops of toroidal magnetic field in a galaxy and the right panel shows the conversion poloidal magnetic field into toroidal magnetic field by differential rotation.

2016). The idea of buoyancy-driven α-effect can be incorporated in the standard mean field dynamo models (Moss et al., 1999). It has also been demonstrated numerically that such a cosmic-ray driven dynamo can lead to amplification of galactic magnetic fields (Hanasz et al., 2004). Another important contribution to large-scale magnetic field can be due to the magneto-rotational instability (MRI), which is a local shear instability occurring in differentially rotating discs which are weakly magnetized (Balbus & Hawley, 1991). This instability was originally proposed to explain the loss of angular momentum in accretion disks. MRI generates turbulence, which in turn amplifies magnetic fields. It can acts as a source of turbulence, especially in the outskirts of the galactic disk where other sources are not active. The emergence of large-scale magnetic field with this instability has been confirmed in numerical simulations (Brandenburg et al., 1995; Stone et al., 1996).

1.5.2 Fluctuation dynamos

The fluctuation dynamo amplifies magnetic fields at scales smaller than the driving scale of turbulence by random stretching of field lines by turbulent velocity (Kazantsev, 1968; Zel'dovich et al., 1984). The fluctuation dynamo operates on a much faster time scale (the turbulent eddy turnover time) in comparison to the large-scale dynamo (time scale decided by rotation or turbulent diffusion) (Kulsrud & Anderson, 1992). The fluctuation dynamo can quickly amplify an initial weak seed magnetic field, saturate and then seed the mean-field dynamo. The mean-field dynamo then orders the field over the size of the system (Ruzmaikin et al., 1988). One can also think of a unified small- and large-scale dynamo (Subramanian, 1999; Subramanian & Brandenburg, 2014; Bhat et al., 2016). Fluctuation dynamos are described in some detail in Chapter 2.

1.6 MHD turbulence

As hydrodynamic turbulence is due to the nonlinear interaction of motions at various scales, MHD turbulence is due to the interaction of MHD waves (in the presence of a large-scale magnetic field serving as a 'guide field'). Small perturbations to the guide field excite propagating MHD waves. These waves, usually Alfvén waves, interact nonlinearly giving rise to MHD turbulence. Unlike hydrodynamic turbulence, the MHD turbulence is anisotropic, especially at small scales, with different powers along the direction parallel and perpendicular to the guide field (Goldreich & Sridhar, 1995). Further details on the theory and simulations of MHD turbulence can be found in Biskamp (2003), Schekochihin & Cowley (2007) and

Tobias et al. (2011).

1.7 Diffusion

Diffusion is the process which involves transport of certain quantities (such as heat, particles and magnetic fields) from a region of high concentration to a region of low concentration, reducing spatial gradients. For example, the smell of perfume in a corner of a room makes it way to every part of the room via diffusion. Also, migration of people around the globe can be thought of as a diffusive process. The theory of diffusion is based on the theory of random walks.

We here derive the diffusion equation in one dimension, assuming that the particles (can be any quantity which is diffusing) undergo the Brownian motion. Consider a population of particles with the number density $n(x,t)$, where t is the time and x is the location on an infinite line (say along x axis). At each time step $\varDelta t$, a particle moves by a step length $\varDelta x$ either to its left or right with equal probability. The particle number density at time $t+\varDelta t$ is

$$n(x,t+\varDelta t)=\frac{1}{2}n(x+\varDelta x,t)+\frac{1}{2}n(x-\varDelta x,t). \tag{1.36}$$

Expanding each term in Eq. (1.36) in Taylor series gives

$$n(x,t+\varDelta t)=n(x,t)+\frac{\partial n}{\partial t}\varDelta t+\cdots, \tag{1.37}$$

$$n(x+\varDelta x,t)=n(x,t)+\frac{\partial n}{\partial x}\varDelta x+\frac{1}{2}\frac{\partial^2 n}{\partial x^2}\varDelta x^2+\cdots, \tag{1.38}$$

$$n(x-\varDelta x,t)=n(x,t)-\frac{\partial n}{\partial x}\varDelta x+\frac{1}{2}\frac{\partial^2 n}{\partial x^2}\varDelta x^2+\cdots. \tag{1.39}$$

Substituting this in Eq. (1.36) we obtain

$$\frac{\partial n}{\partial t}=\frac{1}{2}\frac{\varDelta x^2}{\varDelta t}\frac{\partial^2 n}{\partial x^2}. \tag{1.40}$$

Defining the diffusion coefficient $D=\frac{1}{2}\frac{\varDelta x^2}{\varDelta t}$, we arrive at the diffusion equation in one dimension as

$$\frac{\partial n}{\partial t}=D\frac{\partial^2 n}{\partial x^2}. \tag{1.41}$$

Table 1.1: The exponent μ in $\langle r^2 \rangle \propto t^{\mu}$ characterizes the nature of population evolution.

Value of μ	Particle motion
$0 < \mu < 1$	sub-diffusion
$\mu = 1$	diffusion
$1 < \mu < 2$	super-diffusion
$\mu = 2$	ballistic

The corresponding version in three dimension is

$$\frac{\partial \mathbf{n}}{\partial t} = \mathbf{D} \nabla^2 \mathbf{n}, \tag{1.42}$$

where $\mathbf{D}$ is the diffusion tensor. The relation between the mean square displacement $\langle r^2 \rangle = \langle (x - x_0)^2 + (y - y_0)^2 + (z - z_0)^2 \rangle$, where x_0, y_0, z_0 are position at time $t = 0$ and $\langle \cdots \rangle$ denotes ensemble average, and time t characterizes the particle motion as shown in Table 1.1. For diffusive transport, the mean particle displacement is proportional to square root of time.

1.8 Cosmic rays

Cosmic rays are relativistic charged particles that permeate the ISM of galaxies and are one of its important non-thermal components in addition to magnetic fields. There are detected directly on Earth and observed indirectly through their radio and gamma-ray emissions. Their energy ranges from few MeV to more than $10^{11}\,\mathrm{GeV}$. The energy spectrum for different types of particle is shown in Fig. 1.12. Ninety percent of cosmic rays are protons, 1–2$\%$ are electrons and the rest are heavier nuclei. Cosmic rays are also divided into primary and secondary, where primary cosmic rays refers to particles from sources and secondary cosmic rays refers to particles which are product of spallation reactions of primary cosmic rays with the interstellar gas.

In galaxies, cosmic rays interact with the interstellar gas both collisionally and collisionlessly. The average energy of galactic cosmic ray particles is about few GeVs. Very low energy cosmic rays (2–10$\,\mathrm{MeV}$) interact collisionally ionizing the thermal gas and heating up the interstellar medium. Cosmic rays with energy of few GeV interact with the interstellar medium via magnetic fields. The Larmor radius r_{L} of a cosmic ray particle of non-dimensional charge Z (charge of the particle divided by the proton or electron charge) and

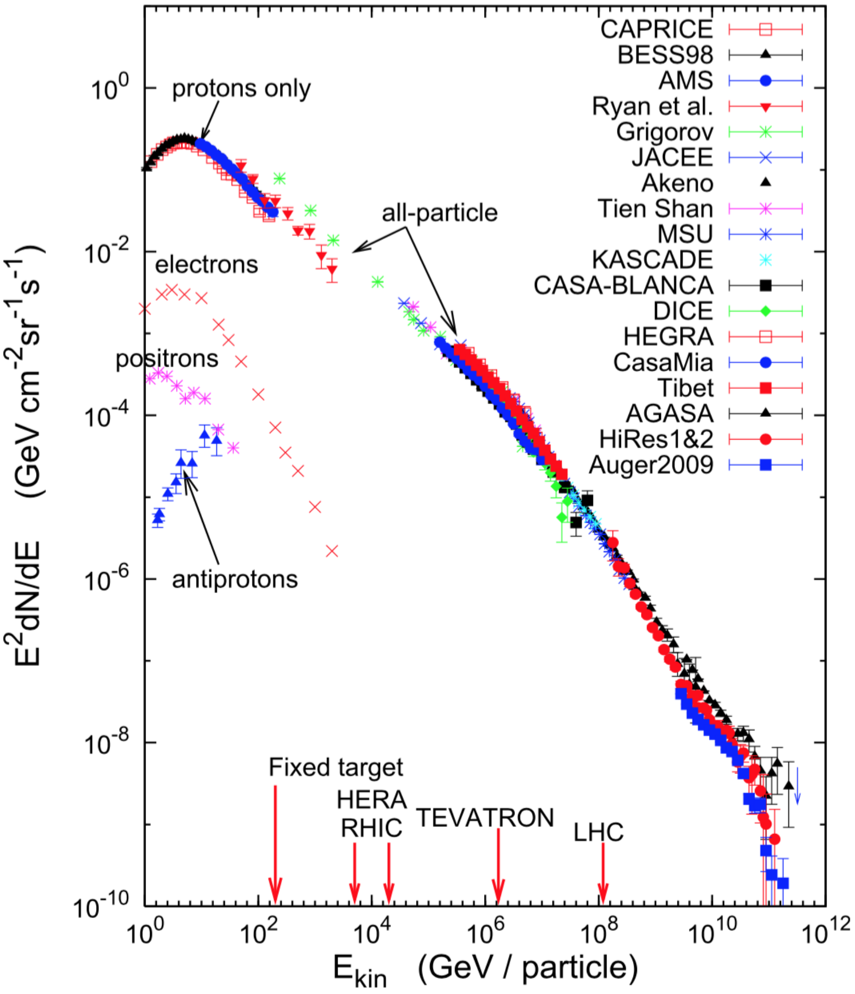

Figure 1.12: The cosmic ray spectrum for different particle types obtained from a number of experiments (Zweibel, 2013). It is a power law spectrum (with energy spectral index $\delta = 2.7$ above 10 GeV) across a huge range of energy scales.

energy E propagating in a magnetic field of strength B is given by

$$r_{\rm L} \simeq 10\,{\rm kpc}\frac{(E/10^8\,{\rm GeV})}{Z(B/1\,\mu{\rm G})}. \tag{1.43}$$

High-energy cosmic rays ($\geq 10^9\,{\rm GeV}$) only weakly interact with the interstellar medium since their Larmor radius ($\approx 20\,{\rm kpc}$ for such a proton in a $5\,\mu$G magnetic field) is the comparable to the size of the galaxy. These high-energy particles are thought to be of extragalactic origin. The energy density of the ion component of the cosmic rays can be measured via observations of diffuse gamma-rays (cosmic ray ions collide with the interstellar particles to produce pions which decay to produce gamma rays) whereas the electron/positron component is mainly observed via synchrotron and inverse Compton emissions. Cosmic rays are thought to be accelerated in strong supernova shocks by first order Fermi acceleration (Bell, 1978a). The shocks have associated magnetic field inhomogeneities both in the upstream and down- stream regions which scatter cosmic rays. In the first order Fermi process, a cosmic ray particle crosses a shock back and forth many times due to scattering by magnetic inhomogeneities, gaining energy with each crossing. This leads to an efficient acceleration and a power-law energy spectrum close to that shown in Fig. 1.12 (Longair, 1994). The subject of cosmic rays is broadly divided into two areas: cosmic ray acceleration and propagation. This work deals with latter.

Cosmic rays propagate diffusively in galaxies (Cesarsky, 1980). This is confirmed by the following observations.

- **Abundance of lighter elements in galactic cosmic rays:** If cosmic rays travel along a straight line at a relativistic speed, they would escape the galaxy in a time $t_{\rm ballistic} \approx 10\,{\rm kpc}/3\times 10^{10}\,{\rm cm\,s^{-1}} \approx 10^4\,{\rm yr}$. However, they are confined in the galaxy for a time much longer than $t_{\rm ballistic}$. This is known by 'dating' samples of galactic cosmic rays observed on or near the Earth.

  Fig. 1.13 shows abundance of elements in galactic cosmic rays in comparison with the solar-system abundances. Be is significantly more abundant in the cosmic rays than in the solar-system. This is explained by the spallation reactions of cosmic rays with the interstellar gas. Some isotopes of Be (like Be^9 and Be^{10}) are radioactive. Fig. 1.14 shows the abundance of various Be isotopes in the observed galactic cosmic rays and in laboratory experiments. The half-life of Be^{10} $\tau_{1/2}$ is known from laboratory experiments to be of the order of $10^7\,{\rm yr}$. The decreases in the number of Be^{10} atoms in comparison with other isotopes is used to measure the lifetime of cosmic rays in

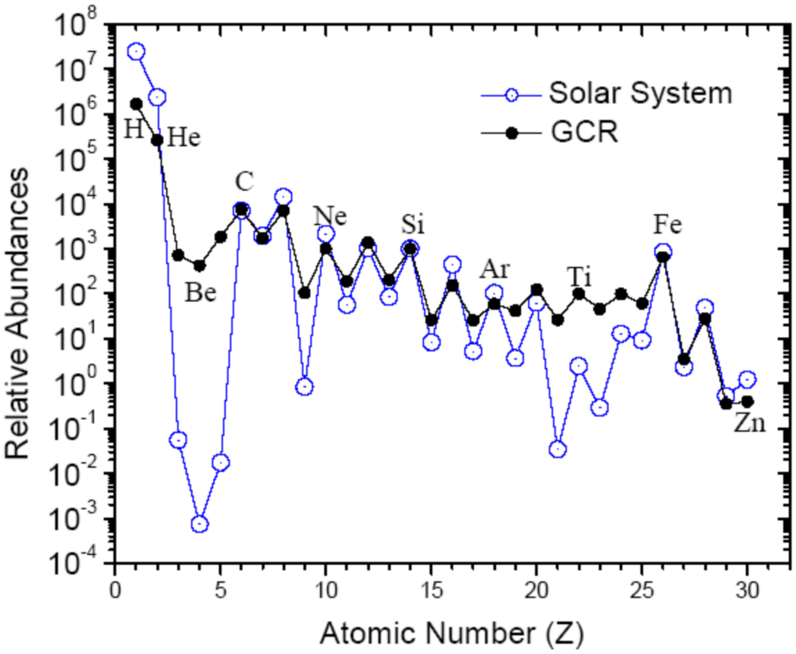

Figure 1.13: Figure taken from ACE News #83 - Oct 6, 2004: http://www.srl.caltech.edu/ACE/ACENews/ACENews83.html. Relative abundance of various elements in solar system (blue) and galactic cosmic rays (black) measured using the Advanced Composition Explorer (ACE) spacecraft managed by National Aeronautics and Space Administration (NASA). Except lighter elements, galactic cosmic ray composition is very similar to the solar abundances. The excess of certain elements (Be is in excess by six orders of magnitude) in galactic cosmic rays is due to interaction of galactic cosmic rays with the interstellar gas.

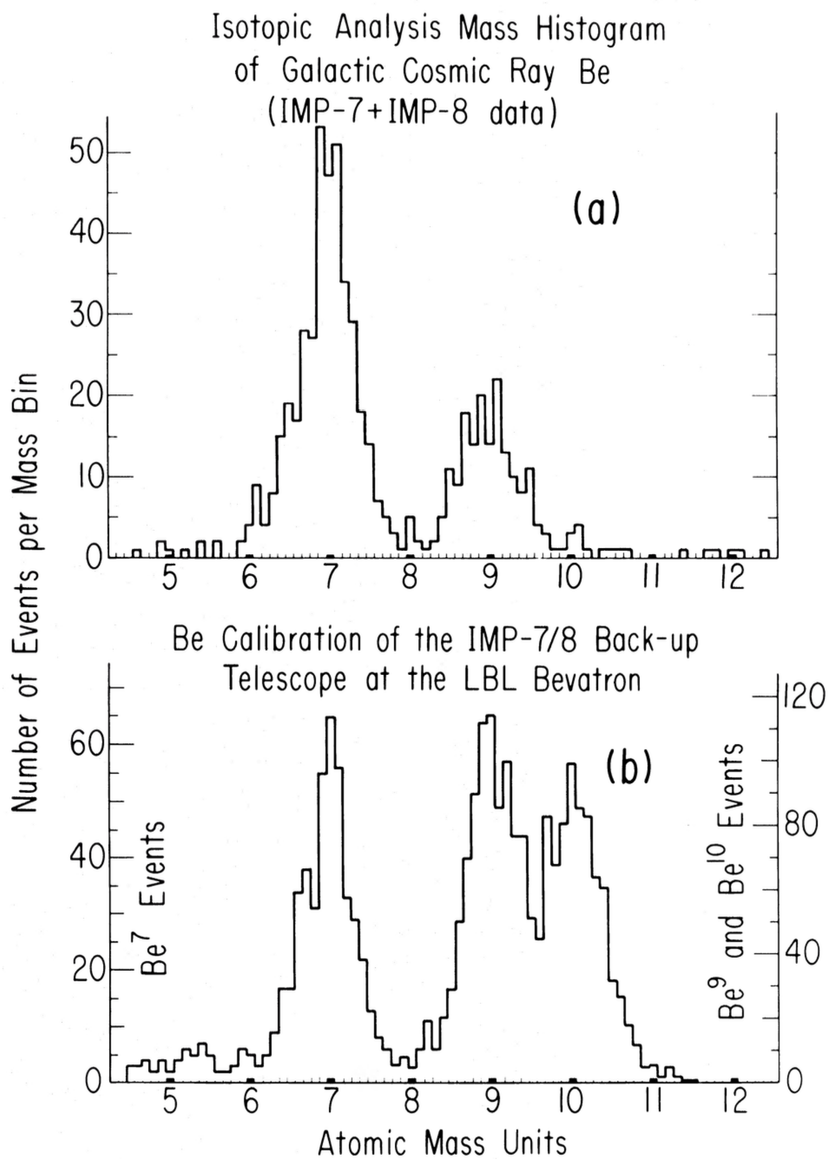

Figure 1.14: Distribution of isotopes of Be in low energy (few GeV) galactic cosmic rays (a) and in laboratory (b) (Garcia-Munoz et al., 1977). The isotopes Be^9 and Be^{10} have much less counts as compared to other isotopes because of the radioactive decay.

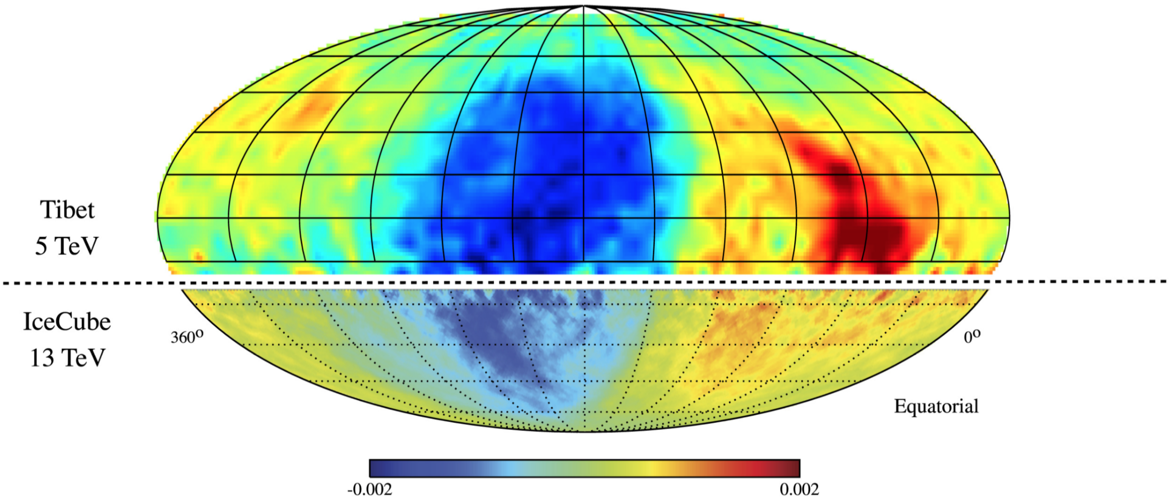

Figure 1.15: Combined cosmic ray anisotropy $\delta_{\rm cr}$ derived from data from Tibet-AS and IceCube experiments (Ahlers & Mertsch, 2017). Even at relatively high energy (10^3 times higher than the average cosmic ray energy of GeV), the level of anisotropy is quite small ($\sim 10^{-3}$) and cosmic ray distribution can be considered almost isotropic.

galaxies. From Fig. 1.14, ratio of the number of counts of Be^{10} to that of Be^{7} (which is not radioactive) in the Galactic cosmic rays is $N(\mathrm{Be}^{10})/N(\mathrm{Be}^{7}) \approx 0.1$. Assuming that both were produced in similar quantities in spallation reactions, radioactive decay law suggests that their abundance can be used to estimate the cosmic ray lifetime within the Galaxy.

$$\frac{N(\mathrm{Be}^{10})}{N(\mathrm{Be}^{7})} \approx \frac{N(\mathrm{Be}^{10})}{N_0(\mathrm{Be}^{10})} = \exp\left(-\frac{0.693}{\tau_{1/2}} t_{\rm confinement}\right), \tag{1.44}$$

where $N_0(\mathrm{Be}^{10})$ is the initial number of Be^{10} atoms and $t_{\rm confinement}$ is the confinement (or diffusion) time of cosmic rays in galaxies. Using $N(\mathrm{Be}^{10})/N_0(\mathrm{Be}^{10}) = 0.1$ and the Be^{10} half lifetime $\tau_{1/2} = 10^7$ yr, we obtain $t_{\rm confinement} \approx 2 \times 10^7$ yr. Since $t_{\rm confinement} \gg t_{\rm ballistic}$, the cosmic rays do not just fly out of galaxies but slowly diffuse through it.

- **High degree of isotropy in cosmic rays:** Cosmic ray particles are travelling at relativistic speed and thus we might expect an anisotropic distribution of cosmic rays as most sources lie in the central regions of galaxy where supernovae go off more frequently. To test this, the cosmic ray flux $\phi_{\rm cr}$ is measured from all arrival directions at the Earth and the level of cosmic ray anisotropy is calculated. The cosmic ray anisotropy

δ_{cr} is given by

$$\delta_{\mathrm{cr}} = 1 - \frac{\phi_{\mathrm{cr}}}{\langle \phi_{\mathrm{cr}} \rangle}, \tag{1.45}$$

where $\langle \cdots \rangle$ denote the averaging. The observed value of $\delta_{\mathrm{cr}} \approx 10^{-3}$ is quite low for cosmic rays of a few TeV as shown in Fig. 1.15[1]. Thus, the cosmic ray distribution is highly isotropic. This contradiction can be resolved if cosmic rays are diffusing instead of travelling along straight paths.

Cosmic rays actually travel at a speed which is very close to the speed of light c. If they are diffusing, let their effective streaming speed be v_{diff}. The relation between the cosmic ray anisotropy δ_{cr} and v_{diff} is given by

$$\frac{v_{\mathrm{diff}}}{c} \approx \delta_{\mathrm{cr}}. \tag{1.46}$$

For $\delta_{\mathrm{cr}} \approx 10^{-3}$ (Fig. 1.15), we get $v_{\mathrm{diff}}/c \approx 10^{-4}$. This estimate also follows from the theory of cosmic ray diffusion (Kulsrud & Pearce, 1969; Wentzel, 1974). Cosmic rays travelling at a speed faster than the local Alfvén speed v_{A} in the ISM excite Alfvén waves via the streaming instability and are then themselves scattered by these waves via wave-particle interaction (described in greater detail in Section 4.4 of Chapter 4). The scattering effectively reduces the streaming velocity of the particles until it is less than the local Alfvén speed and the streaming instability is stabilized. Thus, we would expect $v_{\mathrm{diff}} \approx v_{\mathrm{A}}$. For the hot phase of the ISM, $v_{\mathrm{A}}/c \approx 10^{-4}$, which explains the high degree of isotropy in cosmic ray flux.

These observations confirm that low-energy cosmic rays propagate diffusively within the galaxy due to scattering by magnetic inhomogeneities or MHD waves. These can be generated by cosmic rays themselves via the streaming instability (referred to as intrinsic turbulence) or other sources of turbulence in the ISM (referred to as extrinsic turbulence). Using random walk arguments, the mean free path λ_{cr} of cosmic rays and the diffusion coefficient can be determined. Since the velocity of the particle is nearly constant,

$$\frac{\lambda_{\mathrm{cr}}}{L} = \frac{t_{\mathrm{ballistic}}}{t_{\mathrm{confinement}}}, \tag{1.47}$$

---

[1] For particles below a few TeV, the Larmor radius of particles is quite small and the particle trajectories are significantly affected by the heliospheric magnetic fields. This makes it difficult to reliably measure the anisotropy with low energy GeV cosmic rays. The GeV cosmic rays are expected to be much more isotropic than the TeV cosmic rays.

where L is the size of the system. For GeV-cosmic rays in a galaxy of a size $10\,\mathrm{kpc}$, we obtain $\lambda_{\rm cr} \approx 10\,\mathrm{pc}$. The cosmic ray diffusion coefficient $D_{\rm cr}$ follows as

$$D_{\rm cr} = \frac{1}{2}\frac{\lambda_{\rm cr}^2}{t_{\rm confinement}} \approx 10^{28}\,\mathrm{cm}^2\,\mathrm{s}^{-1}. \tag{1.48}$$

The diffusion coefficient increases with cosmic ray energy and also depends on the properties of the magnetic field in which they propagate. For a typical cosmic ray proton, with energy 1–$10\,\mathrm{GeV}$, in a $5\,\mu\mathrm{G}$ magnetic field, the Larmor radius is about $10^{-6}\,\mathrm{pc}$, which is much smaller than the correlation length of the random magnetic field in the ISM ($\simeq\ 100\,\mathrm{pc}$). Thus, the small-scale structure of the magnetic field (discussed in Chapter 2) is particularly important for the propagation of low-energy cosmic rays (further details in Chapter 3).

The propagation of cosmic rays in galaxies can be studied by treating them as particles or by considering them as a fluid. We mostly treat cosmic rays as relativistic charged particles except in Section 4.11 of Chapter 4, where we also solve the MHD equations with cosmic rays as a diffusive fluid.

1.9 Tracers of galactic magnetic fields

Synchrotron emission

According to classical electrodynamics, accelerated charges radiate (Jackson, 1998). Charged particles in magnetic field experience the Lorentz force and follow a helical path around a magnetic field line gyrating at a frequency $\nu_{\rm g} = qB/2\pi\gamma mc$, where q is the particle charge, B is the magnetic field strength, m is the mass of the particle, c is the speed of light and $\gamma = (1 - v^2/c^2)^{-1/2}$ is the Lorentz factor. These particles radiate. The radiation is polarized with the electric field vector aligned with the particle's acceleration vector.

For a non-relativistic particle ($\gamma \approx 1$), the radiation is emitted at the gyrofrequency ($\nu = \nu_{\rm g}$) and is referred to as cyclotron radiation. The power is radiated in a 'donut' shape around the acceleration direction. When the magnetic field is perpendicular to the line of sight, the acceleration vector performs a simple harmonic motion in the plane perpendicular to the magnetic field and thus linearly polarized radiation is observed. On other hand, if the magnetic field is along the line of sight, the particle is viewed as moving in a circular orbit and circularly polarized radiation is observed. Elliptically polarized radiation is observed for any other arbitrary angle. Cyclotron emission can be used to measure magnetic field strengths around neutron stars. A cyclotron absorption feature at the energy $E = 34\,\mathrm{keV}$ in the binary

X-ray source Hercules X-1 (Gruber et al., 2001) is attributed to hot gas around neutron stars poles. Since the radiation is emitted at the gyrofrequency, one can estimate the magnetic field strength in vicinity of the neutron star poles (h is the Planck's constant):

$$B = \frac{2\pi mc(E/h)}{e} \approx 3 \times 10^{12}\,\mathrm{G}. \tag{1.49}$$

For relativistic particles ($v/c > 0.1$), the radiation is beamed (angular beam width $\simeq 1/\gamma$) in the direction of the particle motion, energy is also radiated at higher harmonics of the gyrofrequency ($n\nu_{\mathrm{g}}$, $n = 2, 3, 4, \cdots$) and the Doppler effect becomes important. All three effects together broaden the emission lines resulting in a continuous spectrum instead of a series of peaks at $\nu = n\nu_{\mathrm{g}}$. The radiation due to relativistic particles is called the synchrotron radiation. Since most of the radiation of a single particle lies within a beam, it is easier to think in terms of a velocity cone. The cone is defined by the velocity vector of a particle spiraling about a magnetic field line, with the axis along the local magnetic field direction, and its precession with gyrofrequency. The synchrotron radiation from a single particle is elliptically polarized because the electric field component parallel to the field varies differently from the component perpendicular to the magnetic field (due to the geometry of the velocity cone). However, for an ensemble of particles of different pitch angles (angle between the particle's velocity vector and the magnetic field vector), the components of elliptical polarization parallel to the magnetic field projection onto the plane of the sky cancel because the beam width on either side of line of sight is very small (since γ is high) and the resulting polarization is linear. The ratio of polarized intensity to total intensity is called the polarization fraction $\mathcal{P}$. If the particles have modest value of γ, the cancellation might not be exact and weak circular polarization is also expected. This low level circularly polarized signal, if detected in the Milky Way, can be used to further understand the properties of the Milky Way magnetic fields (Enßlin et al., 2017).

For a power-law distribution of particle energies,

$$N(E)\mathrm{d}E = CE^{-\delta}\,\mathrm{d}E, \tag{1.50}$$

where $N(E)\,\mathrm{d}E$ is the number density of particles in the energy interval $\mathrm{d}E$, δ is the energy spectral index and C is a constant, the total synchrotron emissivity J as a function of frequency ν and maximum linear polarization fraction $\mathcal{P}_0$ (assuming an uniform magnetic field) are (Ginzburg & Syrovatskii, 1965; Rybicki & Lightman, 1979; Longair, 1994)

$$J(\nu) \propto B_{\perp}^{(\delta+1)/2}\nu^{-(\delta-1)/2}, \tag{1.51}$$

$$\mathcal{P}_0 = \frac{\delta+1}{\delta+7/3}, \tag{1.52}$$

where $B_{\perp}$ is the magnetic field in the plane of the sky, i.e., perpendicular to the line of sight. Note that the maximum linear polarization fraction is independent of the frequency. The energy spectral index δ is related to the synchrotron spectral index α (synchrotron flux $\propto \nu^{-\alpha}$) by $\alpha = (\delta - 1)/2$.

The total radiated power of synchrotron emission depends on m^{-2} (Rohlfs & Wilson, 2004) where m is the mass of the particle and so relativistic electrons radiate 1836^2 times more energy than the relativistic protons. Thus, almost all of the observed synchrotron emission is due to relativistic electrons. The total I and polarized PI synchrotron intensites are given by

$$I = K\int_L n_{\text{cre}}\, B_{\perp}^2\, \mathrm{d}l, \tag{1.53}$$

$$PI = K\int_L n_{\text{cre}}\, \langle B_{\perp}\rangle^2\, \mathrm{d}l, \tag{1.54}$$

where n_{cre} is the number density of cosmic ray electrons, $B_{\perp}$ is the total magnetic field in the plane of sky, $\langle B_{\perp}\rangle$ is the magnetic field averaged in the plane of the sky, L is the path length and K is a constant. :q:

Electrons with energy E in a magnetic field of strength B radiate mostly at the frequency $\nu_{\max}$ (Ruzmaikin et al., 1988)

$$\frac{\nu_{\max}}{1\,\text{MHz}} \simeq 16\frac{B}{1\,\mu\text{G}}\left(\frac{E}{1\,\text{GeV}}\right)^2. \tag{1.55}$$

So for radio frequencies in range $150\,$MHz–$1.5\,$GHz (wavelength ≈ 0.5–$20\,$cm), with typical galactic magnetic field of around $5\,\mu$G, the electron energy using Eq. (1.55) is in the range 1–$10\,$GeV. For electrons in that energy range, the energy spectral index is $\delta \approx 3$ (Fig. 1.12) or equivalently $\alpha \approx 1$. Using Eq. (1.52), the maximum linear polarization fraction $\mathcal{P}_0 \approx 75\%$.

From the observed total synchrotron intensity, an estimate of the magnetic field in the plane of the sky $B_{\perp}$ can be obtained, if independent information about relativistic electron number density is known. In the absence of such an information, to estimate $B_{\perp}$, energy equipartition between cosmic rays and magnetic fields is often assumed (Longair, 1994; Klein

& Fletcher, 2015). In deriving the maximum linear polarization fraction as 75%, uniform magnetic field is assumed but the galactic magnetic field also has a significant random component. This reduces the linear polarization fraction due to further vector cancellation of the polarized signal. Thus, the observed linear polarization fraction $\mathcal{P}$ is always much less than $\mathcal{P}_0$. The change of observed polarization from maximum linear polarization can be used to estimate the ratio of strength of regular magnetic field $\langle B_\perp \rangle$ to random magnetic field $b_\perp$ as follows (Burn, 1966; Sokoloff et al., 1998)

$$\mathcal{P} = \frac{PI}{I} = \mathcal{P}_0 \frac{\langle B_\perp \rangle^2}{\langle B_\perp \rangle^2 + b_\perp^2}. \tag{1.56}$$

The decrease in polarization fraction is referred to as 'depolarization' and various mechanisms that are responsible for depolarization of synchrotron emission are described in Burn (1966) and Sokoloff et al. (1998). Understanding physical mechanisms which lead to depolarization of synchrotron emission can provide further insight into the properties of the average and random ISM magnetic fields. Assuming energy equipartition between cosmic rays and magnetic fields, the synchrotron intensity gives an estimate of the total magnetic field. Polarized synchrotron intensity traces the regular magnetic field and Eq. (1.56) can be used to estimate properties of the random magnetic field component.

Faraday rotation

The polarization plane of linearly polarized emission is rotated when it propagates through a magnetized plasma. This phenomena is known as the Faraday rotation. Physically, this is due to the difference in the refractive index of left- and right- circularly polarized emission in a magnetized plasma. The linearly polarized emission can be decomposed into left- and right- circularly polarized components by superposition principle. Since both components have different refractive indices, a phase difference between the two components develops on propagation. On summing up the two components after passing through the magnetized plasma, the plane of the resulting linearly polarized emission at wavelength λ with intrinsic polarization angle of ψ_0 is rotated by an angle (Longair, 1994; Klein & Fletcher, 2015)

$$\frac{\Delta\psi}{1\,\mathrm{rad}} = \frac{\psi - \psi_0}{1\,\mathrm{rad}} = \frac{\mathrm{RM}}{1\,\mathrm{rad\,m^{-2}}} \frac{\lambda^2}{1\,\mathrm{m}^2}, \tag{1.57}$$

where ψ is the polarization angle after rotation and RM is the rotation measure given by

$$\frac{\text{RM}}{1\,\text{rad}\,\text{m}^{-2}} = 0.81 \int_{0}^{z/1\,\text{pc}} \frac{n_\text{e}}{1\,\text{cm}^{-3}} \frac{B_\parallel}{1\,\mu\text{G}}\, \text{d}\left(\frac{z'}{1\,\text{pc}}\right), \tag{1.58}$$

where z is the length along the line of sight. If the propagation length is larger than the turbulent cell size (which is usually the case in galaxies), the net contribution from the random component of the magnetic field b is zero (since $\langle b \rangle = 0$) and rotation measures observations provide another method to study regular magnetic fields. By convention, RM is positive when the magnetic field is directed towards the observer. Since usually large path lengths are involved, the angle of rotation can be as high as π (or even higher multiples of π) which makes determinations of ψ_0 and RM ambiguous (Ruzmaikin & Sokoloff, 1979). This is referred to as the $n\pi$-ambiguity. To resolve it, observations at more than two wavelengths are required. By measuring the polarization angle (ψ) at three or more wavelengths and fitting a straight line to the (λ^2, ψ) points, RM (the slope) and ψ_0 (the y-intercept) can be determined using Eq. (1.57). A magnetized region which rotates the plane of linear polarization might itself be emitting synchrotron emission when it contains magnetic field, thermal electrons and relativistic electrons. In such a region, the plane of polarized emission from the far side is rotated more than from the near side. This leads to depolarization and such an effect is called the Faraday depolarization. In presence of significant Faraday depolarization, the polarization angle ψ is not a linear function of λ^2 and then it is more appropriate to define the Faraday depth via equation Eq. (1.57) and Eq. (1.58) (Burn, 1966). For multiple rotating and emitting regions along the line of sight (or within the beam of the telescope), a more involved technique called the RM synthesis (Brentjens & de Bruyn, 2005) can be employed. It provides polarized emission at different Faraday depths. RM synthesis corrects for the $n\pi$ ambiguity and is applicable even if observations are available only in a limited part of the wavelength spectrum (Brentjens & de Bruyn, 2005; Heald, 2009). To estimate magnetic field from RM or Faraday depth observations, independent information about thermal electrons n_e is required. In the Milky Way, this is obtained from the dispersion measure of pulsars. The electromagnetic interaction between charged particles and radio waves from pulsars delays the arrival of radiation emitted at different wavelengths, which leads to broadening of the pulse. The delay is inversely proportional to the mass of the particle (Rohlfs & Wilson, 2004) and thus electrons cause longer delays as compared to protons. The dispersion in the pulse thus depends on the number density of the electrons n_e and the dispersion measure DM is given by

$$\frac{\mathrm{DM}}{1\,\mathrm{cm}^{-3}\,\mathrm{pc}} = \int_0^{z/1\,\mathrm{pc}} \frac{n_\mathrm{e}}{1\,\mathrm{cm}^{-3}}\,\mathrm{d}\left(\frac{z'}{1\,\mathrm{pc}}\right), \tag{1.59}$$

where z is the path length along line of sight. Thus, dividing RM as in Eq. (1.58) by DM as in Eq. (1.59), a crude estimate of magnetic field along line of sight can be obtained (Rand & Lyne, 1994). Magnetic field in galaxies can also be studied by measuring RM of background polarized radio sources. Their RM is a combination of intrinsic RM of the source, an intervening galaxy, intergalactic medium and the Milky Way. It is usually very difficult to isolate these contributions. This technique is used to detect magnetic fields in high-redshift galaxies where a statistical study using number of such sources has be conducted (Bernet et al., 2008).

Optical polarization

Dust particles due to their magnetic moment are aligned with the local galactic magnetic field (Davis & Greenstein, 1951). Since the dust grains are non-spherical, the optical starlight from behind the dust has different levels of extinction along the major and minor axis of the grains. This leads to linear polarization of starlight parallel to the local magnetic field component projected onto the plane of the sky. As the level of alignment depends on the properties of the dust grains, especially their size and magnetic properties, the resulting linear polarization also depends on those properties. Using radio (RM) and optical (starlight polarization) observations, a three-dimensional model of the large-scale magnetic field can be constructed, as done for the Small Magellanic Cloud (SMC) by Mao et al. (2008).

Dust polarization

Besides distorting the background optical starlight, dust particles themselves emit in the microwave, sub-millimetre and far-infrared wavebands. This emission is polarized along the major axis of the dust grains, i.e., in the direction perpendicular to the local galactic magnetic field. The properties of polarized emission again depend on the dust grains' properties. The starlight polarization data, when compared with dust polarization data, provide compatible results for the Milky Way magnetic field (Soler et al., 2016).

Zeeman splitting

Magnetic field splits the electronic energy levels of an atom and the splitting depends on the magnetic field strength. This is known as the Zeeman splitting and it was first used to

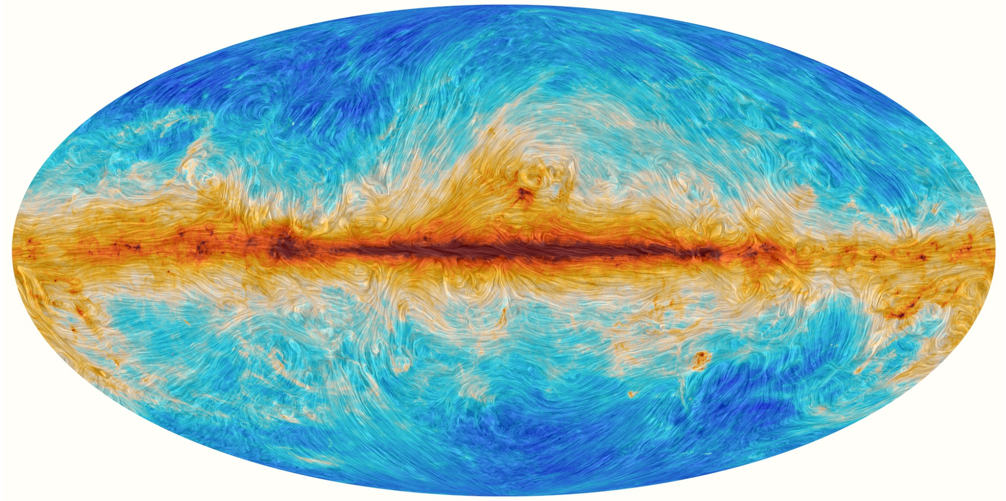

Figure 1.16: Figure taken from Planck's webpage - http://www.esa.int/spaceinimages/Images/2015/02/Polarised_emission_from_Milky_Way_dust. It shows the dust emission at 353 GHz where the color shows the total intensity (blue minimum, intense red maximum) and the striations show the direction of the Milky Way magnetic field projected on the plane of the sky.

measure magnetic fields in sunspots. It is a direct probe of magnetic field, unlike previous tracers. The frequency difference of radio spectral lines due to the splitting is quite small and so it can be used only in regions where magnetic field is strong. Also, it competes with the Doppler broadening of those lines and thus the temperature of region should also be low enough. Thus, it is the best probe for regions with high magnetic fields and low temperature, for example, molecular clouds (Crutcher, 2012).

1.10 Observations of magnetic fields in galaxies

It is difficult to see the overall pattern of the Milky Way's magnetic field since we sitting in it. Planck satellite gives a detailed view of the Milky Way's magnetic field via dust polarization measurements as shown in Fig. 1.16. It shows that the magnetic field is ordered and strongest in the galactic plane. It also shows that the magnetic field in gas clouds (above and below the plane) is turbulent and tangled. Overall, the Milky Way magnetic field is smooth and ordered over large scales but becomes random on smaller scales. The gradient of synchrotron polarization can used to extract properties of the ISM turbulence in the Milky Way (Gaensler et al., 2011; Herron et al., 2017). Fig. 1.17 shows the gradient of observed linear polarization for a small part of the Milky Way galaxy. The statistics of gradient of polarization obtained from observations and numerical simulations (three dimensional MHD turbulence simulations of the ISM with Mach number as a parameter) are compared to conclude that the ISM has a low

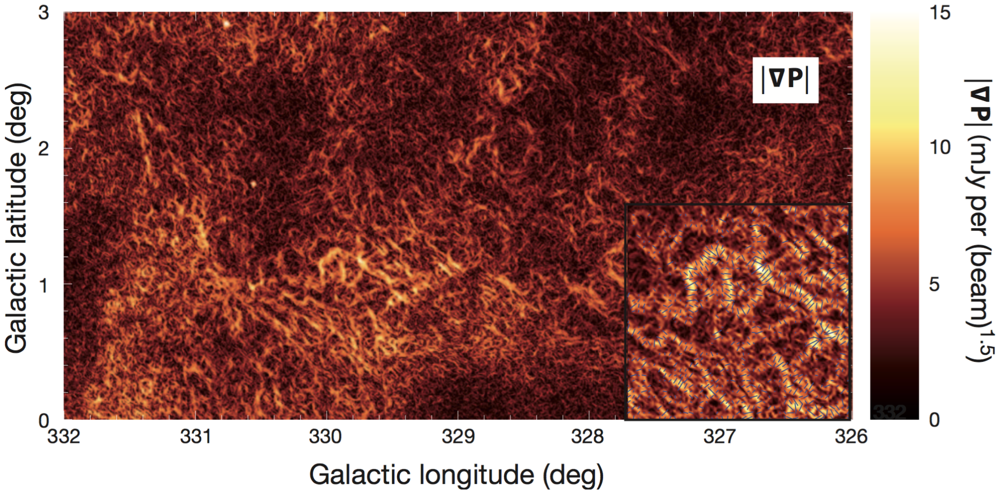

Figure 1.17: Gradient of observed linear polarization for patch of the Milky Way (Gaensler et al., 2011). By comparing statistics of the gradient with that obtained from the numerical simulations, it can be shown that the ISM is turbulent with Mach number approximately equal to 2.

sonic Mach number ($\lesssim 2$). Such a turbulent medium generates spatially intermittent random magnetic fields.

Observing magnetic fields in external galaxies shows the overall pattern of the large-scale magnetic fields. However, the spatial resolution goes down and with the existing radio telescopes it is difficult to directly probe the small-scale ISM properties in those systems. Magnetic fields in the face-on spiral galaxy M51 were studied in great detail by Fletcher et al. (2011). The spiral pattern of the regular magnetic fields as shown in Fig. 1.18 does not produce a similar pattern in the Faraday rotation measurements. Thus, the ordered field is a combination of the large-scale (or mean-field) dynamo generated field and anisotropic turbulent random field. This need not be the case always. For example, in M31, the RM pattern follows the large-scale ordering of the polarized synchrotron intensity (Berkhuijsen et al., 2003). The extracted mean magnetic field is usually decomposed into a set of azimuthal modes (m). For M51, in the disc the mean field is described by the $m = 0, 2$ modes (which agrees with mean-field dynamo theory) and in the halo by a $m = 1$ azimuthal mode. The properties of the small-scale magnetic fields are estimated from the amount of depolarization. In M51, by analyzing synchrotron depolarization, the correlation length of the small-scale magnetic field is estimated to be of the order of $50\,\mathrm{pc}$. Many properties of the observed magnetic fields in the Milky Way and nearby spiral galaxies agrees with the galactic dynamo theory (Beck, 2016).

It is important to measure magnetic fields in high redshift or young galaxies to constrain

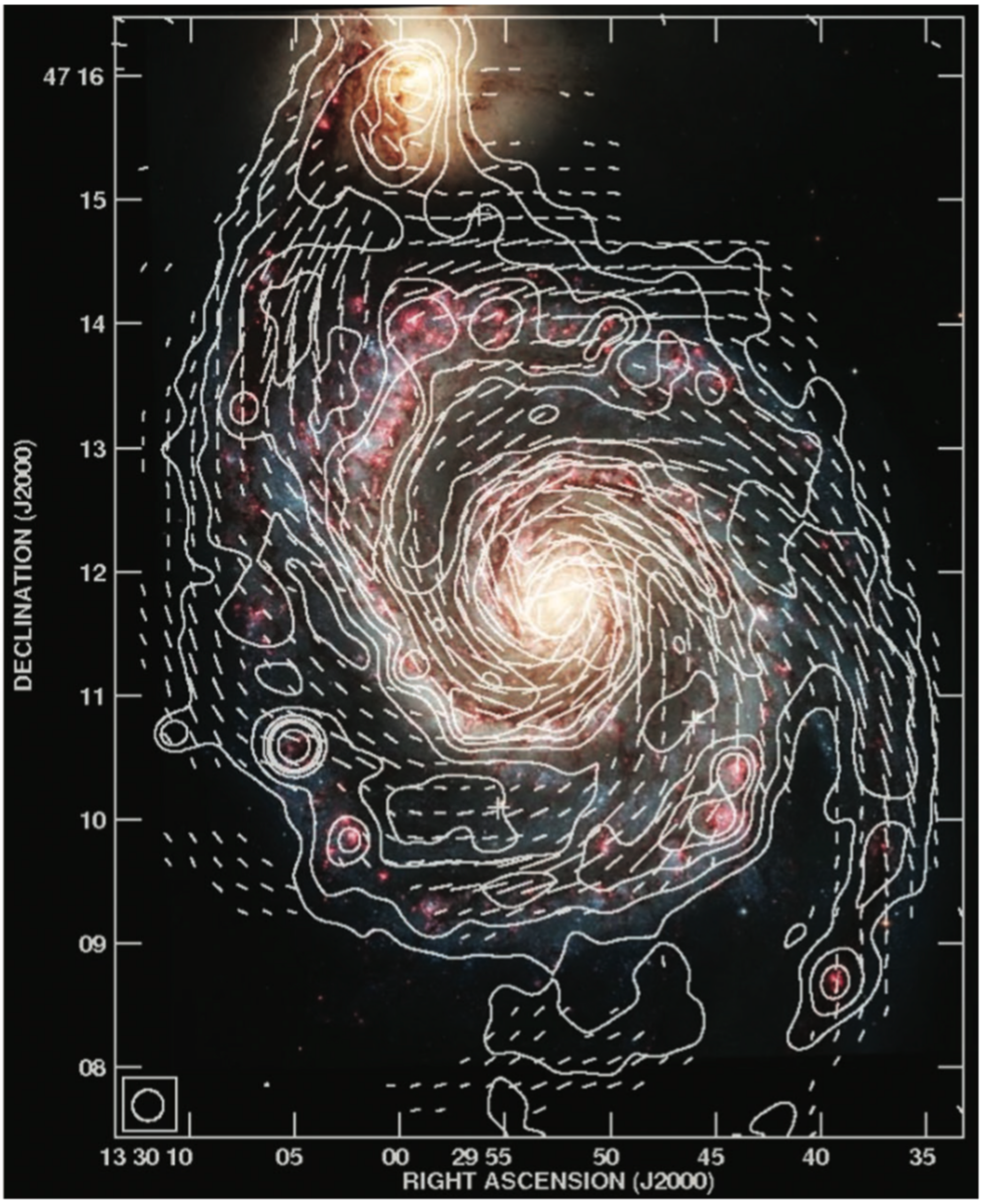

Figure 1.18: Contours of total synchrotron intensity overlaid on the top of the optical image and lines shows the magnetic field vectors obtained from polarized intensity in M51 (Fletcher et al., 2011). The polarized synchrotron intensity traces the ordered magnetic field (field generated by the large-scale dynamo and anisotropic turbulent field).

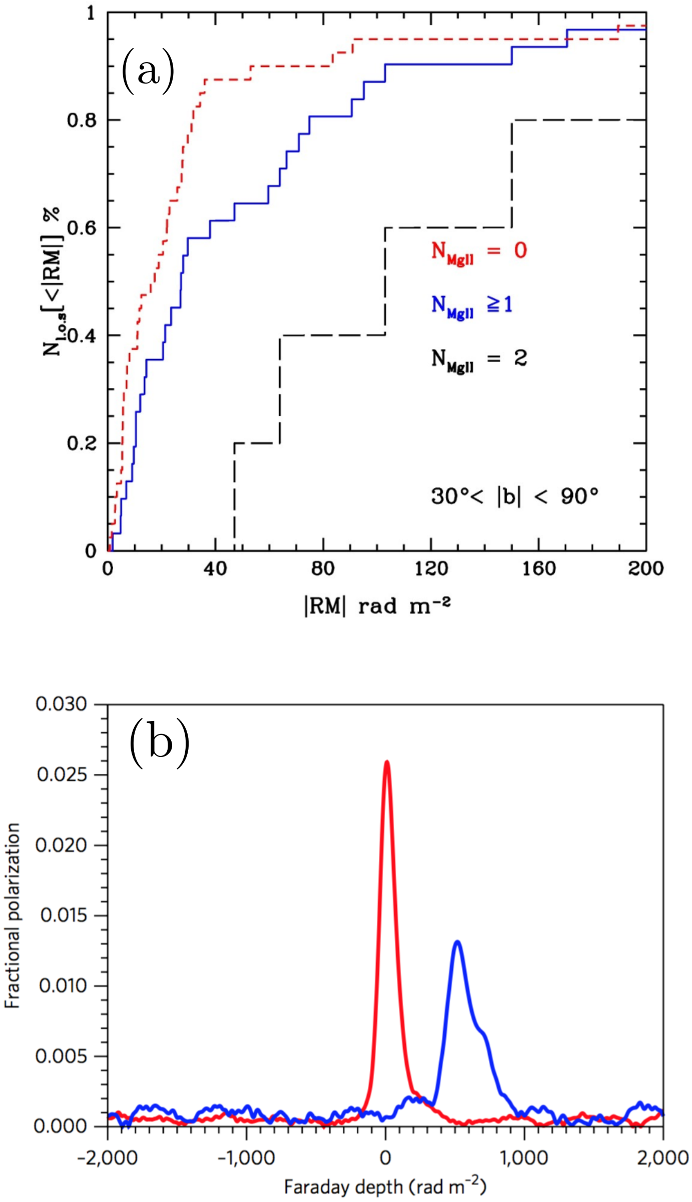

Figure 1.19: (a) A statistical study to detect magnetic field in high redshift galaxies (Bernet et al., 2008). Cumulative histogram showing number of RM measurements with value less than that on the x axis for systems with no MgII absorber (red), one of more MgII absorbers (blue) and two MgII absorbers (black). The systems with MgII absorbers statistically shows higher values of RM. This can be used to study properties of magnetic fields in high redshift galaxies. (b) An observational study to detect magnetic field in an individual high redshift galaxy (Mao et al., 2017). Faraday depth spectra (fractional polarization versus Faraday depth) of two gravitationally lensed images (blue and red) with lensing galaxy at a redshift of 0.439. The difference in the mean and standard deviation of two components is used to infer the magnetic field in the lensing galaxy.

the parameters of the galactic dynamo theory. However, it is extremely difficult to do the same because of limited sensitivity and resolution of the existing radio telescopes. Magnetic fields in young galaxies are studied via numerical simulations (Pakmor et al., 2014; Rodrigues et al., 2015) but there have also been few attempts to study them via observations. Evidence of large-scale magnetic fields in young galaxies is obtained by studying excess of RM in MgII absorption systems (Bernet et al., 2008). MgII absorption line in the spectrum is usually associated with a galaxy. The plane of polarization of the light from the background source is rotated by a galaxy. If the redshift of the absorption line is less than that of the source, the observed RM also has contribution from the foreground galaxy. Fig. 1.19a shows RM in systems with none, one or more and two MgII absorption lines in the spectra. RM is statistically higher for sources with MgII absorbers and is associated with the large-scale field in young galaxies. The magnetic field in an individual high redshift 'lensing' galaxy is estimated by comparing the distribution of Faraday depth spectra between two images of a background source (Mao et al., 2017). Fig. 1.19b shows the Faraday depth spectra of two images. The difference in the mean of two components (difference in RM between two images) gives an estimate of the large-scale magnetic field in the lensing galaxy. And the difference in the standard deviation of the two components (difference in the standard deviation of RM) provides some information about the small-scale magnetic fields. The strength of magnetic fields in the young galaxy is comparable to that in the nearby galaxies. Many such observations of magnetic fields in young galaxies would be useful in confirming various aspects of the galactic dynamo theory.

1.11 Aim and structure of the thesis

Cosmic rays and magnetic fields are important non-thermal components of the ISM in spiral galaxies. The interaction between cosmic rays and magnetic fields is described in Fig. 1.20. In Chapter 2, we first characterize and describe the small-scale structure of intermittent magnetic fields generated by a fluctuation dynamo. Then in Chapter 3, we study the effect of magnetic intermittency in the ISM on cosmic ray propagation. We test the energy equipartition assumption between cosmic rays and magnetic fields in Chapter 4. In Chapter 5, we describe observational signatures of magnetic fields in elliptical galaxies. Beyond confirming existing results, each chapter tries to answer couple of questions. The questions chapter-wise are given below.

Chapter 2: Fluctuation dynamo and its nonlinear states

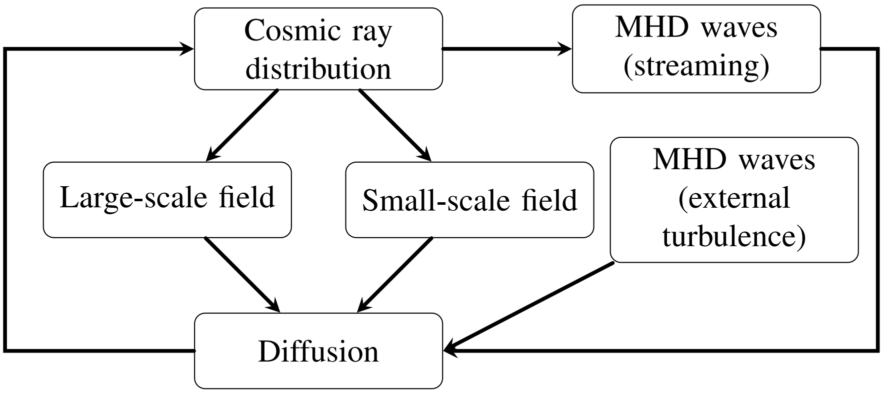

Figure 1.20: Flowchart showing interactions between cosmic rays and magnetic fields in the ISM which leads to cosmic ray diffusion.

- How does the non-linear fluctuation dynamo saturate?
- How does the intermittent structure of the fluctuation dynamo-generated magnetic fields depend upon its nonlinear state and on the magnetic Reynolds number?

Chapter 3: Cosmic ray diffusion in intermittent magnetic fields

- Is the intermittent structure of magnetic field important for cosmic ray diffusion?
- How do magnetic structures alter cosmic ray propagation?

Chapter 4: Correlation between cosmic rays and magnetic fields

- Are cosmic rays and magnetic fields spatially correlated?
- What is the reason for the presence of small-scale cosmic ray structures?
- Does the relation between magnetic fields and cosmic rays change when the pressure due to thermal gas is also included?

Chapter 5: Magnetic fields in elliptical galaxies

- Can magnetic fields be detected in elliptical galaxies and used as a probe of the fluctuation dynamo theory?
- What are the observational signatures of magnetic fields in elliptical galaxies?

Chapter 2

Fluctuation dynamo and its nonlinear states

The small-scale magnetic field in the ISM is generated by a fluctuation dynamo mechanism. The fluctuation dynamo converts kinetic energy of a random flow into small-scale, random magnetic field energy. The magnetic field is amplified exponentially (the kinematic stage) until the back reaction on the flow due to the Lorentz force becomes important and then the dynamo action saturates (the saturated stage). In this chapter, we first look at the kinematic fluctuation dynamo for simple flows and then study the nonlinear fluctuation dynamo in driven turbulence via numerical simulations. We demonstrate that the magnetic field saturates because its amplification and diffusion are both affected by the back reaction. The amplification of the magnetic field is reduced due to a stronger alignment between the velocity field, magnetic field, and electric current density. Furthermore, both aspects of magnetic field amplification, i.e. stretching and compression of field lines, are reduced as the dynamo saturates. The enhancement in diffusion is confirmed by the decrease in the local value of magnetic Reynolds number. Next, we study the spatially intermittent structure of the fluctuation dynamo-generated magnetic fields using the Minkowski functionals. The typical length, width, and thickness of the magnetic structures are obtained for the kinematic and saturated stages. We show that the structures are of a larger size in the saturated stage in comparison to the kinematic stage. The filamentarity and planarity of magnetic structures in nonlinear dynamos approach their asymptotic values as the magnetic Reynolds number increases. This suggest that even though the magnetic Reynolds number is extremely high in most astrophysical systems, the strong (few times the root-mean square value) magnetic field produced by the fluctuation dynamo occupies a significant fraction of the volume.

2.1 Random magnetic fields in the ISM

Several mechanisms produce random magnetic fields in the ISM of spiral galaxies. Tangling of the large-scale magnetic field by turbulent flows produces a volume-filling random field whose statistical properties are controlled by the turbulence. This magnetic field is a byproduct of the mean-field dynamo action. If the turbulent velocity has Gaussian statistical properties, the resulting random magnetic field is also a Gaussian random field. Random motions can also generate a random magnetic field directly through fluctuation dynamo action. The resulting magnetic field is spatially intermittent (magnetic field is concentrated into filaments and ribbons) and has strongly non-Gaussian statistical properties (further described in Section 2.4.2). Another similarly structured contribution is produced by compression in random shock fronts driven by supernova explosions (Bykov & Toptygin, 1985; Federrath et al., 2010). The result of such compression is a complex random magnetic field represented by both Gaussian and non-Gaussian parts (as shown in Chapter 3, these scatter cosmic rays differently). In this section, we estimate the contribution of each of the above mechanisms to the small-scale interstellar magnetic fields. We denote $\mathbf{b}_1$, $\mathbf{b}_2$ and $\mathbf{b}_3$ as the random magnetic fields produced by tangling of the mean field, by the fluctuation dynamo action and by shock compression, respectively.

The tangling of a large-scale magnetic field $\mathbf{B_0}$ by a random flow $\mathbf{u}$ can be described by the induction equation with magnetic diffusion neglected over the timescales of interest, $\partial \mathbf{b}_1/\partial t \approx \nabla \times (\mathbf{u} \times \mathbf{B_0})$. By order of magnitude, $b_1 \simeq u_{\rm rms} B_0 \tau / l_0$, where τ and l_0 are the relevant time and length scales (l_0 being the driving scale of the turbulence). Assuming that τ is equal to the eddy turnover time, $l_0/\, u_{\rm rms}$, we obtain $b_1 \simeq B_0$. This part of the random magnetic field is present wherever $B_0 \neq 0$, i.e., presumably at all positions. As described in Section 1.5.1, the strength of the interstellar large-scale magnetic field is controlled by various global properties of the ISM. Observations suggest $B_0 \simeq 1$–$5\,\mu$G, varying between galaxies and between various locations within a given galaxy (Beck, 2016). Thus, $b_1 \simeq 1$–$5\,\mu$G in the rms sense.

Magnetic structures produced by the kinematic fluctuation dynamo due to a turbulent flow, with the kinetic energy spectrum $E \propto k^{-s}$ at $k \gg 2\pi/l_0$ (where k is the wave number and l_0 is the driving scale of the turbulence), produce magnetic structures of length l_0 (independent of s) that have a typical width of $l_0 \mathrm{Re}_{\rm M}^{-1/2}$ (independent of s) and thickness $l_0 \mathrm{Re}_{\rm M}^{-2/(1+s)}$ (Wilkin et al., 2007). The correlation length of the small-scale random magnetic fields l_b is always less than the driving scale of the turbulence, l_0. Wilkin et al. (2007) find that the magnetic correlation length scale $l_b/l_0 \simeq \mathrm{Re}_{\rm M}^{-0.4}$. Subramanian (1999) suggests that the statistically steady (saturated) state of the dynamo corresponds to the effective value of the magnetic Reynolds number $\mathrm{Re_M} \simeq \mathrm{Re_M^{(crit)}}$, where $\mathrm{Re_M^{(crit)}} \simeq 10^2$–$10^3$ is the critical magnetic Reynolds number for the dynamo action. Then $l_b/l_0 \simeq \mathrm{Re_M^{(crit)}}^{-0.4} \simeq 0.2$–$0.05$. Assuming that the magnetic field strength within such structures is close to energy equipartition with the turbulent energy and there is one such structure in each flow correlation volume l_0^3, the root-mean-square magnetic field strength (averaged over a volume l_0^3, or larger) follows as $b_2 \simeq (l_b/l_0)^{3/2}\, b_\mathrm{eq} \simeq \mathrm{Re_M^{(crit)}}^{-0.6}\, b_\mathrm{eq} \simeq (0.02\text{–}0.06)\, b_\mathrm{eq}$ with $b_\mathrm{eq} = (4\pi\rho u_0^2)^{1/2} \simeq 5\,\mu\mathrm{G}$. Direct numerical simulations suggest that, at high magnetic Reynolds number, a saturated fluctuation dynamo produces a stronger rms magnetic field, $b_2 \simeq 0.1$–$0.7\, b_\mathrm{eq}$ (Haugen et al., 2004a). This implies that random magnetic fields outside the filaments and ribbons contribute significantly to the magnetic energy density or there are a few magnetic structures in each flow correlation cell. Thus, such estimates are not sufficient and direct numerical simulations are required to study the small-scale magnetic fields generated by a nonlinear fluctuation dynamo.

Another contribution to non-Gaussian magnetic fields in the ISM is due to random shock compression. Primary and secondary shock fronts produced by supernova explosions and strong stellar winds can be described as pervasive shock-wave turbulence in the interstellar medium (Bykov & Toptygin, 1987). The typical separation between random shocks in the warm interstellar medium is 10^{16}–$10^{17}\,\mathrm{cm}$ (Bykov, 1988). The magnetic field associated with the shock-wave turbulence has a spectrum close to k^{-2} and is intermittent at scales smaller than the separation of the shock fronts. It is reasonable to expect that the energy density of these random magnetic fields is of the same order of magnitude as the kinetic energy of turbulence, $b_3 \simeq b_\mathrm{eq}$.

Overall, the small-scale magnetic field in the ISM is a combination of non-Gaussian (due to fluctuation dynamo and shocks) and Gaussian (due to tangling of a mean magnetic field) components of comparable energy density. Thus, we consider both the intermittent and Gaussian field in our study of cosmic ray propagation in random magnetic fields (Chapter 3 and Chapter 4).

The magnetic field structure is likely to be different in different phases of the ISM. The warm, partially ionized gas occupies a large fraction of the galactic disc volume and hosts both the large-scale and small-scale dynamos. Hot gas has a scale height larger than the disc half-thickness and flows up to fill the galactic corona. Numerical simulations of the multiphase ISM driven by supernovae (Gent et al., 2013a) suggest that the large-scale magnetic field is stronger in the warm phase whereas random fields are equally present in all the phases of the ISM (Evirgen et al., 2017). So, the structure of the small-scale magnetic field would also vary depending on the phase of the ISM.

In this chapter, we study fluctuation dynamo via numerical simulations. Our goal here is to describe the nonlinear state of the fluctuation dynamo. We explore the saturation mechanism of fluctuation dynamos and then quantitatively discuss the morphology of magnetic structures.

2.2 Introduction to fluctuation dynamos

A fluctuation dynamo is a MHD dynamo produced by a flow which is turbulent and therefore fluctuates in time and space. A weak seed magnetic field in a turbulent electrically conducting fluid either grows or decays. When the field grows, the magnetic field eventually becomes strong enough to react back on the flow via the Lorentz force. This alters the properties of the turbulent flow. However, initially the effect of the Lorentz force is negligible if the magnetic field is weak. The problem then can be studied by solving the induction equation for a prescribed velocity field. This is referred to as the kinematic or linear (since for a prescribed velocity field, the problem is linear in the magnetic field) fluctuation dynamo. The goal is to determine if the magnetic field grows exponentially and to quantify the spatial structure of the amplified magnetic fields. In the nonlinear regime, the magnetic field saturates due to the back reaction of the Lorentz force on the flow. The primary question in the nonlinear regime is to describe the nonlinear state of the fluctuation dynamo and understand the mechanism by which the dynamo saturates. This chapter deals mostly with nonlinear fluctuation dynamos as the kinematic dynamos have been studied more thoroughly.

Dynamo action is impossible for certain kinds of velocity and magnetic fields. For example, Cowling (1933) demonstrated that an MHD dynamo cannot maintain a steady axisymmetric magnetic field and Zel'dovich (1957) showed that a planar velocity flow cannot generate exponentially growing magnetic fields. These results are called antidynamo theorems since they rule out the existence of a dynamo for certain cases, usually for symmetric flow and magnetic field geometries (Moffatt, 1978). Such theorems also establish that the dynamo problem is inherently three dimensional in space.

The magnetic field only grows when the magnetic Reynolds number Re_{M} is greater than the critical magnetic Reynolds number $\mathrm{Re}_{\mathrm{M}}^{(\mathrm{crit})}$, which depends on the properties of the flow. Given a flow, the growth rate of magnetic field depends on Re_{M}. In most astrophysical system, $\mathrm{Re}_{\mathrm{M}} \gg \mathrm{Re}_{\mathrm{M}}^{(\mathrm{crit})}$. Based on the growth rate in the limit $\mathrm{Re}_{\mathrm{M}} \to \infty$, dynamos can be divided into two types: slow and fast dynamos (Vainshtein & Zel'dovich, 1972). If the growth rate remains positive in the limit $\mathrm{Re}_{\mathrm{M}} \to \infty$, then the dynamo is a fast dynamo, otherwise it is a slow dynamo. Since, even at a very high Re_{M}, magnetic fields are observed in most astrophys-

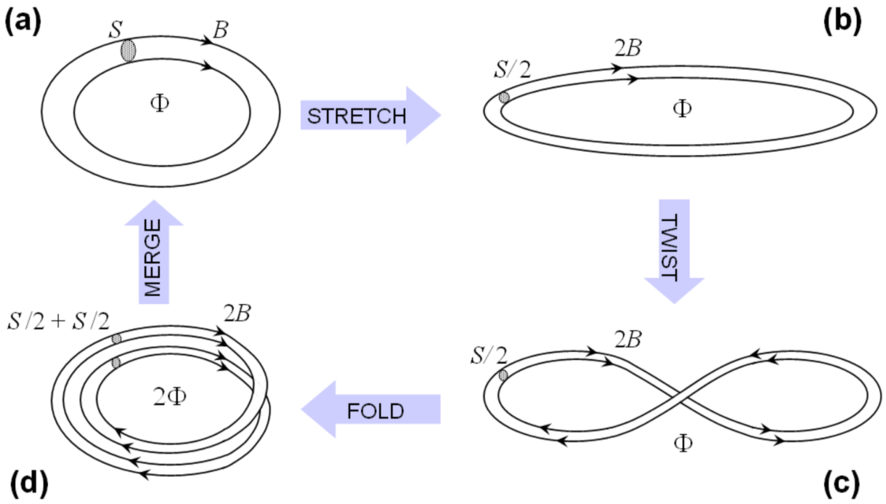

Figure 2.1: The stretch-twist-fold-merge mechanism (image credits: Anvar Shukurov). S and B are the cross section and magnetic field strength of the initial flux tube. $\phi = SB$ is the magnetic flux associated with the tube.

ical systems, such systems probably host fast dynamos. A fast dynamo can be conceptually explained by a Stretch-Twist-Fold (STF) mechanism (Vainshtein & Zel'dovich, 1972; Childress & Gilbert, 1995) illustrated in Fig. 2.1. Assuming flux freezing and incompressible motions, the algorithm to amplify magnetic field via the STF mechanism is as follows. First, the magnetic flux tube is stretched to double its length while preserving its volume, (a) → (b) in Fig. 2.1. This increases the magnetic field strength by a factor of two since the cross section is halved. Then the flux tube is twisted to form a figure eight, (b) → (c) in Fig. 2.1, and folded on itself, (c) → (d) in Fig. 2.1. Now, both loops of the tube have the magnetic field along the same direction and together occupy the same volume as the original flux tube. Both loops of the tube are now merged together into one, (d) → (a) in Fig. 2.1. The last step requires magnetic diffusion for process to become irreversible. The magnetic field is doubled for each cycle and increases by a factor of 2^n after n such steps. The growth rate is $\ln 2/T$, where T denotes the period of the STF cycle, is independent of the magnetic diffusivity or Re_M and thus this is a fast dynamo. The growth in magnetic energy is at the expense of the kinetic energy of the STF motions. Once the magnetic field becomes strong enough, the Lorentz forces reacts back on the flow. In the STF mechanism, this would imply difficulty in either the stretching and twisting due to magnetic tension or the merging of loops becoming slower (Brandenburg & Subramanian, 2005; Seta et al., 2015).

Kazantsev (1968) solved the kinematic fluctuation dynamo problem analytically for an isotropic, incompressible, mirror-symmetric, single-scale, homogeneous and Gaussian random velocity field, which is also δ-correlated in time. The magnetic field power spectrum M_k in the Kazantsev model is a power-law $M_k \propto k^{3/2}$, independent of the slope of the velocity power spectrum in the inertial range (Kulsrud & Anderson, 1992). Though the scaling obtained by Kazantsev (1968) is for a single-scale flow, it also emerges in more general cases in numerical simulations.

It is difficult to solve the complete nonlinear dynamo problem analytically and thus the nonlinear case is mostly studied via numerical simulations. Both the Navier–Stokes and induction equations are solved numerically with a random forcing (Meneguzzi et al., 1981; Cattaneo, 1999; Haugen et al., 2004a; Schekochihin et al., 2004; Brandenburg & Subramanian, 2005; Cho & Ryu, 2009; Cattaneo & Tobias, 2009; Bushby et al., 2010; Federrath et al., 2011; Favier & Bushby, 2012; Sur et al., 2012; Beresnyak, 2012; Brandenburg et al., 2012; Bhat & Subramanian, 2013; Federrath et al., 2014; Federrath, 2016; Sur et al., 2018). The numerical studies deal with both incompressible and compressible plasma. Dynamos with an incompressible plasma are more efficient than the dynamos in a compressible medium due to higher generation of vorticity in the incompressible medium (Haugen et al., 2004b; Federrath et al., 2011). Since we are here interested in the physics of the saturation mechanism, we will focus only on the dynamos in an incompressible flow.

Magnetic diffusion or dissipation occurs via reconnecting flux tubes and thus reconnection is necessary for dynamo action. This further clarifies the role of diffusion. Too much diffusion kills the dynamo and on the other hand too little diffusion makes dynamo action impossible. To study dynamo action, diffusion must be included as that is the only term in the induction equation which can change magnetic field topology (Tobias et al., 2011). It is important to change magnetic field topology for fields to grow and for the solution to become the eigenfunction of the induction equation. Also, in the absence of diffusion, the eigenfunction eventually becomes spatially non-differentiable because of the lack of smoothing. Thus, it is important to consider diffusion to explore a dynamo. Some numerical studies include only the induction term, with no explicit magnetic diffusion. They therefore rely upon numerical dissipation. Unfortunately, the numerical diffusion is neither easily quantifiable nor controllable and thus in our simulations we always include explicit diffusion.

For nonlinear fluctuation dynamos in an incompressible plasma, there are three important scales in the problem: the driving scale of the turbulent flow $2\pi/k_{\mathrm{F}}$, the viscous scale l_ν and the resistive scale l_η. Based on the magnetic Prandtl number $\mathrm{Pr_M} = \mathrm{Re_M}/\mathrm{Re}$, fluctuation dynamos can be divided into small and large $\mathrm{Pr_M}$ cases. $\mathrm{Pr_M}$ is greater than 1 for hot diffuse plasma (interstellar and intergalactic medium) and $\mathrm{Pr_M}$ is much smaller than 1 for dense plasma (planets, stars and liquid metal dynamo experiments). For $\mathrm{Pr_M} \gg 1$, the resistive

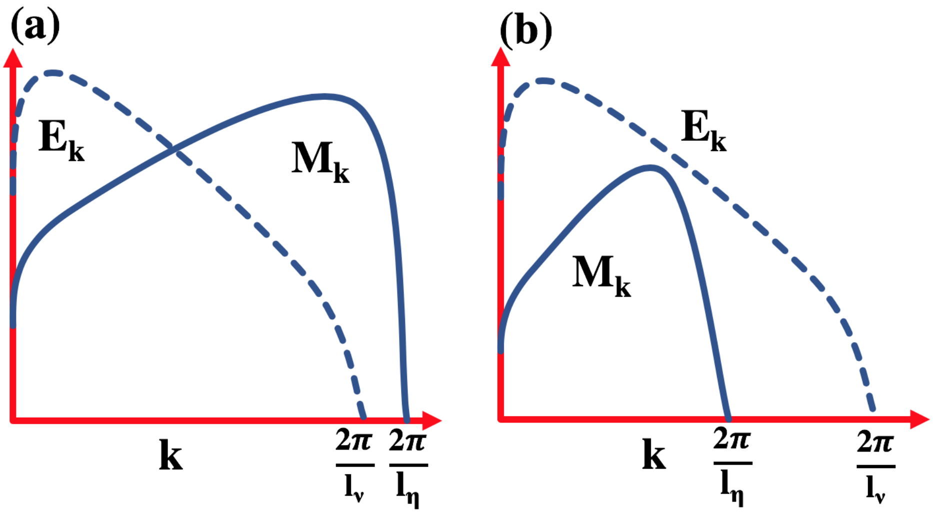

Figure 2.2: Log-log plots of kinetic (E_k, dashed) with a well-defined inertial range and magnetic (M_k, solid) energy spectra for the fluctuation dynamo at $\mathrm{Pr_M} \gg 1, l_\eta \ll l_\nu$ (a) and $\mathrm{Pr_M} \ll 1, l_\eta \gg l_\nu$ (b).

scale is smaller than the viscous scale ((a) in Fig. 2.2) and thus the magnetic dissipation occurs where the velocity field is smooth (all velocity fluctuations are damped out at the viscous scale). On the other hand, for $\mathrm{Pr_M} \ll 1$, the resistive scale is within the inertial range of the fluid turbulence ((b) in Fig. 2.2) and so the magnetic dissipation occurs in the region where the velocity field is turbulent or spatially rough. It is harder to excite a dynamo with rough velocity fields (Boldyrev & Cattaneo, 2004). The small-scale eddies in the flow rotate faster and assuming that the magnetic field is frozen in the fluid, the smallest eddies stretches the magnetic field lines and thus amplifies the field most efficiently. For the same l_ν, the magnetic fluctuations are damped at scales much larger for dynamos with $\mathrm{Pr_M} \ll 1$ than that in $\mathrm{Pr_M} \gg 1$ case. Thus, the magnetic field grows at a larger number of scales (including the fastest scale close to l_ν) for $\mathrm{Pr_M} \gg 1$, making it a more efficient dynamo. The result has also been confirmed numerically. The critical magnetic Reynolds number $\mathrm{Re_M^{(crit)}}$, which is a threshold for dynamo action to occur, increases with decreasing $\mathrm{Pr_M}$ in numerical simulations (Haugen et al., 2004a; Schekochihin et al., 2005, 2007; Iskakov et al., 2007). For studying the saturation mechanism of fluctuation dynamos, we use numerical simulations at $\mathrm{Pr_M} = 1$ ($l_\eta = l_\nu$), to make sure that both resistive and viscous scales are resolved equally. On other hand, to study the dependence of magnetic structures on the magnetic Reynolds number $\mathrm{Re_M}$, we keep the underlying turbulent flow or Re the same and vary $\mathrm{Re_M}$. So, then we look at simulations with $\mathrm{Pr_M} \geq 1$.

2.3 Kinematic dynamos

In kinematic fluctuation dynamos, for a given velocity $\mathbf{u}(\mathbf{x},t)$, the evolution of the magnetic field $\mathbf{b}(\mathbf{x},t)$ is governed by the induction equation alone,

$$\frac{\partial \mathbf{b}}{\partial t} = \nabla \times (\mathbf{u} \times \mathbf{b}) + \eta \nabla^2 \mathbf{b}, \tag{2.1}$$

where η is the magnetic diffusivity (considered constant here). For various velocity fields, we solve Eq. (2.1) in a periodic box of dimensionless size $(2\pi)^3$ with 128^3, 256^3 and 512^3 points, using sixth-order finite differences in space and a third-order Runge-Kutta scheme in time. To ensure that $\nabla \cdot \mathbf{b} = 0$, we numerically solve for the magnetic vector potential. We define the magnetic Reynolds number $\mathrm{Re_M} = 2\pi\, u_{\mathrm{rms}}/k_{\mathrm{F}}\eta$, where k_{F} is the forcing scale of the turbulent velocity flow and u_{rms} is the root-mean-square (rms) velocity. Dynamo action occurs, i.e., the magnetic field grows exponentially, if $\mathrm{Re_M}$ exceeds a critical magnetic Reynolds number, $\mathrm{Re_M^{(crit)}}$, whose value depends on the velocity field. We look for solutions of the form $\mathbf{b}(\mathbf{x},t) = \mathbf{b}(\mathbf{x}) \exp(\gamma_{\mathrm{g}} t)$, where $\mathbf{b}(\mathbf{x})$ is the eigenfunction of the induction equation and γ_{g} is the growth rate.

The first flow we consider is the Roberts flow given by

$$\mathbf{u}(\mathbf{x}) = (\cos(k_{\mathrm{F}y} y), \sin(k_{\mathrm{F}x} x), \sin(k_{\mathrm{F}y} y) + \cos(k_{\mathrm{F}x} x)), \tag{2.2}$$

where $k_{\mathrm{F}x}$ and $k_{\mathrm{F}y}$ are the forcing wave numbers in the x and y directions respectively. Here, for simplicity, we consider $k_{\mathrm{F}x} = k_{\mathrm{F}y} = k_{\mathrm{F}}$. The flow is independent of the spatial coordinate z but has a z component, which depends on x and y. Thus, the anti-dynamo theorem of Zel'dovich (1957) does not prevent the magnetic field from growing exponentially if $\mathrm{Re_M} > \mathrm{Re_M^{(crit)}}$. With this flow, for $k_{\mathrm{F}} = 1$, $\mathrm{Re_M^{(crit)}} \approx 50$. Time evolution of magnetic fields for various values of $\mathrm{Re_M}$ and k_{F} is shown in Fig. 2.3. It shows that the magnetic field grows exponentially for various values of $\mathrm{Re_M}$ and k_{F}. The velocity and magnetic field for $k_{\mathrm{F}} = 1$ and $\mathrm{Re_M} = 1250$ is shown in Fig. 2.4. The magnetic field is concentrated along the separatrix of the flow (the boundary across which u_z changes sign in Fig. 2.4a). Thus, in three dimensions as shown in Fig. 2.5, the magnetic structures are of a similar shape and are equidistant. At high $\mathrm{Re_M}$, the magnetic field is localized to such regions, which enhances diffusion. This can also be seen in Fig. 2.6 where $k_{\mathrm{F}} = 5$ and so 5 cells are formed along each direction. This eventually leads to decay of the magnetic field at very high $\mathrm{Re_M}$ and thus a dynamo with the Roberts flow is a slow dynamo.

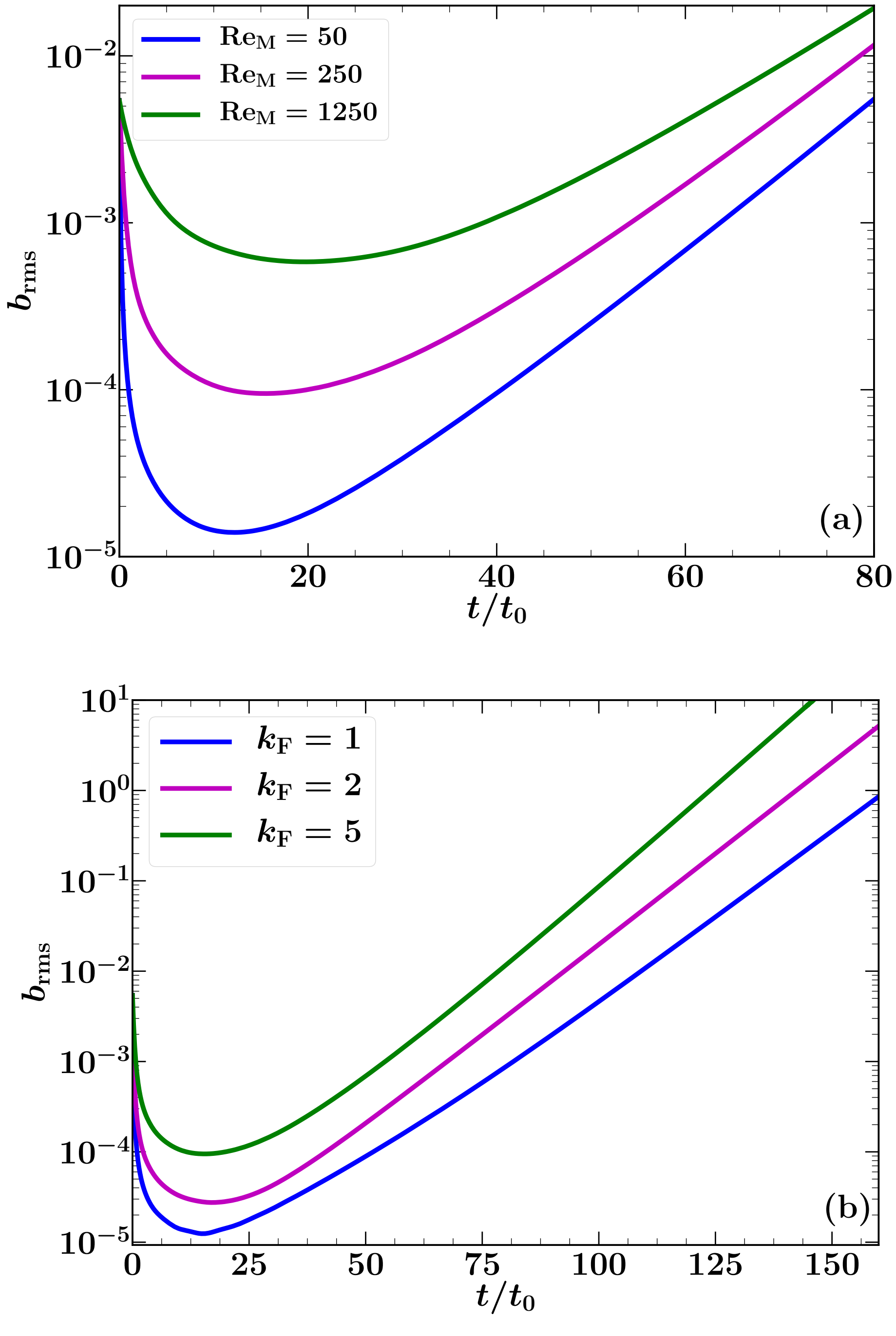

Figure 2.3: The evolution of the magnetic field obtained in the Roberts flows in a periodic box of non-dimensional size $(2\pi)^3$ with 128^3 mesh points for various $\mathrm{Re_M}$ with $k_{\rm F} = 5$ (a) and for various forcing wave numbers $k_{\rm F}$ with $\mathrm{Re_M} = 1250$ (b). $t_0 = 1/\,u_{\rm rms}k_{\rm F}$ is the eddy turnover time.

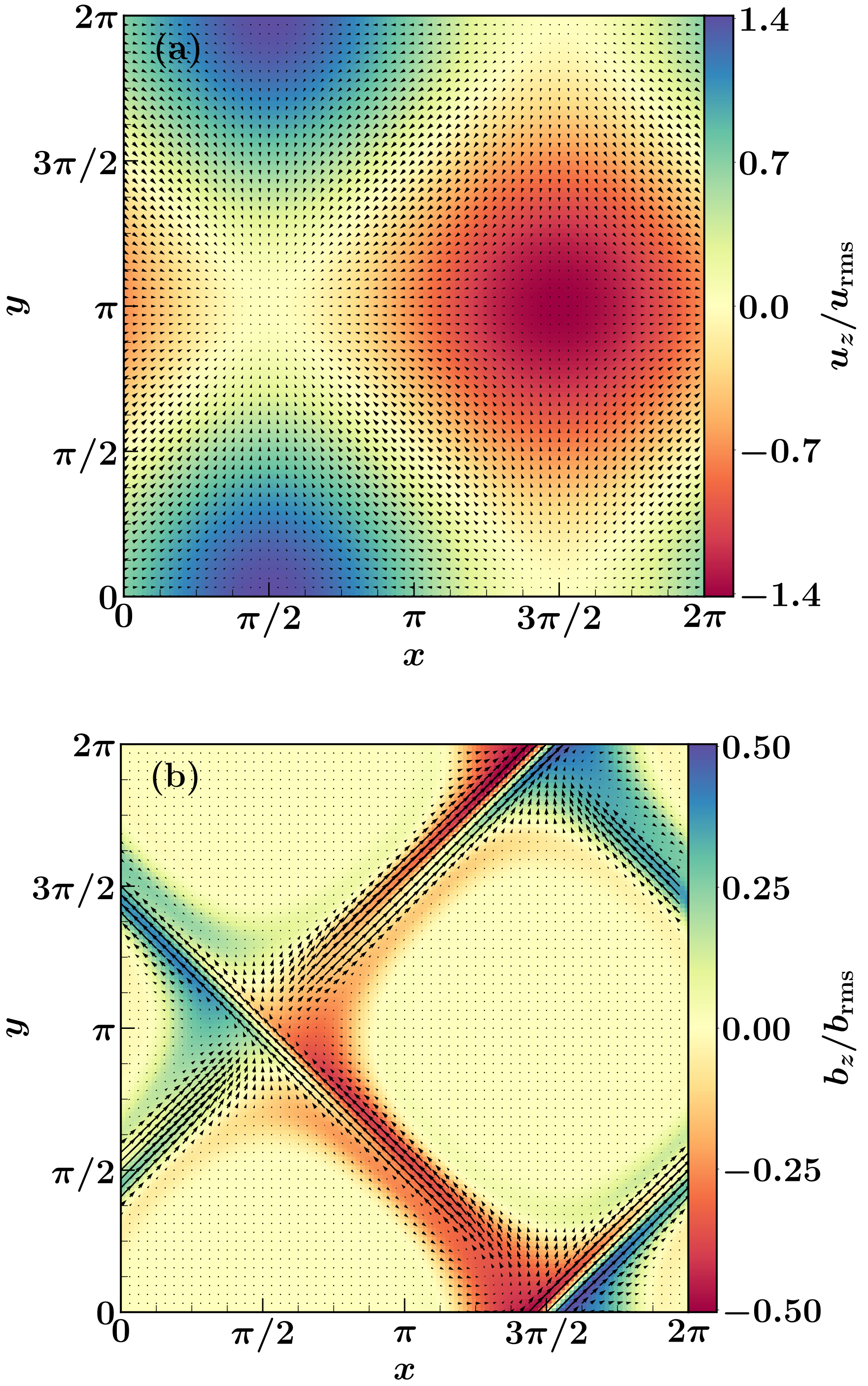

Figure 2.4: (a) The 2D cut in the xy-plane of the velocity field through the middle of the domain with vectors $(u_x/\,u_{\rm rms}, u_y/\,u_{\rm rms})$ and colours showing the magnitude of $u_z/\,u_{\rm rms}$ for the Roberts flow with $k_{\rm F} = 1$ and $\mathrm{Re_M} = 1250$ in a 128^3 simulation. (b) As (a) but for the exponentially growing magnetic field.

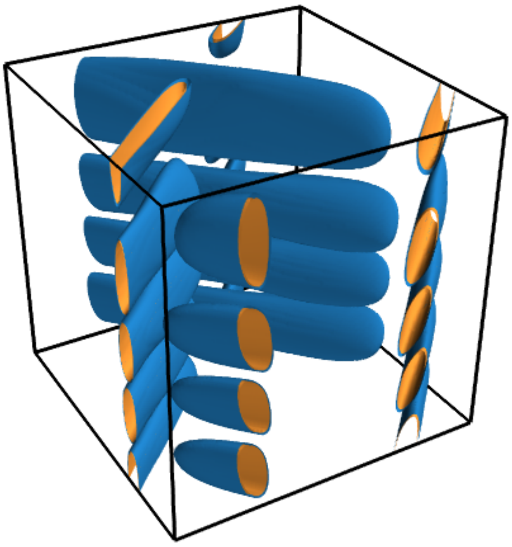

Figure 2.5: Isosurfaces of $b^2/b_{\mathrm{rms}}^2 = 2$ (blue) and $b^2/b_{\mathrm{rms}}^2 = 3$ (yellow) for the magnetic field generated by using the Roberts flow with $k_{\mathrm{F}} = 1$ and $\mathrm{Re}_{\mathrm{M}} = 1250$ in a 128^3 simulation.

The Roberts flow is a special case of a general class of flows called the ABC flows given by

$$\begin{aligned}\mathbf{u}(\mathbf{x}) =& (A\sin(k_{\mathrm{F}z}z) + C\cos(k_{\mathrm{F}y}y),\\ & B\sin(k_{\mathrm{F}x}x) + A\cos(k_{\mathrm{F}z}z),\\ & C\sin(k_{\mathrm{F}y}y) + B\cos(k_{\mathrm{F}x}x)),\end{aligned} \tag{2.3}$$

where $k_{\mathrm{F}x}, k_{\mathrm{F}y}, k_{\mathrm{F}z}$ are the forcing wave numbers in the three coordinate directions and A, B and C are constants. For this flow, when $k_{\mathrm{F}x} = k_{\mathrm{F}y} = k_{\mathrm{F}z} = 1$ and $A = B = C = 1$, $\mathrm{Re}_{\mathrm{M}}^{(\mathrm{crit})} \approx 94$. The velocity and magnetic field for $k_{\mathrm{F}x} = k_{\mathrm{F}y} = k_{\mathrm{F}z} = 1$, $A = B = C = 1$ and $\mathrm{Re}_{\mathrm{M}} = 1250$ is shown in Fig. 2.7. Here, the magnetic field is stronger around the separatrix but is also non-zero in other regions. As shown in Fig. 2.8, the magnetic structures are of ellipsoidal shape but placed randomly within the domain. The ABC flow is supposed to be a fast dynamo but it is difficult to demonstrate this conclusively (Bouya & Dormy, 2015).

The velocity flows can also be time dependent. One such flow is the Galloway–Proctor

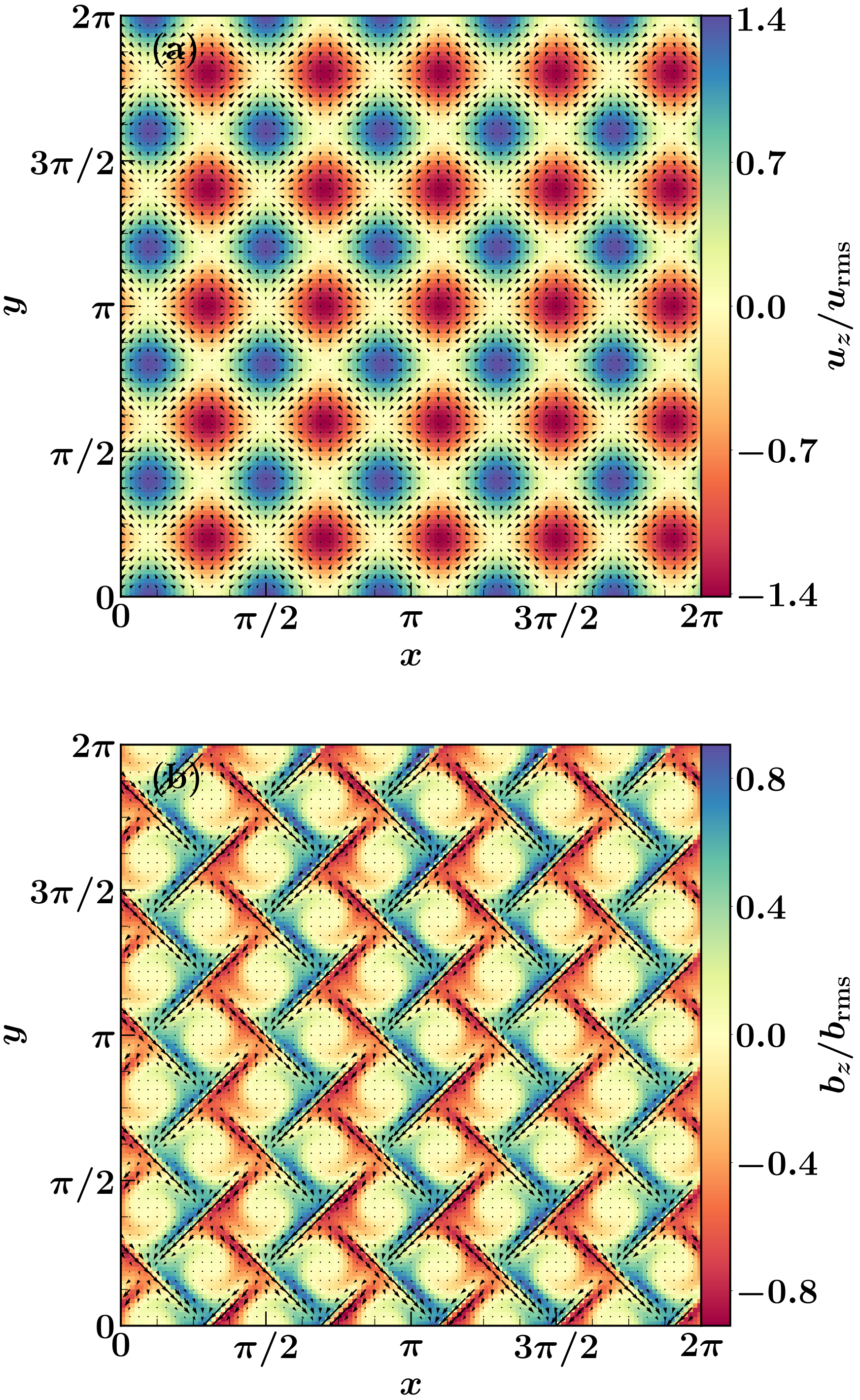

Figure 2.6: As in Fig. 2.4 but for $k_{\rm F} = 5$.

flow (Galloway & Proctor, 1992) and one of its forms is given by

$$\begin{aligned}\mathbf{u}(\mathbf{x},t) =& (A\sin(k_{\mathrm{F}z}z+\sin\omega t)+C\cos(k_{\mathrm{F}y}y+\cos\omega t),\\ & A\cos(k_{\mathrm{F}z}z+\sin\omega t),\\ & C\sin(k_{\mathrm{F}y}y+\cos\omega t)),\end{aligned} \tag{2.4}$$

where $k_{\mathrm{F}y}, k_{\mathrm{F}z}$ are wave numbers in the y and z directions, A and C are constants, and ω is the frequency of the changing flow. This flow is known to be a fast dynamo. For $k_{\mathrm{F}y} = k_{\mathrm{F}z} = 1$, $\omega = 1$ and $A = C = \sqrt{3/2}$, the velocity field and growing solution of the magnetic field are shown in Fig. 2.9. The three–dimensional magnetic structures are shown in Fig. 2.10, which are again of fixed shapes and are located at an equal distance from one another.

Another very efficient dynamo is due to the following flow (Willis, 2012):

$$\mathbf{u}(\mathbf{x}) = (2/\sqrt{3})(\sin y\cos z, \sin z\cos x, \sin x\cos y). \tag{2.5}$$

called the W flow here and it has $\mathrm{Re}_{\mathrm{M}}^{(\mathrm{crit})} \approx 11$. In the case of the periodic box, the W flow is closest to the most optimal time-independent flow for dynamo action (Willis, 2012). The dynamo-generated magnetic field in a periodic box with 256^3 points obtained for the W flow is shown in Fig. 2.11.

These Lagrangian chaotic flows are useful to understand basics aspects of the fluctuation dynamo (such as when does the magnetic field grow and how the flow circumvents anti-dynamo theorems). Moreover, the properties of the velocity field can easily be related to the features in the magnetic field that it generates. The magnetic structures generated by such flows are usually of a simple shape, often with regular spacing between them (Fig. 2.5, Fig. 2.8 and Fig. 2.10), e.g., convection-like cells for the Roberts flow and ellipsoids for the ABC and W flows. However, these are single-scale flows and lack many properties of the turbulent flows (such as multiple scales and an energy cascade). Also, most of the above flows are not mirror-symmetric and produce a large-scale magnetic field. The magnetic field correlation scale is comparable to the driving scale (roughly equal to the size of the box for cases with $k_{\mathrm{F}} = 1$) as can be seen from two dimensional vector plots of the dynamo-generated magnetic fields.

Finally, we consider a multi-scale flow to generate small-scale random magnetic fields, referred to here as the KS (Kolmogorov scaling) flow. The velocity field, $\mathbf{u}$, is constructed by superposing Fourier modes with a range of wavenumbers, k, and a chosen energy spectrum

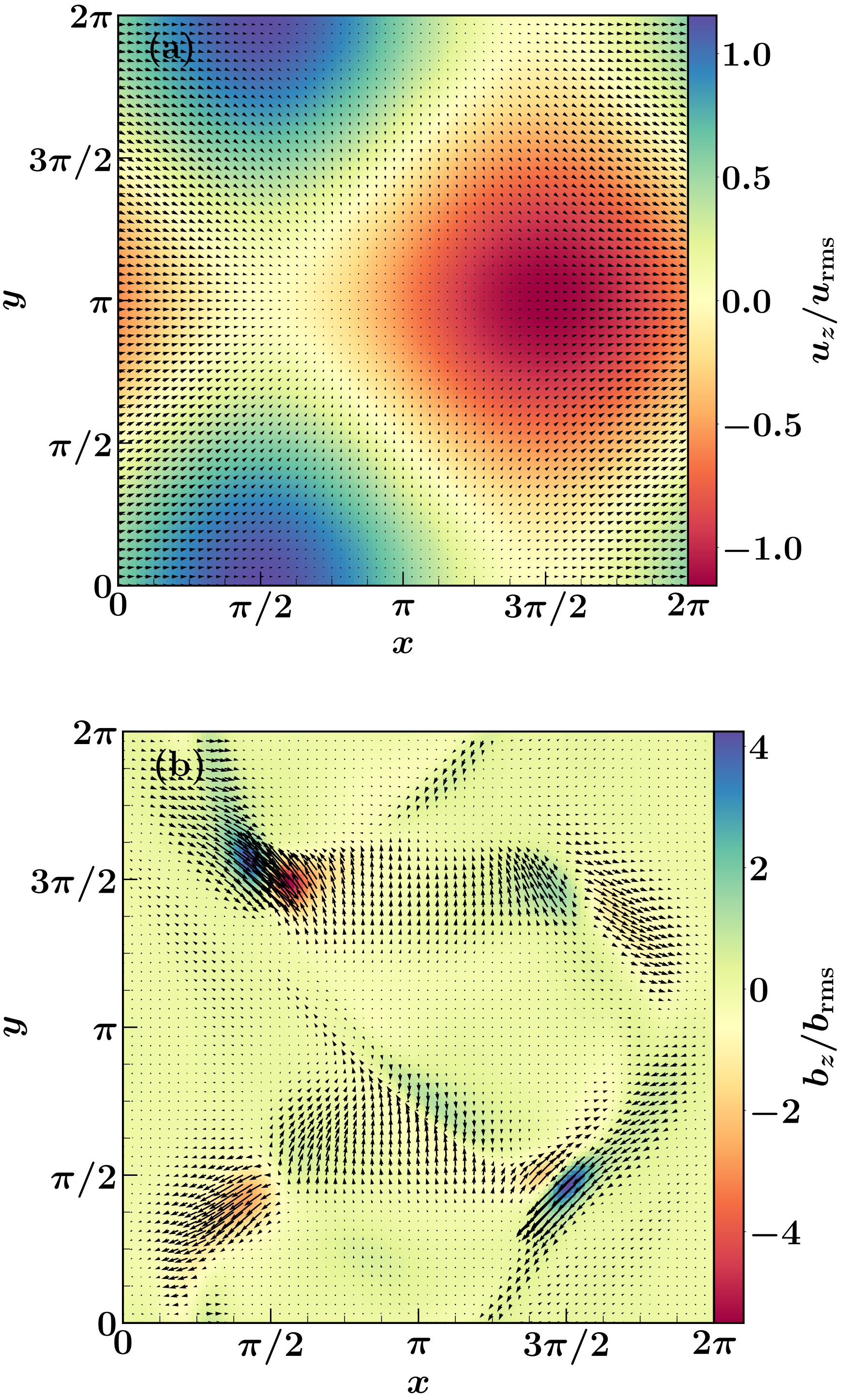

Figure 2.7: As in Fig. 2.4 but for the ABC flow with $A = B = C = 1$, $k_{\mathrm{F}x} = k_{\mathrm{F}y} = k_{\mathrm{F}z} = 1$ and $\mathrm{Re}_{\mathrm{M}} = 1250$.

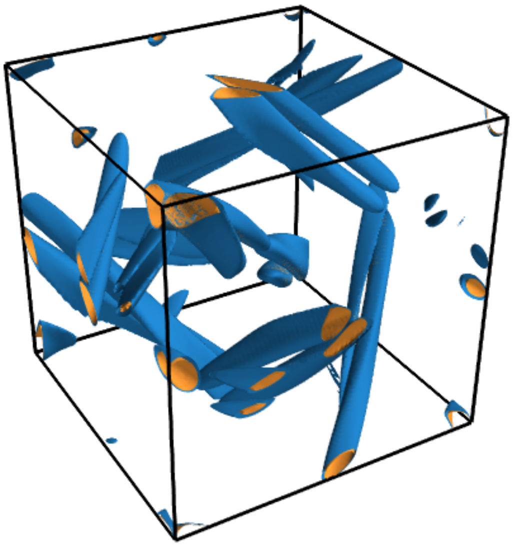

Figure 2.8: Isosurfaces of $b^2/b^2_{\rm rms} = 3$ (blue) and $b^2/b^2_{\rm rms} = 4$ (yellow) for the magnetic field generated by the ABC flow with $A = B = C = 1$, $k_{{\rm F}x} = k_{{\rm F}y} = k_{{\rm F}z} = 1$ and $\mathrm{Re}_{\rm M} = 1250$ in a 128^3 simulation. The magnetic structures are of various sizes and are randomly oriented.

E_k (Fung et al., 1992; Wilkin et al., 2007)

$$\mathbf{u}(\mathbf{x}, t) = \sum_{n=0}^{N-1} \left[\mathbf{C}_n(\mathbf{k}_n)\cos\phi_n + \mathbf{D}_n(\mathbf{k}_n)\sin\phi_n\right], \tag{2.6}$$

where $\phi_n = \mathbf{k}_n \cdot \mathbf{x} + \omega_n t$, $\mathbf{k}_n$ is a randomly oriented wavevector of magnitude k_n, and $\omega_n = [k_n^3 E_k]^{1/2}$ is the frequency at that scale. The vectors $\mathbf{C}_n(\mathbf{k}_n)$ and $\mathbf{D}_n(\mathbf{k}_n)$ have random directions in the plane perpendicular to $\mathbf{k}_n$, so that the flow is incompressible ($\nabla \cdot \mathbf{u} = 0$). Their magnitudes determine the power spectrum E_k, and are chosen such that $E_k \propto k^{-5/3}$. We chose $N = 40$ with $2\pi/L \leq \mathbf{k}_n \leq 8\pi/L$ such that the flow is periodic, where $L = 2\pi$ is the width of our periodic box which is also equal to the outer (or largest) scale of the velocity flow. For this flow, we use 512^3 points and obtain $\mathrm{Re}_{\rm M}^{(\rm crit)} \approx 750$. The magnetic field generated by the KS flow in shown in Fig. 2.12. It is spatially intermittent. The magnetic structures shown in Fig. 2.13 are randomly oriented and are of various shapes and sizes. The probability distribution function (PDF) of a single component of magnetic field is shown in Fig. 2.14. The distribution is far from a Gaussian distribution with heavy tails. The shell-averaged power spectrum of magnetic field for various $\mathrm{Re}_{\rm M}$ is shown in Fig. 2.15. Independent of $\mathrm{Re}_{\rm M}$, the spectra at small wave numbers roughly follows the Kazantsev spectrum, $M_k \propto k^{3/2}$.

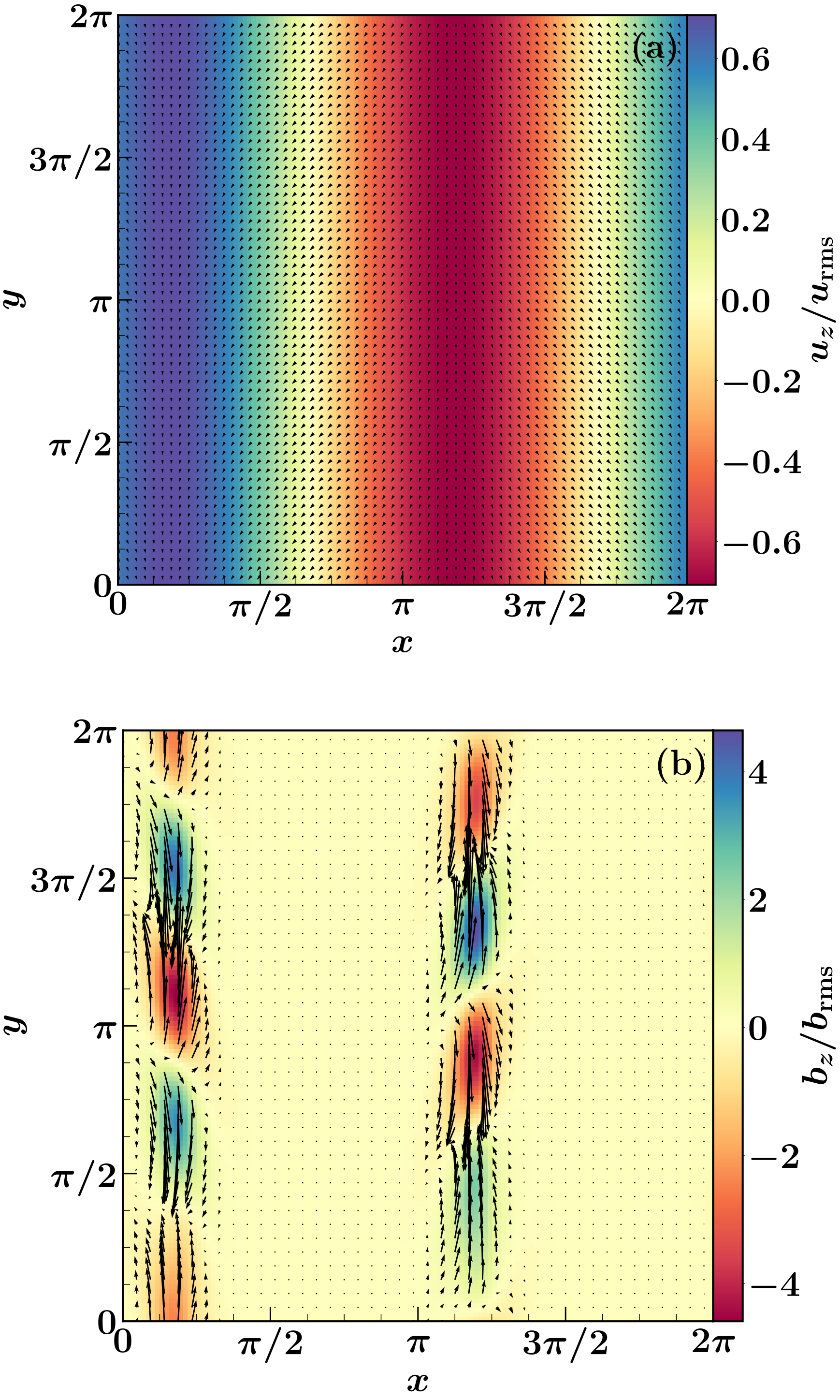

Figure 2.9: As in Fig. 2.4 but for the Galloway–Proctor flow with $k_{{\rm F}y} = k_{{\rm F}z} = 1$, $\omega = 1$, $A = C = \sqrt{3/2}$ and $\mathrm{Re_M} = 1250$.

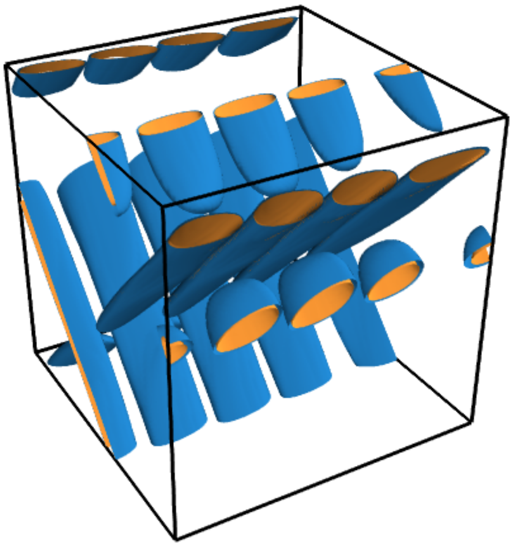

Figure 2.10: Isosurfaces of $b^2/b_{\mathrm{rms}}^2 = 3$ (blue) and $b^2/b_{\mathrm{rms}}^2 = 4$ (yellow) for the magnetic field generated by using the Galloway–Proctor flow with $k_{\mathrm{F}y} = k_{\mathrm{F}z} = 1$, $\omega = 1$, $A = C = \sqrt{3/2}$ and $\mathrm{Re_M} = 1250$ in a 128^3 simulation. The magnetic structures are of a fixed shape and are equidistant.

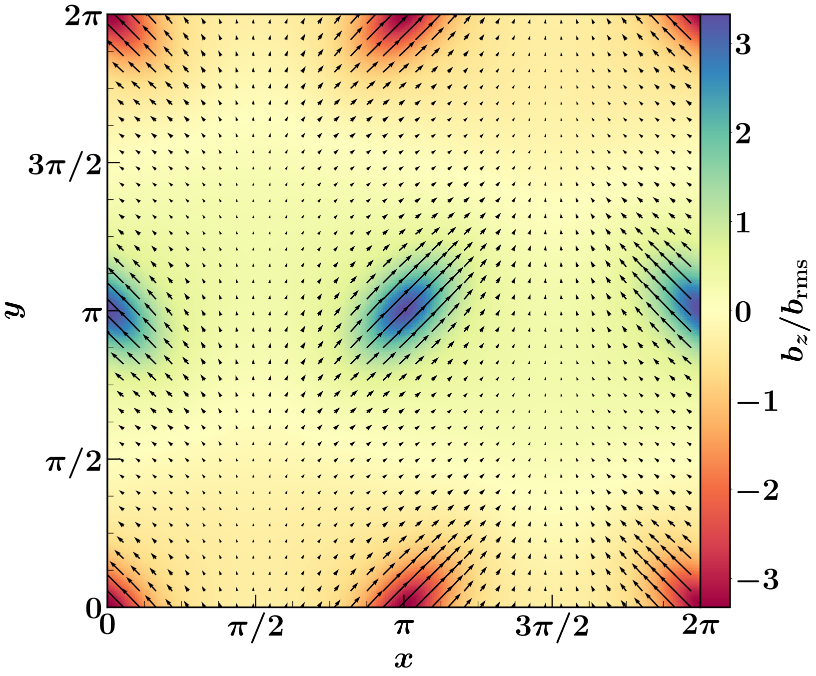

Figure 2.11: A 2D cut in the xy-plane through the middle of the domain with vectors $(b_x/b_{\mathrm{rms}}, b_y/b_{\mathrm{rms}})$ and colours showing the magnitude of b_z/b_{rms} for the W flow with $\mathrm{Re_M} = 314$ in a periodic box of non-dimensional size $(2\pi)^3$ with 256^3 points.

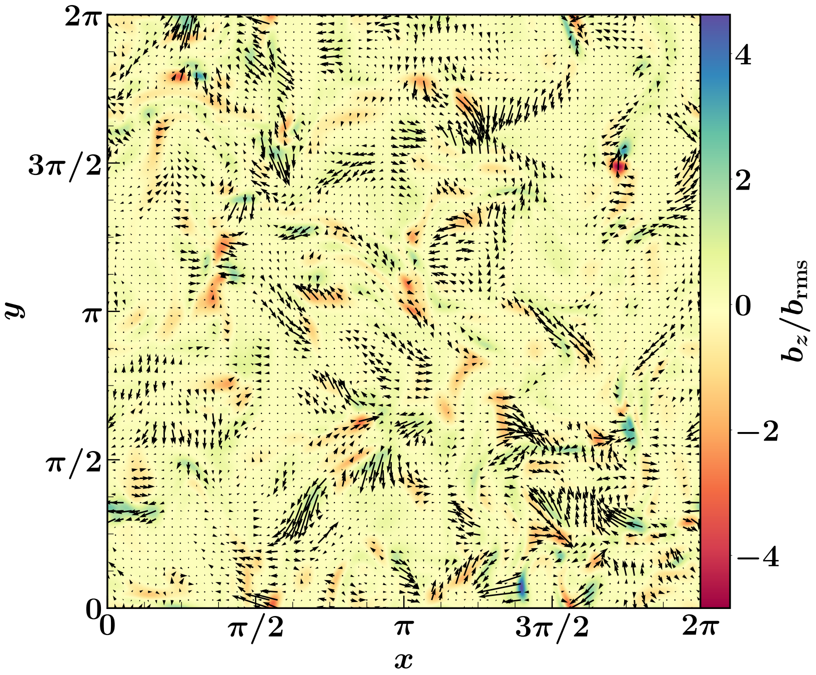

Figure 2.12: A 2D cut in the xy-plane through the middle of the domain with vectors $(b_x/\,b_{\rm rms}, b_y/\,b_{\rm rms})$ and colours showing the magnitude of $b_z/\,b_{\rm rms}$ for the KS flow with $\mathrm{Re_M} = 4800$ in a periodic box of a non-dimensional size 2π with 512^3 mesh points

For cosmic ray propagation in Chapter 3 and Chapter 4, we use magnetic fields generated by the W and KS flows.

2.4 Non-linear fluctuation dynamo

2.4.1 Basic equations and numerical modelling

To study magnetic fields in random flows which are driven by a prescribed forcing, we solve the continuity (Eq. (2.7)), induction (Eq. (2.8)) and Navier-Stokes (Eq. (2.9)) equations using the Pencil Code [1](see Chapter A for the solution of Sod shock tube problem) in a periodic box of non-dimensional size $(2\pi)^3$ with 256^3 and 512^3 points. The equations are solved with sixth-order finite differences in space and a third-order Runge-Kutta in time (for a discussion on this numerical scheme see Brandenburg, 2003). We consider the turbulent medium to be isothermal with equation of state $p = c_s^2\rho$, where p is the pressure, c_s is the sound speed and ρ is the density.

---

[1] http://pencil-code.nordita.org/

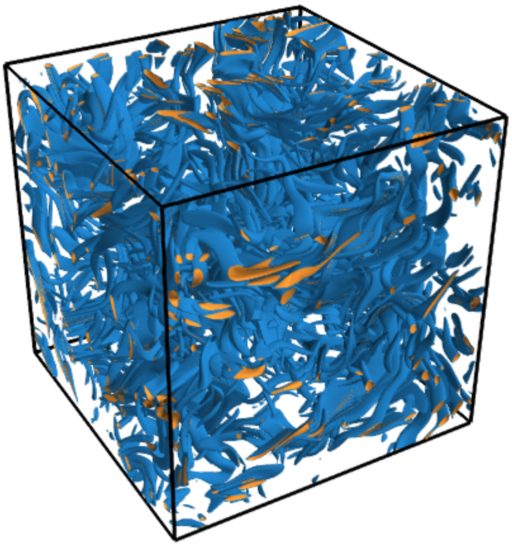

Figure 2.13: Isosurfaces of $b^2/b_{\rm rms}^2 = 3$ (blue) and $b^2/b_{\rm rms}^2 = 4$ (yellow) for the magnetic field generated by the KS flow with $\mathrm{Re_M} = 4800$ in a periodic box of a non-dimensional size $(2\pi)^3$ with 512^3 mesh points. The magnetic filaments are of various shapes and sizes.

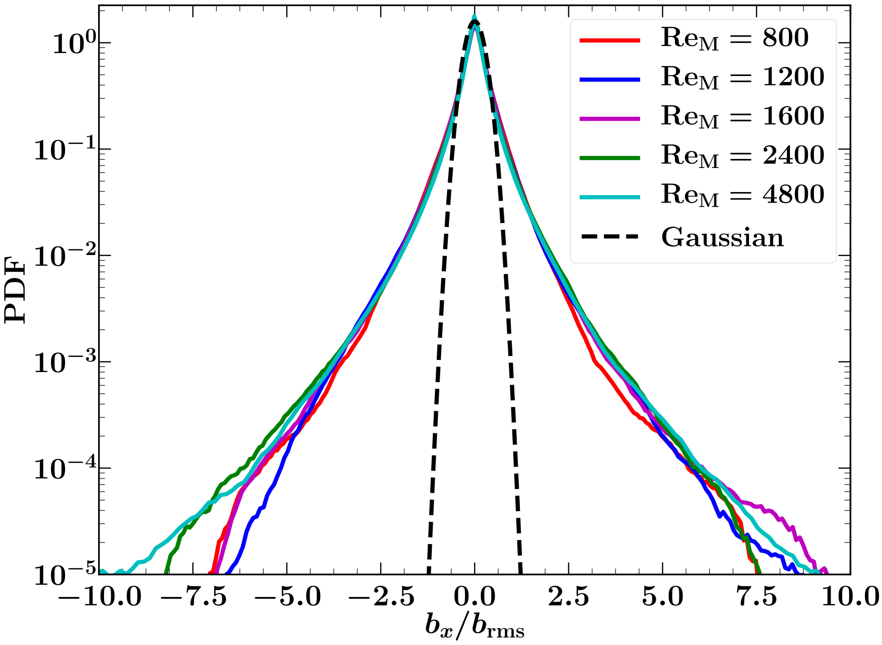

Figure 2.14: The probability density function of the single magnetic field component $b_x/b_{\rm rms}$ generated by the KS flow for various values of magnetic Reynolds number $\mathrm{Re_M}$ as specified in the legend. The dashed curve shows a Gaussian distribution. The distribution is strongly non-Gaussian with long tails.

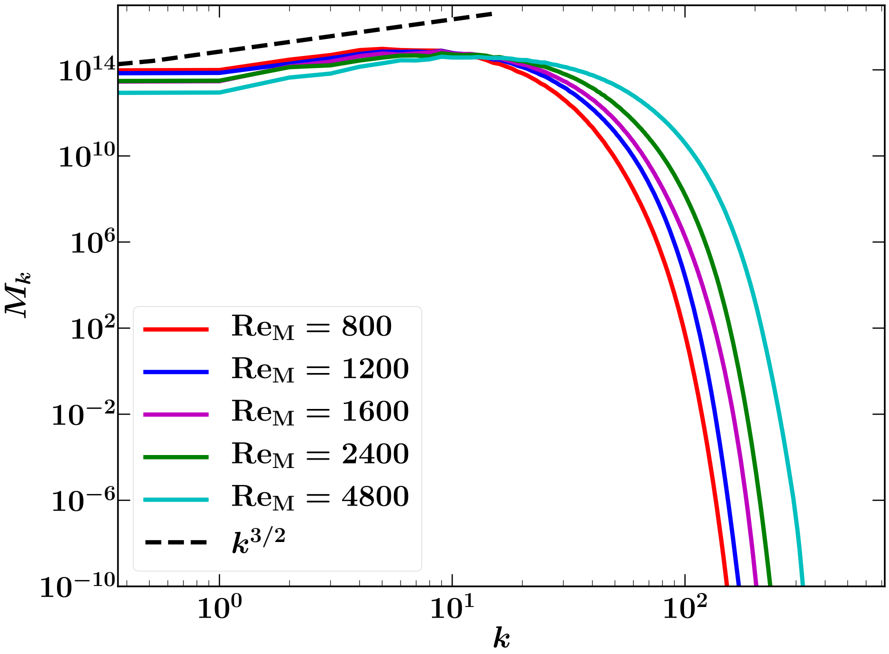

Figure 2.15: The magnetic field spectra M_k for various magnetic Reynolds numbers $\mathrm{Re_M}$ (specified in the legend) in the KS flow. The spectrum at smaller wave numbers follows the Kazantsev spectrum, $M_k \propto k^{3/2}$ (dashed) and the resistive scale increases with $\mathrm{Re_M}$.

The governing equations are as follows,

$$\frac{\partial \rho}{\partial t} + \nabla \cdot (\rho \mathbf{u}) = 0, \tag{2.7}$$

$$\frac{\partial \mathbf{b}}{\partial t} = \nabla \times (\mathbf{u} \times \mathbf{b}) + \eta \nabla^2 \mathbf{b}, \tag{2.8}$$

$$\frac{\partial \mathbf{u}}{\partial t} + \mathbf{u} \cdot \nabla \mathbf{u} = \frac{-\nabla p}{\rho} + \frac{\mathbf{j} \times \mathbf{b}}{c\rho} + \nu \left(\nabla^2 \mathbf{u} + \frac{1}{3} \nabla \nabla \cdot \mathbf{u} + 2\mathbf{S} \cdot \nabla \ln \rho \right) + \mathbf{F}, \tag{2.9}$$

where $\mathbf{u}$ is the velocity field, $\mathbf{b}$ is the magnetic field, η is the magnetic diffusivity, $\mathbf{j}$ is the electric current density, ν is the viscosity, $S_{ij} = \frac{1}{2}\left(u_{i;j} + u_{j;i} - \frac{2}{3}\delta_{ij} \nabla \cdot \mathbf{u}\right)$ is the rate of strain tensor and $\mathbf{F}$ is the forcing function. For simplicity, both η and ν are considered constants. Eq. (2.8) is solved in terms of the vector potential to ensure that the magnetic field obtained is always divergence free.

We drive the flow with a mirror-symmetric, nearly incompressible (flows with Mach numbers less than 0.1) and δ-correlated in time forcing (Haugen et al., 2004a) of the form

$$\mathbf{F}(\mathbf{x}, t) = \mathrm{Re}\{N \mathbf{F}_{\mathbf{k}(t)} \exp[\mathrm{i}\mathbf{k}(t) \cdot \mathbf{x} + \mathrm{i}\phi(t)]\}, \tag{2.10}$$

where $\mathbf{k}$ is the wave vector, $\mathbf{x}$ is the position vector and $\pi < \phi \leq \pi$ is a random phase. To ensure that the forcing is effectively δ-correlated in time, $\mathbf{k}$ and ϕ are changed at each time step δt. Also, to ensure that the time-integrated force is independent of the time step δt, the normalization N is chosen to be proportional to $\delta t^{-1/2}$. By dimensional analysis, $N = F_0 c_s (|\mathbf{k}| c_s / \delta t)^{1/2}$, where F_0 is the non-dimensional amplitude chosen such that the maximum Mach number is low enough ($u_{\mathrm{rms}}/c_s \lesssim 0.1$) to avoid strong shocks. We randomly select many wave vectors $\mathbf{k}$ which are multiples of $2\pi/L$ (to make sure the flow is periodic) of magnitude k in a chosen range. Then we select an arbitrary unit vector $\mathbf{e}$ (neither parallel nor anti-parallel to $\mathbf{k}$) [2] and force the system at each time step with

$$\mathbf{F_k} = \frac{\mathbf{k} \times \mathbf{e}}{\sqrt{\mathbf{k}^2 - (\mathbf{k} \cdot \mathbf{e})^2}}. \tag{2.11}$$

The average of wave numbers at which the flow is driven is denoted by k_{F}. Even when the flow is periodic, k_{F} need not be an integer.

The turbulent flow is characterized by the hydrodynamic Reynolds number Re and magnetic Reynolds number $\mathrm{Re_M}$. They are defined using the rms velocity u_{rms} with respect to the forcing scale based on the average wave number [3] k_{F} as

$$\mathrm{Re} = \frac{u_{\mathrm{rms}}}{\nu} \frac{2\pi}{k_{\mathrm{F}}}, \quad \mathrm{Re_M} = \frac{u_{\mathrm{rms}}}{\eta} \frac{2\pi}{k_{\mathrm{F}}}, \tag{2.12}$$

respectively. The ratio of $\mathrm{Re_M}$ to Re is the magnetic Prandtl number

$$\mathrm{Pr_M} = \frac{\mathrm{Re_M}}{\mathrm{Re}} = \frac{\nu}{\eta}. \tag{2.13}$$

We use non-dimensional units for all physical variables. The lengths are in units of the domain size, speed in units of the initial isothermal sound speed $c_{s,0}$, time in terms of the eddy turnover time $t_0 = 1/\, u_{\mathrm{rms}} k_{\mathrm{F}}$, density in units of the initial density ρ_0 and the magnetic field in units of $\left(4\pi\rho_0 c_{s,0}^2\right)^{1/2}$.

For the first set of simulations, with parameters given in Table 2.1, the turbulent motions are driven between the wave numbers $k = 1$ and $k = 2$ and thus $k_{\mathrm{F}} \approx 1.5$. A constant density, zero velocity and a very weak random magnetic field with zero net flux are initialized in the

---

[2] We find the basis vectors ($\mathbf{e}_1$ and $\mathbf{e}_2$) in the plane perpendicular to the vector $\mathbf{k}$ and chose an angle ϕ_{r} randomly in the range $0 \leq \phi_{\mathrm{r}} < 2\pi$. Then arbitrary unit vector $\mathbf{e}$ is computed as $\cos\phi_{\mathrm{r}}\, \mathbf{e}_1 + \sin\phi_{\mathrm{r}}\, \mathbf{e}_2$. This is done to ensure that the resulting forcing vector is isotropic.

[3] It is also common to define the hydrodynamic and magnetic Reynolds number with respect to the forcing wave number instead of the driving length scale. Then the Reynolds numbers are smaller by a factor 2π than the values we quote.

Table 2.1: Parameters of various nonlinear fluctuation dynamo simulations in a numerical domain of size $(2\pi)^3$ with 256^3 mesh points. In all cases, the forcing scale k_F is approximately equal to 1.5 (flow driven at $k = 1$ and $k = 2$), the forcing amplitude $F_0 = 0.02$, the magnetic Prandtl number $\mathrm{Pr_M} = 1$ and the rms velocity in the saturated state is $u_\mathrm{rms} \approx 0.11$. The Reynolds number, the magnetic Reynolds number, both based on the forcing scale $2\pi/k_\mathrm{F}$, the rms magnetic field in the saturated state b_rms, the ratio of magnetic to kinetic energy in the saturated state $\varepsilon_\mathrm{M}/\varepsilon_\mathrm{K} = b_\mathrm{rms}^2/\, u_\mathrm{rms}^2$, the correlation length of the velocity field in the kinematic stage $l_{u\mathrm{kin}}$, the correlation length of the magnetic field in the kinematic stage $l_{b\mathrm{kin}}$, the correlation length of the velocity field in the saturated stage $l_{u\mathrm{sat}}$ and the correlation length of the magnetic field in the saturated stage $l_{b\mathrm{sat}}$ are also given.

η, ν	$\mathrm{Re_M}, \mathrm{Re}$	b_rms	$\varepsilon_\mathrm{M}/\varepsilon_\mathrm{K}$	$l_{u\mathrm{kin}}$	$l_{b\mathrm{kin}}$	$l_{u\mathrm{sat}}$	$l_{b\mathrm{sat}}$
10×10^{-4}	449	0.033	0.08	3.14	1.82	3.77	1.95
5×10^{-4}	898	0.042	0.14	3.20	1.26	3.45	1.76
4×10^{-4}	1122	0.048	0.20	3.01	0.94	3.64	1.76
3×10^{-4}	1496	0.049	0.21	3.01	0.88	3.39	1.57
2.5×10^{-4}	1796	0.054	0.25	2.95	0.75	3.58	1.57
2×10^{-4}	2244	0.055	0.26	2.95	0.69	3.33	1.56

domain. Since the flow is nearly incompressible, density does not vary much throughout the simulation. The magnetic field grows only for $\mathrm{Re_M} \geq \mathrm{Re_M^{(crit)}}$, the critical magnetic Reynolds number. For $\mathrm{Pr_M} = 1$, $\mathrm{Re_M^{(crit)}} \sim 220$ (Haugen et al., 2004a).

The evolution of the rms velocity u_rms and magnetic b_rms fields is shown in Fig. 2.16 for $\mathrm{Re_M} = 1122$. The flow speed is controlled by the forcing function and thus remains nearly constant throughout the whole time. Most of the fluctuations in u_rms are due to the system adapting to the imposed driving. The magnetic field, decays until it becomes an eigenstate of the induction equation. Then it grows exponentially defining the kinematic stage. As it becomes stronger, the magnetic field starts to influence the flow and slows down the exponential increase. Finally, when the magnetic field becomes strong enough, it stops growing and reaches a statistically steady state in the saturated stage. The exponential growth and then saturation of the magnetic fields occurs in all runs of Table 2.1.

The shell-averaged (one-dimensional) power spectrum for various stages of magnetic field evolution is shown in Fig. 2.17. At all times, the kinetic energy spectrum roughly follows the Kolmogorov spectrum, $E_k \propto k^{-5/3}$, confirming that the velocity flow is turbulent. The shell-averaged magnetic field spectrum in the kinematic stage has a maximum at larger wave numbers and the slope of the spectrum agrees with that derived analytically by Kazantsev (1968), $M_k \propto k^{3/2}$. Kazantsev's theory assumes that the turbulent flow is δ-correlated in time, which is the case in our simulations. However, the slope of the spectrum in the kinematic stage remains the same even when the forcing has a finite but small correlation time (Bhat & Subramanian, 2014). As the magnetic field grows, the power shifts to smaller wave

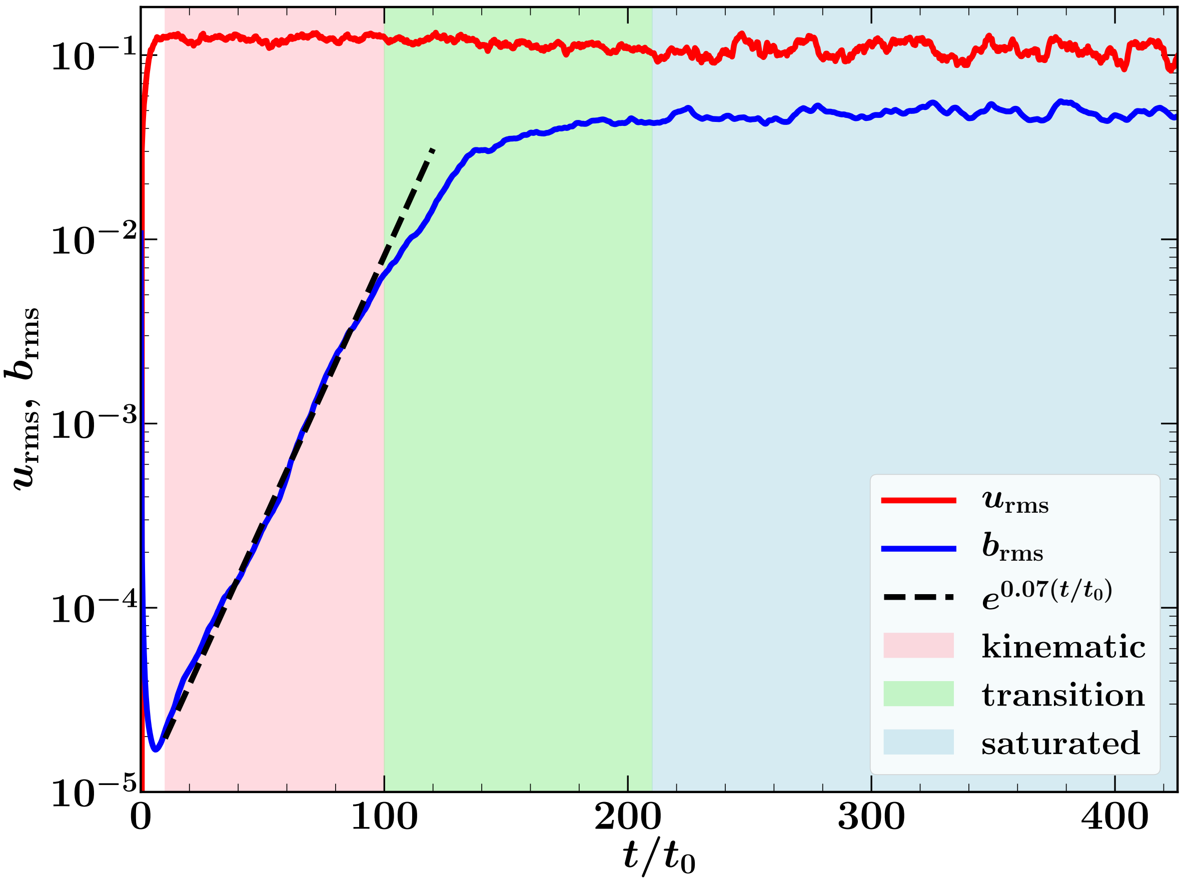

Figure 2.16: Root mean square (rms) of the velocity field $u_{\rm rms}$ and magnetic field $b_{\rm rms}$ as functions of normalized time t/t_0 (where $t_0 = 1/u_{\rm rms}k_{\rm F}$, the eddy turnover time) for $\mathrm{Re}_{\rm M} = 1122$. The randomly initialized magnetic field first decreases till it evolves into an eigenfunction of the induction equation and then increases exponentially with time (black-dashed) during the kinematic stage (area shaded in light red). As magnetic field grows, its feedback on the flow slows down the exponential increase (the transition stage, area shaded in light green). Finally, the magnetic field reaches a statistically steady state in the saturated stage (area shaded in light blue).

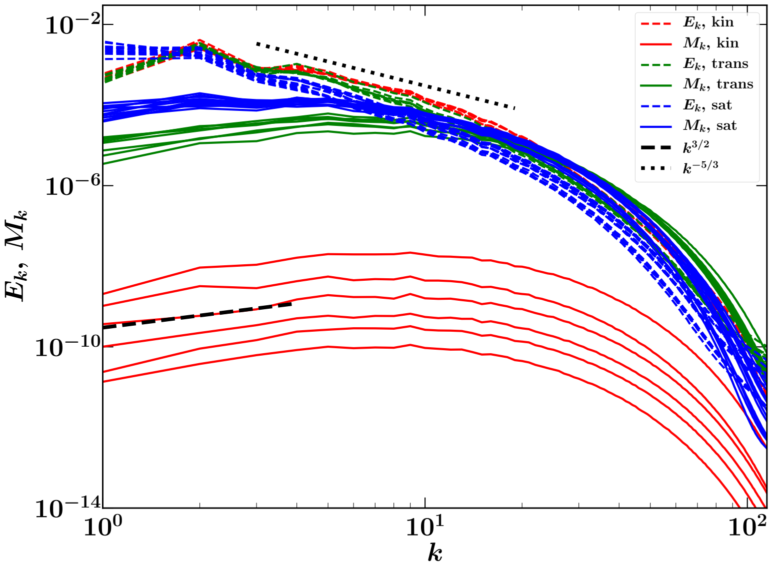

Figure 2.17: The shell-averaged (one-dimensional) kinetic E_k (dashed) and magnetic M_k (solid) energy spectra in the kinematic (red), transition (green) and saturated (blue) stages for $\mathrm{Re}_{\mathrm{M}} = 1122$. The kinetic energy spectrum roughly follows the Kolmogorov spectrum, $E_k \propto k^{-5/3}$ (dotted, black). The magnetic spectra are initially peaked at large wave numbers with $M_k \propto k^{3/2}$ (dashed, black) at smaller wave numbers (Kazantsev, 1968). As the magnetic field saturates, the power shifts to smaller wave numbers and the magnetic spectrum flattens.

numbers and the spectrum becomes much flatter. The precise reason for the change in spectra upon saturation is still not known.

2.4.2 Spatially intermittent nature of the dynamo generated magnetic fields

Intermittency in a random distribution can be confirmed by looking at its probability distribution function (PDF) and by comparing the calculated kurtosis (Eq. (2.14)) of the distribution with that of the Gaussian distribution. Also, the correlation length of the field gives further information about the volume filling nature of the field. Here, using these tools we discuss the spatial intermittency of the velocity and magnetic fields in non-linear fluctuation dynamos.

Fig. 2.18 shows the PDF of a single component of the velocity field $u_x/\,u_{\mathrm{rms}}$ in the kinematic and saturated stages for $\mathrm{Re}_{\mathrm{M}} = 1122$ and $\mathrm{Re}_{\mathrm{M}} = 2244$. The PDF is nearly Gaussian for both the kinematic and saturated stages. This is primarily due to the nearly incompressible forcing in the Navier–Stokes equation. This can be further confirmed by calculating the

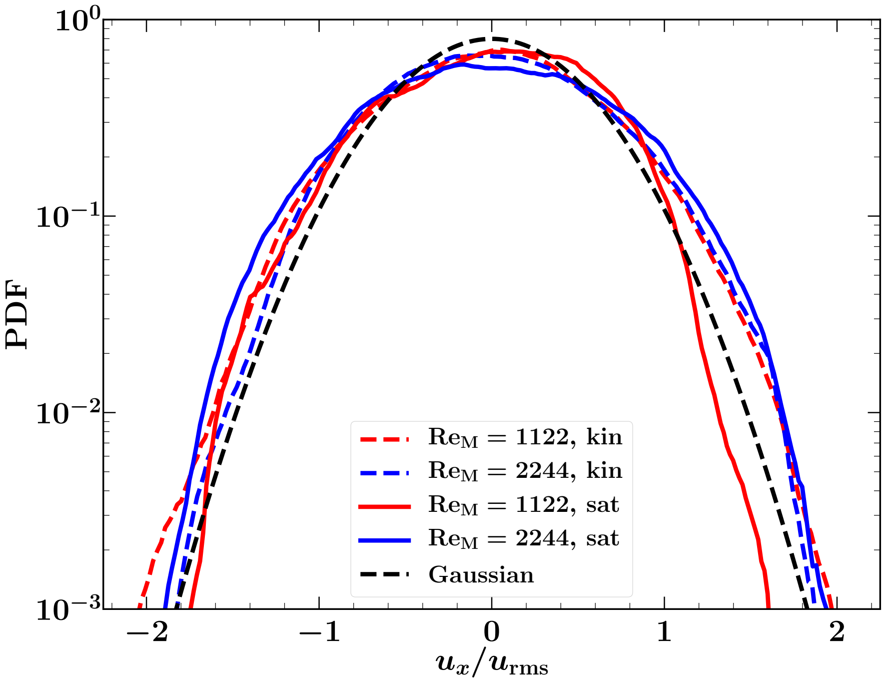

Figure 2.18: The PDF of the normalized velocity field component $u_x/\,u_{\rm rms}$ for $\mathrm{Re_M} = 1122$ and $\mathrm{Re_M} = 2244$ in the kinematic (dashed) and saturated (solid) stages for the value of $\mathrm{Re_M}$ given in the legend. The velocity field is roughly Gaussian (dashed, black) in both the stages for both $\mathrm{Re_M}$.

kurtosis for the velocity field $\mathbf{u}$

$$\mathrm{Kurt}(\mathbf{u}) = \frac{\langle \mathbf{u}^4 \rangle}{\langle \mathbf{u}^2 \rangle^2}, \tag{2.14}$$

where $\langle \cdots \rangle$ refers to the spatial average over the domain. For all cases of Table 2.1, the kurtosis of the velocity field is very close to $\mathrm{Kurt} = 3$, a Gaussian distribution. The correlation length of the velocity field l_u is calculated from the turbulent energy power spectrum E_k as

$$l_u = \frac{\pi}{2} \frac{\int_0^\infty 2\pi k^{-1} E_k \,\mathrm{d}k}{\int_0^\infty E_k \,\mathrm{d}k}, \tag{2.15}$$

and is given in Table 2.1. We confirm that roughly the same values are obtained by integrating the autocorrelation function of the velocity fields. The correlation length of the velocity field is roughly half of the numerical box size (2π). This can also be seen from Fig. 2.19. It decreases slightly as Re increases. It increases in the saturated stage as compared to the kinematic stage for all $\mathrm{Re_M}$. The velocity field thus becomes more volume filling as the magnetic field saturates. This is directly attributable to the dynamical effects of the magnetic fields.

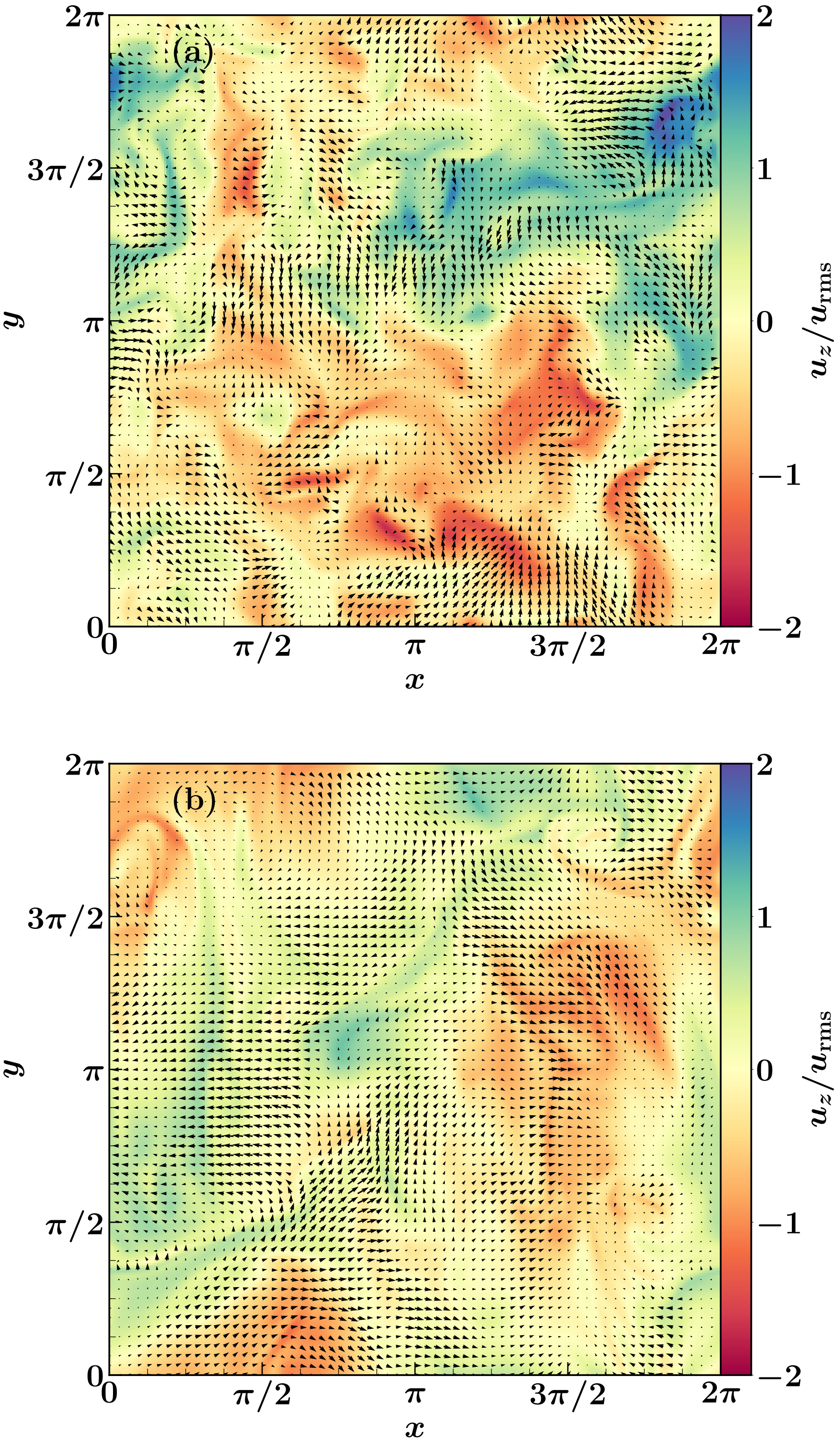

Figure 2.19: A 2D cut in the xy-plane with vectors $(u_x/\,u_{\rm rms}, u_y/\,u_{\rm rms})$ and colour showing the magnitude of $u_z/\,u_{\rm rms}$ in the kinematic (a) and saturated (b) stages with $\mathrm{Re}_\mathrm{M} = 2244$. The velocity field in both the stages looks qualitatively the same. The structures are of the size of half of the domain.

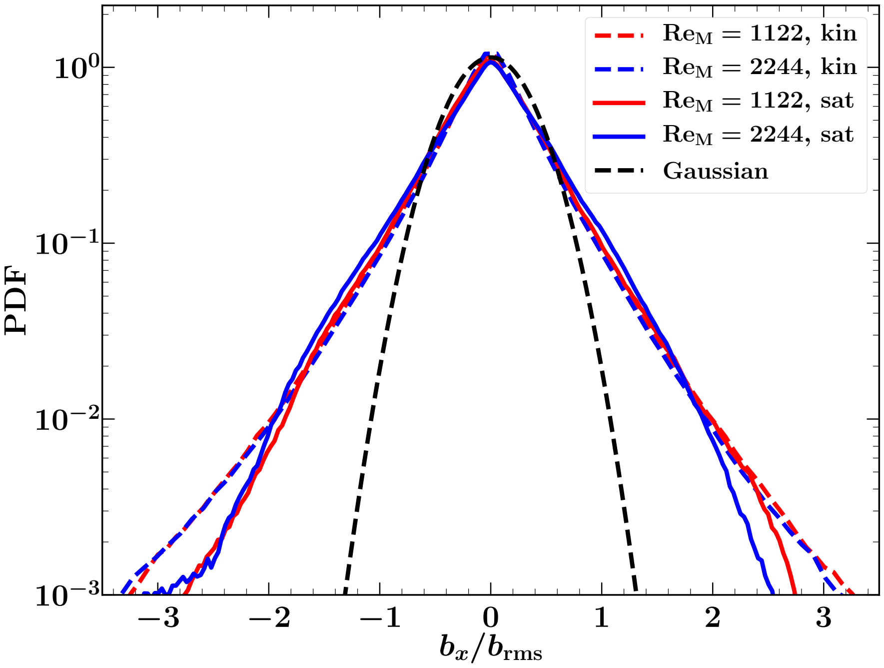

Figure 2.20: The PDF of the normalized magnetic field component $b_x/\,b_{\mathrm{rms}}$ for $\mathrm{Re_M} = 1122$ and $\mathrm{Re_M} = 2244$ in the kinematic (dashed) and saturated (solid) stages for the values of $\mathrm{Re_M}$ given in the legend. The magnetic field for both $\mathrm{Re_M}$ in both stages is far from a Gaussian (dashed, black). It has heavy tails which is a sign of intermittency.

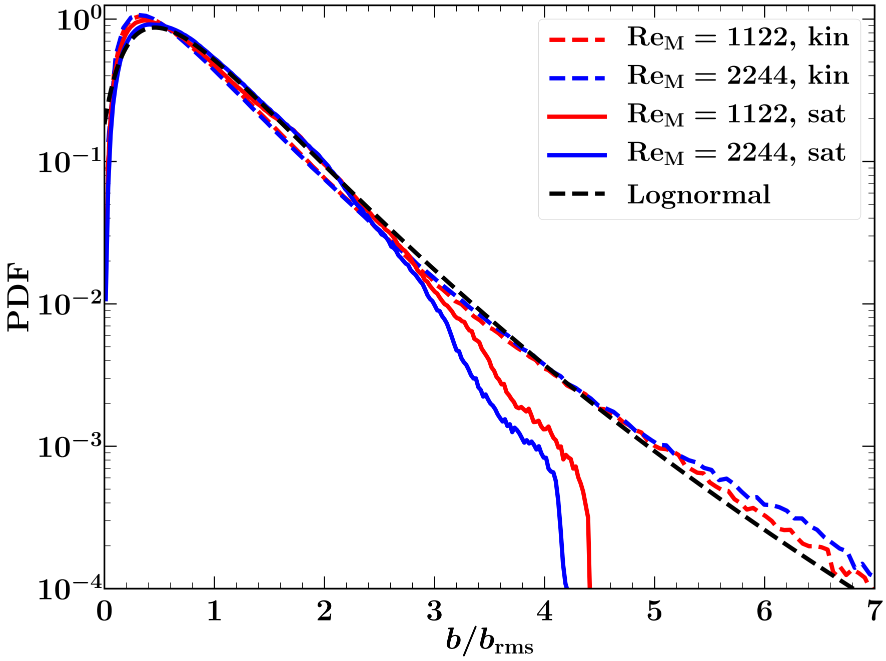

Figure 2.21: The PDF of the normalized magnetic field strength $b/\,b_{\rm rms}$ for $\mathrm{Re_M} = 1122$ and $\mathrm{Re_M} = 2244$ in the kinematic (dashed) and saturated (solid) stages for the values of $\mathrm{Re_M}$ given in the legend. The PDF of the magnetic field in the kinematic state follows a lognormal distribution (dashed, black). The magnetic field is more intermittent in the kinematic stage than in the saturated stage.

Even though the velocity field is Gaussian, the magnetic field in both the kinematic and saturated stages is spatially intermittent. This can be seen from the PDFs of a normalized component of the magnetic field $b_x/\,b_{\rm rms}$ in Fig. 2.20. The distribution is far from a Gaussian one and has long heavy tails at higher values of the magnetic field strength. The magnetic field in the kinematic stage is more intermittent than that in the saturated stage. This can be seen in Fig. 2.21 which shows the PDF of the strength of the magnetic field $b/\,b_{\rm rms}$ for $\mathrm{Re_M} = 1122$ and $\mathrm{Re_M} = 2244$ in the kinematic and saturated stages. The PDF of the kinematic magnetic field follows a lognormal distribution and it has heavier tails in comparison to that for the saturated magnetic field. The two-dimensional vector plots of the magnetic fields in Fig. 2.22 also show larger structures in the saturated stage. This can be further confirmed by calculating the kurtosis of the magnetic field distribution $\mathrm{Kurt}(\mathbf{b})$. The kurtosis of the kinematic magnetic field for $\mathrm{Re_M} = 1122$ is 5.29 but is 3.32 in the saturated stage. Thus, the saturated magnetic field is more volume filling or less intermittent than the kinematic magnetic field. The magnetic field correlation length l_b is calculated using Eq. (2.15) by replacing E_k with M_k, the magnetic field power spectrum. The magnetic field correlation length in the kinematic $l_{b\rm kin}$ and saturated $l_{b\rm sat}$ stages is given in Table 2.1. The magnetic

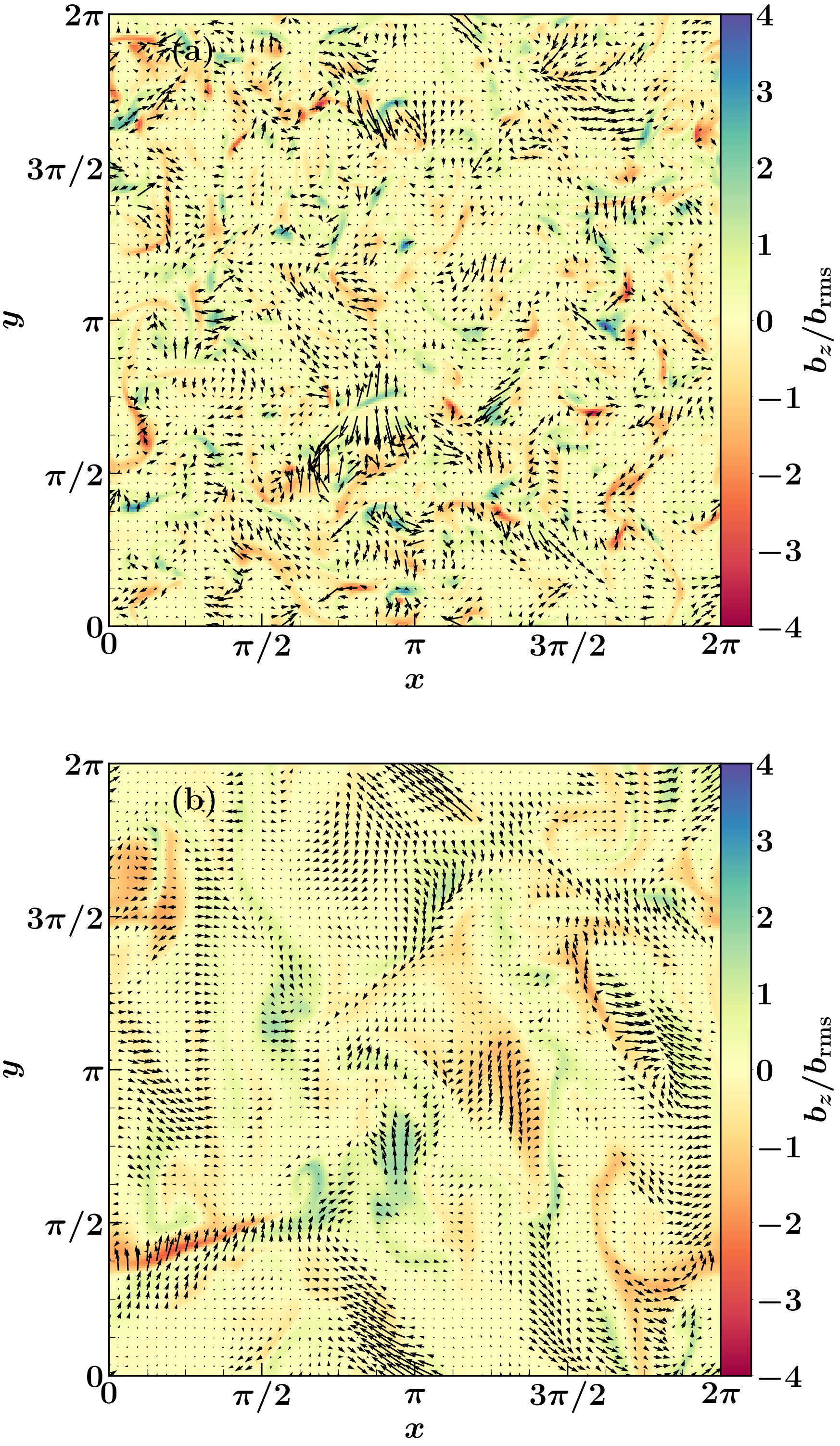

Figure 2.22: As Fig. 2.19 but for the magnetic field. The magnetic field in the kinematic stage is intermittent with random magnetic structures. In the saturated stage, the field remains intermittent but the structures are larger.

field correlation length decreases as $\mathrm{Re_M}$ increases, both for the kinematic and saturated stages. Thus, the magnetic field intermittency increases as $\mathrm{Re_M}$ increases. It is also clear that $l_{b\mathrm{sat}} > l_{b\mathrm{kin}}$ for all $\mathrm{Re_M}$ which confirms again that the magnetic field in the kinematic stage is less volume filling. This is true regardless of the choice of $\mathrm{Re_M}$ and agrees with previous numerical studies (Cho & Ryu, 2009; Bhat & Subramanian, 2013). A higher correlation length in the saturated stage also indirectly implies the observed change in magnetic energy spectra.

The structure of velocity and magnetic fields can also partly explain the ratio of magnetic to kinetic energy densities ($\varepsilon_{\mathrm{M}}/\varepsilon_{\mathrm{K}}$). In the saturated state, $\varepsilon_{\mathrm{M}}/\varepsilon_{\mathrm{K}} < 1$ (Table 2.1). Suppose the total turbulent kinetic energy is E_{struc}, assumed uniform throughout the whole volume V (this is a justified assumption because the velocity field distribution is Gaussian). Then the kinetic energy density is approximately equal to E_{struc}/V. The magnetic field is intermittent with equipartition ($\mathrm{Pr_M} = 1$) energy density in a smaller fraction of the total volume, V_{b}/V. Then the total magnetic energy is approximately equal to $E_{\mathrm{struc}}(V_{\mathrm{b}}/V)$. Thus, the average magnetic energy density is smaller than the average kinetic energy density and the ratio is less than unity.

2.4.3 Saturation of the fluctuation dynamo

Previous studies of the saturation mechanism

The exponentially growing magnetic field of the kinematic phase also leads to the exponential growth of the Lorentz force applied to the plasma, which makes the problem nonlinear. This slows down the growth and finally leads to the saturation of the dynamo (Fig. 2.16). The nature and spatial coherence of the field in the saturated state is of paramount importance to the study of the evolution of galactic magnetic fields (Arshakian et al., 2009) and in the interpretation of cluster observations (Enßlin & Vogt, 2006). However, details of the saturation mechanism remain poorly understood. Some ideas are discussed below (Schekochihin et al., 2004; Brandenburg & Subramanian, 2005; Cattaneo & Tobias, 2009; Tobias et al., 2011).

- **Energy equipartition argument.** It is reasonable to expect that the magnetic energy will saturate when it becomes comparable to the turbulent kinetic energy. However, in our numerical simulations we find that the ratio of magnetic to kinetic energy ($\varepsilon_{\mathrm{M}}/\varepsilon_{\mathrm{K}}$ in Table 2.1) much less than one. Thus, the equipartition argument does not seem to be true.

- **Marginally stable state as the saturated state.** Since a dynamo is a type of instability, we can expect that the nonlinearity effectively transforms the system back to its critical state, i.e., the magnetic Reynolds number ($\mathrm{Re_M} = UL/\eta$, where U is the characteristic velocity, L is the characteristic length scale and η is the magnetic diffusivity) in the saturated state is close to the critical magnetic Reynolds number, $\mathrm{Re_M^{(crit)}}$. This implies that for a fixed η, either U or L or both should decrease on saturation. We see in our simulations (Table 2.1) that the correlation length of the velocity field actually increases when the field saturates and thus L does not decrease. This could imply reduction in the velocity field amplitude. Such a reduction will be a huge jump, especially for very high $\mathrm{Re_M}$, which is not observed in our numerical simulations. The local magnetic Reynolds number $(\mathrm{Re_M})_{\mathrm{loc}} = |\nabla \times (\mathbf{u} \times \mathbf{b})|/|\eta \nabla^2 \mathbf{b}|$ can decrease without changing U or L. However, we later show in the section, that even in the saturated state, the local magnetic Reynolds number throughout the volume varies from much smaller than $\mathrm{Re_M^{(crit)}}$ to much larger than this critical number. The mean of the local magnetic Reynolds number does decrease but not to the critical value.

- **Velocity field modification.** Magnetic field only grows for velocity fields with certain properties. If these properties are altered, the field could stop growing. It has been shown using numerical simulations with single-scale flows that the chaotic properties of the flow (quantified by Lyapunov exponents) are suppressed significantly upon saturation, suggesting weaker stretching of magnetic field lines by the flow (Cattaneo et al., 1996; Kim, 1999). Due to the reduced stretching, the magnetic field amplification is diminished and the field saturates. However, in a recent simulations of a fluctuation dynamo driven by convection (involving multiple scales), it is shown that such stretching does not decrease drastically as the field saturates (Favier & Bushby, 2012).

  Another suggestion is that the velocity field, in response to the growing magnetic field, acquires a nonlinear velocity component (a velocity drift which is assumed to be proportional to the Lorentz force) in addition to the turbulent component (Subramanian, 1999, 2003). The induction equation is then solved analytically including this additional velocity component. The solution leads to an effectively stronger magnetic diffusion which saturates the field and also implies that the eigenfunction of the saturated magnetic field is similar to the marginal eigenfunction (Subramanian, 1999). So, in such a situation, the saturated magnetic power will be concentrated at larger scales compared to the kinematic stage (as power at smaller scales decreases when $\mathrm{Re_M}$ decreases). This in turn implies flatter magnetic field spectrum at low wave numbers in the saturated stage, which is seen in Fig. 2.17. The saturated state in this model is independent of the small-scale properties of the system such as magnetic diffusivity and viscosity. In galaxies, such an additional drift can be due to ambipolar diffusion in partially ionized gas (Subramanian, 1998).

Such models assume that the growing magnetic field instills a property in the velocity field which kills the growth. This is achieved by reducing amplification (Cattaneo et al., 1996) or enhancing diffusion (Subramanian, 1999). Models based on the modification of the velocity field alone may not be true as shown by a numerical experiment done by Cattaneo & Tobias (2009)[4]. They solved the nonlinear fluctuation dynamo equations and obtained the saturated velocity and magnetic fields. Then using the saturated velocity field, with the same magnetic Reynolds number as before, they solved only the induction equation (i.e. the kinematic fluctuation dynamo problem, so the velocity field does not change with time) with a random initial seed magnetic field. They found that the magnetic field actually again grows exponentially. This clearly shows that the modified velocity field alone is not responsible for the saturation of the fluctuation dynamo and a constant interaction between the velocity and magnetic field is required to maintain the saturated state. However, in the saturation model with a nonlinear drift proportional to the Lorentz force (Subramanian, 1999), the velocity field does depend on the magnetic field and thus there is a constant interaction between the two quantities. So, such a model is consistent with the findings of Cattaneo & Tobias (2009).

- **Folded magnetic field structure and scale-by-scale energy equipartition.**

  For $\mathrm{Pr_M} \gg 1$, Schekochihin et al. (2002) proposed a folded structure for small-scale magnetic fields generated by a fluctuation dynamo. Fig. 2.23 shows such a structure where the magnetic field consists of reversing magnetic field lines. The length and thickness of the folds are of the order of the viscous scale l_ν and the resistive scale l_η respectively. Schekochihin et al. (2004) claim that the nonlinearity becomes significant when the inertial forces balance the magnetic tension in the Navier–Stokes equation, i.e., $\mathbf{u} \cdot \nabla \mathbf{u} \approx \mathbf{b} \cdot \nabla \mathbf{b}$ (it is assumed that the magnetic pressure balances the fluid pressure). The term $\mathbf{u} \cdot \nabla \mathbf{u}$ can be approximated as u^2/l_ν, where u is the typical velocity. For estimating $\mathbf{b} \cdot \nabla \mathbf{b}$, we use the folded structure of the field. As shown in Fig. 2.23, the magnetic field direction changes most rapidly over the shorter scale l_η and remain roughly same within the scale l_ν. Thus, $\mathbf{b} \cdot \nabla \mathbf{b}$ can be approximated as b^2/l_ν, where b is the typical magnetic field. So, equating the two terms gives $u^2 \approx b^2$ at the viscous scale. The magnetic field growth stops first at the viscous scale when the

---

[4] A similar experiment was done by Tilgner & Brandenburg (2008) for non-linear mean field dynamos.

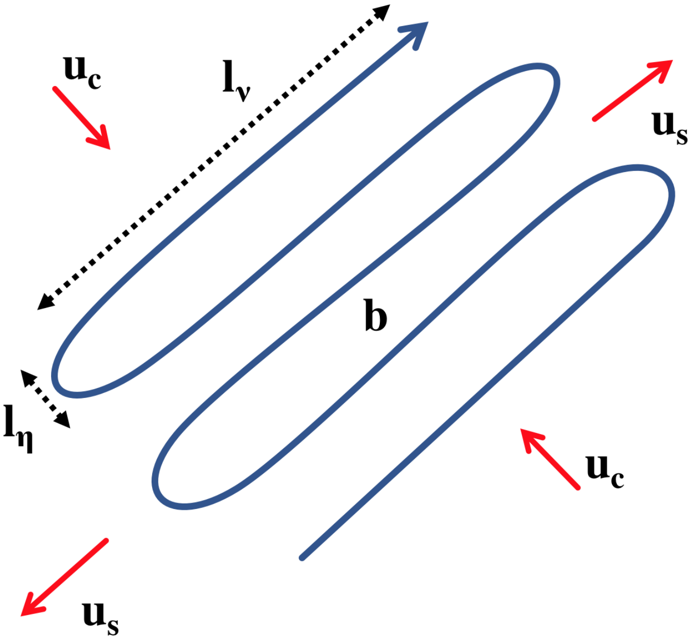

Figure 2.23: Schematic of the folded structure of the magnetic field. The field is amplified by turbulent velocity via its stretching $\mathbf{u_s}$ and compressive $\mathbf{u_c}$ components. The field reverses several times within a magnetic structure. The field direction changes along the smaller length scale which is comparable to the resistive scale l_η and the length of the folds are the order of the viscous scale l_ν.

magnetic field is in equipartition with the velocity field at that scale. Amplification can continue at larger scales until a similar equipartition level is reached. The saturation mechanism continues on a scale-by-scale basis until it reaches the correlation length of the velocity field. Thus, the magnetic field energy saturates by successive equipartition with kinetic energy at each scale, starting from the viscous scale.

The theory of folded magnetic structures might not be true in all cases. Fig. 2.24 shows a slice of the magnetic field in the saturated state for a fluctuation dynamo in a periodic box of dimensionless size $(2\pi)^3$ with 256^3 mesh point, $\mathrm{Pr_M} = 50, \mathrm{Re_M} = 200, \mathrm{Re} = 4$ and the average forcing wave number $k_\mathrm{F} \approx 1.5$. Folded magnetic structures can be seen in Fig. 2.24 but there are also structures with no magnetic field reversals (for example the one within the blue circle in Fig. 2.24). It also worth reiterating that the correlation length of both the velocity and magnetic fields increases as the field saturates, thus the length scales themselves might change (the spectrum shifts to smaller wave numbers). However, we do confirm in Fig. 2.25, that $\mathbf{u} \cdot \nabla \mathbf{u} \approx \mathbf{b} \cdot \nabla \mathbf{b}$, although those two quantities are not correlated.

- **Plasma effects.** Since the resistive scale is quite small (high $\mathrm{Re_M}$), plasma effects

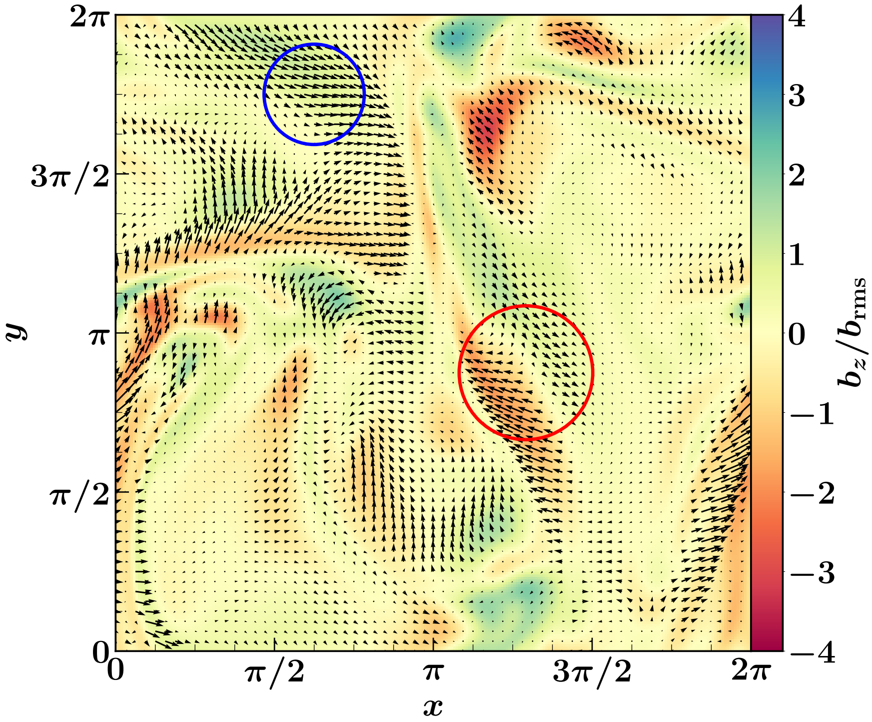

Figure 2.24: A 2D cut in the xy-plane with vectors $(b_x/\,b_{\rm rms}, b_y/\,b_{\rm rms})$ and colours showing the magnitude of $b_z/\,b_{\rm rms}$ in the saturated stage with $\mathrm{Pr}_{\rm M} = 50$. The red circle shows a magnetic structure where the field reverses and the blue circle shows a strong magnetic structure where such a reversal is not observed. At high $\mathrm{Pr}_{\rm M}$, magnetic structures with both the presence and absence of field reversals within them are observed (and are also seen in previous studies, e.g. Brandenburg & Subramanian, 2005).

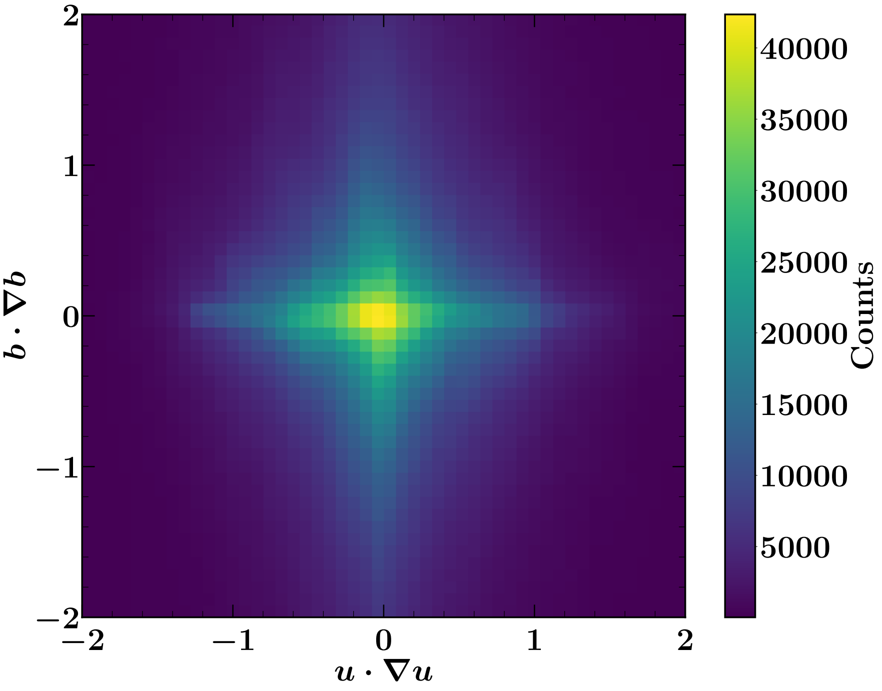

Figure 2.25: Two dimensional correlation of $\mathbf{u} \cdot \nabla \mathbf{u}$ and $\mathbf{b} \cdot \nabla \mathbf{b}$ for a run with $\mathrm{Pr_M} = 50$. Both quantities are approximately equal in magnitude and uncorrelated.

might play an important role at smaller scales. In fully ionized plasma, the viscosity becomes anisotropic with respect to the magnetic field direction and actually then the Braginskii viscosity (Braginskii, 1965) is more appropriate. Unlike bulk fluid viscosity, the Braginskii viscosity only dissipates those motions which affect magnetic fields. Thus, the back reaction of the field starts much earlier, leading to saturation of magnetic fields at a much lower value than the equipartition value and much larger magnetic field length scales (Malyshkin & Kulsrud, 2002). However, in this model an additional problem arises. When magnetic field is weak (which is the case initially), various plasma instabilities are excited (Schekochihin & Cowley, 2007). Such process can be studied using numerical simulations of the plasma dynamo (Rincon et al., 2016; St-Onge & Kunz, 2018), which considers magnetic field amplification in a collisionless plasma. In a partially ionized plasma, ambipolar diffusion will further enhance magnetic diffusion (Zweibel, 2002), which might also affect the saturation mechanism. Since, we assume the MHD approximation, we cannot test such effects with our simulations.

Our approach to study the saturation of the fluctuation dynamo

Cattaneo & Tobias (2009) suggests that the saturated velocity field amplifies a seed field as long as it is not aligned with the saturated magnetic field. This motivates us to look at the alignment of the magnetic field with the velocity as a possible mechanism for the saturation. Such an alignment has been studied in the context of convectively driven fluctuation dynamos (Brandenburg et al., 1996; Favier & Bushby, 2012), MHD turbulence in the presence of a strong guide field (Mason et al., 2006) and decaying isotropic MHD turbulence (Servidio et al., 2008). For the numerical simulations described in Table 2.1, we calculate the angle between the velocity $\mathbf{u}$ and magnetic field $\mathbf{b}$ and the current density $\mathbf{j}$ and magnetic field. The cosine of the relevant angles are given by

$$\cos(\theta)_{\mathbf{u},\,\mathbf{b}} = \frac{\mathbf{u}\cdot\mathbf{b}}{|\mathbf{u}||\mathbf{b}|}, \tag{2.16}$$

and

$$\cos(\theta)_{\mathbf{j},\,\mathbf{b}} = \frac{\mathbf{j}\cdot\mathbf{b}}{|\mathbf{j}||\mathbf{b}|}, \tag{2.17}$$

respectively. When the cosine of the angle is zero, both the vectors are perpendicular and when it is unity, both are perfectly aligned. Fig. 2.26 and Fig. 2.27 show the probability density function of these cosines in the kinematic and saturated stages for $\mathrm{Re}_{\mathrm{M}} = 1122$ and $\mathrm{Re}_{\mathrm{M}} = 1496$. Since the cosines of both angles are symmetric about $\mathbf{b} = \mathbf{0}$, we only plot their magnitude. For both values of Re_{M}, the cosine of the angle between the velocity and magnetic field $\cos(\theta)_{\mathbf{u},\,\mathbf{b}}$ tend to have higher values in the saturated stage than in the kinematic stage. This implies that the magnetic field is more aligned with the velocity field as the field saturates. This in turn decreases the induction term $\nabla\times(\mathbf{u}\times\mathbf{b})$ and thus reduces the amplification of the magnetic field. However, there is a significant fraction of the volume where the two fields are not aligned and so the amplification is not completely supressed. This minimum level of amplification is required to balance the diffusion. The cosine of the angle between the current density and magnetic field $\cos(\theta)_{\mathbf{j},\,\mathbf{b}}$ also has higher values in the saturated stage. This decreases the back reaction of the field on the flow via the Lorentz force term $\mathbf{j}\times\mathbf{b}$. Thus, the field becomes closer to a force-free form as it saturates. Overall, because of the enhanced local alignment between the velocity and magnetic field, the field is less amplified. And due to the increase in the local alignment between the current density and magnetic field, the back reaction of field on the flow decreases. Thus, the field is amplified less and also it affects the flow less, as it saturates. This conclusions also applies in the regions of stronger field (higher b/b_{rms} in Fig. 2.26 and Fig. 2.27). However, the level of alignment between the velocity and magnetic field is higher in the strong field regions in both the kinematic and saturated stages. This suggests that the strong field regions require a larger reduction in amplification by alignment. The distribution of $\cos(\theta)_{\mathbf{j},\,\mathbf{b}}$ in the kinematic stage shows some dependence upon the field strength but in the saturated stage the difference is less pronounced. In the kinematic stage, alignment is weakest in the strong field region suggesting that in the strong field regions, not only because of its higher strength but also because of lower level of alignment, the field produces a stronger back reaction on the flow.

Another important question is whether the alignment between the velocity and magnetic fields and the magnetic field and current density occur in the same spatial region. To answer this, we show the cross-correlation between the two angles in Fig. 2.28. Fig. 2.28a and Fig. 2.28b shows the correlation in the kinematic and saturated stages respectively. In both cases, most of the points are at high values of $\cos(\theta)_{\mathbf{u},\,\mathbf{b}}$ and $\cos(\theta)_{\mathbf{j},\,\mathbf{b}}$. This suggests that the velocity, magnetic field and current density are always nearly aligned to each other. It is difficult to see any further difference between the kinematic and saturated stages in Fig. 2.28a and Fig. 2.28b. Fig. 2.28c and Fig. 2.28d show the same correlation but only for strong field regions $(b/\,b_{\rm rms} > 1.5)$. In Fig. 2.28c, the kinematic stage shows higher correlation in regions with high $\cos(\theta)_{\mathbf{u},\,\mathbf{b}}$ and low $\cos(\theta)_{\mathbf{j},\,\mathbf{b}}$, which is very less probable in the saturated stage (Fig. 2.28d). This shows that the active induction in the kinematic stage decreases on saturation. Once the field saturates, the induction is relatively less necessary (required only to counter the diffusion) and thus the regions with high $\cos(\theta)_{\mathbf{u},\,\mathbf{b}}$ are comparatively less, as shown in Fig. 2.28d. The comparison between Fig. 2.28c and Fig. 2.28d also implies that the field geometry grows in such way so as to maximize the Lorentz force, especially in the strong field regions. However, the Lorentz force is initially limited by the amplitude of the magnetic field. Once the field saturates, the back reaction is no longer necessary and thus the regions with low $\cos(\theta)_{\mathbf{j},\,\mathbf{b}}$ are less probable, as shown in Fig. 2.28d.

To summarize, the magnetic field saturates via alignment between the velocity and magnetic field vectors and the magnetic field and current density vectors. This strongly suggests the field saturates by reduction in amplification. The level of alignment does not completely inhibit the amplification, so there is always some field generated to balance the resistive decay. This in turn also implies that the back reaction due to the generated field will always remain significant. Thus, even though both velocity and magnetic field reach a statistically steady state (Fig. 2.16), it is the mutual interaction between the two quantities which maintains that state.

Further, we would like to know which aspect of the amplification, i.e. stretching or compression, is diminished as the field saturates. To test this, we consider the alignment of the magnetic field with the eigenvectors of the rate of strain tensor. The symmetric 3×3 matrix

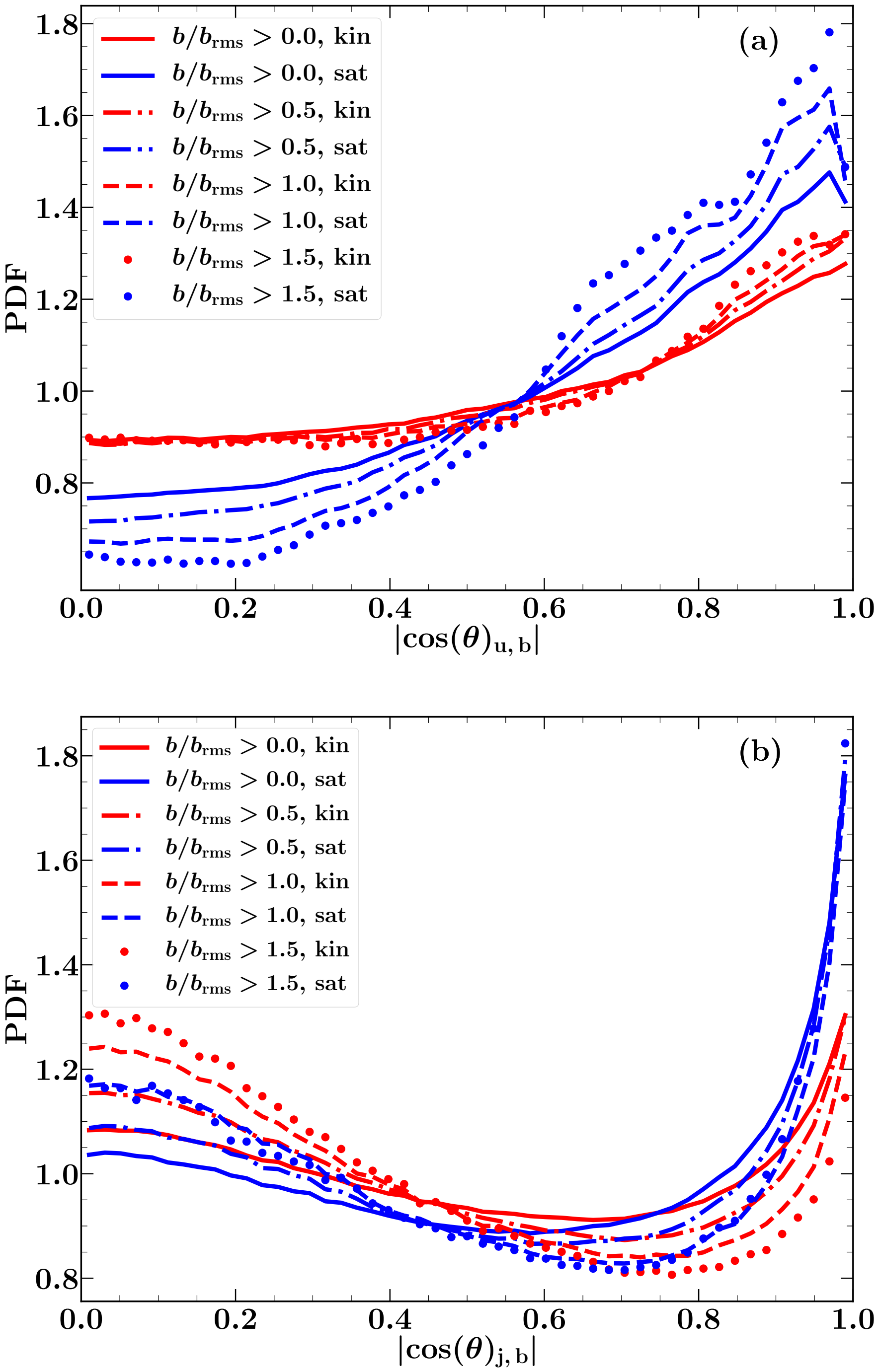

Figure 2.26: The total and conditional probability distribution functions of the cosines of the angles between $\mathbf{u}$ and $\mathbf{b}$, $\cos(\theta)_{\mathbf{u},\,\mathbf{b}}$ (a) and between $\mathbf{j}$ and $\mathbf{b}$, $\cos(\theta)_{\mathbf{j},\,\mathbf{b}}$ (b) for $\mathrm{Re}_\mathrm{M} = 1122$ in the kinematic (red) and saturated (blue) states. The magnetic field in the saturated stage is more aligned with velocity field (reducing the induction effects) as compared to kinematic stage. The magnetic field also become better aligned with the electric current density, reducing the back reaction on the velocity field.

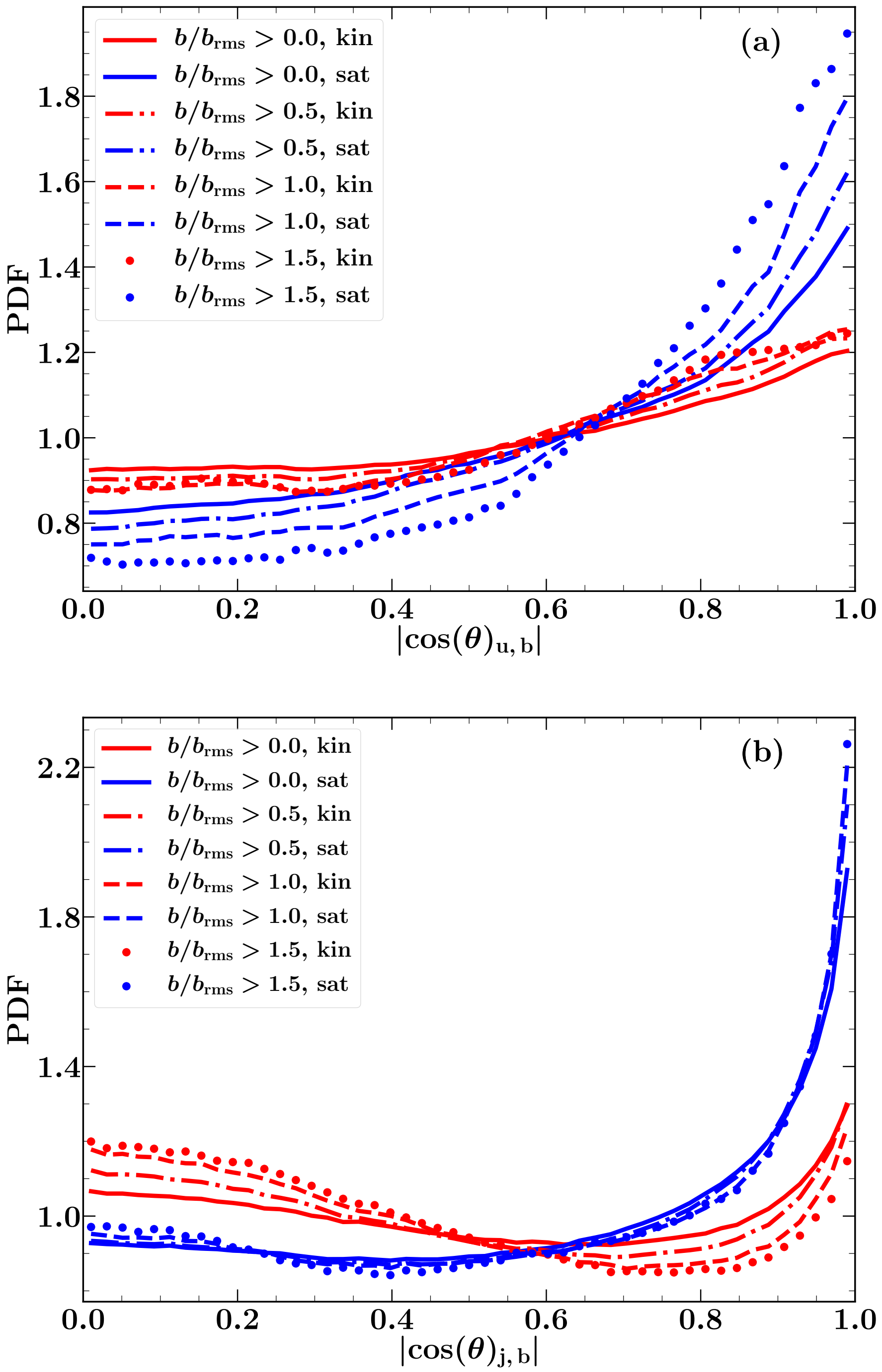

Figure 2.27: As Fig. 2.26 but for $\mathrm{Re_M} = 1496$.

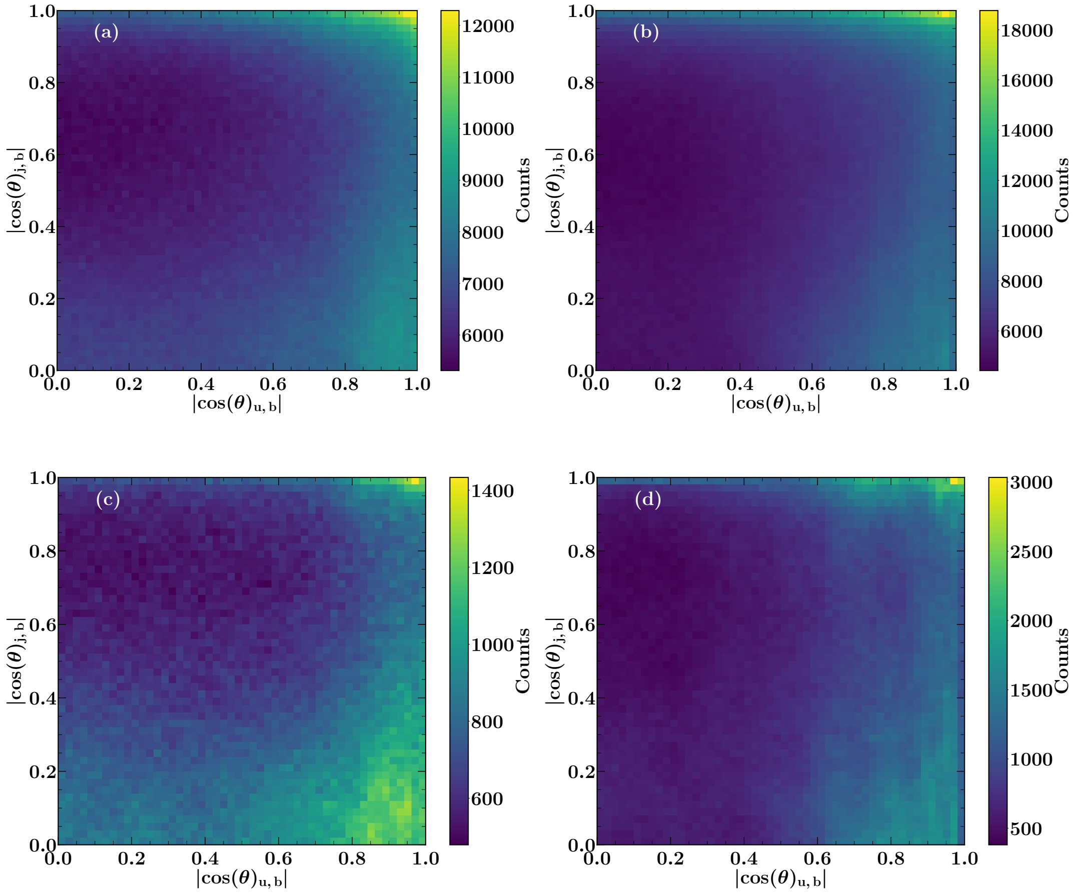

Figure 2.28: The cross correlation of $\cos(\theta)_{\mathbf{u},\mathbf{b}}$ and $\cos(\theta)_{\mathbf{j},\mathbf{b}}$ in the kinematic (a,c) and saturated (b,d) stages for $\mathrm{Re_M} = 1122$. Panels (a) and (b) refers to the whole domain and the difference between them is not significant. Panels (c) and (d) refers to only the strong field regions ($b/\,b_{\mathrm{rms}} \geq 1.5$). The yellow patch close to low $\cos(\theta)_{\mathbf{j},\mathbf{b}}$ and high $\cos(\theta)_{\mathbf{u},\mathbf{b}}$ in the kinematic stage vanishes for the saturated stage. The peak in the count is always at high $\cos(\theta)_{\mathbf{u},\mathbf{b}}$ and high $\cos(\theta)_{\mathbf{j},\mathbf{b}}$, which implies significant alignment between magnetic field, velocity field and current density.

$S_{ij} = \frac{1}{2}(u_{i;j} + u_{j;i})$ is calculated at each point in the domain using sixth-order finite differences and its eigenvalues and eigenvectors are calculated. The eigenvalues are arranged in an increasing order, say $\lambda_1 < \lambda_2 < \lambda_3$. The corresponding eigenvectors are $\mathbf{e}_1, \mathbf{e}_2, \mathbf{e}_3$. The sum of the eigenvalues is close to zero since the flow is nearly incompressible. λ_1 is always negative and the vector $\mathbf{e}_1$ corresponds to the direction of local compression, λ_3 is always positive and the vector $\mathbf{e}_3$ corresponds to the direction of local stretching and λ_2 can be obtained from $\lambda_1 + \lambda_2 + \lambda_3 \approx 0$. We then calculate the alignment with the magnetic field $\mathbf{b}$ of the vector representing the local compression $\mathbf{e}_1$ and the local stretching $\mathbf{e}_3$. The corresponding cosine of the angle between them are given by

$$\cos(\theta)_{\mathbf{e}_1,\mathbf{b}} = \frac{\mathbf{e}_1 \cdot \mathbf{b}}{|\mathbf{e}_1||\mathbf{b}|} \tag{2.18}$$

and

$$\cos(\theta)_{\mathbf{e}_3,\mathbf{b}} = \frac{\mathbf{e}_3 \cdot \mathbf{b}}{|\mathbf{e}_3||\mathbf{b}|} \tag{2.19}$$

respectively. Fig. 2.29 shows the PDF of the cosines in the kinematic and saturated stages for $\mathrm{Re_M} = 1796$. In most of the volume, the direction of the magnetic field is perpendicular to the direction of the local compression (Fig. 2.29a), which leads to amplification of magnetic field due to compression. The magnetic field in the kinematic stage is found to be more perpendicular to the direction of compression as compared to the saturated stage. The PDF of the angle between the direction of local stretching and the magnetic field $\cos(\theta)_{\mathbf{e}_3,\mathbf{b}}$ has maximum at $\cos(\theta)_{\mathbf{e}_3,\mathbf{b}} = 0$ and $\cos(\theta)_{\mathbf{e}_3,\mathbf{b}} = 1$ in the kinematic stage. The magnetic field amplification is maximum when the direction of local stretching is aligned with the direction of the magnetic field. In the saturated stage, however all angles are nearly equiprobable. These results are more pronounced for the strong field regions ($b/\,b_{\mathrm{rms}} \geq 1$). However, as can be seen in Fig. 2.29, the difference between the PDFs in the kinematic and saturated stages is not very strong and thus we can conclude that a small reduction in local stretching and compression of magnetic fields contributes towards the saturation of the fluctuation dynamo.

We now directly consider the equation for magnetic energy evolution and calculate its growth and the dissipation terms separately. Using the induction equation, we derive the equation for the evolution of the magnetic energy, E_M. Taking the dot product of Eq. (2.8) with $\mathbf{b}$ and integrating over the periodic cube (V), we obtain

$$\int_V \mathbf{b} \cdot \frac{\partial \mathbf{b}}{\partial t}\,\mathrm{d}V = \int_V \mathbf{b} \cdot [\nabla \times (\mathbf{u} \times \mathbf{b})]\,\mathrm{d}V + \int_V \eta \mathbf{b} \cdot \nabla^2 \mathbf{b}\,\mathrm{d}V. \tag{2.20}$$

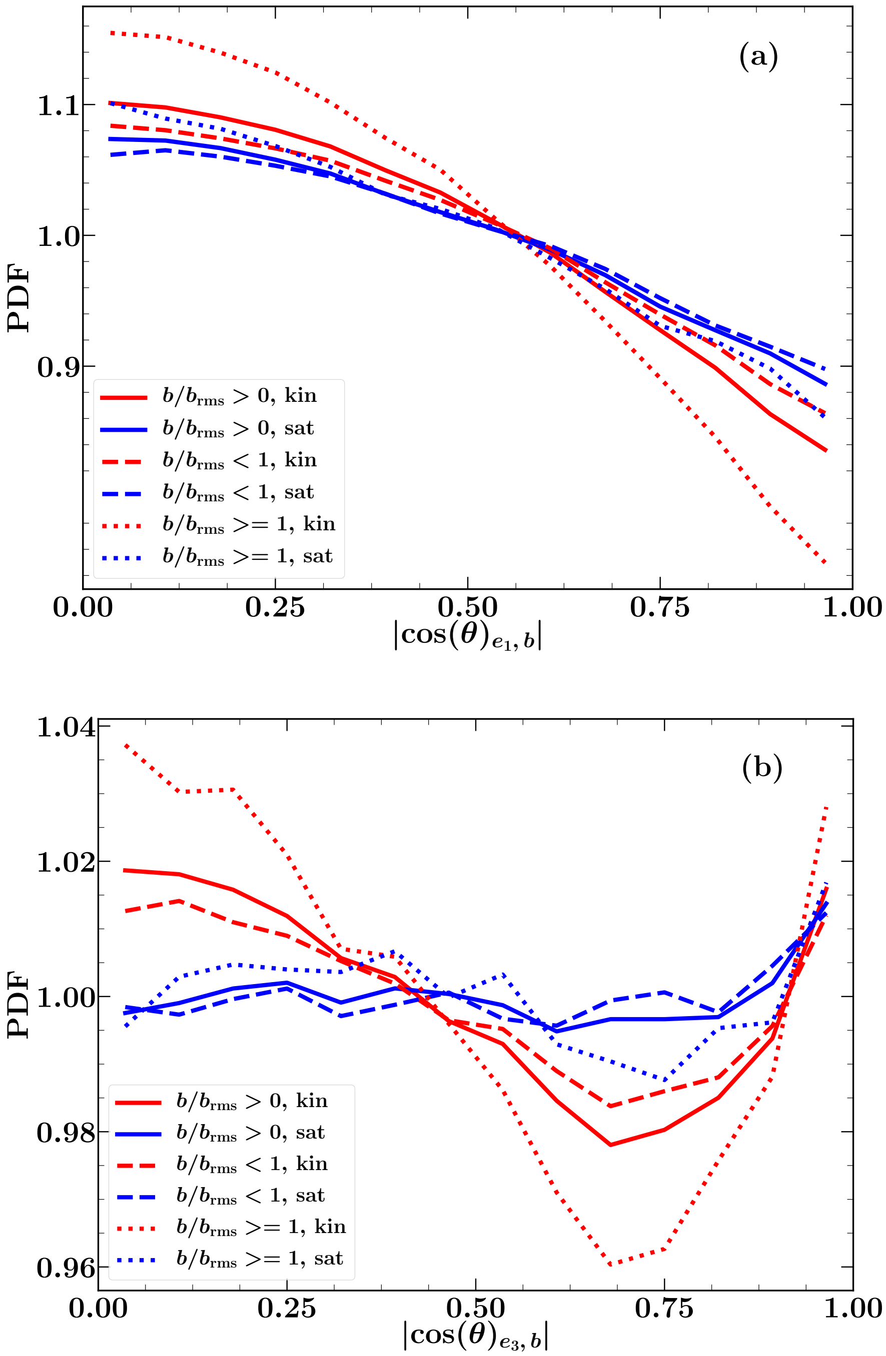

Figure 2.29: The total and conditional PDFs of the cosine of the angle between the direction of local compression and the magnetic field $\cos(\theta)_{\mathbf{e}_1,\mathbf{b}}$ (a) and between the direction of local stretching and the magnetic field $\cos(\theta)_{\mathbf{e}_3,\mathbf{b}}$ (b) for $\mathrm{Re}_\mathrm{M} = 1796$ in the kinematic (red) and saturated (blue) stages.

The left-hand side of Eq. (2.20), which is equivalent to $\frac{\partial E_M}{\partial t} = \frac{1}{2}\frac{\partial}{\partial t}\int_V \mathbf{b}^2 \,\mathrm{d}V$, is the rate of change of the magnetic energy. The right-hand side contains two terms: the first one is responsible for the increase in the magnetic energy due to the interaction of the magnetic field with the velocity field and the second term represents the reduction in the magnetic energy due to resistive losses. The first term can be further simplified as follows:

$$\iiint_V \mathbf{b}\cdot[\nabla\times(\mathbf{u}\times\mathbf{b})]\,\mathrm{d}V, \tag{2.21}$$

$$=\iiint_V [\mathbf{b}\cdot(\mathbf{b}\cdot\nabla\mathbf{u}-\mathbf{u}\cdot\nabla\mathbf{b}+\cancelto{0}{(\nabla\cdot\mathbf{b})}\cdot\mathbf{u}-\cancelto{0}{(\nabla\cdot\mathbf{u})\mathbf{b}})]\,\mathrm{d}V, \tag{2.22}$$

$$=\iiint_V [b_i b_j \partial_j u_i - \mathbf{b}\cdot(\mathbf{u}\cdot\nabla\mathbf{b})]\,\mathrm{d}V, \tag{2.23}$$

$$=\iiint_V [b_i b_j S_{ij} - \mathbf{u}\cdot\frac{1}{2}\nabla\mathbf{b}^2]\,\mathrm{d}V, \tag{2.24}$$

$$=\iiint_V [b_i b_j S_{ij} - \frac{1}{2}\nabla\cdot(\mathbf{u}\mathbf{b}^2)+\frac{1}{2}\mathbf{b}^2\cancelto{0}{(\nabla\cdot\mathbf{u})}]\,\mathrm{d}V, \tag{2.25}$$

$$=\iiint_V b_i b_j S_{ij}\,\mathrm{d}V - \frac{1}{2}\iint_S (\mathbf{u}\mathbf{b}^2)\cdot\hat{\mathbf{n}}\,\mathrm{d}S, \tag{2.26}$$

where the surface integral in Eq. (2.26) vanishes because of the periodic boundary conditions. Thus, the increase in the magnetic energy is due to the $\iiint_V (b_i b_j S_{ij})\,\mathrm{d}V$ only. The second term in Eq. (2.20), which reduces the magnetic energy, can also be further simplified as follows:

$$\eta\iiint_V \mathbf{b}\cdot\nabla^2\mathbf{b}\,\mathrm{d}V, \tag{2.27}$$

$$=\eta\iiint_V \mathbf{b}\cdot[\nabla\cancelto{0}{(\nabla\cdot\mathbf{b})}-\nabla\times(\nabla\times\mathbf{b})]\,\mathrm{d}V, \tag{2.28}$$

$$=-\eta\iiint_V \mathbf{b}\cdot[\nabla\times(\nabla\times\mathbf{b})]\,\mathrm{d}V, \tag{2.29}$$

$$=-\eta\iiint_V (\nabla\times\mathbf{b})^2\,\mathrm{d}V, \tag{2.30}$$

$$=-\eta\iiint_V \mathbf{j}^2\,\mathrm{d}V. \tag{2.31}$$

Combining Eq. (2.26) and Eq. (2.31), the magnetic energy evolution equation can therefore be written as

$$\frac{\partial E_M}{\partial t} = \iiint_V b_i b_j S_{ij}\,\mathrm{d}V - \eta\iiint_V \mathbf{j}^2\,\mathrm{d}V. \tag{2.32}$$

The term contributing to the energy growth, $b_i b_j S_{ij}$, is calculated at each point in the

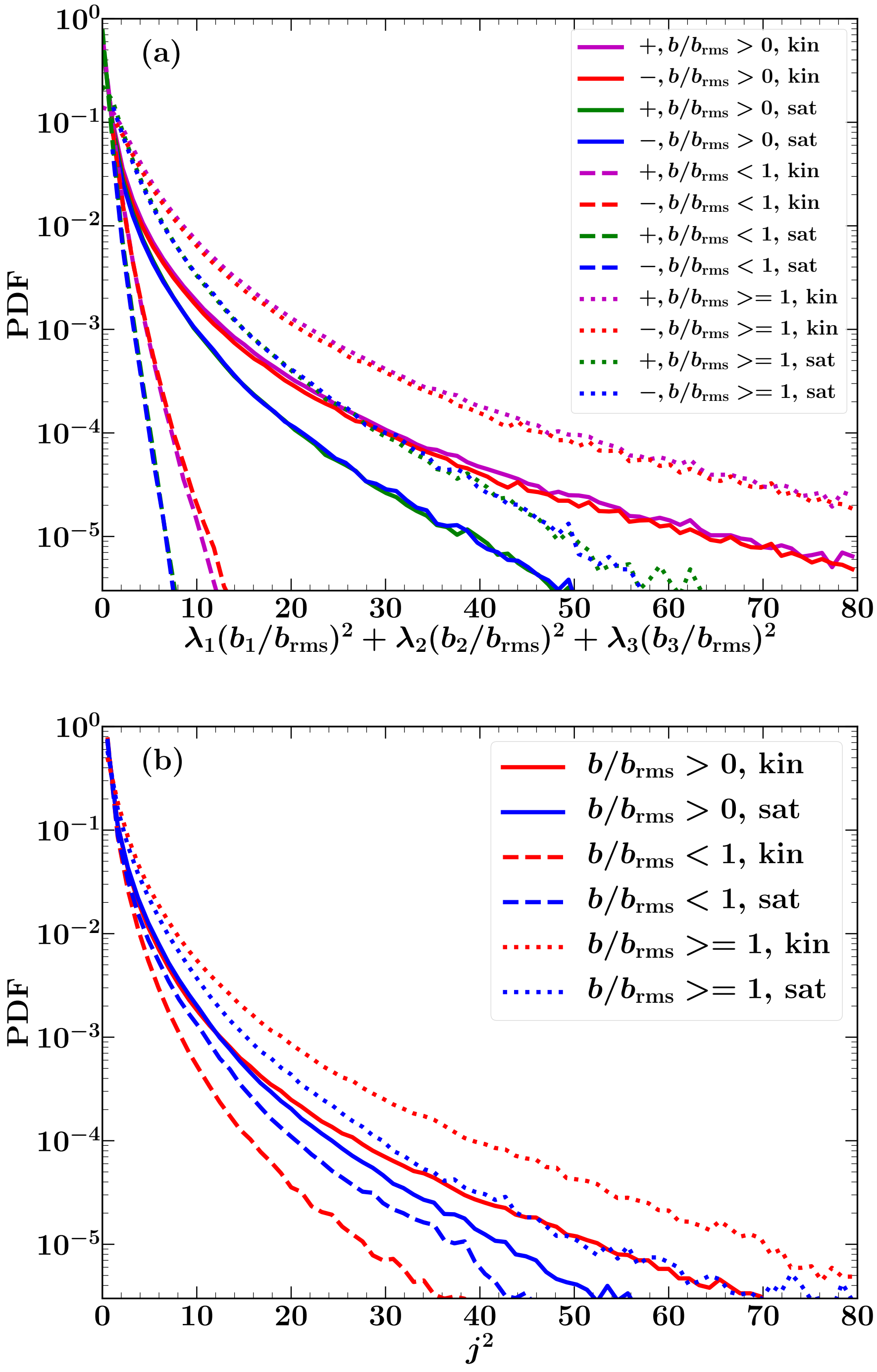

Figure 2.30: The total and conditional PDFs of the local growth term $\lambda_1 \mathbf{b}_1^2 + \lambda_2 \mathbf{b}_2^2 + \lambda_3 \mathbf{b}_3^2$ (a) and the local dissipation term $\mathbf{j}^2$ (b) in the kinematic (red) and saturated (blue) stages for $\mathrm{Re_M} = 1122$. When the local growth term is negative, its magnitude is plotted and this denoted by '$-$' in the legend. Both the local growth and dissipation terms over the entire volume decreases on saturation. This is true same in both the weak and strong field regions, except for the local dissipation term, which increases in the weak field regions.

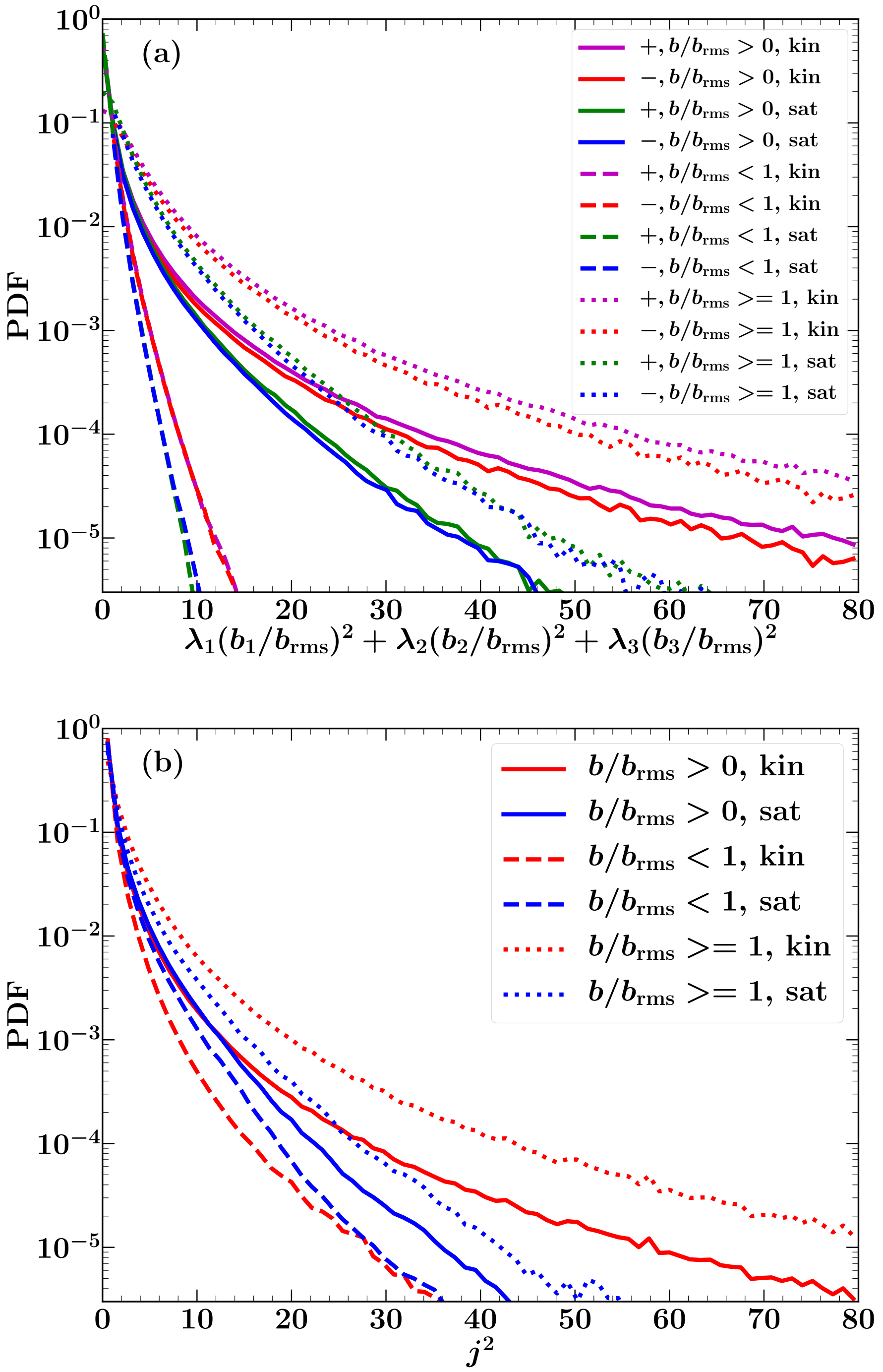

Figure 2.31: As Fig. 2.30 but for $\mathrm{Re_M} = 1796$.

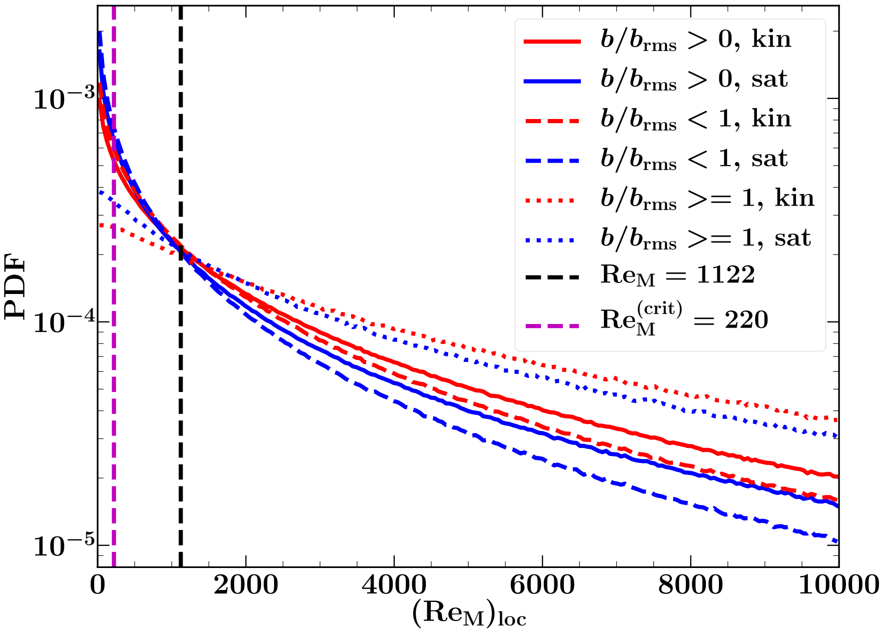

Figure 2.32: The total and conditional PDFs of the local magnetic Reynolds number $(\mathrm{Re_M})_{\mathrm{loc}}$ in the kinematic (red) and saturated (blue) stages with $\mathrm{Re_M} = 1122$. The purple dashed line shows the critical magnetic Reynolds number $\mathrm{Re_M^{(crit)}} = 220$ and the black dashed line shows $\mathrm{Re_M}$ for this run.

volume as follows. First, we project the magnetic field vector $\mathbf{b}$ along each of the eigenvectors of the rate of strain tensor, $\mathbf{e}_1, \mathbf{e}_2, \mathbf{e}_3$. Let this be $\mathbf{b}_1, \mathbf{b}_2, \mathbf{b}_3$. Now, the growth term is calculated by computing $\lambda_1 \mathbf{b}_1^2 + \lambda_2 \mathbf{b}_2^2 + \lambda_3 \mathbf{b}_3^2$ at each point in space. This is called the local growth term. The local growth term can be positive or negative (λ_1 is negative and λ_3 is positive). The term contributing to the decay in energy is calculated by computing $\mathbf{j}^2$ (η is constant) at each point in space. This is referred the local dissipation term. Fig. 2.30 and Fig. 2.31 show the total and conditional PDFs of the local growth and dissipation terms in the kinematic and saturated stages for $\mathrm{Re_M} = 1122$ and $\mathrm{Re_M} = 1796$ respectively. As seen in Fig. 2.30a and Fig. 2.31a, the local growth term decreases on saturation and this is equally true for strong and weak field regions. The dissipation term also decreases on saturation as shown in Fig. 2.30b and Fig. 2.31b. This also true for strong field regions but for the weak field regions the dissipation increases.

So, to calculate the overall decrease or increase in magnetic energy at each point in the domain, we calculate the local magnetic Reynolds number. Both terms in Eq. (2.32) are calculated at each point in the volume, and the local magnetic Reynolds number is defined as

$$(\mathrm{Re_M})_{\mathrm{loc}} = \frac{|b_i b_j S_{ij}|}{|\eta \mathbf{j}^2|}. \tag{2.33}$$

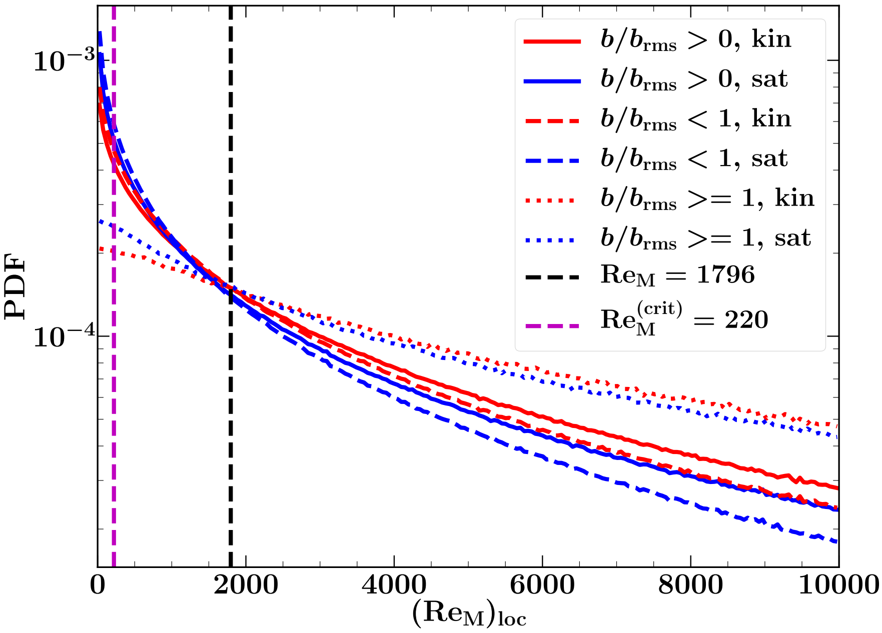

Figure 2.33: As Fig. 2.32 but for $\mathrm{Re_M} = 1796$.

Another way is to define it directly via the induction equation at each point, i.e.,

$$(\mathrm{Re_M})_{\rm loc} = \frac{|\nabla \times (\mathbf{u} \times \mathbf{b})|}{|\eta \nabla^2 \mathbf{b}|}. \tag{2.34}$$

We confirm that $(\mathrm{Re_M})_{\rm loc}$ calculated using Eq. (2.33) and Eq. (2.34) give numerically very similar values. Fig. 2.32 and Fig. 2.33 show the total and conditional PDFs of the local magnetic Reynolds number in the kinematic and saturated stages. $(\mathrm{Re_M})_{\rm loc}$ varies from values much less than to much greater than $\mathrm{Re_M^{(crit)}}$ in both kinematic and saturated stages. Thus, magnetic field grows and decays in different parts of the volume but remains in a statistically steady state overall. On saturation, both Fig. 2.32 and Fig. 2.33 show that $(\mathrm{Re_M})_{\rm loc}$ decreases. The mean value of the local magnetic Reynolds number over the entire domain does decreases but not to the critical value. This effectively implies enhanced diffusion, which leads to the saturation of the fluctuation dynamo.

To summarize, the fluctuation dynamo saturates due to both a reduction in the amplification of magnetic field and an enhancement in the magnetic field diffusion. The amplification is reduced because of the increased alignment between the velocity and magnetic fields. Furthermore, the current density and magnetic field are also statistically better aligned in the saturated stage. The decrease in the magnetic field amplification is due to a reduction in both the stretching and compression of magnetic field lines by the velocity field. The magnetic

Table 2.2: Four Minkowski functions V_0, V_1, V_2, V_3, their geometrical interpretation and definitions for a three dimensional structure. $\mathrm{d}V$ is the volume element, $\mathrm{d}S$ is the surface element, and κ_1 and κ_2 are the principle curvatures of the surface of a structure.

Minkowski functional	Geometric interpretation	Expression
V_0	Volume	$\int\int\int \mathrm{d}V$
V_1	Surface area	$(1/6)\int\int \mathrm{d}S$
V_2	Integral mean curvature	$(1/6\pi)\int\int(\kappa_1+\kappa_2)\,\mathrm{d}S$
V_3	Euler characteristics	$(1/4\pi)\int\int(\kappa_1\kappa_2)\,\mathrm{d}S$

field diffusion is enhanced overall since the local magnetic Reynolds number, though varying over a wide range from much less than to much higher than the critical value, statistically decreases within the volume.

2.5 Magnetic field morphology

2.5.1 Minkowski functionals

As shown in Section 2.4.2, the magnetic field generated by a fluctuation dynamo is intermittent, i.e., it is concentrated in filaments, sheets and ribbons. To characterize the magnetic structures, we use the Minkowski functionals (Minkowski, 1903). These measures have already been used to study structures in numerical simulations and observational data. In existing numerical studies, they are used to study the large–scale structure of the universe (Schmalzing et al., 1999), magnetic structures generated by a kinematic fluctuation dynamo (Wilkin et al., 2007), vorticity structures in hydrodynamic turbulence (Leung et al., 2012) and current sheets in magnetohydrodynamic turbulence (Zhdankin et al., 2014). Minkowski functionals and quantities derived from them are also used to study observational data such as cosmic microwave background anisotropy maps (Schmalzing & Gorski, 1998), galaxy surveys (Bharadwaj et al., 2000) and neutral hydrogen density in the interstellar medium of our galaxy (Makarenko et al., 2015). The morphology of a d–dimensional structure can be described by $d+1$ Minkowski functionals. In three dimension, there are the four Minkowski functionals, described in Table 2.2. We calculate the Minkowski functionals using Crofton's formulae (Crofton, 1868; Legland et al., 2011) and then calculate the typical length scales (l_1, l_2, l_3) of a three dimensional structure as (Sahni et al., 1998; Schmalzing et al., 1999)

$$l_1 = \frac{V_0}{2V_1}, \quad l_2 = \frac{2V_1}{\pi V_2}, \quad l_3 = \frac{3V_2}{4V_3}. \tag{2.35}$$

Table 2.3: Minkowski functionals V_0, V_1, V_2, V_3, their analytical expression (Schmalzing et al., 1999) and values calculated using analytical expression and obtained numerically, for a sphere with the centre at (π, π, π) of radius $r = \pi$ in a periodic box of size $(2\pi)^3$ with 128^3 grid points.

Minkowski functional	Expression	Calculated	Numerical
V_0	$(4/3)\pi r^3$	129.11	129.87
V_1	$(2/3)\pi r^2$	20.59	20.67
V_2	$(4/3)r$	4.18	4.19
V_3	1.0	1.0	1.0

We associate the smallest length scale with the thickness T of the structures, the next largest length scale with the width W and the largest length scale with the length L, i.e., if $l_1 \leq l_2 \leq l_3$, then $T = l_1, W = l_2$ and $L = l_3$. The thickness, width and length can be further used to obtain dimensionless measures of the shape of a structure: planarity p and filamentarity f, given by

$$p = \frac{W - T}{W + T}, \quad f = \frac{L - W}{L + W}. \tag{2.36}$$

By definition, $0 \leq p$ and $f \leq 1$. We first test the algorithm for simple shapes for which the planarity and filamentarity are known.

Planarity and filamentarity for simple shapes

For simple shapes, planarity and filamentarity are known: $p \approx f \approx 0$ for a sphere, $p \approx 0, f \approx 1$ for a filament and $p \approx 1, f \approx 0$ for a pancake. To test the numerical calculations, we generate simple three-dimensional spheroidal shape,

$$\alpha(x - a)^2 + \beta(y - b)^2 + (z - c)^2 \leq r^2; \quad \alpha, \beta \geq 1, \tag{2.37}$$

where (a, b, c) is the centre of the spheroid, r is the radius, and α and β are the parameters which control the shape. We generate structures of this type in a cubic domain. We set 1 if the left–hand side of Eq. (2.37) is less than or equal to r^2 and 0 otherwise. We then vary parameters α and β to create various shapes. For $\alpha = \beta = 1$, the structure is a sphere of a radius r. All four Minkowski functionals are known for a sphere (Schmalzing et al., 1999) and their corresponding values are given in Table 2.3. Fig. 2.34a shows a few structures for various α and β. On increasing β, but keeping α constant at 1, a sphere ($\alpha = \beta = 1$) changes to a pancake ($\alpha = 1, \beta \gg 1$). This is shown by the solid line in Fig. 2.34b. Then, increasing α, but keeping $\beta \gg 1$ constant, we obtain a filament ($\alpha = \beta \gg 1$). This shown by the dashed line in Fig. 2.34b. Finally, decreasing both α and β, we return to a sphere,

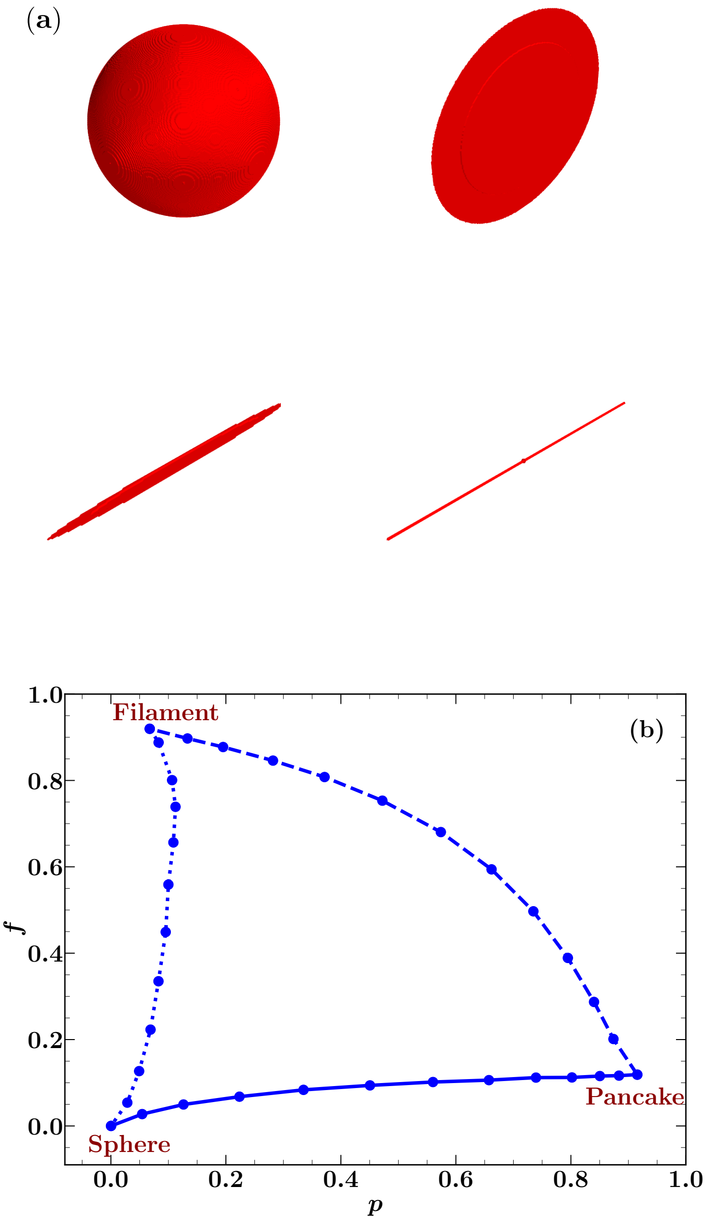

Figure 2.34: (a)The iso-surfaces of simple structures, showing the transition from a sphere to a filament. Planarity and filamentarity (p, f) for these shapes are: sphere $(2 \times 10^{-4}, 3 \times 10^{-5})$, pancake $(0.92, 0.12)$, thick filament $(0.47, 0.75)$ and thin filament $(0.07, 0.92)$. (b) The (p, f) plane showing the transition between various shapes as α and β are varied in Eq. (2.37) (the Blaschke diagram). Solid line: $\alpha = 1$ constant, β increasing, the transition from a sphere to a pancake. Dashed line: α increasing, $\beta \gg 1$ constant, the transition from a pancake to a filament. Dotted line: $\alpha \gg 1$ decreasing to $\alpha = 1$, $\beta \gg 1$ decreasing to $\beta = 1$, transition from a filament to a sphere.

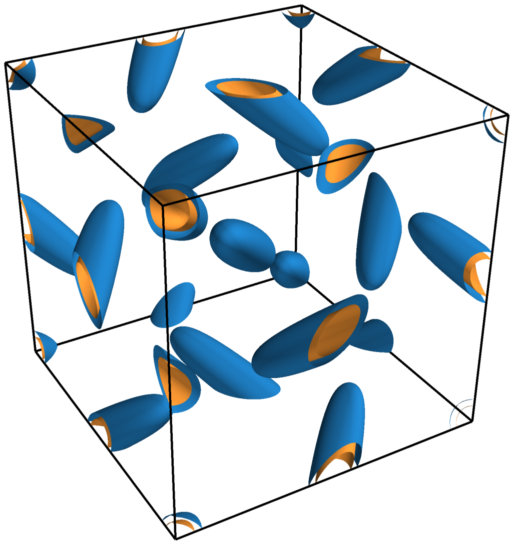

Figure 2.35: Isosurfaces of $b/\,b_{\rm rms} = 2$ (blue) and $b/\,b_{\rm rms} = 3$ (yellow) for the magnetic field generated by using the W flow (Eq. (2.5)) with $\mathrm{Re_M} = 314$ in a periodic box of non-dimensional size $(2\pi)^3$ with 256^3 grid points.

which is represented by the dotted line in Fig. 2.34b. The calculations of p and f for simple shapes on a cubic grid agree with our expectations and confirm the reliability of the numerical algorithm.

2.5.2 Structures in kinematic dynamos

We now consider the size and shape of magnetic structures generated by kinematic fluctuation dynamos. First, we calculate these for magnetic structures generated by the W flow (Eq. (2.5)), shown in Fig. 2.35. The structures are of ellipsoidal shape and are smaller in size for higher magnetic field levels.

The length, width and thickness of magnetic structures as functions of the field strength ($\alpha = b/\,b_{\rm rms}$) is shown in Fig. 2.36a. All three length scales decrease as α increases and the rate of decrease is roughly the same for all of them. Fig. 2.36b shows the planarity and filamentarity as functions of α. The filamentarity increases as the field strength increases but the planarity remains roughly the same. This can also be seen from Fig. 2.35, where structures with $\alpha = b/\,b_{\rm rms} = 3$ (shown in yellow) are embedded within structures with $\alpha = b/\,b_{\rm rms} = 2$ (shown in blue). Their planarity is roughly the same but the structure with $\alpha = 3$ is more filamentary than that with $\alpha = b/\,b_{\rm rms} = 2$.

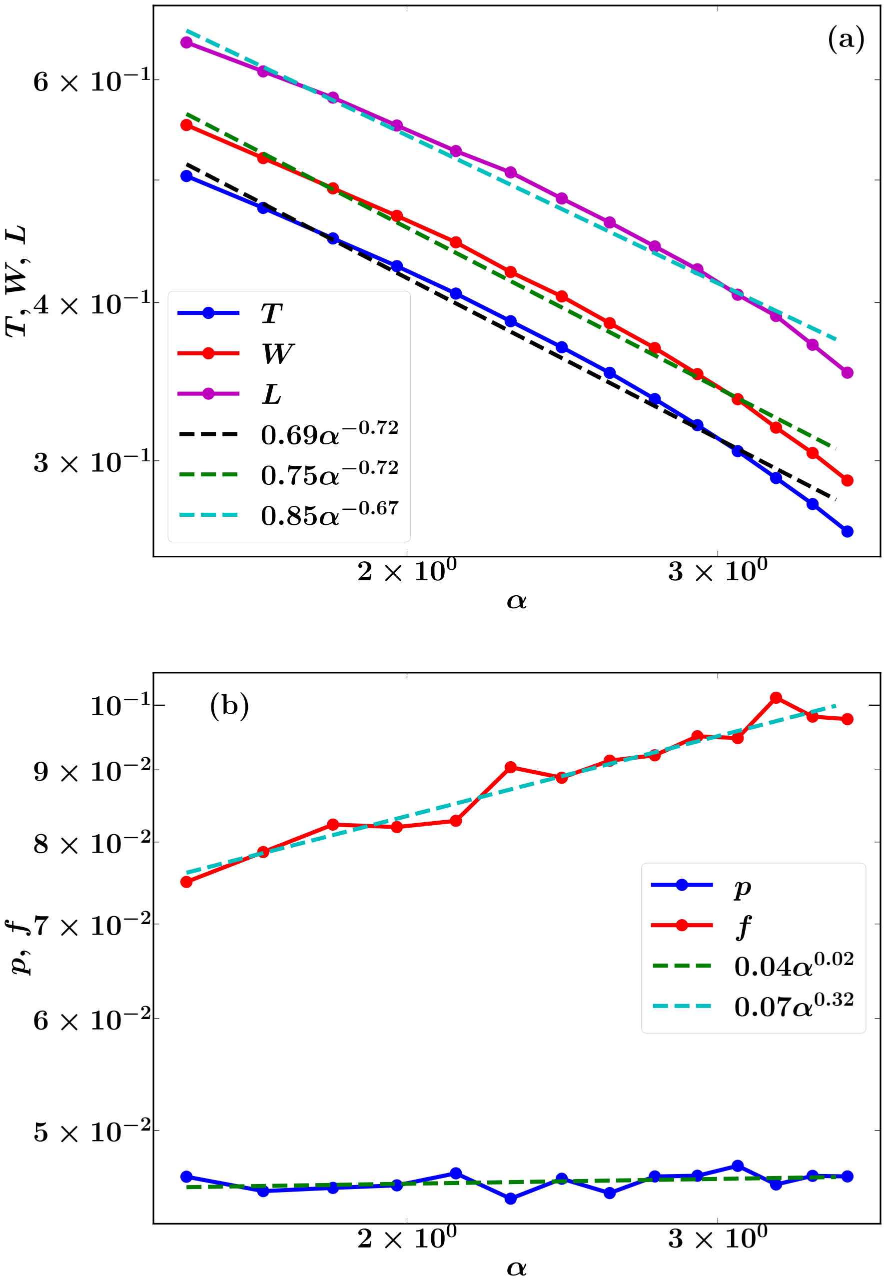

Figure 2.36: (a) Thickness T, width W and length L of magnetic structures obtained using the W flow as a function of the level of magnetic field $\alpha = b/b_{\rm rms}$. All three dimensions decrease as magnetic field strength (α) increases and at approximately the same rate. (b) Planarity p and filamentarity f for those structures as a function of the magnetic field strength level α. $f > p$, so the structures are filamentary. Also, p roughly remains constant as α increases but f increases. This can be confirmed in qualitative terms by a visual inspection of Fig. 2.35.

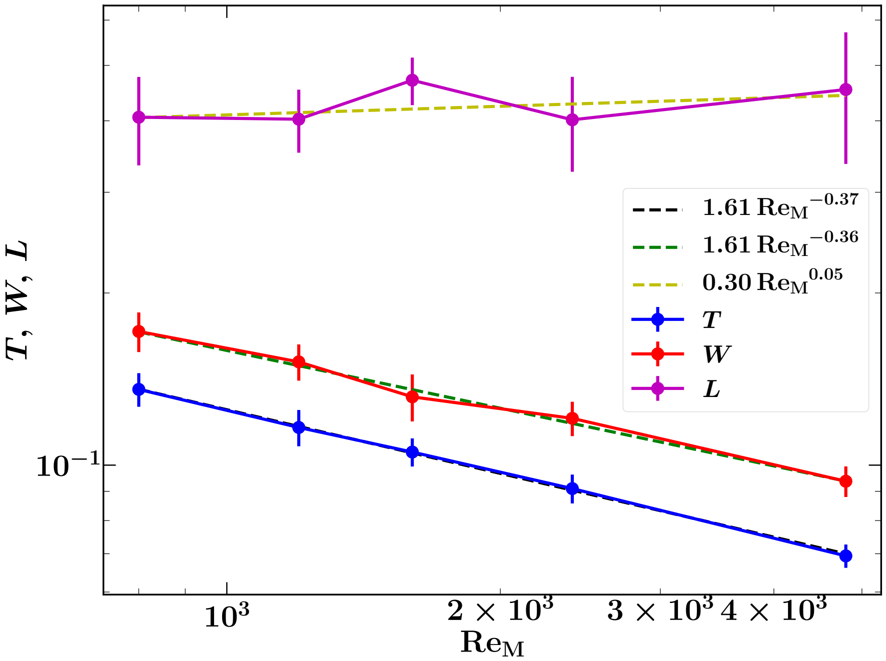

Figure 2.37: Average length (L), thickness (T) and width (W) of magnetic structures generated by a kinematic fluctuation dynamo with the KS flow as functions of $\mathrm{Re_M}$. The average is calculated over 30 magnetic field levels between $\alpha = b/\,b_\mathrm{rms} = 2.5$ and $\alpha = b/\,b_\mathrm{rms} = 4.5$. The length roughly remains constant as $\mathrm{Re_M}$ changes. The other two length scales, T and W, decrease as $\mathrm{Re_M}$ increases, approximately as $\mathrm{Re_M^{-0.4}}$.

Next, we calculate magnetic structures produced by a kinematic fluctuation dynamo with the KS flow. Fig. 2.12 and Fig. 2.13 show the magnetic field produced by the KS flow at $\mathrm{Re_M} = 4800$. To determine the dependence of these scales on $\mathrm{Re_M}$, we average them over a range of magnetic field levels $\alpha = b/\,b_{\mathrm{rms}}$ for each $\mathrm{Re_M}$. Fig. 2.37 shows the average length, width and thickness as functions of $\mathrm{Re_M}$. The largest length scale, L, is independent of $\mathrm{Re_M}$. The length of the structures depends on the driving scale of the flow since the magnetic correlation function of the fastest growing dynamo mode decreases exponentially after that scale (Zeldovich et al., 1990; Subramanian, 1999). Even in the folded structure of magnetic field (Schekochihin et al., 2002, 2004) shown in Fig. 2.23, the length of folds is of the order of the viscous scale, which is independent of the $\mathrm{Re_M}$. Thus, the length in Fig. 2.37 remains constant for all $\mathrm{Re_M}$ (given that the underlying flow is the same). This result agrees with the earlier work of Wilkin et al. (2007). The second largest length scale, the width of the magnetic structures, W, is actually the dissipation scale l_η which can be obtained by balancing the rate of magnetic dissipation with the local shearing rate (Subramanian, 1998). An estimate of W can be obtained as follows: $\eta/W^2 \simeq u_{\mathrm{rms}}/l_0$, where η is the magnetic resistivity, u_{rms} is the rms turbulent velocity and l_0 is the driving scale of the turbulence. This gives $W \simeq l_0(\eta/\,u_{\mathrm{rms}}l_0)^{1/2} = l_0\mathrm{Re_M^{-0.5}}$. In Fig. 2.37, the width of magnetic structures decreases as $\mathrm{Re_M^{-0.4}}$ which is close to this $\mathrm{Re_M}$ dependence. The difference from expected scaling can be attributed to the limited numerical resolution. This result does not really agree with Wilkin et al. (2007) who obtain $W \propto \mathrm{Re_M^{-0.55}}$. For the smallest length scale, the thickness of the structure T, we find $\mathrm{Re_M}$ dependence to be very similar to that for W. This results does not agree with Wilkin et al. (2007), where they obtained $T \propto \mathrm{Re_M^{-0.75}}$. They justify this scaling by balancing the induction and dissipation of the magnetic field. However, such a scaling is valid only for $\mathrm{Pr_M} \lesssim 1$ and our runs with KS flow are of $\mathrm{Pr_M} \gg 1$ (effective $\mathrm{Re} \approx 16$ and $\mathrm{Re_M^{(crit)}} = 750$). The difference in $\mathrm{Re_M}$ scalings with Wilkin et al. (2007) is probably due to following two reasons. First, our simulations are at a higher resolution (512^3) as compared to theirs (128^3) and thus magnetic structures, especially at higher $\mathrm{Re_M}$, are better resolved in our case. Second and most importantly, Wilkin et al. (2007) considers values of $\mathrm{Re_M}$ which are both lower and higher than $\mathrm{Re_M^{(crit)}}$, whereas we only consider $\mathrm{Re_M} > \mathrm{Re_M^{(crit)}}$. This is because we strongly believe that those two regimes $\left(\mathrm{Re_M} < \mathrm{Re_M^{(crit)}} \text{ and } \mathrm{Re_M} \geq \mathrm{Re_M^{(crit)}}\right)$ are physically different and must not be considered together to characterize the length scales of magnetic structures as functions of $\mathrm{Re_M}$.

Table 2.4: Parameters of various runs for the nonlinear fluctuation dynamo in a numerical domain of $(2\pi)^3$ in size with 512^3 mesh points. In all cases, the forcing scale is $k_{\rm F} \approx 5$, the forcing amplitude is $F_0 \approx 0.02$ and the hydrodynamic viscosity is $\nu = 4 \times 10^{-4}$. The magnetic diffusivity η, the rms velocity in the saturated stage $u_{\rm rms}$, the Reynolds number Re, the magnetic Reynolds number $\rm Re_M$, the magnetic Prandtl number $\rm Pr_M$ and the critical magnetic Reynolds number $\rm Re_M^{(crit)} (\approx 220 Pr_M^{-1/2})$ are given.

η	$u_{\rm rms}$	Re	$\rm Re_M$	$\rm Pr_M$	$\rm Re_M^{(crit)}$
4×10^{-4}	0.11	346	346	1.00	220
3×10^{-4}	0.11	346	461	1.33	191
2×10^{-4}	0.10	314	628	2.00	156
1×10^{-4}	0.09	283	1131	4.00	110
7.5×10^{-5}	0.09	283	1508	5.33	95
5×10^{-5}	0.09	283	2261	8.00	78

2.5.3 Structures in nonlinear dynamos

In this section, we consider the magnetic structures in the saturated stage with the aim to describe how the nonlinearity affects magnetic structures and to check whether the analysis of the shape and size of magnetic structures provides any additional insight into the saturation mechanism. For this study, we use runs with parameters given in Table 2.4. We make sure the flow is roughly the same for all $\rm Re_M$ and choose $k_{\rm F} \approx 5$, so there is a sufficient number of magnetic structures within the volume.

Fig. 2.38a shows the length, thickness and width of magnetic structures obtained by averaging over 30 values of threshold magnetic field strengths ($\alpha = b/\, b_{\rm rms}$) ranging from $\alpha = 2.5$ to $\alpha = 4$. Based on the arguments given in the Section 2.5.2, at least for the kinematic stage, we would expect that the length will remain constant with $\rm Re_M$ and other two scales will decrease as $\rm Re_M^{-0.5}$. As seen in Fig. 2.38a, the length remains roughly constant initially but then increases slightly after $\rm Re_M \approx 600$ and again remains roughly constant. This is due to the decrease in the Reynolds number Re as can be seen from Table 2.4. The other two scales decrease as $\rm Re_M^{0.5}$. All three scales are larger in the saturated stage than in the kinematic stage. This suggests that the magnetic structures become larger as the magnetic field saturates. This is also the reason that the magnetic field correlation length scale increases as the field saturates (also shown in Table 2.1). The $\rm Re_M$ scaling is roughly the same for both the kinematic and saturated stages. Fig. 2.38b shows the planarity and filamentarity of magnetic structures as functions of $\rm Re_M$. The filamentarity is always higher than the planarity and thus the magnetic structures are more like filaments in both the kinematic and saturated stages. Initially, as $\rm Re_M$ increases, the filamentarity increases and the planarity decreases. Then, after a certain

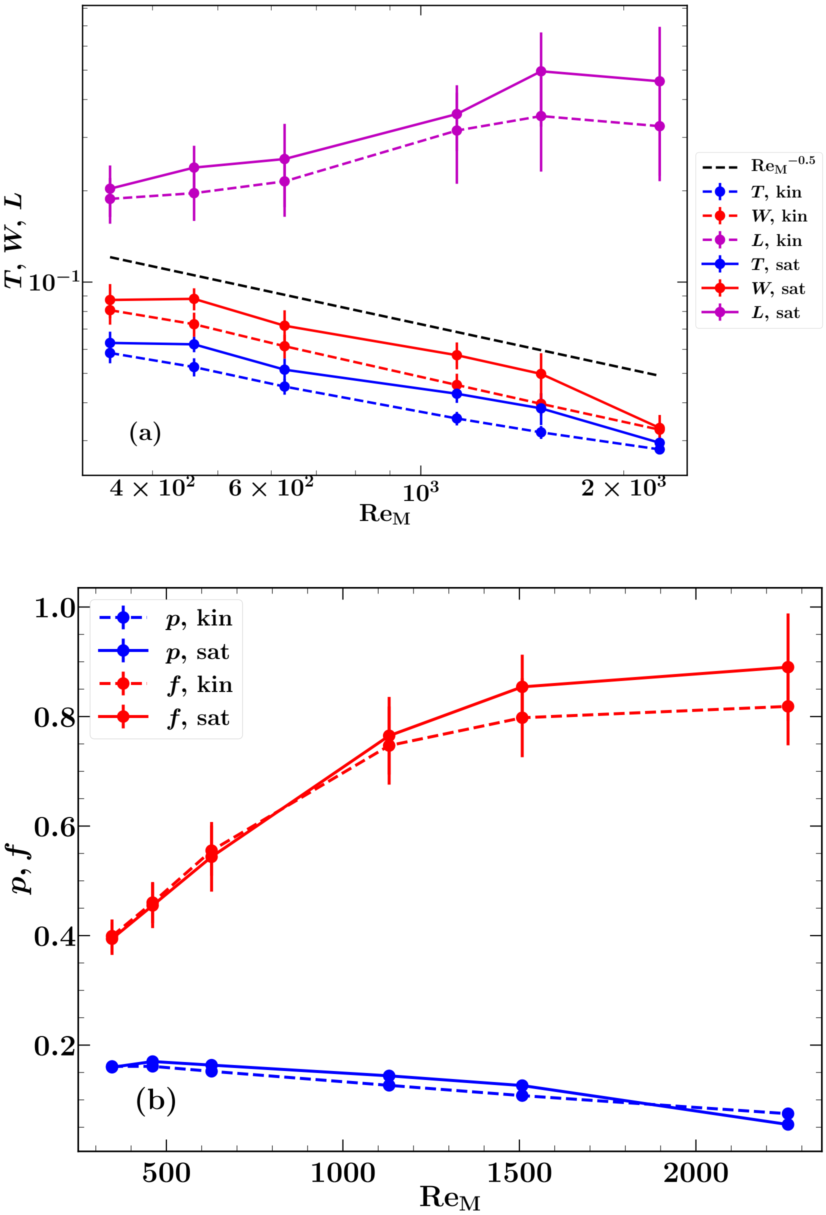

Figure 2.38: (a) Average length (L), thickness (T) and width (W) of magnetic structures in the kinematic (dashed, color) and saturated stages (solid, color) of the nonlinear fluctuation dynamo as functions of $\mathrm{Re_M}$. The length of the structures L roughly remains the same with $\mathrm{Re_M}$. The slight increase in the length after $\mathrm{Re_M} \approx 600$ is because of the decrease in Re (see Table 2.4). The width and thickness of the magnetic structures both decrease as $\mathrm{Re_M^{-0.5}}$. The $\mathrm{Re_M}$ dependence of the size of the structures is approximately the same in both the kinematic and saturated stages. (b) Planarity (p) and filamentarity (f) of the magnetic structures functions of $\mathrm{Re_M}$ for the kinematic (dashed, color) and saturated (solid, color) stages. As $\mathrm{Re_M}$ increases, the filamentarity increases and the planarity decreases but they seem to approach an asymptotic value after $\mathrm{Re_M} \approx 1200$. The trend with respect to $\mathrm{Re_M}$ is the same for both the kinematic and saturated stages.

$\mathrm{Re_M}$ (≈ 1200 in Fig. 2.38b), the filamentarity approaches and planarity seem to approach an asymptotic value. The asymptotic nature of planarity and filamentarity needs to be further confirmed with runs at a higher resolution and at higher values of $\mathrm{Re_M}$ but based on the trend in Fig. 2.38b, they seem to approach a near-asymptotic value. This would suggest that, even at high $\mathrm{Re_M}$, the magnetic structures with strength considerably higher than the rms value have significant size ($f_{\mathrm{Re_M}\to\infty} \neq 1$, $p_{\mathrm{Re_M}\to\infty} \neq 0$ and $L \propto \mathrm{Re_M^0}$, thus W and T are always greater than zero) and occupy a significant fraction of the volume. However, the dependence of these morphological measures on $\mathrm{Re_M}$ is the same for the kinematic and saturated stages and thus such a morphological analysis does not give any hint about the saturation mechanism of nonlinear fluctuation dynamos.

2.6 Discussion and conclusions

Magnetic fields generated by fluctuation dynamos are spatially intermittent, and the intermittency decreases as the field saturates. First, we studied the nonlinear state of the fluctuation dynamo and showed that the magnetic field saturation is due to a decrease in the field amplification and a corresponding increase in the field diffusion. Both the stretching and compression of magnetic field lines, that lead to amplification of magnetic fields, are reduced on saturation. The local magnetic Reynolds number $(\mathrm{Re_M})_{\mathrm{loc}}$ decreases slightly overall confirming that the diffusion of magnetic field is also enhanced on saturation. However, $(\mathrm{Re_M})_{\mathrm{loc}}$ varies from values much smaller to much larger than $\mathrm{Re_M^{(crit)}}$ throughout the volume and thus models which predict $\mathrm{Re_M} \to \mathrm{Re_M^{(crit)}}$ on saturation are probably not true. Next, we have studied the morphology of magnetic structures in the dynamo-generated fields. The structures are of a larger size in the saturated stage as compared to the kinematic stage. In both cases, the largest length scale is independent of $\mathrm{Re_M}$ and the other two scales decrease as $\mathrm{Re_M^{-0.5}}$. The planarity and filamentarity seem to approach an asymptotic value as $\mathrm{Re_M}$ increases and thus the magnetic field generated by a fluctuation dynamo always occupies a significant fraction of the volume in astrophysical systems.

Chapter 3

Cosmic ray diffusion in intermittent magnetic fields

The propagation of cosmic rays in turbulent magnetic fields is, on average, a diffusive process driven by the random walk of magnetic field lines and the scattering of the charged particles by random magnetic fluctuations. As described in Chapter 2, interstellar magnetic fields can be highly intermittent, consisting of intense magnetic filaments and ribbons. Previous studies of cosmic ray propagation have largely overlooked the intermittency in the magnetic field distribution, instead adopting Gaussian random magnetic fields. In this chapter, we use test-particle simulations to calculate cosmic ray diffusivity in intermittent magnetic fields generated by a kinematic fluctuation dynamo. The results are compared with those obtained from a non-intermittent magnetic field with an identical power spectrum. We show that the presence of magnetic intermittency significantly enhances diffusivity for low-energy cosmic ray particles, even in presence of a mean magnetic field. High-energy cosmic ray diffusion is unaffected by magnetic field intermittency. We demonstrate that the results can be interpreted in terms of a correlated random walk, which in turn implies that cosmic rays, when considered as a fluid in the continuum approximation, could be better modeled with the telegraph equation instead of the diffusion equation.

3.1 Introduction

Cosmic ray propagation in random magnetic fields is diffusive when averaged over time and length scales large compared to the Larmor scales. The cosmic ray diffusion is due to the combination of two processes: particles following tangled magnetic field lines and the scattering of particles by random magnetic fluctuations. Fig. 3.1 schematically shows the possible trajectories of a low-energy cosmic ray particle (a particle with Larmor radius less than the correlation length of the magnetic field). Fig. 3.1a shows a particle following a magnetic field line and the particle turns only when the magnetic field line turns, which is inevitable in tangled magnetic fields. The particle faithfully follows field lines and the diffusion of charged particles due to this transport is governed completely by the spread of field lines in turbulent magnetic fields. The turbulent nature of the magnetic field lines can be thought of as a 'random walk' process and the diffusion of particles due to this mechanism is known as Field Line Random Walk (FLRW) limit (Jokipii & Parker, 1969). The diffusion of particles due to FLRW is independent of the particle energy at least in this limit since it only depends on the trajectories of the gyrocenters of the particles and not their Larmor radius. Also, the particle's pitch angle (the cosine of the angle between the magnetic field and the velocity of the particle) is conserved in the FLRW limit. Fig. 3.1b shows a particle following the field line for some time but then it reverses its direction due to scattering, though still staying on the same field line. Such scattering referred to as parallel scattering, gives rise to diffusion along magnetic field lines, referred to as parallel diffusion. Fig. 3.1c shows a particle following a field line but then getting scattered and moving to another nearby field line. The diffusion because of this scattering is perpendicular to the field line and is referred to as perpendicular diffusion. The parallel and perpendicular scattering are caused by fluctuations in magnetic fields. These fluctuations can be due to the existing turbulence in the medium or can also be generated by cosmic rays themselves via the streaming instability (Kulsrud & Pearce, 1969; Skilling, 1975). Depending on the spatial structure of the random magnetic field, the parallel scattering can also induce perpendicular scattering and vice-versa. Unlike FLRW, both parallel and perpendicular scattering depends on the Larmor radius (or the energy of the particle). In such scattering events, the particle's pitch angle is not conserved and the changes in pitch angle can also be considered as a random walk process. Over a long time scale, the particle's pitch angle also diffuses.

High-energy particles (particles with Larmor radius greater than the correlation length of the magnetic field) scatter even before they complete one Larmor-orbit since they encounter a magnetic field which is uncorrelated with the magnetic field at its starting point. Thus they do

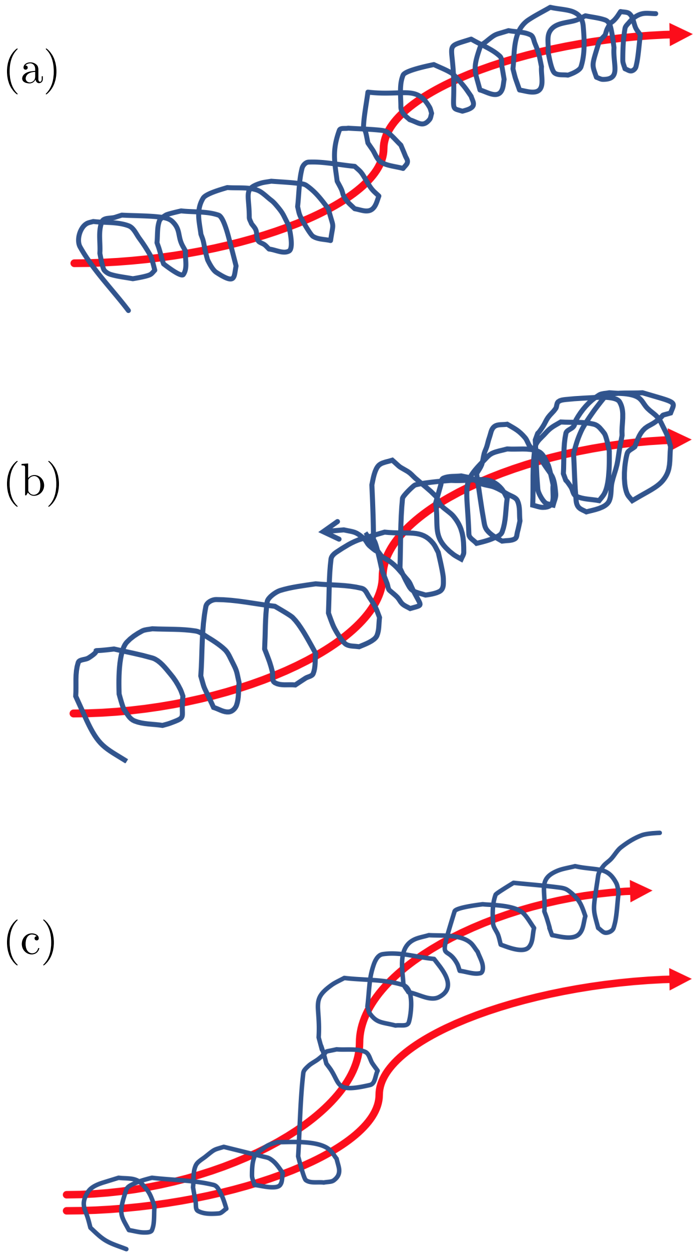

Figure 3.1: Trajectories of a low-energy particle in a turbulent magnetic field. a) Particle following a field line giving rise to Field Line Random Walk (FLRW) limit for an ensemble of particles over a long time. b) Particle following the field line initially but is then backscattered, eventually giving rise to diffusion along the magnetic field line for an ensemble of particles over a long time. c) Particle after following field line for some time, jumps to another field line, which over a long time for an ensemble of particles gives rise to diffusion perpendicular to the magnetic field line.

not follow any of the trajectories shown in Fig. 3.1. The process is a pure Brownian motion and over a long time with a large number of scatterings, diffusion sets in.

Throughout the discussion so far, we have only been considering the trajectory of a single particle. However, diffusion is a stochastic process and thus it is impossible to predict the exact trajectory of a single particle (or exact motion of a single field line in FLRW limit). We thus study the process for an ensemble of particles (or equivalently an ensemble of initial conditions for a single particle or equivalently different realizations of the magnetic field) and look at their behaviour, on averaging over the ensemble. Fig. 3.1 thus shows the trajectory of an 'average' particle in a random magnetic field.

The propagation of cosmic rays is sensitive to rather subtle details of the magnetic field in which they move (as can be inferred from Fig. 3.1). Almost all existing studies of cosmic ray propagation employ Gaussian random magnetic fields (for which the probability distribution function of each vector component is Gaussian and their first two moments are sufficient to completely describe it). The spectrum provides a complete statistical description of a Gaussian random magnetic field and the propagation of cosmic rays in an isotropic Gaussian random magnetic field has been the subject of many studies (Berezinskii et al., 1990; Michalek & Ostrowski, 1997; Giacalone & Jokipii, 1999; Casse et al., 2002; Schlickeiser, 2002; Parizot, 2004; Candia & Roulet, 2004; DeMarco et al., 2007; Globus et al., 2008; Shalchi, 2009; Plotnikov et al., 2011; Harari et al., 2014; Snodin et al., 2016; Subedi et al., 2017). For a given energy of a particle, the cosmic ray diffusivity in a Gaussian random field is completely determined by the correlation length of the magnetic field. However, radio (Gaensler et al., 2011; Haverkorn & Spangler, 2013; Jelić et al., 2015; Herron et al., 2017, 2018), submillimeter (Arzoumanian et al., 2011; Zaroubi et al., 2015; Planck Collaboration et al., 2016), and neutral hydrogen (Heiles & Troland, 2005; Kalberla & Kerp, 2016; Kalberla et al., 2017) observations suggest that the magnetic field in the ISM is strongly non-Gaussian, spatially intermittent and filamentary. Spatially, the magnetic field is essentially concentrated in structures (filaments, ribbons, and sheets) surrounded by weaker fluctuations. As explained in Chapter 2, such an intermittent field is also expected theoretically, as a result of turbulent dynamo action (Schekochihin et al., 2004; Wilkin et al., 2007) and random shock compression (Bykov & Toptygin, 1985, 1987; Bykov, 1988). The magnetic field generated by dynamo action in galaxy clusters is also likely to be intermittent (Ruzmaikin et al., 1989; Subramanian et al., 2006). In such an intermittent magnetic field, we expect that the propagation of charged particles is controlled not only by its correlation length (or its power spectrum) but also by the size and separation of the magnetic structures. The influence of such a complex magnetic field upon cosmic ray propagation is poorly understood. Existing theories based on the quasilinear approximation (Jokipii, 1966; Berezinskii et al., 1990; Schlickeiser, 2002), or its nonlinear extensions and other alternatives (Yan & Lazarian, 2002; Matthaeus et al., 2003; Shalchi, 2009), do not consider intermittency. Recent test particle simulations used magnetic fields obtained from simulations of MHD turbulence (Dmitruk et al., 2004; Reville et al., 2008; Beresnyak et al., 2011; Lynn et al., 2012; Weidl et al., 2015; Cohet & Marcowith, 2016). These models are free from the assumption of Gaussian statistics but they do not isolate explicitly any specific effects of magnetic intermittency. There have been no systematic attempts to examine the significance of realistic, physically realizable magnetic intermittency in three dimensions.

Our goal here is to identify and isolate the effects of magnetic field intermittency on cosmic ray diffusion (Shukurov et al., 2017). For this, we use test particle simulations (Giacalone & Jokipii, 1999; Casse et al., 2002; Desiati & Zweibel, 2014; Snodin et al., 2016), integrating the equation of motion for a large number of particles in a statistically isotropic and prescribed magnetic field. The magnetic field is obtained as a solution of the induction equation with a prescribed velocity field that drives the fluctuation dynamo (Section 2.3 in Chapter 2). This produces a physically realizable, intermittent magnetic field. The degree of intermittency depends on the magnetic Reynolds number $\mathrm{Re_M}$. As $\mathrm{Re_M}$ increases, the magnetic structures occupy a smaller proportion of the volume. The intermittency introduces two distinct particle propagation regimes, one within a magnetic structure and another between them. Cosmic ray particles are strongly scattered by the magnetic structures and are scattered comparatively less between them. By comparing particle diffusion in an intermittent field with that in a magnetic field lacking such a structure, but with an identical power spectrum, we demonstrate that intermittency can significantly enhance diffusion, and so diffusion of low-energy cosmic rays cannot be described in terms of the magnetic power spectrum alone.

3.2 Intermittent and non-intermittent magnetic fields

An intermittent magnetic field is obtained by solving the induction equation with prescribed velocity field (W and KS) as described in Section 2.3 of Chapter 2. The isotropic random magnetic field is denoted by $\mathbf{b}$. To explore the effects of a mean magnetic field, we also consider particle propagation in a magnetic field given by $\mathbf{B} = \mathbf{b} + \mathbf{B}_0$, where $\mathbf{B}$ is the total magnetic field and $\mathbf{B}_0$ is an imposed uniform magnetic field.

To identify the effects of magnetic intermittency on cosmic ray diffusion, we consider a Gaussian random magnetic field having the same power spectrum, $M(k)$, as the intermittent magnetic field. Such a Gaussian random field is obtained as follows: First, a spatial Fourier transform of the intermittent magnetic field is taken and then the phase of each complex mode is changed to a random number uniformly distributed between 0 and 2π. Then the inverse Fourier transform gives a Gaussian magnetic field (this is not strictly a Gaussian random field but due to randomization, it is way more Gaussian than the intermittent field) with unchanged $M(k)$, but with coherent structures destroyed (Chapter 7 in Biskamp, 2003; Waelkens et al., 2009; Snodin et al., 2013). The structural difference between intermittent and Gaussian random magnetic fields is illustrated in Fig. 3.2 and Fig. 3.3 which show the isosurfaces of magnetic field strength and Fig. 3.4 and Fig. 3.5 which show the magnetic fields in cross section through the middle of the numerical domain. The intermittent fields (Fig. 3.2a, Fig. 3.3a, Fig. 3.4a and Fig. 3.5a) contain magnetic structures where the magnetic field is concentrated whereas the corresponding Gaussian fields (Fig. 3.2b, Fig. 3.3b, Fig. 3.4b and Fig. 3.5b) lack any such structure. The spectra (Fig. 3.6) of the intermittent and randomized magnetic fields is identical but the probability distribution functions (PDFs) of a the individual components of the intermittent and randomized field shown in Fig. 3.7, are completely different. The intermittent field has long heavy tails in the PDFs, whereas the randomized field has a Gaussian probability distribution.

3.3 Cosmic ray propagation

The propagation of cosmic rays in random magnetic fields depends primarily on the ratio between the Larmor radius r_L of the particle gyration and the length scale of magnetic field variations, i.e., the correlation length l_b (related to the driving scale of turbulence l_0). The Larmor radius and frequency of a relativistic particle of the rest mass m_0 and charge q, travelling at a speed v_0 in a magnetic field of strength B, are given by

$$r_\mathrm{L} = \frac{\gamma m_0 c v_0}{qB} \qquad \text{and} \qquad \omega_0 = \frac{v_0}{r_\mathrm{L}}, \tag{3.1}$$

respectively, where $\gamma = (1 - v_0^2/c^2)^{-1/2}$ is the Lorentz factor, and c is the speed of light in vacuum.

We consider relativistic charged particles propagating in a static magnetic field, $\mathbf{B}(\mathbf{x})$. The trajectory of each particle satisfies

$$\frac{\mathrm{d}^2\mathbf{r}}{\mathrm{d}t^2} = \frac{v_0}{r_\mathrm{L}} \frac{\mathrm{d}\mathbf{r}}{\mathrm{d}t} \times \frac{\mathbf{B}}{B_\mathrm{rms}}, \tag{3.2}$$

where $\mathbf{r}$ is the particle's position, v_0 is its speed, $\mathbf{B}/\,B_\mathrm{rms}$ is the total magnetic field nor-

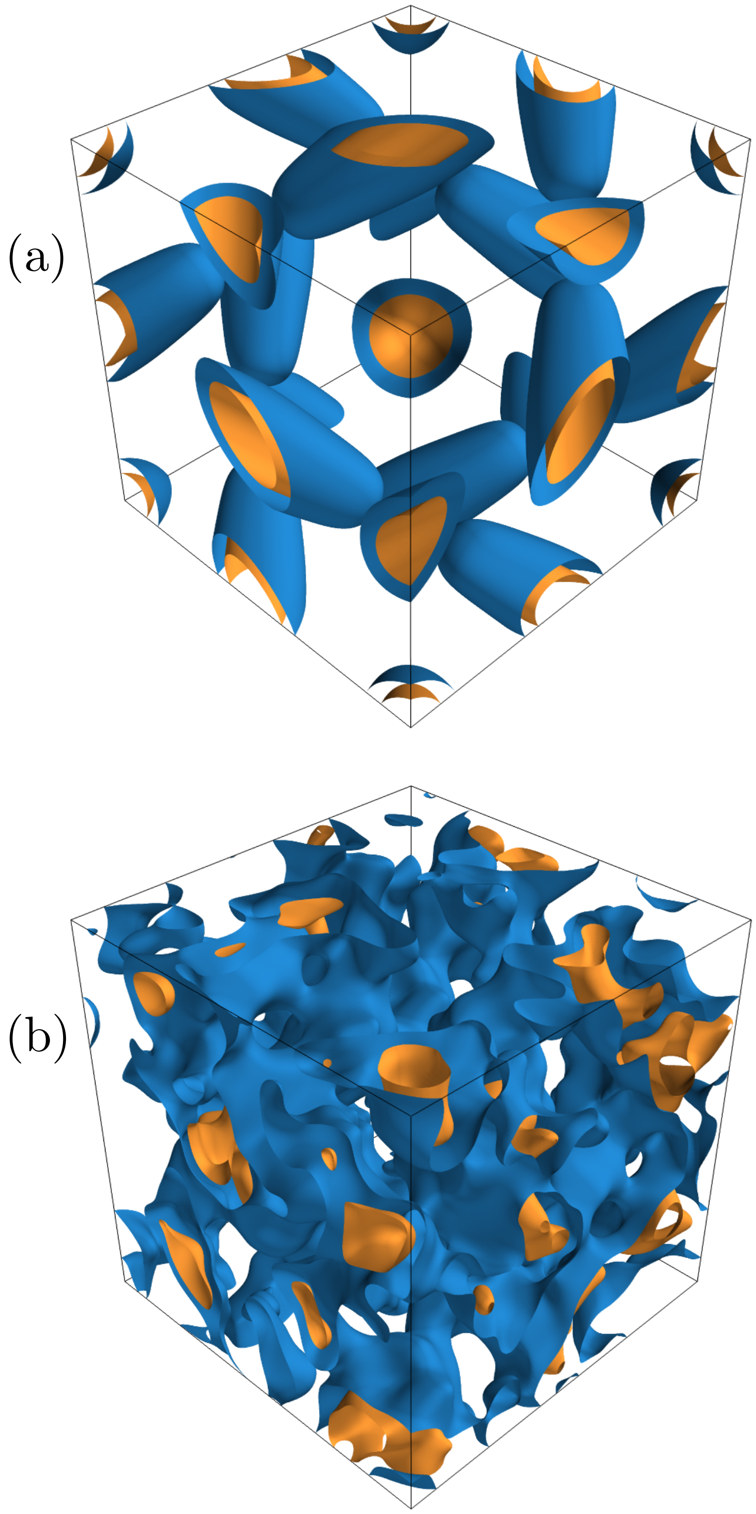

Figure 3.2: Isosurfaces of $b^2/b^2_{\mathrm{rms}} = 2.5$ (blue) and $b^2/b^2_{\mathrm{rms}} = 5$ (yellow) for the intermittent magnetic field at $\mathrm{Re}_{\mathrm{M}} = 314$ generated by the W flow (a) and for the same magnetic field after randomizing phases (b). Intermittent field shows filaments of fixed shape (a specific consequence of this choice of flow) whereas randomized field lacks such elongated structures.

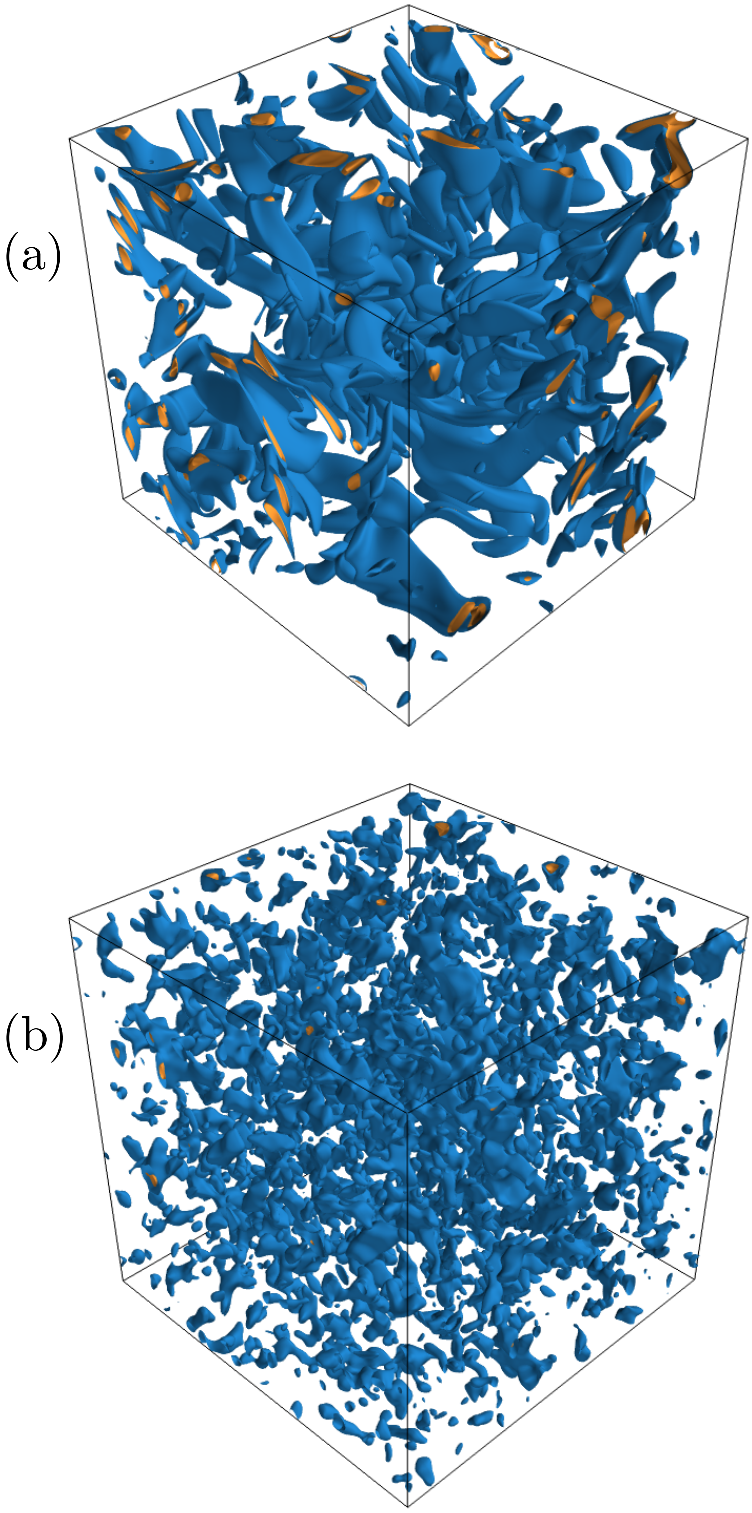

Figure 3.3: As Fig. 3.2 but now for the KS flow with $\mathrm{Re}_\mathrm{M} = 3182$. Intermittent field (a) shows filaments of various width, length, and thickness, whereas randomized (b) field lacks such structures.

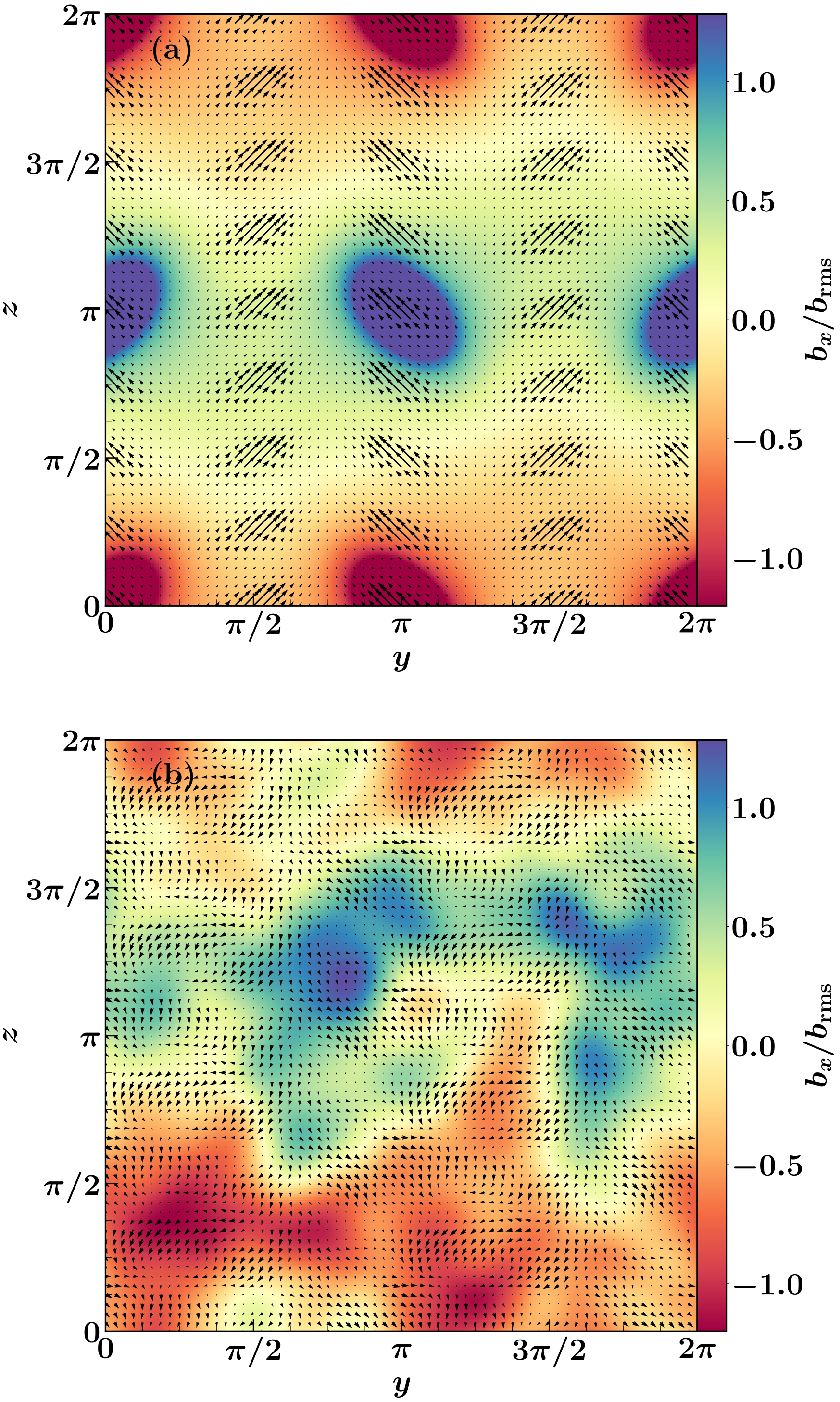

Figure 3.4: 2D cut in the yz–plane through the middle of the domain with vectors for $(b_y/\, b_{\rm rms}, b_z/\, b_{\rm rms})$ and colours showing the magnitude of $b_x/\, b_{\rm rms}$ for intermittent (a) and randomized (b) magnetic field generated using the W flow for $\mathrm{Re_M} = 314$. For intermittent magnetic field the colours are saturated for both positive and negative values to match the scale of the randomized field. The intermittent magnetic field is more ordered and stronger in the filaments, whereas the randomized field lacks such structures.

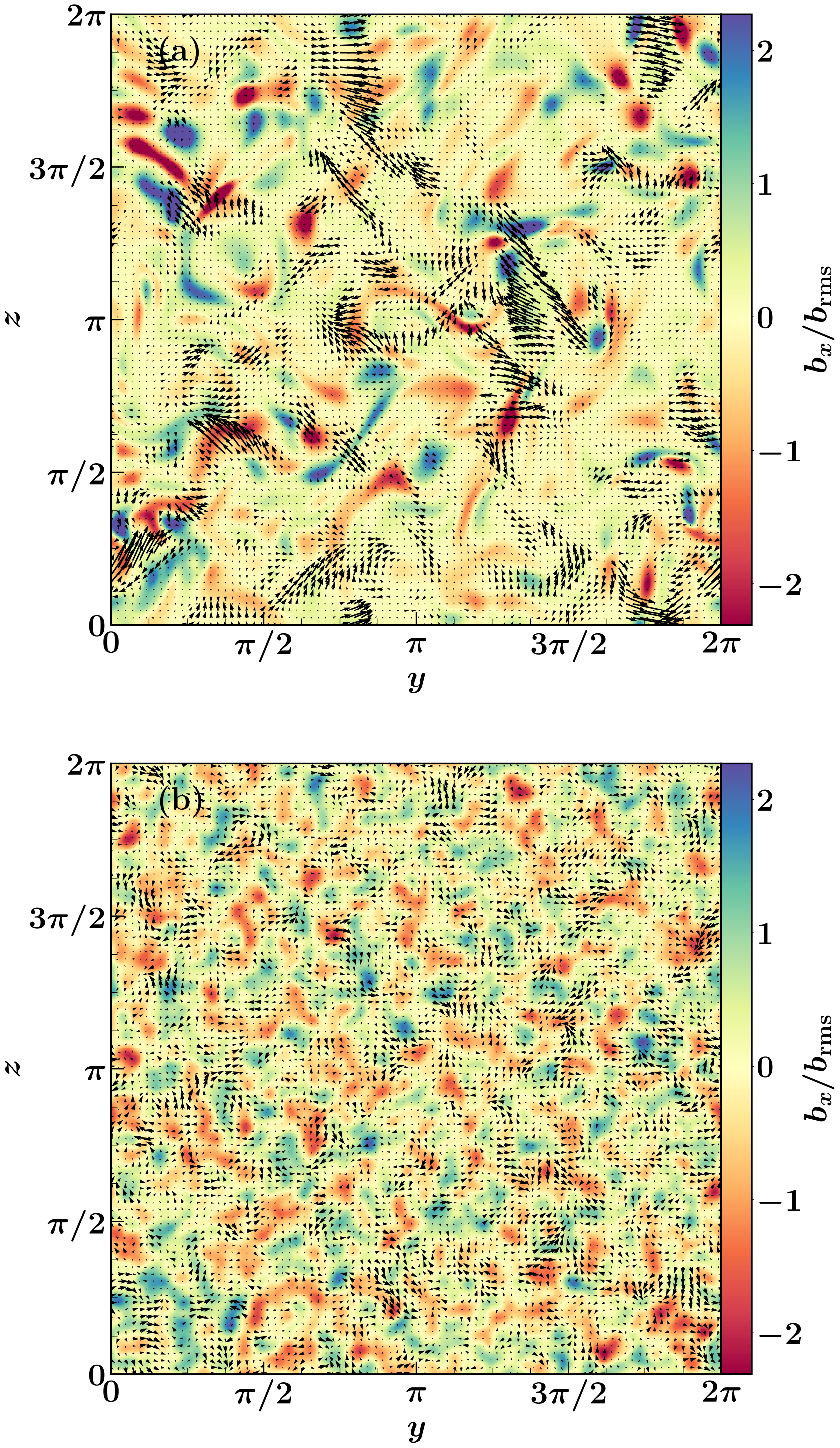

Figure 3.5: A Fig. 3.4 but now for the KS flow for $\mathrm{Re}_\mathrm{M} = 3182$. For intermittent magnetic field (a) the colours are saturated for both positive and negative values to match the scale of the randomized field (b) (see the x-axis of Fig. 3.7 for the actual difference in numbers). The randomized field lacks structures seen in the intermittent field.

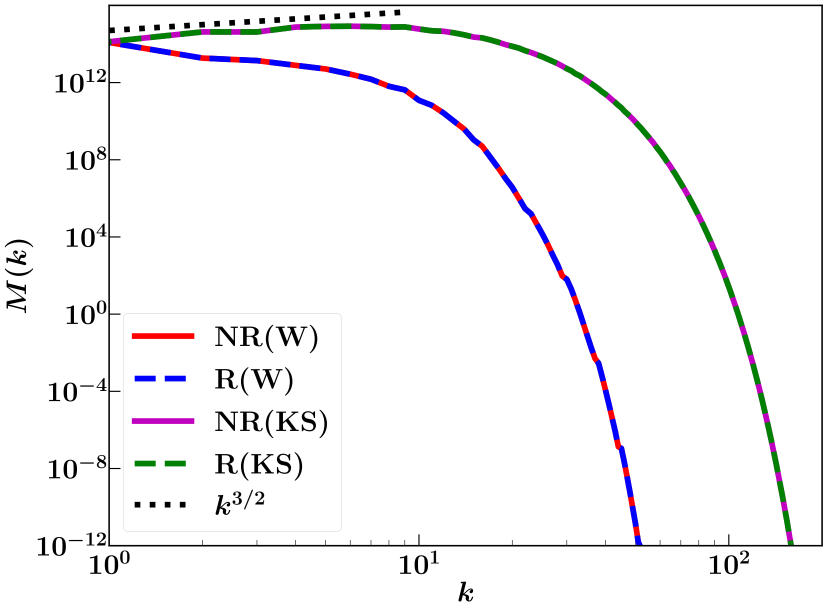

Figure 3.6: Spectra of intermittent NR (red, magneta) and randomized R (blue dashed, green dashed) magnetic fields generated using W flow ($\mathrm{Re_M} = 314$) and KS flow ($\mathrm{Re_M} = 1082$) respectively. For both flows, the spectra of intermittent and randomized magnetic fields is identical. For KS flow, the spectra agrees with the Kazantsev scaling (Kazantsev, 1968) $k^{3/2}$ (black dotted) power law spectrum at small wavenumbers. The scaling holds only for flows which are δ-correlated in time and only the KS flow is time dependent.

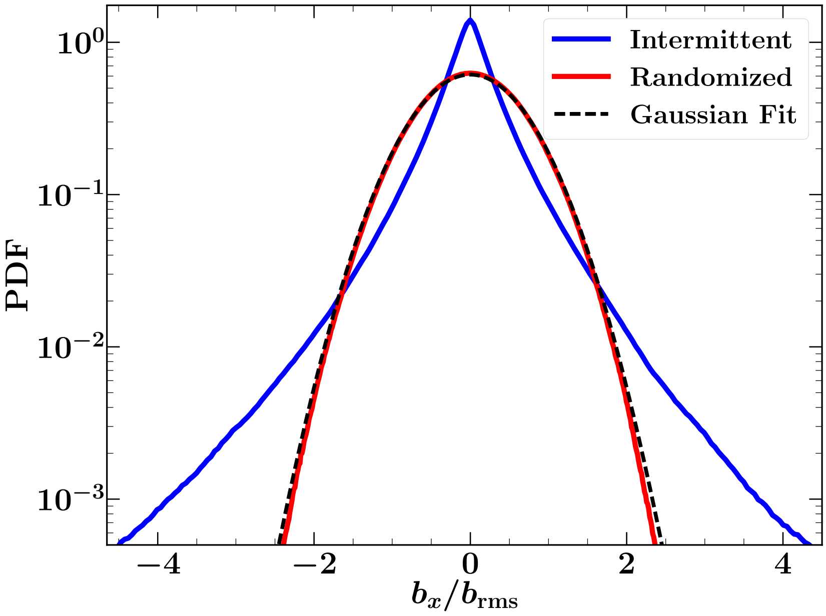

Figure 3.7: PDFs of $b_x/\,b_{\mathrm{rms}}$ for intermittent (blue) and randomized (red) magnetic field generated using the KS flow for $\mathrm{Re_M} = 3182$. Both have zero mean but the intermittent magnetic field has long tails, whereas the randomized field (obtained by Fourier phase randomization) has a Gaussian PDF (dashed).

malized to its rms value $B_{\rm rms}$, and $r_{\rm L}$ is the Larmor radius (defined with respect to $B_{\rm rms}$). The timescale over which interstellar magnetic fields change significantly is of the order of the eddy turnover time in interstellar turbulence, $10^7\,{\rm yr}$ (Beck et al., 1996). This timescale is longer than the (diffusive) confinement time of cosmic rays in galaxies, which is of the order of $10^6\,{\rm yr}$ (Berezinskii et al., 1990). It is therefore customary to neglect any time dependence of the magnetic field in Eq. (3.2) and, correspondingly, neglect any electric fields (Giacalone & Jokipii, 1999; Casse et al., 2002). This means that the speed of each particle remains constant. This is equivalent to neglecting particle acceleration to relativistic energies, a process physically distinct from diffusive particle propagation (which is the focus of this chapter). Since we consider static magnetic field, the diffusive reacceleration (Strong et al., 2007; Grenier et al., 2015), which is due to moving magnetic inhomogeneities, is also neglected.

We solve Eq. (3.2) numerically for an ensemble of cosmic ray particles ($\geq 10,000$ particles), all of the same speed v_0, but each of a random initial position and velocity direction. The initial conditions are chosen randomly, and are uniformly distributed over all positions and directions. For a given particle energy, we find the shortest Larmor time ($2\pi/\omega_0$) based on the maximum magnetic field strength in the domain and then fix the time step as $10^{-3}(2\pi/\omega_0)$, to ensure that we resolve all particle gyrations. We also check that the particle energy is conserved (to the accuracy of the numerical scheme) throughout the total propagation time T. For a given magnetic field configuration, the nature of the trajectories depends only on the parameter $r_{\rm L}/l_b$, a measure of the particle energy, as illustrated in Fig. 3.8. By construction, the static magnetic field through which the particle propagates is periodic in all three directions, with period $L = 2\pi$ (in numerical units, equivalent to the driving scale of the turbulence, l_0). Even though the magnetic field is periodic, the particle trajectories are not: they enter and leave the domain at different positions. There is an important distinction between the Eulerian frame of the computational domain and the Lagrangian frame of each particle. Whilst the magnetic field is periodic in the Eulerian sense, there is no periodicity in the magnetic field along each particle trajectory (however many times the particle enters and leaves the domain).

Fig. 3.8 shows the trajectories of particles of low (Fig. 3.8a) and high (Fig. 3.8b) energy in the intermittent magnetic field, respectively. The latter move faster (note the different axis scales in the two panels) and, at the scale of the left-hand panel, the trajectory of the higher-energy particle is nearly straight almost everywhere. Fig. 3.9 shows the corresponding trajectories in the randomized magnetic field (low and high energy particles are shown in Fig. 3.9a and Fig. 3.9b respectively). The trajectories in the randomized magnetic field

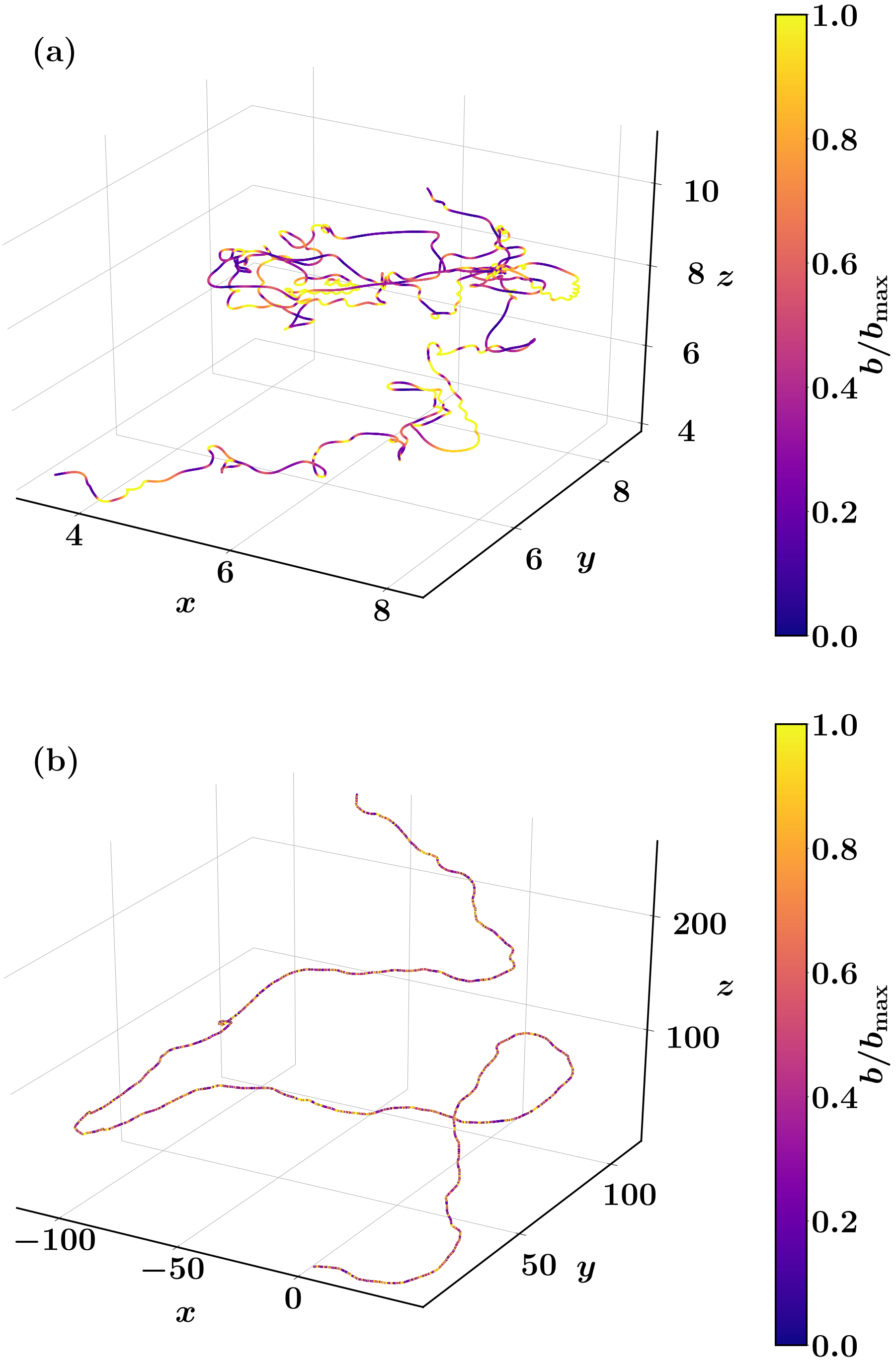

Figure 3.8: Single particle trajectories for $r_{\mathrm{L}}/l_b = 0.45$ (a) and 13 (b) in the intermittent magnetic field of Fig. 3.5a. Colours shows the strength of the magnetic field along the trajectory normalized to its maximum value along the part of trajectory shown. For $r_{\mathrm{L}}/l_b = 0.45$, the particle path is more tangled than for $r_{\mathrm{L}}/l_b = 13$ where the particle motion is almost ballistic between rare scattering events. Also note different spatial scales.

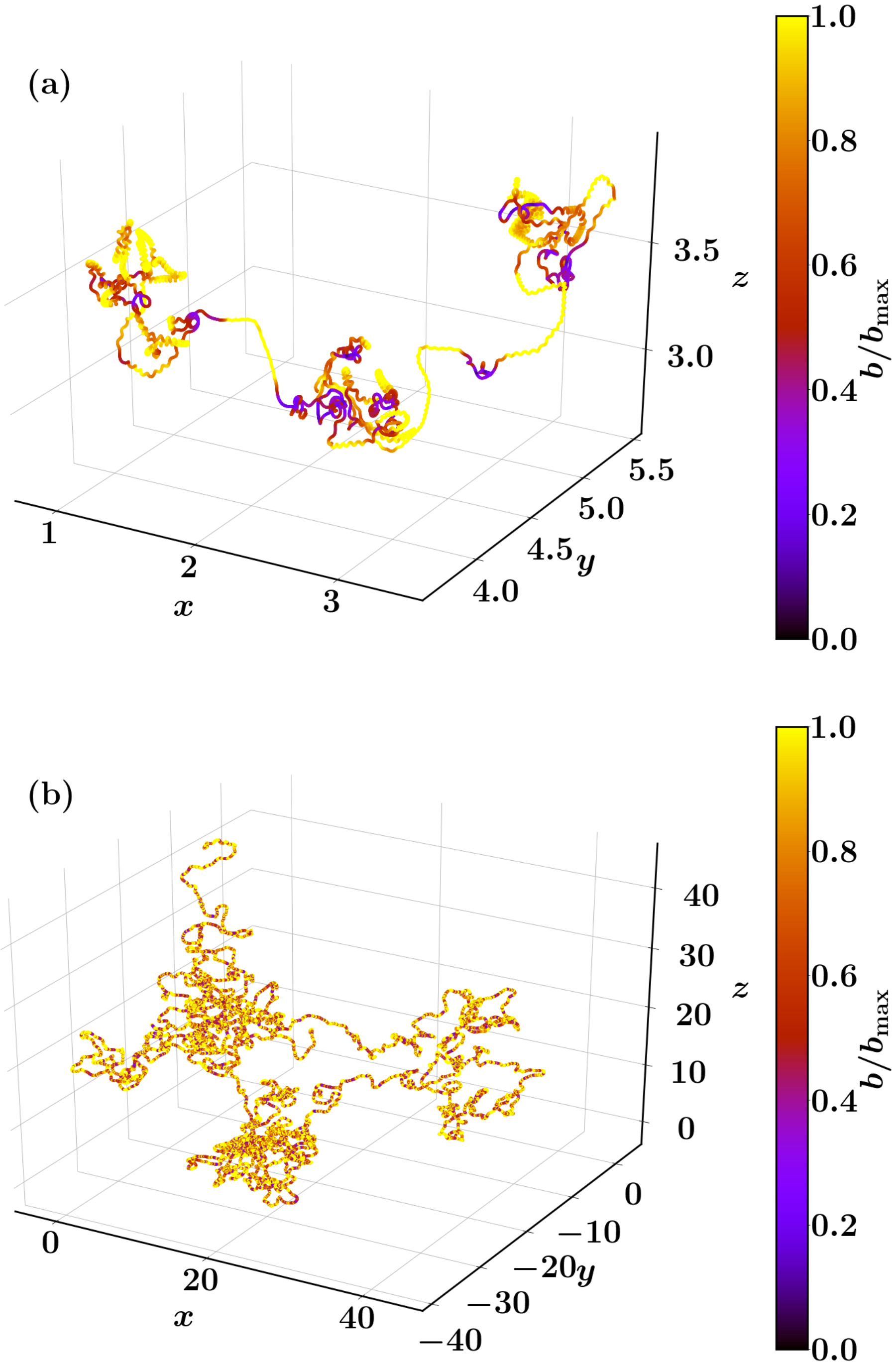

Figure 3.9: Same as Fig. 3.8 but for the randomized magnetic field. More scattering events are seen in these trajectories in comparison to the particle trajectories in the intermittent magnetic field.

visually show more frequent scattering events in comparison to that in the intermittent magnetic field. From this conclusion, we expect that the diffusion coefficient would be higher for intermittent magnetic fields.

A very high-energy particle, with $r_{\mathrm{L}} \gg l_b$, is typically deflected (or scattered) by only a small angle (of order l_b/r_{L}) from its initial path over a distance l_b and its trajectory is, therefore, rather insensitive to the structural properties of the magnetic field at scales smaller than r_{L}. By the central limit theorem, the statistical properties of an ensemble of cosmic ray particles become Gaussian after a large number of such deflections. Particles of smaller energies, $r_{\mathrm{L}} \lesssim l_b$, are more sensitive to the fine structure of the magnetic field, and it is not obvious how such structures would affect the cosmic ray diffusion. The aim of this chapter is to clarify this.

The random nature of the magnetic field makes the particle propagation diffusive at sufficiently large spatial and temporal scales. Without a mean field ($\mathbf{B}_0 = \mathbf{0}$), the propagation is isotropic. We therefore calculate the isotropic diffusion coefficient as,

$$\kappa = \lim_{t\to\infty} \kappa(t), \qquad \kappa(t) = \frac{1}{6t}\langle |\mathbf{r}(t) - \mathbf{r}(0)|^2 \rangle, \tag{3.3}$$

where $\mathbf{r}(t) = (x(t), y(t), z(t))$ is the particle position at time t and the angular brackets denote averaging over the ensemble of particles. In the presence of a mean magnetic field, the isotropic diffusion coefficient can be broken down into a parallel diffusion coefficient in the direction of the mean field and a perpendicular diffusion coefficient perpendicular to the mean field. For a mean field $\mathbf{B}_0$ directed along the x-axis, we define parallel and perpendicular diffusion coefficients as,

$$\kappa_{\parallel} = \lim_{t\to\infty} \frac{1}{2t}\langle \Delta x(t)^2 \rangle, \quad \kappa_{\perp} = \lim_{t\to\infty} \frac{1}{4t}\langle [\Delta y(t)^2 + \Delta z(t)^2] \rangle. \tag{3.4}$$

3.4 Effect of magnetic intermittency on cosmic ray diffusion

We first calculate the cosmic ray diffusion coefficient as a function of energy, r_{L}/l_0. Fig. 3.10 shows the dependence of the cosmic ray diffusion coefficient on r_{L}/l_0 for $B_0 = 0$. The energy dependence changes at $r_{\mathrm{L}}/l_0 \approx 1$. For $r_{\mathrm{L}}/l_0 \gg 1$, $\kappa \propto r_{\mathrm{L}}^2$. This is the high-energy limit and agrees with previous results (Parker, 1965; Aloisio & Berezinsky, 2004; Parizot, 2004; Globus et al., 2008; DeMarco et al., 2007; Beresnyak et al., 2011; Plotnikov et al., 2011; Harari et al., 2014; Snodin et al., 2016; Subedi et al., 2017). This scaling is also confirmed

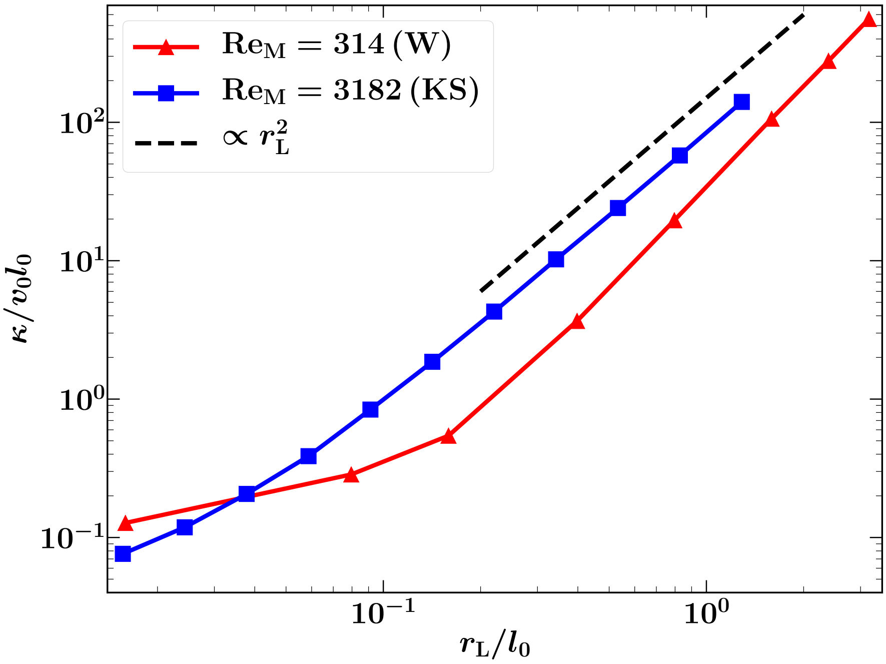

Figure 3.10: The cosmic ray diffusion coefficient for the W flow, $\mathrm{Re_M} = 314$ (red) and the KS flow, $\mathrm{Re_M} = 3182$ (blue) as a function of r_L/l_0. For $r_\mathrm{L} \gg l_0$, the diffusion coefficient follows the high-energy scaling $\kappa \propto r_\mathrm{L}^2$ (dashed black).

in laboratory experiments with random magnetic fields in a laser-produced plasma (Chen et al., 2018). The high-energy scaling can be explained as follows. High-energy cosmic ray particles, with $r_\mathrm{L} \gg l_b$ (l_b, correlation length of the small-scale magnetic field, is less than l_0), are scattered even before completing one gyro-orbit. Over a long time, the particle performs pure Brownian motion and diffusion sets in. The isotropic diffusion coefficient for the Brownian motion is given by $\kappa = \frac{1}{3} l v_0$, where l is the step length of the random walk and v_0 is the particle velocity. Since a particle scatters at least once within one gyro-orbit, $l \approx r_\mathrm{L}$. Thus, for an ensemble of high-energy particles,

$$\kappa = \frac{1}{3} l v \approx r_\mathrm{L} v_0 \propto r_\mathrm{L}^2. \tag{3.5}$$

For low-energy particles ($r_\mathrm{L}/l_0 < 1$), all three diffusion processes: FLRW, parallel scattering, and perpendicular scattering are significant. In this energy range, the FLRW limit in the isotropic random magnetic field provides the upper limit for the isotropic diffusion coefficient. However, the FLRW limit is never seen in test particle simulations, since the other two scattering mechanisms are always significant. It is extremely difficult to disentangle the contribution of the FLRW to overall diffusion from the particle scattering part. The diffu-

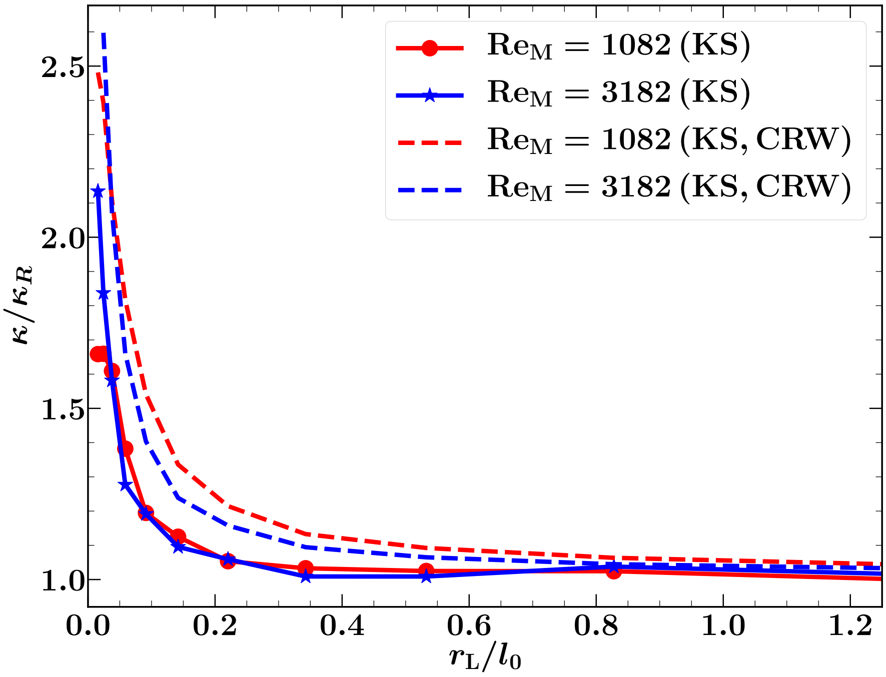

Figure 3.11: The ratio of diffusion coefficients from intermittent, κ, and randomized, κ_{R}, magnetic fields for the KS flow, $\mathrm{Re_M} = 1082$ (red), 3182 (blue). The dashed lines of same colour show the corresponding CRW model, Eq. (3.15).

sion coefficient for the FLRW limit can be calculated by following magnetic field lines. The FLRW diffusion coefficient (derived analytically and then confirmed numerically), assuming that the effective velocity of the ensemble of particles is equal to the Alfvén speed, for an isotropic Gaussian random magnetic field (Sonsrettee et al., 2015) is

$$\kappa_{\mathrm{FLRW}} = \sqrt{\frac{2}{3\pi}} l_b \, b_{\mathrm{rms}}, \tag{3.6}$$

where l_b is the correlation length and b_{rms} is the root mean square strength of the random magnetic field in units of rms Alfvén velocity. The coefficient in Eq. (3.6) is obtained analytically only for a isotropic Gaussian random magnetic field. For our simulation with $\mathrm{Re_M} = 3182$ (where $l_b/l_0 \approx 0.0244$) for the KS flow, the FLRW diffusion coefficient calculated using Eq. (3.6) is $\kappa_{\mathrm{FLRW}}/v_0 l_0 \approx 0.011$. The diffusion coefficient for particles in randomized magnetic fields with $r_{\mathrm{L}} \le l_b$ (or $r_{\mathrm{L}}/l_0 \le 0.0244$) is less than κ_{FLRW}, as can be inferred from Fig. 3.10 and Fig. 3.11 to be $\kappa/v_0 l_0 \approx 0.004$.

At lower energies, the dependence of κ on particle energy is weaker than Eq. (3.5) and is sensitive to the magnetic structure. We expect magnetic intermittency to be important at those energies where

$$r_\mathrm{L}/l_0 < 1. \tag{3.7}$$

The role of magnetic intermittency is demonstrated in Fig. 3.11, showing the ratio of the diffusivity κ, calculated with a dynamo generated intermittent magnetic field, to that in the corresponding randomized field, κ_R. At high energies (large r_L/l_0), $\kappa/\kappa_\mathrm{R} \simeq 1$, suggesting that the magnetic structures play no role in determining the diffusion coefficient of those particles. However, κ/κ_R increases rapidly up to more than 2.5 at lower energies: magnetic structures enhance diffusion when the inequality Eq. (3.7) is satisfied. We find that the ratio κ/κ_R at fixed r_L/l_0 increases with Re_M for a given flow. At high values of r_L/l_0, the diffusivity still depends on Re_M via changes in the magnetic correlation length, but not via the Re_M-dependent intermittency, as suggested by Fig. 3.11 where κ/κ_R tends to unity as r_L/l_0 increases.

3.5 Mean field and classical scattering results

The ISM contains both fluctuating (small-scale) and mean (large-scale) magnetic fields and thus large-scale fields also play a role in cosmic ray propagation. The particles tend to gyrate along the large-scale field lines and are scattered by the small-scale magnetic fluctuations. Thus, the diffusion of the particles is still due to the small-scale field. The diffusion coefficient κ_{ij} can be derived analytically using the velocity correlation function for particles via the Taylor-Green-Kubo (TKG) formula (Taylor, 1922; Green, 1951; Kubo, 1957) [1]

$$\kappa_{ij} = \int_0^\infty \langle v_i(t_0) v_j(t_0+t)\rangle \, \mathrm{d}t, \tag{3.8}$$

where $v_i(t)$ is the particle velocity along ith direction at time t and $\langle\cdots\rangle$ denotes average over an ensemble of particle trajectories. The exact analytical calculation, even for a very simple mean field (such as uniform or sinusoidal or slowly varying), is extremely difficult because the fluctuations would have a complicated effect as a function of both space and time on the velocity correlation function. Thus, here we use the physically motivated generic form of the velocity correlation function to calculate the diffusion coefficients.

In presence of a mean field, the diffusion coefficients are defined along two directions: parallel to the mean field and perpendicular to the mean field. Thus, we only concentrate

---

[1] This formula is always applicable but it is easier to use this for analytical derivation of diffusion coefficient when mean field is present since the exact solution for the unperturbed helical trajectory of a particle is known analytically. This diffusion coefficient is exactly equivalent to that obtained using Eq. (3.3).

on the velocity correlation function parallel $\left(\langle v'v\rangle_{\parallel}\right)$ and perpendicular $(\langle v'v\rangle_{\perp})$ to the mean field. Assuming that the particles gyrate around the mean magnetic field with Larmor frequency $\omega_0 = qB_0/\gamma m_0 c$ (defined via Eq. (3.1), where B_0 is the strength of mean field) and are scattered because of magnetic fluctuations, we can disentangle the effect of each type of field on the velocity correlation function. In the absence of any fluctuations, the particles would follow a helical path with $\langle v'v\rangle_{\perp} \approx v^2\cos(\omega_0 t)$. Now when magnetic fluctuations are considered, the particles get randomly scattered, deviate from their initial helical trajectories and finally the velocity correlation falls off to zero at large times. The fluctuations introduce a decorrelation in velocity. We assume correlation decreasing exponentially at a rate τ (also referred to as the scattering time in Gleeson (1969)). For simplicity, we assume that the rate is independent of time and direction. In general τ might be different in parallel and perpendicular directions depending on the structure of the field but for isotropic magnetic fluctuations they are roughly the same. Considering the effect of the mean and fluctuating field, the velocity correlation functions in the parallel and perpendicular directions are written as

$$\langle v'v\rangle_{\perp} \approx v^2\cos(\omega_0 t)e^{-t/\tau}, \tag{3.9}$$

$$\langle v'v\rangle_{\parallel} \approx v^2 e^{-t/\tau}. \tag{3.10}$$

Integrating Eq. (3.9) and Eq. (3.10), we obtain

$$\kappa_{\perp} = v^2\frac{\tau}{1+\omega_0^2\tau^2}, \tag{3.11}$$

$$\kappa_{\parallel} = v^2\tau. \tag{3.12}$$

The ratio of perpendicular to parallel diffusion coefficients, $\kappa_{\perp}/\kappa_{\parallel}$, is therefore

$$\frac{\kappa_{\perp}}{\kappa_{\parallel}} = \frac{1}{1+\omega_0^2\tau^2} = \frac{1}{1+v^2\tau^2/r_{\mathrm{L}}^2} \approx \frac{1}{1+\left(\lambda_{\parallel}/r_{\mathrm{L}}\right)^2}, \tag{3.13}$$

where $\lambda_{\parallel} \approx v\tau$ (since v is the velocity along the mean magnetic field) is the parallel mean free path and r_{L} is the Larmor radius of the particle. The derived ratio Eq. (3.13) agrees with that obtained using classical scattering theories (Gleeson, 1969; Forman & Gleeson, 1975; Bieber & Matthaeus, 1997).

Since the large-scale component is correlated over several kpc whereas the small-scale component has a correlation length less than the driving scale of turbulence ($\sim\ 0.1\,\mathrm{kpc}$), for our numerical simulations we add a uniform mean field (B_0) directed along the x-axis to the random magnetic fields described in Section 3.2. In presence of a mean field, r_{L} is

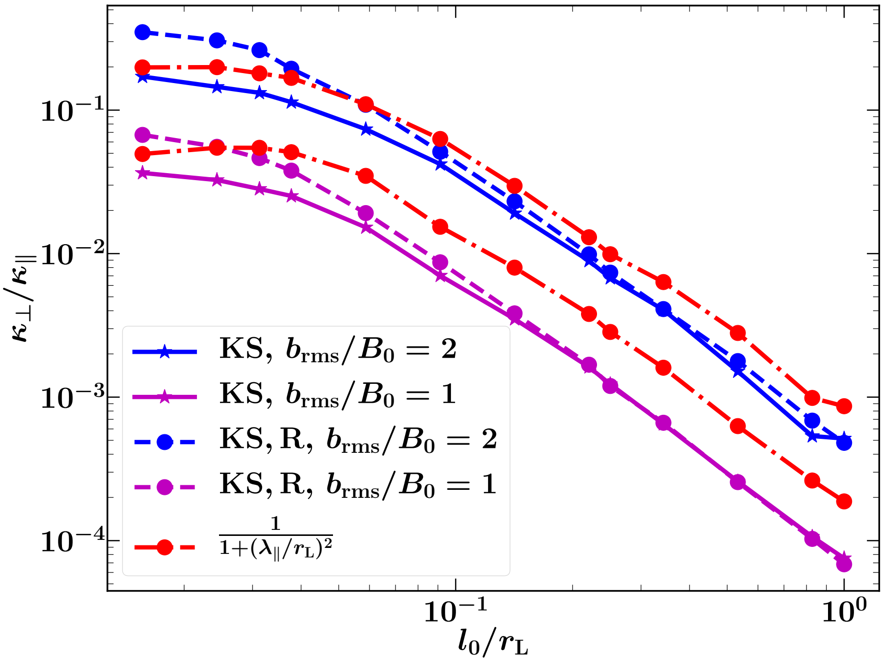

Figure 3.12: The ratio of perpendicular, $\kappa_\perp$, to parallel, $\kappa_\parallel$, diffusion coefficients for intermittent (solid lines) and randomized (dashed lines) magnetic fields in the presence of a mean magnetic field $b_\mathrm{rms}/B_0 = 1$ (magenta), 2 (blue) for the KS flow. The red dash–dotted line shows the ratio obtained using Eq. (3.13) for each case.

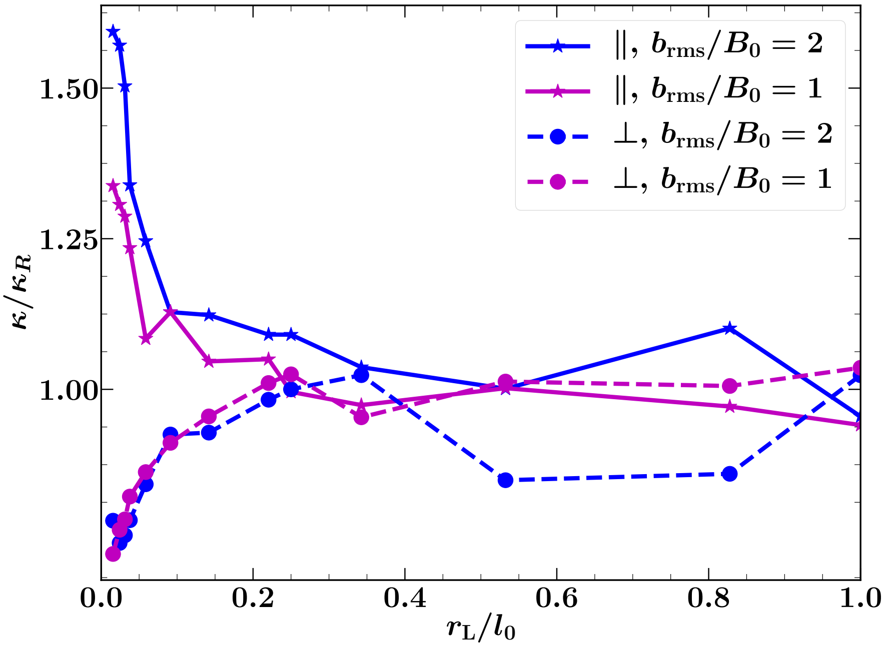

Figure 3.13: The ratio of diffusion coefficients from intermittent, κ, and randomized, κ_R magnetic fields in the presence of a mean magnetic field $b_\mathrm{rms}/B_0 = 1$ (magenta), 2 (blue) for the KS flow, $\mathrm{Re}_\mathrm{M} = 3182$; $\kappa_\parallel$ and $\kappa_\perp$ are shown solid and dashed, respectively.

defined with respect to the root mean square of the total magnetic field $(b_{\rm rms}^2 + B_0^2)^{1/2}$. In the presence of a mean magnetic field, cosmic ray particles are scattered stronger in the direction perpendicular to the mean field (or the guiding field) than along it, so typically, $\kappa_\perp/\kappa_\| \ll 1$. This is shown in Fig. 3.12. To compare the numerically obtained result with Eq. (3.13), $\lambda_\|$ is calculated from the numerically obtained $\kappa_\|$ using the relation $\kappa_\| = v_0\lambda_\|$, where v_0 is the speed of the particle. The numerical results for both the intermittent and randomized magnetic fields agrees with Eq. (3.13), independent of the strength of the mean magnetic field $(b_{\rm rms}/B_0)$.

Fig. 3.13 illustrates the effects of magnetic field intermittency in the presence of a mean magnetic field, presenting the ratio of the parallel and perpendicular diffusivities in the intermittent and Gaussian magnetic fields. A mean magnetic field somewhat reduces the effect of intermittency but does not eliminate it even for $b_{\rm rms}/B_0 = 1$. In the presence of a mean field, for low cosmic ray energies, magnetic intermittency enhances $\kappa_\|$ (i.e. $\kappa_\| > \kappa_{\|{\rm R}}$) and reduces $\kappa_\perp$ (i.e. $\kappa_\perp < \kappa_{\perp_{\rm R}}$). This can be explained as follows. Magnetic intermittency increases τ (particles need a larger number of scatterings or need longer time to diffuse), thus using Eq. (3.12) we conclude that the $\kappa_\|$ increases when magnetic structures are present. Also using Eq. (3.11) (for $\omega_0\tau \gg 1$, which is typically the case because low-energy particles perform several gyrations before they diffuse) we conclude that the perpendicular diffusion decreases when the magnetic field is intermittent. Again as explained for the isotropic case in Section 3.4 magnetic intermittency, even in presence of a mean field, is only important for low-energy cosmic rays.

3.6 Cosmic ray propagation as a correlated random walk

The Brownian motion is a widely used model for diffusive processes. This is the simplest type of random walk where each step is made in a direction independent of the previous one. However, a charged particle moves differently. As illustrated in Fig. 3.14, the direction of its motion after deflection by a magnetic structure is correlated with the previous direction. The deflection angle θ is related to $r_{\rm L}$, the angle between the velocity and magnetic field, β ($\neq 0$, which is equivalent to assuming that the particle is gyrating around $\mathbf{B}$ in Fig. 3.14), and the magnetic structure width d,

$$\theta \simeq d/(r_{\rm L}\sin\beta). \tag{3.14}$$

This is a correlated random walk (CRW) (Gillis, 1955). The CRW diffusivity depends on $\langle\cos\theta\rangle$, where angular brackets denote the ensemble average. The mean-square displacement

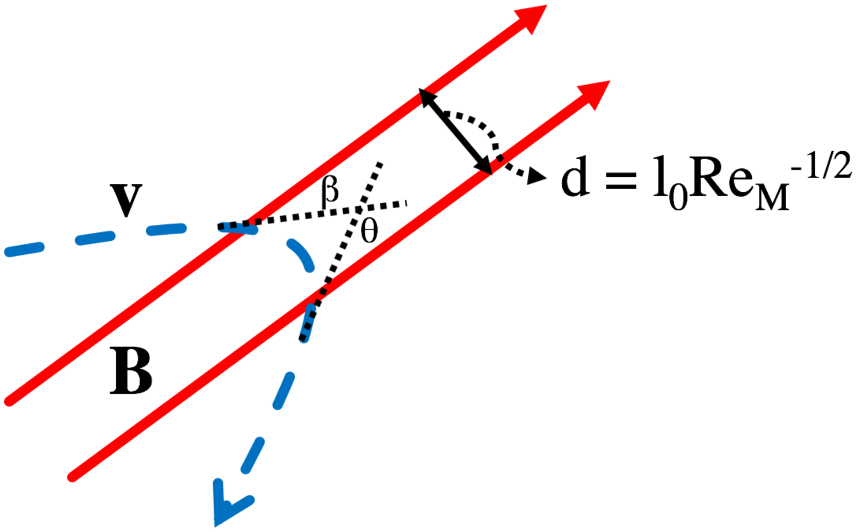

Figure 3.14: A charged particle with the pitch angle β is deflected by an angle θ in a magnetic structure of a thickness d. The dashed-line represents the particle moving out of the paper and going back in again to represent the gyration of the particle around the magnetic field shown in red, which is assumed to be in the plane of the paper.

in the CRW initially derived in two dimensions (Kareiva & Shigesada, 1983), implies the following three dimensional diffusivity (Chen & Renshaw, 1992):

$$\kappa = \frac{\langle l^2 \rangle}{6\tau} + \frac{\langle l \rangle^2}{3\tau}\frac{\langle \cos\theta \rangle}{1 - \langle \cos\theta \rangle}, \tag{3.15}$$

with $\tau = \langle l \rangle / v$, v the particle speed and l the step length. Here the first term is due to the usual Brownian motion and the second term represents the contribution due to the correlation in particle trajectory. $\langle \cos\theta \rangle$ cannot be equal to one in Eq. (3.15) as $\cos\theta$ for each particle cannot be equal to one since the random walk model assumes that the particle scatters from its initial trajectory.

To derive $\langle \cos\theta \rangle$ in the simulations, the particle trajectories were sampled at an interval equal to the local Larmor time, the deflection angle for each particle in the ensemble is calculated and then an ensemble average of the numerically computed deflection angles is obtained. The sampling frequency does not affect the results (Codling & Hill, 2005; Rosser et al., 2013).

The accuracy of the Eq. (3.15) is confirmed by Fig. 3.15 that shows the variation of κ with $\langle \cos\theta \rangle$, where κ is obtained numerically for both the intermittent and randomized magnetic fields and in each case the corresponding κ predicted from Eq. (3.15) is also shown. For τ in Eq. (3.15), we have used r_{L}/v_0, where r_{L} is the local Larmor radius. The agreement is

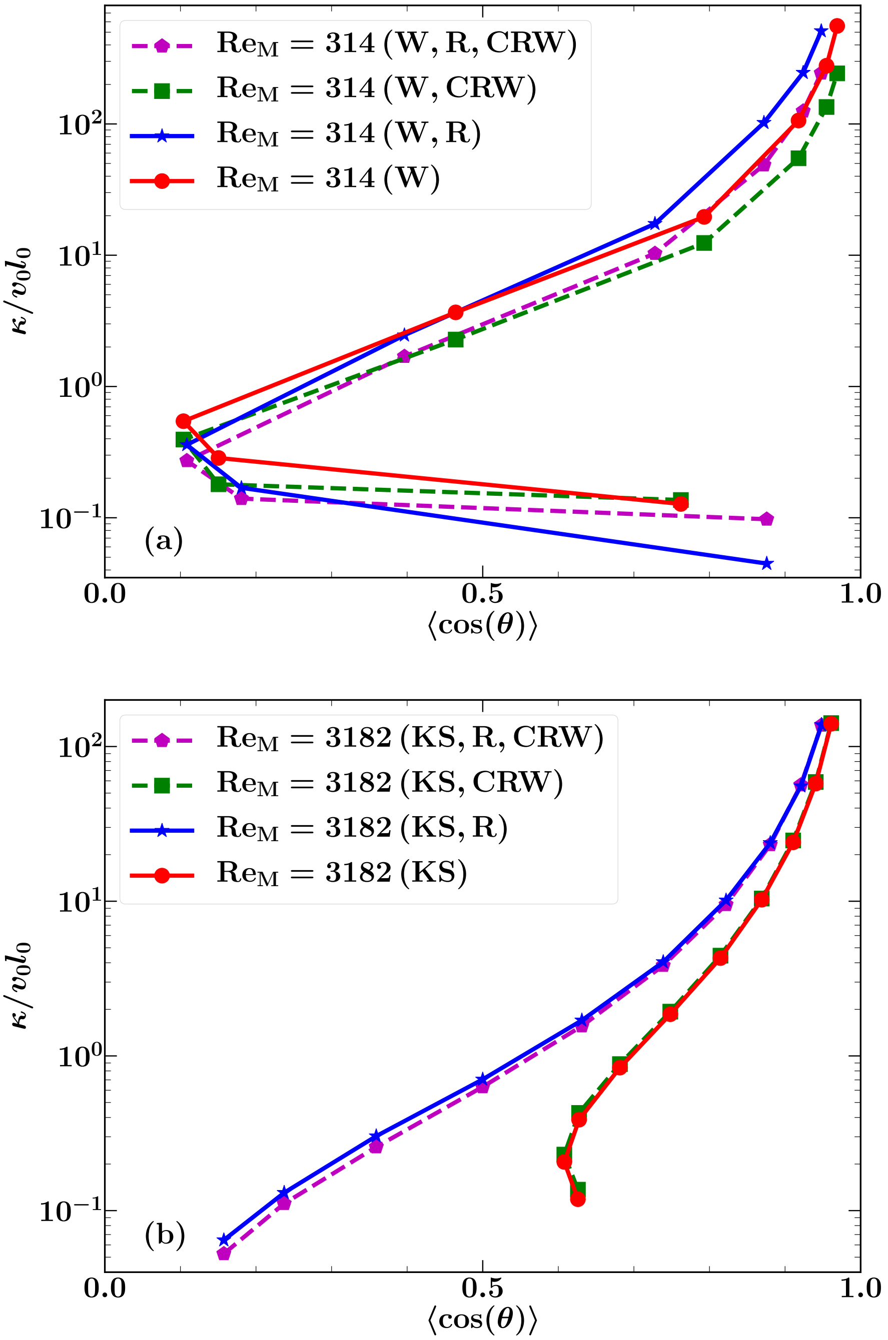

Figure 3.15: The dependence of cosmic ray diffusivity in intermittent and randomized magnetic fields on $\langle\cos\theta\rangle$ (solid lines) for W (a) and KS (b) flow. The corresponding CRW approximations (Eq. (3.15) with $\langle\cos\theta\rangle$ calculated from the simulated particle trajectories) are shown with dashed lines. The different data points refer to different values of r_L/l_0. These results are obtained for $B_0 = 0$.

remarkably good for the W flow and excellent for the less structured magnetic field resulting from the KS flow. This confirms directly that the cosmic ray propagation is a CRW with the diffusivity given by Eq. (3.15). This applies to both intermittent and Gaussian random magnetic fields (Fig. 3.15). We note that as r_{L} increases, the first term in Eq. (3.15) increases and dominates at higher r_{L}. For $r_{\mathrm{L}} \gg l_0$, the second term in Eq. (3.15) is negligible, which reduces the equation to an expression for the diffusivity in case of Brownian motion.

3.7 Diffusion or telegraph equation?

In the continuum limit, the Brownian motion model leads to the diffusion equation whereas the correlated random walk leads to the telegraph equation. For a correlated random walk, the telegraph equation (in a simplified case of one-dimension) can be derived as follows (Codling et al., 2008). Consider a population of particles which moves either left or right along an infinite line (say along the x-axis) at finite speed v. At location x and time t, let the number of particles moving right and left be $\alpha(x,t)$ and $\beta(x,t)$, respectively. Thus, the total particle number density is $n(x,t) = \alpha(x,t) + \beta(x,t)$. At each time step, Δt, each particle either changes direction and moves a distance Δx along the new direction with probability $\lambda\Delta t$, or moves in its previous direction by Δx with probability $1-\lambda\Delta t$. This introduces a correlation with the previous step, quantified by λ, with the previous step. At a time $t+\Delta t$ and location x, the number density of particles moving right and left, respectively, is given by

$$\alpha(x,t+\Delta t) = (1-\lambda\Delta t)\alpha(x-\Delta x,t) + \lambda\Delta t\beta(x-\Delta x,t), \tag{3.16}$$

$$\beta(x,+t+\Delta t) = \lambda\Delta t\alpha(x+\Delta x,t) + (1-\lambda\Delta t)\beta(x+\Delta x,t). \tag{3.17}$$

Expanding Eq. (3.16) and Eq. (3.17) in Taylor series gives

$$\alpha + \Delta t\frac{\partial\alpha}{\partial t} + \ldots = (1-\lambda\Delta t)\left[\alpha + (-\Delta x)\frac{\partial\alpha}{\partial x} + \ldots\right] + \lambda\Delta t\left[\beta + (-\Delta x)\frac{\partial\beta}{\partial x} + \ldots\right], \tag{3.18}$$

$$\beta + \Delta t\frac{\partial\beta}{\partial t} + \ldots = \lambda\Delta t\left[\alpha + \Delta x\frac{\partial\alpha}{\partial x} + \ldots\right] + (1-\lambda\Delta t)\left[\beta + \Delta x\frac{\partial\beta}{\partial x} + \ldots\right]. \tag{3.19}$$

Taking limit $\varDelta x, \varDelta t \to 0$ with $\varDelta x/\varDelta t \to v$ gives

$$\frac{\partial \alpha}{\partial t} = -v\frac{\partial \alpha}{\partial x} + \lambda(\beta - \alpha), \tag{3.20}$$

$$\frac{\partial \beta}{\partial t} = v\frac{\partial \beta}{\partial x} - \lambda(\beta - \alpha). \tag{3.21}$$

Adding Eq. (3.20) and Eq. (3.21) and differentiating with respect to t gives

$$\frac{\partial^2(\alpha + \beta)}{\partial t^2} = v\frac{\partial^2(\beta - \alpha)}{\partial x \partial t}. \tag{3.22}$$

Subtracting Eq. (3.20) from Eq. (3.21) and differentiating with respect to x gives

$$\frac{\partial^2(\beta - \alpha)}{\partial x \partial t} = v\frac{\partial^2(\alpha + \beta)}{\partial x^2} - 2\lambda\frac{\partial(\beta - \alpha)}{\partial x}. \tag{3.23}$$

Substituting Eq. (3.23) in Eq. (3.22),

$$\frac{\partial^2(\alpha + \beta)}{\partial t^2} = v^2\frac{\partial^2(\alpha + \beta)}{\partial x^2} - 2v\lambda\frac{\partial(\beta - \alpha)}{\partial x}. \tag{3.24}$$

Using Eq. (3.20) and Eq. (3.21) in Eq. (3.24) gives

$$\frac{\partial^2(\alpha + \beta)}{\partial t^2} = v^2\frac{\partial^2(\alpha + \beta)}{\partial x^2} + 2\lambda\left[-\frac{\partial \beta}{\partial t} + \lambda(\beta - \alpha) - \frac{\partial \alpha}{\partial t} - \lambda(\beta - \alpha)\right]. \tag{3.25}$$

Now recalling that $n = \alpha + \beta$ in Eq. (3.25) gives

$$\frac{\partial^2 n}{\partial t^2} + 2\lambda\frac{\partial n}{\partial t} = v^2\frac{\partial^2 n}{\partial x^2}. \tag{3.26}$$

Eq. (3.26) is the telegraph equation in one dimension. This equation represents a correlated random walk and is still globally unbiased (there is no overall preferred direction for particle motion) like Brownian motion, it just considers the local bias (controlled by λ) of the particles (in case of cosmic rays, the local bias is due to particle tendency to gyrate around magnetic field lines in magnetic structures, till it gets scattered). Dividing Eq. (3.26) by 2λ gives

$$\frac{1}{2\lambda}\frac{\partial^2 n}{\partial t^2} + \frac{\partial n}{\partial t} = \frac{v^2}{2\lambda}\frac{\partial^2 n}{\partial x^2}. \tag{3.27}$$

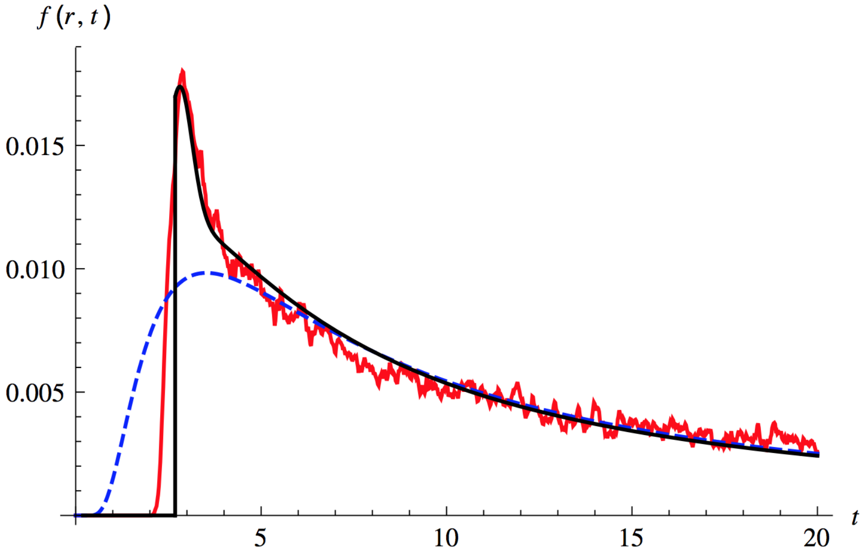

Figure 3.16: Figure taken from Tautz & Lerche (2016). Isotropic cosmic ray intensity f as a function of time t obtained by solving the diffusion equation (blue dashed), by solving the telegraph equation (black) and that obtained from test-particle simulations (red). Initially, the telegraph equation better captures the ballistic behaviour of the particles but over long time, both the diffusion equation and the telegraph equation give similar solutions. Both f and t are given in arbitrary units.

Introducing $v^2/2\lambda$ as the diffusion coefficient D and $1/2\lambda$ as the correlation time τ, we get

$$\tau\frac{\partial^2 n}{\partial t^2}+\frac{\partial n}{\partial t}=D\frac{\partial^2 n}{\partial x^2}. \tag{3.28}$$

The corresponding three-dimensional version of the telegraph equation with $\mathbf{D}$ as the diffusion tensor is

$$\tau\frac{\partial^2 n}{\partial t^2}+\frac{\partial n}{\partial t}=\mathbf{D}\nabla^2 n. \tag{3.29}$$

The late-time ($t \gg \tau$) solution of both the diffusion and the telegraph equations are similar (Codling et al., 2008; Tautz & Lerche, 2016; Rodrigues et al., 2018). However, as shown in Fig. 3.16, the telegraph equation provides a better representation of the initial phase of particle motion. Also, unlike the diffusion equation which assumes information travelling at infinite speed, the particles move at finite speed when the telegraph equation is considered. For example, solving the diffusion equation is equivalent to assuming that the particles fill the entire available volume instantaneously, which is not the case for the telegraph equation. Thus, the telegraph equation provides a more realistic behaviour for particles travelling at finite speed, especially during early times (when they haven't scattered much). The initial ballistic effect might be important, especially, to model cosmic ray propagation close to sources and the transport of highly energetic solar particles (Effenberger & Litvinenko, 2014) as well as particle propagation near magnetic null points (Snodin et al., 2006). The correlation time (τ) in the telegraph equation can be interpreted as the time it takes for the particles to become diffusive (Rodrigues et al., 2018).

However, some authors claim that the norm of the solution for the telegraph equation will not be conserved initially, which implies an unphysical situation where the number of particles is not conserved (Malkov & Sagdeev, 2015; Tautz & Lerche, 2016). This is not really true because those authors consider only one initial condition whereas the telegraph equation is second order in time and requires two initial conditions. When both initial conditions (at time $t = 0$, total number of particles N is constant and $\partial N/\partial t = 0$) are considered, the total number of particles does remain constant for all times (Rodrigues et al., 2018).

3.8 Discussion and conclusions

We have demonstrated that cosmic ray propagation in random magnetic fields is affected by magnetic intermittency in the range of energies given by Eq. (3.7), or

$$\frac{E}{1\,\mathrm{GeV}} < 10^9 \frac{l_0}{1\,\mathrm{kpc}} \frac{B}{1\,\mu\mathrm{G}}. \tag{3.30}$$

In the interstellar medium of spiral galaxies, $l_0 \simeq 100\,\mathrm{pc}$ and $B \simeq 10\,\mu\mathrm{G}$ (Beck, 2016) and for ultra-relativistic protons, this energy range is $E \lesssim 10^9\,\mathrm{GeV}$. In galaxy clusters, $l_0 \simeq 10\,\mathrm{kpc}$, $B \simeq 2\,\mu\mathrm{G}$ (Govoni & Feretti, 2004; Schekochihin & Cowley, 2006) and $E \lesssim 10^{10}\,\mathrm{GeV}$. However, for very high-energy particles, the Larmor radius is of the order of the size of the system and the particles do not diffuse. Thus, in galaxies and galaxy clusters, magnetic field intermittency affects almost all the low-energy diffusing cosmic rays. We note that magnetic intermittency may also affect ultra-high energy cosmic rays that propagate non-diffusively. This is because the ultra-high energy cosmic ray particles are deflected less in the intermittent magnetic field as compared to the Gaussian random magnetic field because the probability of missing a magnetic structure (which implies negligible deflection) is higher in the intermittent field. In Gaussian random magnetic field, the particles are deflected uniformly throughout the volume. Thus, magnetic intermittency is likely to affect inference for the sources of ultra-high energy cosmic rays from their observed arrival directions.

We have shown that the the diffusive propagation of cosmic rays in any random magnetic fields (either Gaussian or non-Gaussian) is described as a correlated random walk, rather than a Brownian motion. This implies that in the continuum limit, cosmic rays are better modelled with the telegraph equation rather than the diffusion equation.

Chapter 4

Correlation between cosmic rays and magnetic fields

Synchrotron radiation from cosmic rays is one of the main observational probes of the galactic magnetic fields. The interpretation of synchrotron intensity data requires knowledge of the cosmic ray number density and cosmic rays are often assumed to be in energy equipartition (i.e. tightly correlated) with the magnetic field energy density. However, there are no compelling observational or theoretical reasons to expect such tight correlation to hold across all scales. In this chapter, we use test-particle simulations (including several aspects of cosmic ray–magnetic field interactions) and MHD simulations to study the correlation between cosmic rays and magnetic fields. We trace the motion of protons through a random magnetic field to clarify the cosmic ray distribution at scales comparable to the driving scale of turbulence. We find that there is no spatial correlation between the cosmic ray number density and the magnetic field energy density at these scales. Moreover, their distributions are approximately statistically independent. We also find that low-energy cosmic rays can be trapped between two magnetic mirrors, whose location depends more on the structure of the magnetic field lines than on the field strength. These conclusions can significantly change the interpretation of synchrotron observations and thus our understanding of the strength and structure of magnetic fields in the Milky way and other spiral galaxies.

4.1 Introduction

The synchrotron emissivity $\mathscr{E}$ depends on the number density of cosmic ray electrons $n_{\rm cre}$ and magnetic field in the plane of the sky (or perpendicular to the line of sight l), $B_\perp$. The synchrotron intensity I, at any given position (x, y) in the sky is the integral of synchrotron emissivity over the path length L

$$I(x,y) = K \int_L \mathscr{E}(x,y)\,\mathrm{d}l = K \int_L n_{\rm cre}\, B_\perp^2\,\mathrm{d}l, \tag{4.1}$$

where K is a constant and the synchrotron spectral index is assumed to be unity. The determination of magnetic field strength $B_\perp$ from synchrotron intensity requires knowledge of the number density of cosmic ray electrons. This information can be obtained from independent observations of gamma-ray emission or X-ray emission by inverse Compton scattering. In the absence of such information, one of the following is assumed to infer magnetic field strength from the synchrotron intensity data:

- energy equipartition between total cosmic ray energy density $\mathcal{E}_{\rm cr}$ and magnetic field energy density $\mathcal{E}_B$, i.e., $\mathcal{E}_{\rm cr} \approx \mathcal{E}_B$ or equivalently pressure equality where the pressures due to cosmic rays and magnetic fields are assumed equal to each other;
- minimum energy assumption: minimize energy required to produce the observed synchrotron radiation (minimizing $\mathcal{E}_{\rm cr} + \mathcal{E}_B$);
- uniform cosmic ray electron density, i.e., $n_{\rm cre} \approx \text{ constant}$.

If energy equipartition is assumed, two further assumptions are made since most of the cosmic ray energy is due to protons but the synchrotron emission is produced by electrons. Firstly, it is assumed that the cosmic ray protons have a similar spatial distribution as cosmic ray electrons. Secondly, the ratio of the number of protons to the number of electrons is assumed to be a fixed constant, $K_0 = 100$ for the ISM close to the Sun (Bell, 1978b). Then magnetic field strength can be estimated from the synchrotron observations. The magnetic field strength obtained by assuming an equipartition argument is very similar to that obtained from the minimum energy estimate (Sect. 19.5 in Longair, 1994; Sect. 3.2.2 in Klein & Fletcher, 2015). The assumption of uniform cosmic ray electron distribution might be true over large length scales ($\gtrsim 1 - 2\,\mathrm{kpc}$) since assuming a uniform cosmic ray distribution as opposed to the equipartition assumption was better at matching the radio observations with the large-scale magnetic fields obtained using the mean-field dynamo theory (Moss et al., 2007).

The following two arguments are used to justify energy equipartition between cosmic rays and magnetic fields. The first one is that both the cosmic rays and magnetic fields have a common source of energy (supernova explosions) and thus, in an energy equilibrium state, they would equally share the total energy from the source. Cosmic rays are accelerated in supernova shocks (Bell, 1978a,b; Blandford & Ostriker, 1978; Drury, 1983). Supernovae are also a major driver of the ISM turbulence, which amplifies galactic magnetic fields. Thus, cosmic ray and magnetic field energies are derived from a single source and over large length- and time- scales, both components would have roughly equal energy. This only applies to large scales where a dynamic equilibrium between two components can be considered. This is also probably true only for systems where an equilibrium has time to be established, i.e., galaxies at the present epoch. It is unlikely that the equipartition assumption holds for active systems such as young galaxies, starburst galaxies and galaxy clusters. However, the equipartition assumption is widely used to obtain magnetic field strengths from synchrotron intensity, independent of the spatial resolution of observations and the system under consideration (Beck & Krause, 2005). The second argument for equipartition is that the cosmic rays are confined by magnetic fields and thus a correlation between them is expected (Burbidge, 1956; Stepanov et al., 2009, 2014). Both these arguments may sound convincing but are not completely compelling. There are a few observational signatures in support of the energy equipartition at larger scales ($\geq \ \mathrm{kpc}$) in the ISM of star-forming galaxies (Seta & Beck, 2019), but the detailed physics of each argument is yet to be explored. Thus, it is important to test the validity of the energy equipartition assumption.

4.2 Energy equipartition argument: previous tests and our approach

The minimum energy assumption was first applied to study energy content in cosmic rays and magnetic fields in the jet of M87 using the optical and radio emissions from the system (Burbidge, 1956). Since then, energy equipartition assumption is used to obtain magnetic field strength in various systems. Duric (1990)[1] suggested that the range of possible magnetic field strengths in spiral galaxies can at most be an order of magnitude below and above that obtained assuming energy equipartition. The conclusion is justified as follows. If the magnetic field is significantly weaker than the equipartition value, the particles would not be confined within the disk (relativistic charged particles cannot be confined by thermal

---

[1] This paper is titled “Equipartition: fact or fiction?”.

gas) and thus they would escape at relativistic speeds. This would imply almost no synchrotron emission from the disc. On the other hand, if the magnetic field is far stronger than the equipartition value, the particles would be confined close to their sources for a long time. The synchrotron–emitting cosmic ray electrons would suffer strong energy loss within a short span of time (or over a short length scale). This would imply a very high synchrotron emissivity but only in small regions around the sources. Neither of the above situations is actually seen in synchrotron observations of spiral galaxies. Also, a weakness of this type of argument is that cosmic ray diffusivity depends not on the total magnetic field strength but on the ratio of the random to large-scale magnetic field strengths. Chi & Wolfendale (1993) used gamma-ray observations from the Compton Gamma Ray Observatory to obtain the proton number density in the Large and Small Magellanic Clouds (LMC and SMC). They showed that energy equipartition does not hold for these irregular galaxies. However, Mao et al. (2012), using more recent gamma-ray data from the Fermi Large Area Telescope, concluded that the equipartition does not seem to be violated in the LMC. The slope of radio-FIR correlation indirectly constrains the relationship between the energy densities of cosmic ray electrons and magnetic fields. Based on the radio-FIR correlation studies, it has been concluded that the energy equipartition assumption is invalid on scales smaller than a few kpc and may hold on larger scales (Hoernes et al., 1998; Berkhuijsen et al., 2013; Basu & Roy, 2013). Yoast-Hull et al. (2016) analyze the gamma-ray spectra and the radio spectra in the central molecular zones of three starburst galaxies (M82, NGC 253 and Arp 220) to test the energy equipartition assumption. They concluded that the equipartition does not hold in these dynamic systems.

The energy equipartition assumption, when applied on large scales, seems to hold for a number of systems (Beck, 2016). However, there are also cases where this is not true. Also, it is a *convenient* assumption (synchrotron emission depends on two quantities: cosmic ray electron number density and magnetic fields, but assuming a relation between two quantities provides information about magnetic field strength from a single observational probe) and not a physical law. So we do not expect it to be always applicable. We here first test the correlation between cosmic rays and magnetic fields (equivalent to a local energy equipartition assumption) using test-particle simulations in random (Gaussian and non-Gaussian) magnetic fields by constructing cosmic ray distribution from their trajectories (Seta et al., 2018). This is important to capture the effects of magnetic field structure. Then we also solve MHD equations coupled with equation for cosmic rays (Section 4.11), now treated as an advective-diffusive fluid, to test the equipartition assumption including cosmic ray-thermal gas coupling.

4.3 Construction of cosmic ray number density from test-particle simulations

The cosmic ray diffusion coefficient is calculated from trajectories as described in Section 3.3. The intermittent and non-intermittent magnetic fields (both having same power spectrum) used in this chapter are shown in Fig. 3.5a and Fig. 3.5b respectively. Fig. 4.1 shows the isotropic diffusion coefficient as a function of time for intermittent (Fig. 4.1a) and non-intermittent magnetic fields (Fig. 4.1b). In each case, there is an initial phase of ballistic particle motion, in which $\kappa(t)$ is approximately linear in t, followed by a diffusive phase where $\kappa(t)$ settles to its asymptotic, time-independent value. The start of the diffusive phase, t_d, is the time when the slope of $\kappa(t)$ becomes small, $\mathrm{d}\kappa/\mathrm{d}t \simeq 10^{-6} v_0 l_0 \omega_0$; this time is indicated by a vertical dashed line in Fig. 4.1.

To obtain the number density of cosmic rays, n_cr, from the test-particle simulations, we calculate the coordinates of each particle modulo $L = 2\pi$ (the size of the periodic box), i.e., relative to the periodic magnetic field. Next, we divide the periodic domain into 512^3 cubes and count the number of particles within each cube. The size of the cubes was chosen to match the spatial resolution of the magnetic field, which was obtained from a dynamo simulation on a 512^3 grid, but we have checked that the results are not very sensitive to the size of the cubes. The result is the instantaneous number density of the particles $\tilde{n}(\mathbf{x}, t)$. We then average the density of particles within each cube over a sufficiently long period T ($\gg t_\mathrm{d}$), to obtain the cosmic ray density

$$n_\mathrm{cr}(\mathbf{x}) = \frac{1}{T - t_\mathrm{d}} \int_{t_\mathrm{d}}^{T} \tilde{n}(\mathbf{x}, t')\,\mathrm{d}t'. \tag{4.2}$$

We have checked that the results are not dependent on the sampling time ($\mathrm{d}t'$) as long as it is smaller than a few times the Larmor time $2\pi/\omega_0$. But for lower sampling rate the simulation has to be averaged over a longer total time (higher T) to collect sufficient statistics. We note that particles of different energies were simulated over different periods T to obtain roughly the same $\langle n_\mathrm{cr}(\mathbf{x})\rangle$ at all energies.

4.4 Pitch angle scattering

In addition to following magnetic field lines, cosmic ray particles are scattered by magnetic fluctuations at a scale comparable to their gyroradius, the condition often referred to as the

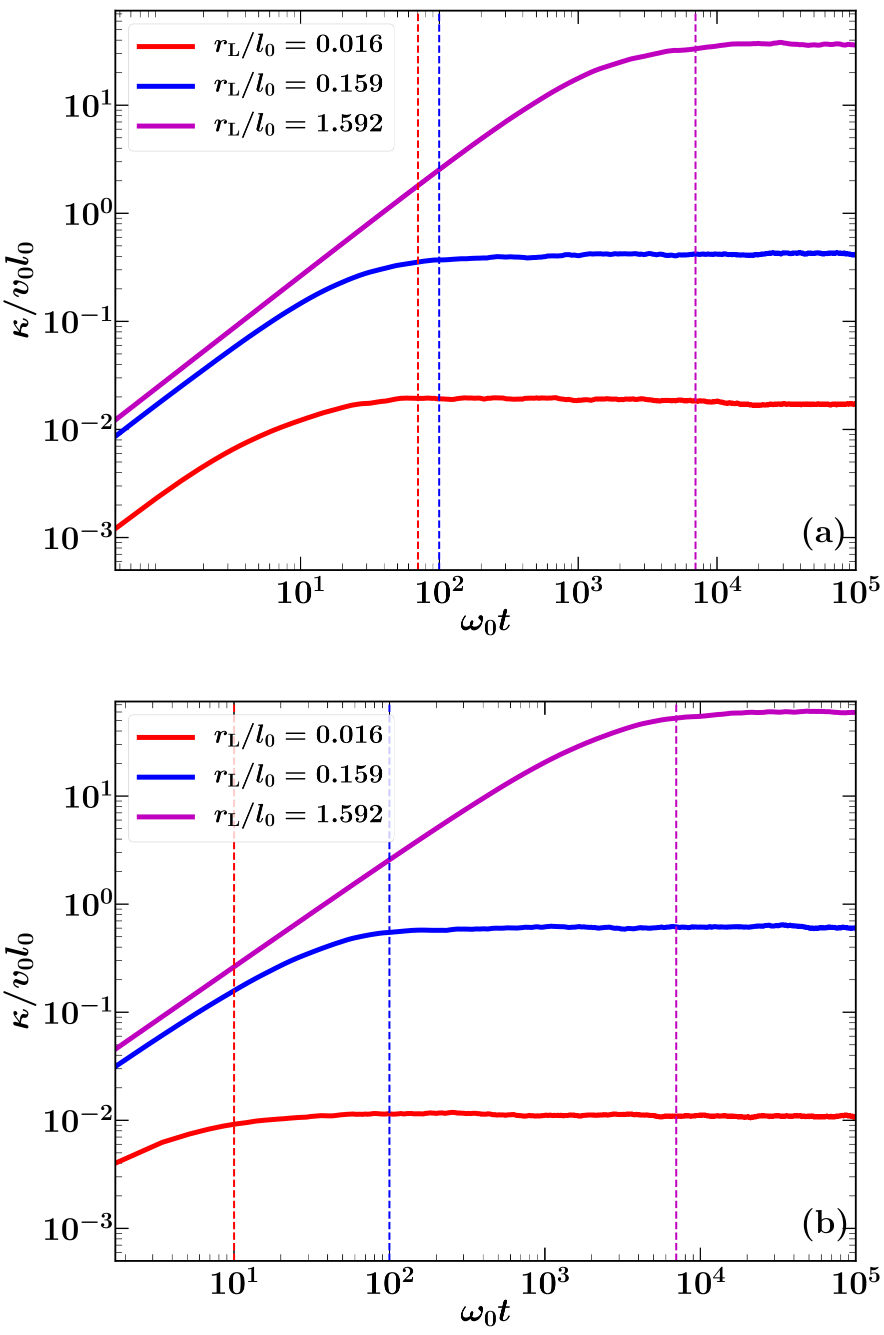

Figure 4.1: Normalized cosmic ray diffusivity $\kappa/v_0 l_0$ as a function of normalized time $\omega_0 t$ for $r_L/l_0 = 0.016, 0.159, 1.592$ for the intermittent (a) and randomized (b) magnetic fields shown in Fig. 3.5. The dashed lines of the corresponding colours show the time t_d after which the propagation becomes diffusive: $\kappa(t) \approx \kappa$ at $t > t_d$. For low energy particles ($r_L \leq l_b$), the diffusivity in the intermittent magnetic field is larger than in the randomized (Gaussian) field of identical power spectrum as discussed in Section 3.4.

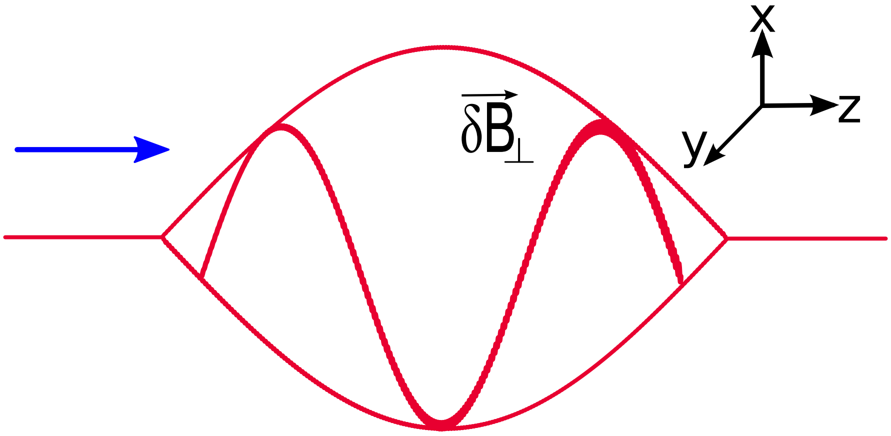

Figure 4.2: Cosmic ray (velocity direction shown by blue arrow) interacting with a localized magnetic fluctuation of magnitude δB with mean field along the z-axis.

'gyroresonance'. The scattering changes the direction of motion, and thus the cosine of the pitch angle μ of the particle, defined via

$$\mu \equiv \cos\theta = \frac{\mathbf{v}\cdot\mathbf{B}}{|\mathbf{v}||\mathbf{B}|}, \tag{4.3}$$

also changes, where $\mathbf{v}$ is the velocity of the particle and $\mathbf{B}$ is the magnetic field. The process is known as the pitch angle scattering (PAS). It leads to diffusion of particles in the momentum space of the particle (still preserving energy), which in turn gives rise to their diffusion in the physical space.

We here derive how the pitch angle of a particle changes when it encounters a magnetic fluctuation whose properties (wavelength and amplitude) are known. As described in Kulsrud (2005), we consider a localized MHD wave packet (magnetic fluctuation) polarized in the x-direction in the presence of a uniform magnetic field B_0 along the z-axis as shown in Fig. 4.2. Before a cosmic ray particle (travelling from the left in Fig. 4.2) encounters the wave packet, it gyrates around the background uniform magnetic field $B_0\hat{\mathbf{z}}$ with frequency ω_0. Consider an MHD perturbation in the form of a plane wave,

$$\delta B_\perp = \delta B \sin(kz - \omega_A t), \tag{4.4}$$

where δB is the amplitude, k is the wavenumber (here assumed positive), and ω_A is the frequency of the wave. The velocity of the particle along the $\hat{\mathbf{y}}$ direction due to the background magnetic field $B_0\hat{\mathbf{z}}$ alone is

$$v_y = v_\perp \sin(\omega_0 t + \phi), \tag{4.5}$$

where $v_\perp$ is the component of velocity perpendicular to $B_0\hat{\mathbf{z}}$ and ϕ is the phase between the cosmic ray velocity vector and the wave vector. The z position of the cosmic ray particle is $z_0 + v_z t$, where z_0 is the initial position. The $\hat{\mathbf{z}}$-component of the Lorentz force, using Eq. (4.4) and Eq. (4.5), is therefore

$$\begin{aligned}\frac{e}{c}\left(\mathbf{v}\times\mathbf{B}\right)_z &= \frac{e}{c} v_y \delta B_\perp \\ &= \frac{e}{c} v_\perp \delta B \sin(kz_0 + kv_z t - \omega_A t)\sin(\omega_0 t + \phi) \\ &= \frac{e}{2c} v_\perp \delta B \left[\cos[(kv_z - \omega_A + \omega_0)t + (kz_0 + \phi)]\right. . \\ &- \cos[(kv_z - \omega_A - \omega_0)t + (kz_0 - \phi)]]. \end{aligned} \tag{4.6}$$

For $v_z > 0$, the first term in the square bracket of the Eq. (4.6) has very high frequency and averages out to 0. However, the second term may have significant contribution if $kv_z - \omega_A - \omega_0 = 0$ and this is precisely the gyroresonance condition (since $\omega_A \ll \omega_0$ for relativistic particles). Also, for cosmic rays travelling with speed close to the speed of light, $v_z \gg v_\mathrm{A}$. For a MHD fluctuation in three dimensions the analogous gyroresonance condition is

$$k_\| \sim \frac{1}{\mu r_\mathrm{L}}, \tag{4.7}$$

where μ is the pitch angle of the particle, r_L is the particle gyroradius, and $k_\|$ is component of the wave vector along the direction of background magnetic field, B_0.

If the gyroresonance condition is satisfied, the change in the particle momentum along the $\hat{\mathbf{z}}$ direction due to particle's interaction with the wave packet follows from Eq. (4.6) as

$$
\begin{aligned}
\delta p_z &= \frac{e}{c}\int (\mathbf{v}\times\mathbf{B})_z \mathrm{d}t \\
&= \frac{e\delta B v_\perp}{2c}\cos(kz_0-\phi)\frac{2\pi}{k(v_z-v_\mathrm{A})} \\
&\approx \frac{e\delta B v_\perp}{2c}\cos(kz_0-\phi)\frac{2\pi}{kv_z},\ \text{ since } v_z \gg v_\mathrm{A}, \\
&= \frac{\pi e\delta B v_\perp}{c\omega_0}\cos(kz_0-\phi),\ \text{ since } kv_z=\omega_0+\omega_A\approx\omega_0, \\
&= \pi\gamma m v_\perp\left(\frac{\delta B}{B_0}\right)\cos(kz_0-\phi),\ \text{ since } \omega_0=\frac{eB_0}{\gamma mc}, \\
&\approx \pi p_\perp\left(\frac{\delta B}{B_0}\right)\cos(\phi'),
\end{aligned}
\tag{4.8}
$$

where v_A is the velocity of the wave (usually an Alfvén wave), $p_\perp$ is the momentum in the direction perpendicular to the magnetic field and $\phi' = kz_0 - \phi$ is the relative phase between the cosmic ray particle and the wave. [2]

The interaction between the cosmic ray and the wave packet changes only the pitch angle. Considering the angle between the particle momentum and the magnetic field to be θ, define $\mu = \cos(\theta)$. Here $p\cos(\theta) = p_z$ changes as given by Eq. (4.8). As the process conserves energy ($\delta p = 0$) it implies that

$$\delta p_z = \delta(p\cos(\theta)) = (\delta p)\cos(\theta) + p\delta(\cos(\theta)) = -p\sin(\theta)\delta\theta = -p_\perp\delta\theta. \tag{4.9}$$

Substituting Eq. (4.8) in Eq. (4.9) we can calculate change in θ as

$$\delta\theta = -\pi\left(\frac{\delta B}{B_0}\right)\cos(\phi^{'}). \tag{4.10}$$

The change in pitch angle of a cosmic ray particle due to PAS is governed by Eq. (4.10). This change in pitch angle leads to the diffusion of cosmic rays in real space. It is clear that $\delta\theta \approx \delta B/B_0$ and thus $\delta B/B_0$ is the control parameter for PAS efficiency.

Numerically, we test the gyroresonance condition. We consider a single particle motion by solving the Lorentz force equation (Eq. (3.2)) in the presence of a uniform magnetic field, B_0, and a localized MHD wave packet of the form Eq. (4.4) with chosen k and δB. We keep

---

[2] Note a minor typographical error in Eq. (4.8) of Kulsrud (2005), where the calculated expression for δp_z depends on θ, which is not correct physically since once the gyroresonance condition is satisfied, the amount of scattering depends only on the amplitude of the magnetic fluctuation and not on particle properties.

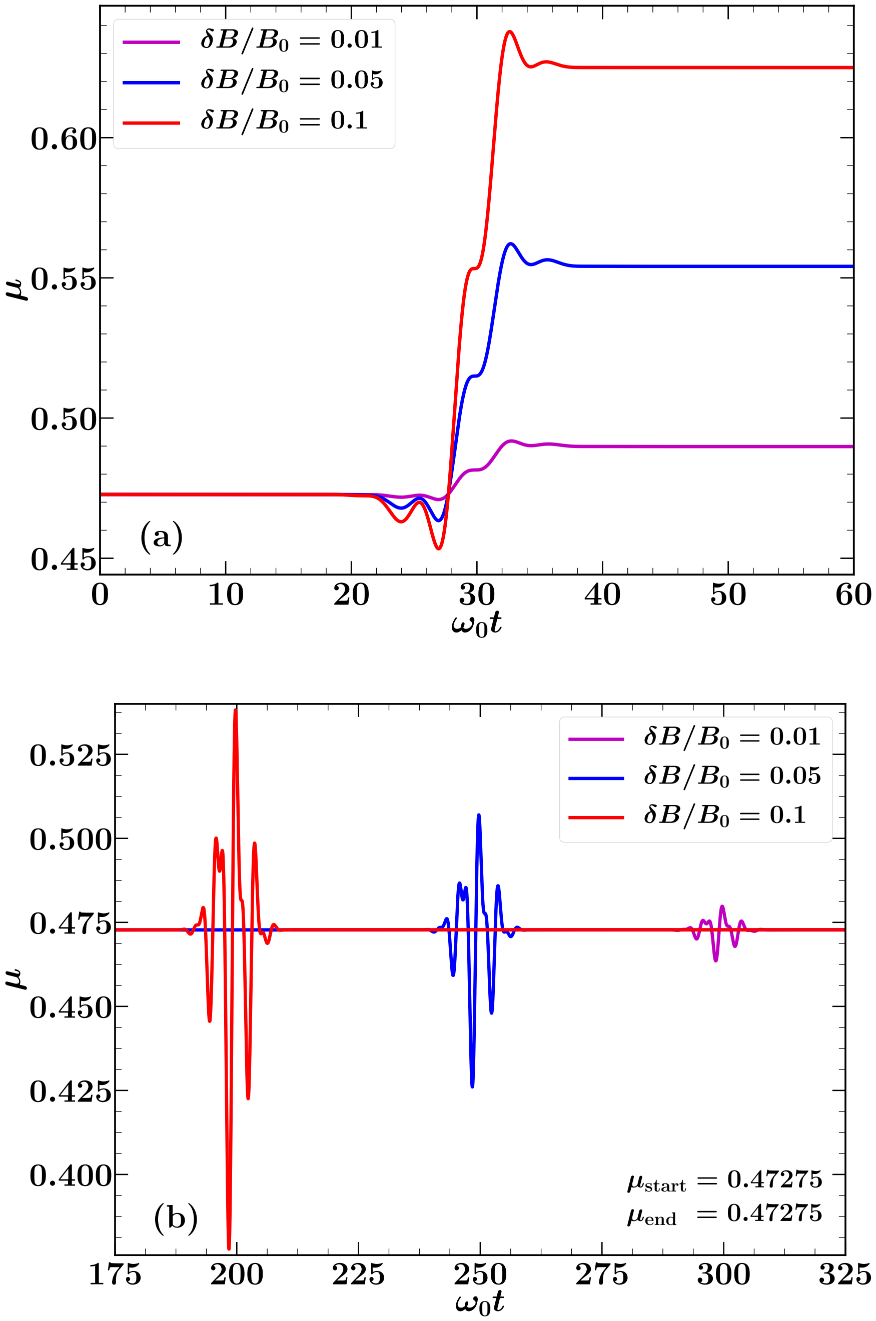

Figure 4.3: Pitch angle μ calculated from the trajectory of a single particle obtained numerically as a function of normalized time $\omega_0 t$ for the case where the gyroresonance condition holds (a) and doesn't hold (b). When gyroresonance condition is satisfied, the particle is scattered and its pitch angle changes. Also for such a scattering $\delta\mu \propto \delta B/B_0$ as shown in (a). When the gyroresonance condition doesn't hold, the particle's pitch angle varies across the magnetic fluctuation but returns back to its initial pitch angle once the particle crosses the fluctuation. Thus, $\delta\mu = 0$ for the case (b). To avoid overlap in (b), the time axis for case $\delta B/B_0 = 0.01$ and $\delta B/B_0 = 0.1$ are shifted by $+50$ and -50 normalized time units respectively.

varying the wavelength $(2\pi/k)$ of the fluctuation from values much smaller than the Larmor radius r_{L} of the particle to values much larger than r_{L}. The pitch angle changes only when the gyroresonance condition $2\pi/k \approx r_{\mathrm{L}}$ is satisfied and $\delta\mu \propto \delta B/B_0$ as expected from Eq. (4.10) and as shown in Fig. 4.3a. In Fig. 4.3a cosmic rays (for all values of $\delta B/B_0$) enter and leave the wave packet at the same time $\omega_0 t \approx 30$, thus jump in $\delta\mu$ is at the same point for all of them. If the gyroresonance condition is not satisfied, the particle pitch angle changes when it is travelling through the wave packet, but then it returns back to its initial value on exit from the wave packet. This happens independently of the magnitude of $\delta B/B_0$, as illustrated in Fig. 4.3b.

4.5 Magnetic field at the Larmor scale

The efficiency of PAS depends on the amplitude of the magnetic fluctuation, $\delta B/B_0$, at the Larmor scale. Suitable magnetic fluctuations can be a part of a magnetic energy spectrum that extends from much larger scales, or be excited by cosmic rays themselves via the streaming instability (Kulsrud & Pearce, 1969; Wentzel, 1974; Kulsrud, 2005). The fluctuations due to the MHD cascade from larger scales to the Larmor scale are usually referred to as the extrinsic turbulence and those due to cosmic ray themselves are referred to as the intrinsic turbulence. The waves in the latter case are also sometimes called 'self-generated waves' (since particles are scattered by the waves that they themselves generate). Here, we estimate $\delta B/B_0$ for each case.

4.5.1 Intrinsic turbulence: self-generated waves

The magnitude of the magnetic fluctuations that are associated with pitch angle scattering due to self-generated waves is estimated as follows. When the velocity of cosmic rays is greater than the local Alfvén speed, the streaming instability excites Alfvén waves of a wavelength comparable to the particles' Larmor radius (Kulsrud & Pearce, 1969; Wentzel, 1974). Cosmic rays (originally propagating at speeds very close to the speed of light) are slowed down by pitch angle scattering until they move with the local Alfvén speed. We assume that the cosmic rays (ensemble of cosmic ray particles), moving initially with the speed of light, transfer all of their momentum to Alfvén waves (no damping processes are assumed). Using conservation of momentum we can then estimate the maximum possible amplitude of these waves.

The initial momentum of cosmic rays is

$$p = n_{\rm cr}\gamma m v \simeq n_{\rm cr}\gamma m c, \tag{4.11}$$

where $n_{\rm cr}$ is the number density of cosmic ray particles, m is the proton mass, v is the particle speed (taken to be close to c, the speed of light) and γ is the Lorentz factor.

When all the momentum has been transferred to Alfvén waves, the bulk speed of the ensemble of cosmic ray particles reduces to the Alfvén speed (as then the instability is suppressed). Momentum conservation then implies that

$$p = \frac{\delta B^2}{8\pi}\frac{1}{v_{\rm A}} + n_{\rm cr}\gamma m v_{\rm A}, \tag{4.12}$$

where δB is the amplitude of the Alfvén waves generated by the streaming instability, and $v_{\rm A}$ is the local Alfvén speed. The energy density of magnetic fluctuations is $\delta B^2/8\pi$ and they travel at the speed $v_{\rm A}$, thus their effective momentum is $\delta B^2/8\pi v_{\rm A}$.

Combining Eq. (4.11) and Eq. (4.12), we obtain

$$\begin{aligned} n_{\rm cr}\gamma m c &\simeq \frac{\delta B^2}{8\pi}\frac{1}{v_{\rm A}} + n_{\rm cr}\gamma m v_{\rm A}, \\ n_{\rm cr}\gamma m (c - v_{\rm A}) \simeq n_{\rm cr}\gamma m c &\simeq \frac{\delta B^2}{8\pi}\frac{1}{v_{\rm A}}, \quad \text{since } c \gg v_{\rm A}, \\ \frac{\epsilon_{\rm cr}}{c} &\simeq \frac{\delta B^2}{8\pi}\frac{1}{v_{\rm A}}, \end{aligned} \tag{4.13}$$

where $\epsilon_{\rm cr} = n_{\rm cr}\gamma m c^2$ is the energy density of cosmic rays

Assuming that the energy density of cosmic rays is comparable to the energy density of the magnetic field at much larger scales, $\epsilon_{\rm cr} \simeq B_0^2/(8\pi)$, it follows from Eq. (4.13) that

$$\frac{\delta B}{B_0} \simeq \left(\frac{v_{\rm A}}{c}\right)^{1/2}. \tag{4.14}$$

The pitch angle scattering is most efficient in the hot phase of the ISM (Kulsrud & Pearce, 1969; Cesarsky & Kulsrud, 1981; Kulsrud, 2005), where $B \simeq 5\mu$G and $n \simeq 10^{-3}$cm^{-3} for the thermal gas number density, so the Alfvén speed is of the order of $10^7\,{\rm cm\,s^{-1}}$. Eq. (4.14) then yields $\delta B/B_0 \simeq 10^{-2}$. Since the damping of Alfvén waves is neglected, this is an upper limit.

A similar estimate can be obtained without direct appeal to the energy equipartition between the magnetic fields and cosmic rays at larger scales. Farmer & Goldreich (2004), using properties of MHD turbulence, obtain $\delta B/B_0 \simeq (r_\mathrm{L}/l_0)^{1/4}$, where r_L is the Larmor radius of the particle and l_0 is the outer scale of turbulence ($\sim 100\,\mathrm{pc}$ for the ISM). For a $5\,\mathrm{GeV}$ proton in a $5\,\mu\mathrm{G}$ magnetic field, the Larmor radius of the particle is $10^{12}\,\mathrm{cm}$. Thus, at the Larmor scale, $\delta B/B_0 \simeq (10^{12}/10^{20})^{1/4} \simeq 10^{-2}$, which agrees with our estimate in the previous paragraph. This does not necessarily imply the equality between two physical processes, it just shows that those two physical processes give rise to magnetic fluctuations which are similar in strength.

4.5.2 Extrinsic turbulence: MHD turbulence cascade

The spectrum of hydromagnetic turbulence in the ISM extends to very small scales. Schekochihin et al. (2009) suggest that the spectrum of kinetic Alfvén waves is truncated by dissipation at scales as small as the thermal electron Larmor radius, which is approximately $3 \times 10^6\,\mathrm{cm}$ in the warm ionized ISM. This scale is much smaller than the typical Larmor radius ($r_\mathrm{L} \approx 10^{12}\,\mathrm{cm}$ for a $5\,\mathrm{GeV}$ proton in a $5\,\mu\mathrm{G}$ magnetic field) of cosmic rays and thus the magnetic turbulence due to sources other than cosmic rays also contribute to fluctuations at the Larmor scale.

The Alfvén turbulence is excited isotropically at a large scale l_max, usually the driving scale of turbulence ($l_\mathrm{max} \sim 100\,\mathrm{pc}$ for spiral galaxies and $l_\mathrm{max} \sim 10\,\mathrm{kpc}$ for galaxy clusters) with magnetic fluctuations $\delta B \sim B_0$ (B_0 is the background mean field, $\sim$ 5–10 μG for spiral galaxies and 1–5 μG for galaxy clusters). The energy cascades isotropically at larger scales, where the gas is collisional, up to a transition scale $l_\mathrm{t} \sim 1\,\mathrm{pc}$ (Brandenburg & Subramanian, 2005) and then the cascade is anisotropic (Goldreich & Sridhar, 1995, 1997). The slope of isotropic Alfvén wave turbulence spectrum is $k^{-5/3}$ and then at smaller scales $k_\parallel^{-2}$, for perturbations parallel to the magnetic field and $k_\perp^{-5/3}$, for perturbations perpendicular to the magnetic field. For the gyroresonance condition (Eq. (4.7), Farmer & Goldreich, 2004), only the fluctuations parallel to the magnetic field matters.

Thus, to estimate the magnitude of the fluctuations at the Larmor scale r_L we extrapolate the amplitude of fluctuations from the large scale l_max to r_L in two steps as illustrated in Fig. 4.4. First, from l_max to l_t via $M(k) \sim k^{-5/3}$ and then from l_t to r_L for $M(k_\parallel) \sim k_\parallel^{-2}$. So for the first part,

$$\begin{aligned} M(k) &\sim k^{-5/3}, \quad \delta B^2(k)/k \sim k^{-5/3}, \\ \delta B(k) &\sim k^{-1/3}, \quad \delta B(l) \sim l^{1/3}, \\ \Longrightarrow \frac{\delta B(l_{\max})}{\delta B(l_{\mathrm{t}})} &= \left(\frac{l_{\max}}{l_{\mathrm{t}}}\right)^{1/3}. \end{aligned} \tag{4.15}$$

Using $l_{\max} \sim 100\,\mathrm{pc}$, $\delta B(l_{\max}) \sim 5\,\mu\mathrm{G}$ in Eq. (4.15) for the ISM of spiral galaxies, we obtain

$$\delta B(l_{\mathrm{t}}) \approx \frac{5\,\mu\mathrm{G}}{100^{1/3}} \sim 1\,\mu\mathrm{G}. \tag{4.16}$$

For the second range from l_{t} to r_{L} using only the component parallel to the magnetic field.

$$\begin{aligned} \frac{\delta B(l_{\mathrm{t}})}{\delta B(r_{\mathrm{L}})} &= \left(\frac{l_{\mathrm{t}}}{r_{\mathrm{L}}}\right)^{1/2}, \\ \frac{\delta B(l_{\mathrm{t}})}{\delta B(r_{\mathrm{L}})} &\approx \left(\frac{1}{10^{-6}}\right)^{1/2} \approx 10^{3}, \\ \delta B(r_{\mathrm{L}}) &\approx 10^{-3}\,\mu\mathrm{G}. \end{aligned} \tag{4.17}$$

Thus, for the ISM of spiral galaxies, $\delta B(r_{\mathrm{L}})/B_0 \simeq 10^{-4}$.

The relative magnitude of the magnetic fluctuations due to the extrinsic turbulence at the Larmor radius of a $5\,\mathrm{GeV}$ particle is of the order of $\delta B/B_0 \simeq 10^{-4}$, which is negligible in comparison that of the self-generated waves in Section 4.5.1.

In our test-particle simulations, magnetic field is imposed and steady, so the streaming instability cannot occur. We, therefore, parametrize the PAS of cosmic rays by self-generated waves by rotating the velocity vector of each particle every Larmor time $2\pi/\omega_0$ by an angle given by Eq. (4.10) with $\delta B/B_0 = 10^{-2}$ and ϕ' uniformly distributed between 0 and 2π. We test this model numerically for particles propagating in a uniform magnetic field by solving the Lorentz force equation Eq. (3.2). Without the PAS, particles in a uniform magnetic field do not diffuse. However, when PAS is included, the particles scatter and over a sufficiently long time, diffusive behaviour develops as shown in Fig. 4.5. The parallel, $\kappa_{\parallel}$, and perpendicular, $\kappa_{\perp}$, diffusion coefficients are calculated using Eq. (3.4). Initially, the particles perform a ballistic motion along the uniform magnetic field and gyrate in the perpendicular direction. After a large number of scatterings ($t_{\mathrm{d}} \approx 5 \times 10^5$ Larmor times in Fig. 4.5), the diffusion sets in. In Fig. 4.5, $\kappa_{\perp}/\kappa_{\parallel} \approx 10^{-7}$ because the ensemble of particles have a larger mean

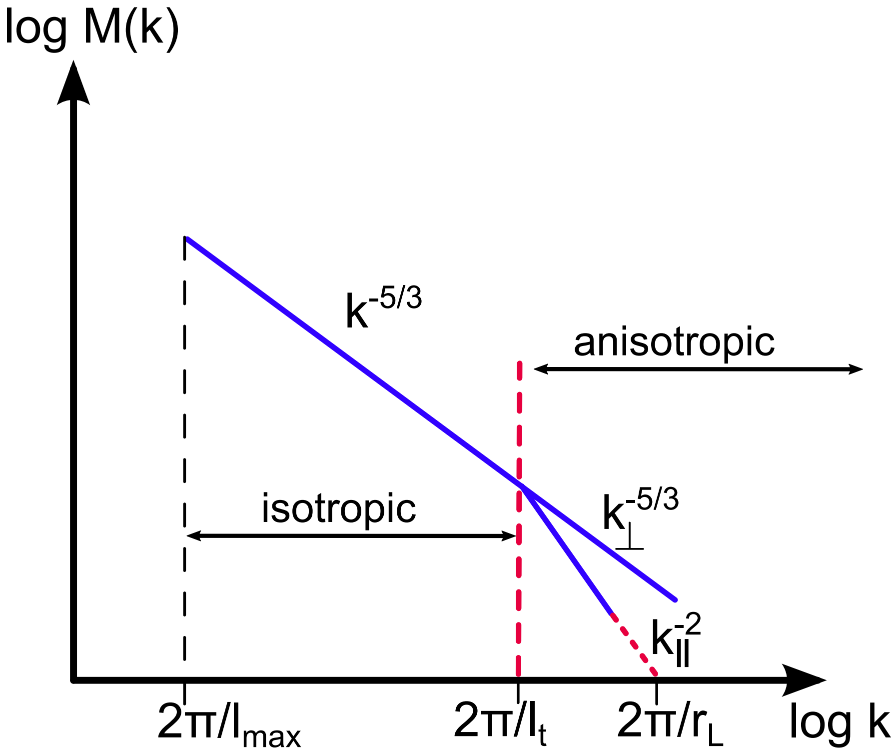

Figure 4.4: Sketch of the power spectrum of the random magnetic field showing the energy cascade from a larger scale ($l_{\rm max}$, usually the driving scale of turbulence) to the Larmor radius ($r_{\rm L}$) of the particle. The field is isotropic up to a transition scale ($l_{\rm t}$) and then it becomes anisotropic (Goldreich & Sridhar, 1995). When the turbulence is anisotropic, the power spectrum for parallel fluctuations is steeper than that for the perpendicular case. However, for the gyroresonance condition (Eq. (4.7)) only the fluctuations parallel to the field are important and thus we only consider that for our estimate.

free path along the direction of the uniform magnetic field. This is just a numerical test and not of any significance for the ISM because the ISM magnetic field has a significant random component. The process involves not only diffusion in the physical space but also diffusion in pitch angle, so we verify this by calculating the time correlation function of the pitch angle

$$\langle \mu(t)\mu(0)\rangle = \frac{\sum_{i=1}^{N} \mu_i(t)\mu_i(0)}{\mu_i(0)^2}, \tag{4.18}$$

where $\mu_i(t)$ is the pitch angle of ith particle at time t and N is total number of particles. As shown in Fig. 4.6, the $\langle \mu(t)\mu(0)\rangle$ decreases from unity, becoming negligible after $t \simeq t_\mathrm{d}$ when the pitch angle decorrelates. This confirms that the pitch angle also diffuses. It is non-trivial to calculate pitch angle diffusion coefficient numerically since pitch angle is a bounded quantity (it lies in $[-1, 1]$).

4.6 Spatial intermittency of cosmic ray distribution

We first look at the spatial distribution of cosmic rays as a function of particle's energy or Larmor radius (r_L). Fig. 4.7 shows the probability density function (PDF) of the particle number density n_cr obtained in intermittent (Fig. 4.7a) and randomized (Fig. 4.7b) magnetic fields. For cosmic rays of relatively high energy ($r_\mathrm{L}/l_b > 1$ or $r_\mathrm{L}/l_0 > 0.0244$), the number density n_cr is very nearly uniform in space, and its PDF is Gaussian. At lower energies, the PDF has a long, heavy tail at large n_cr, which signifies the presence of spatially localized structures in the cosmic ray distribution. It is remarkable that the distribution of (low energy) cosmic rays is intermittent in both intermittent and Gaussian magnetic fields. The PDF of n_cr in presence of a mean magnetic field of various strengths, with (Fig. 4.8a) and without (Fig. 4.8b) particle pitch angle scattering (PAS), is shown in Fig. 4.8. The mean magnetic field does not eliminate the tail in the PDF and even makes it heavier.

Cosmic rays fill all the volume available. However, the distribution for low energy cosmic rays (especially for $r_\mathrm{L}/l_0 = 0.0016$ or $r_\mathrm{L}/l_b \simeq 0.06$) is not homogeneous. Random magnetic fields produce cosmic ray distributions where a significant fraction of the volume is occupied by strong particle concentrations. The PDFs of n_cr shown in Fig. 4.7 have a nearly Gaussian core that contains most of the particles and has n_cr close to its mean value. The tail represents rare but intense small-scale spatial structures.

Fig. 4.9 shows the number density of cosmic rays, obtained as described in Section 4.3, in the intermittent magnetic field. Fig. 4.9a shows the cosmic rays structures in three dimensions. This is further illustrated in Fig. 4.9b, which shows strong peaks in n_cr against weak but

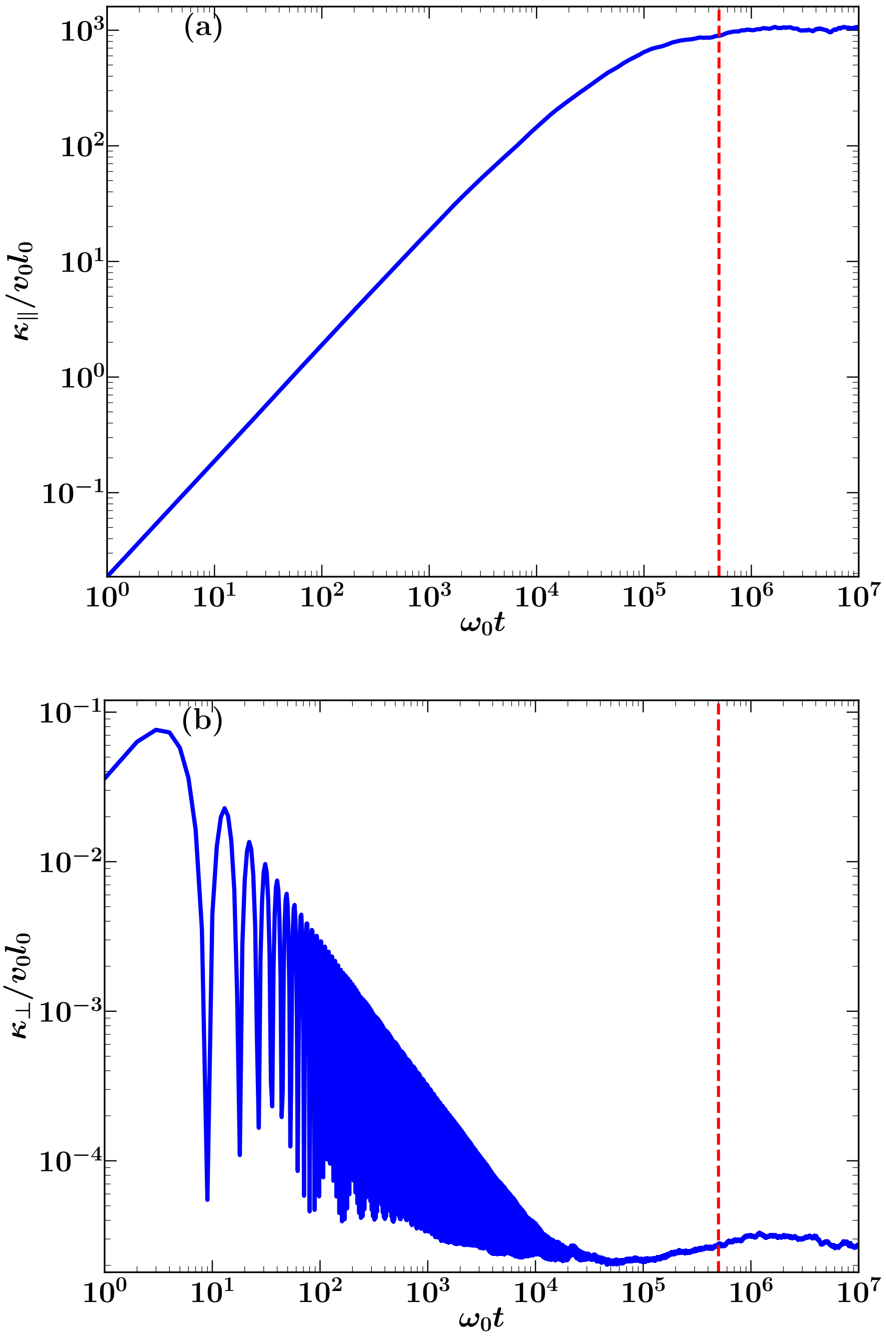

Figure 4.5: Normalized parallel $\kappa_\parallel/v_0 l_0$ (a) and perpendicular $\kappa_\perp/v_0 l_0$ (b) cosmic ray diffusivity as a function of normalized time $\omega_0 t$ for particles propagating in a uniform magnetic field but with pitch angle scattering (PAS) model included. Initially, the particle gyrates around magnetic field and thus $\kappa_\parallel$ varies linearly with time and because of gyration the $\kappa_\perp$ oscillates. After sufficient scattering, the diffusion sets in both in the direction parallel and perpendicular to the imposed uniform magnetic field. The red dotted line shows the diffusion time t_d.

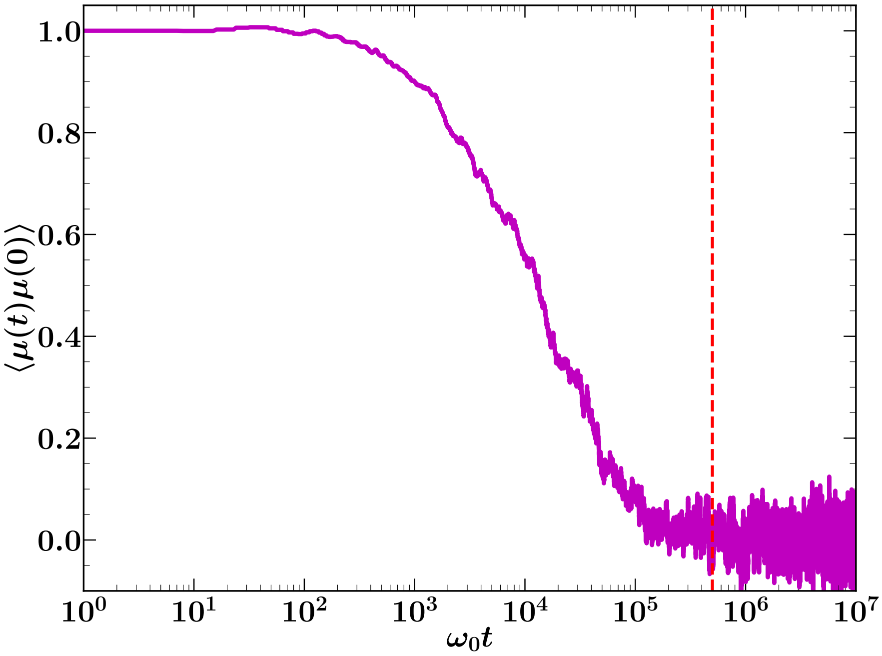

Figure 4.6: Time correlation function of pitch angle μ as a function of normalized time $\omega_0 t$ for particles propagating in a uniform magnetic field with PAS included. The correlation gradually decreases and drops to ≈ 0 once the diffusion sets in. This can also be used to determine the diffusion time $t_{\rm d}$ (shown by the red dotted line).

fluctuating background (core part of the cosmic ray distribution in Fig. 4.7a). The distribution is inhomogeneous and evidently sensitive to the magnetic field structure. The distribution of cosmic rays is affected by both the mean magnetic field and pitch angle scattering. As shown in Fig. 4.8, the mean magnetic field enhances the intermittency in the cosmic ray distribution, whereas pitch angle scattering reduces it. Fig. 4.10 illustrates how the shape and number of structures in the cosmic ray distribution are affected. With a mean field, the structures are more numerous and many extend along the mean field direction, the x-axis in Fig. 4.10a. This effect becomes significant when $B_0/\,b_{\rm rms} \geq 1$. On the other hand, pitch angle scattering enhances cosmic ray diffusion and, consequently, reduces their intermittency, as shown in the Fig. 4.10b.

The degree of intermittency can be measured in terms of the parameter $f = \langle n_{\rm cr}\rangle^2/\langle n_{\rm cr}^2\rangle$, the volume filling factor (Table 4.1). For high-energy particles, $r_{\rm L}/l_0 = 0.1592$ or $r_{\rm L}/l_b \simeq 6.52$, f is close to unity, indicating a homogeneous particle distribution. This feature of the cosmic ray distribution is further detailed in Fig. 4.11 where we show the dependence of the fractional volume of a region where $n_{\rm cr}/\langle n_{\rm cr}\rangle \geq \nu$ on ν for the configurations of Table 4.1. Particles of sufficiently high energy, $r_{\rm L}/l_b \gg 1$, are not sensitive to the fine

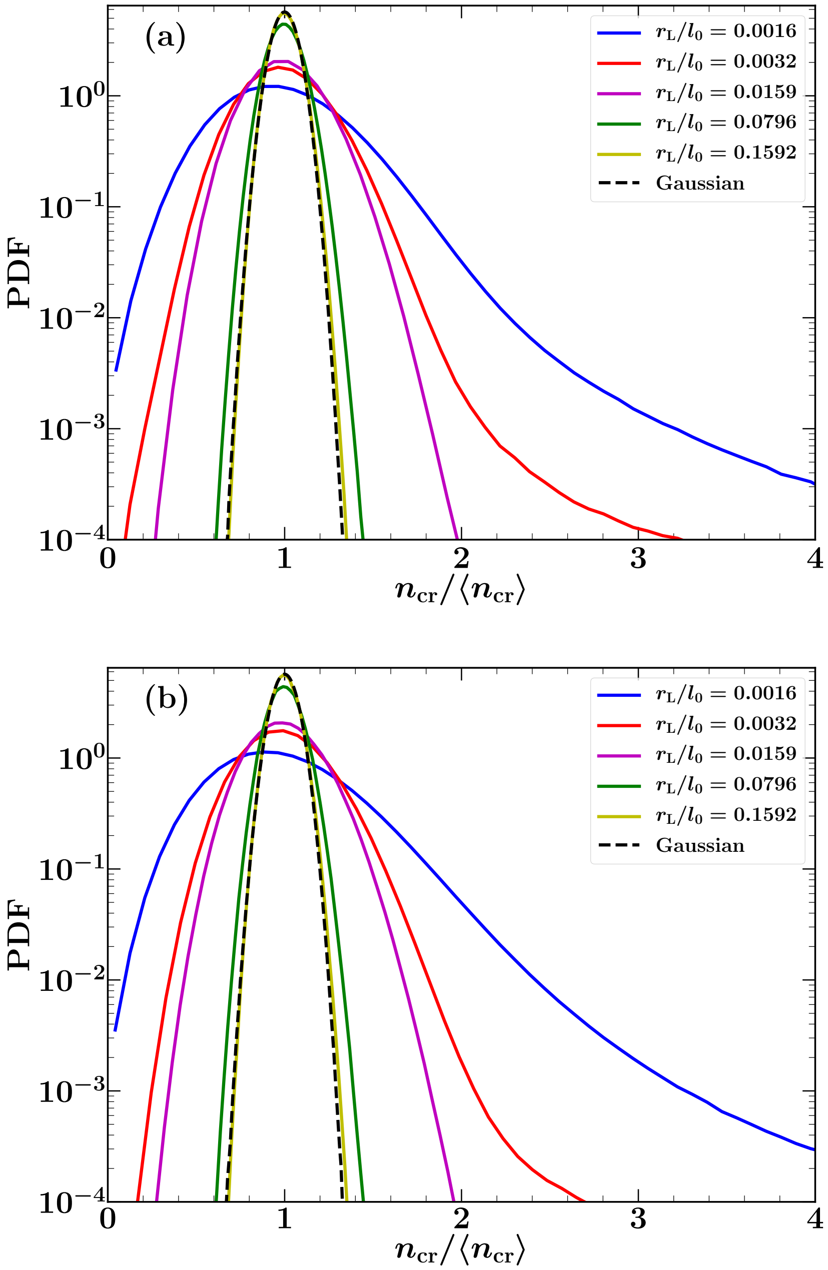

Figure 4.7: Probability density function (PDF) of the relative number density of cosmic ray particles, $n_{\mathrm{cr}}/\langle n_{\mathrm{cr}}\rangle$, where $\langle n_{\mathrm{cr}}\rangle$ is the mean cosmic ray number density over the numerical domain, for various r_{L}/l_0 in intermittent (a) and randomized (Gaussian) magnetic fields (b), with no mean-field and no pitch angle scattering (PAS). Long tails are a signature of intermittent structures in the cosmic ray distribution. For high-energy particles, the distribution is nearly Gaussian (with width increasing as energy decreases) in both intermittent and Gaussian magnetic fields, but below a certain energy ($r_{\mathrm{L}} \lesssim l_b$) long tails develop. A black dashed line shows the PDF of a random variable drawn from a Gaussian distribution with unit mean value and standard deviation of 0.07 (obtained by fitting the Gaussian).

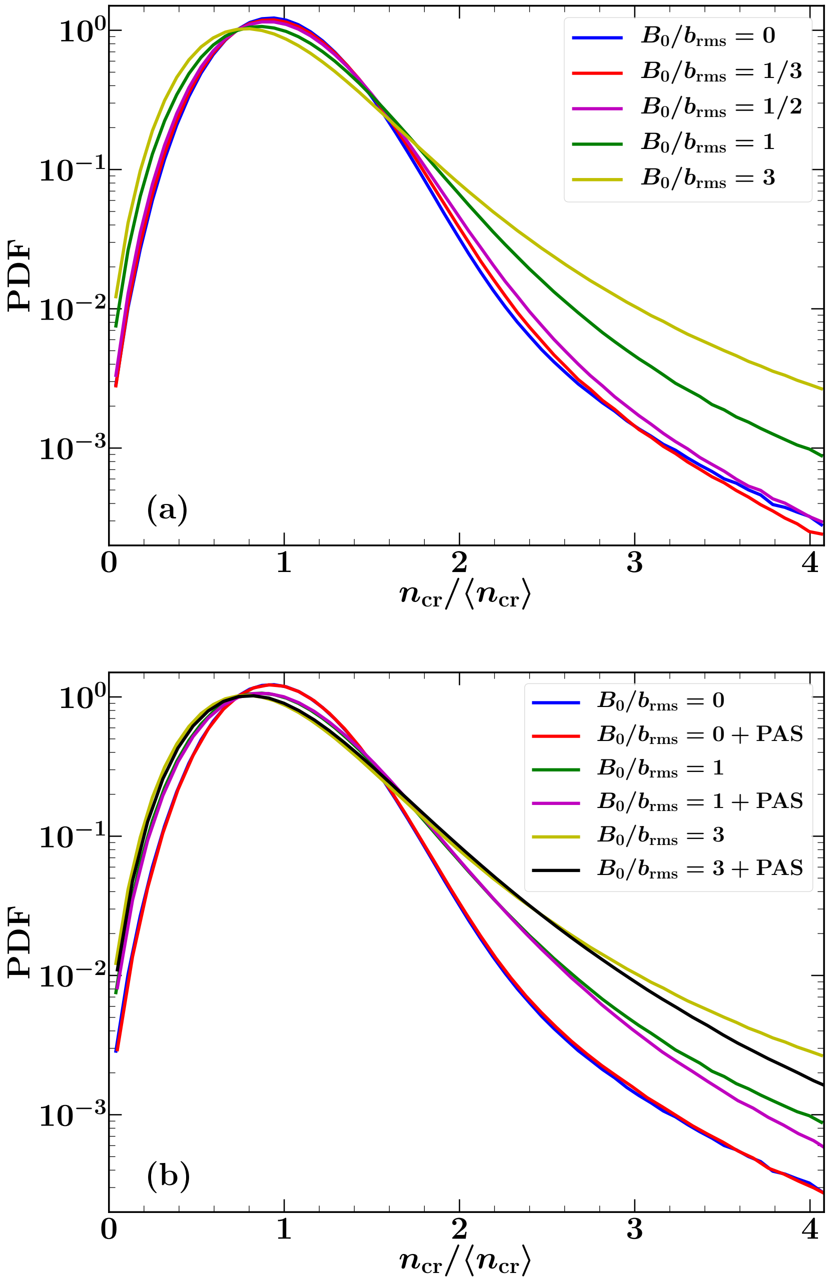

Figure 4.8: PDF of $n_{\rm cr}/\langle n_{\rm cr}\rangle$ for $r_{\rm L}/l_0 = 0.0016$ in the intermittent field with an imposed mean field of various magnitudes B_0 (a) and with the pitch angle scattering further included (b). Intermittency in the cosmic ray distribution increases as the mean field becomes stronger, especially for $B_0/\,b_{\rm rms} \geq 1$, manifested in heavier tails at larger $n_{\rm cr}/\langle n_{\rm cr}\rangle$. The pitch angle scattering enhances diffusion and thus decreases the level of intermittency.

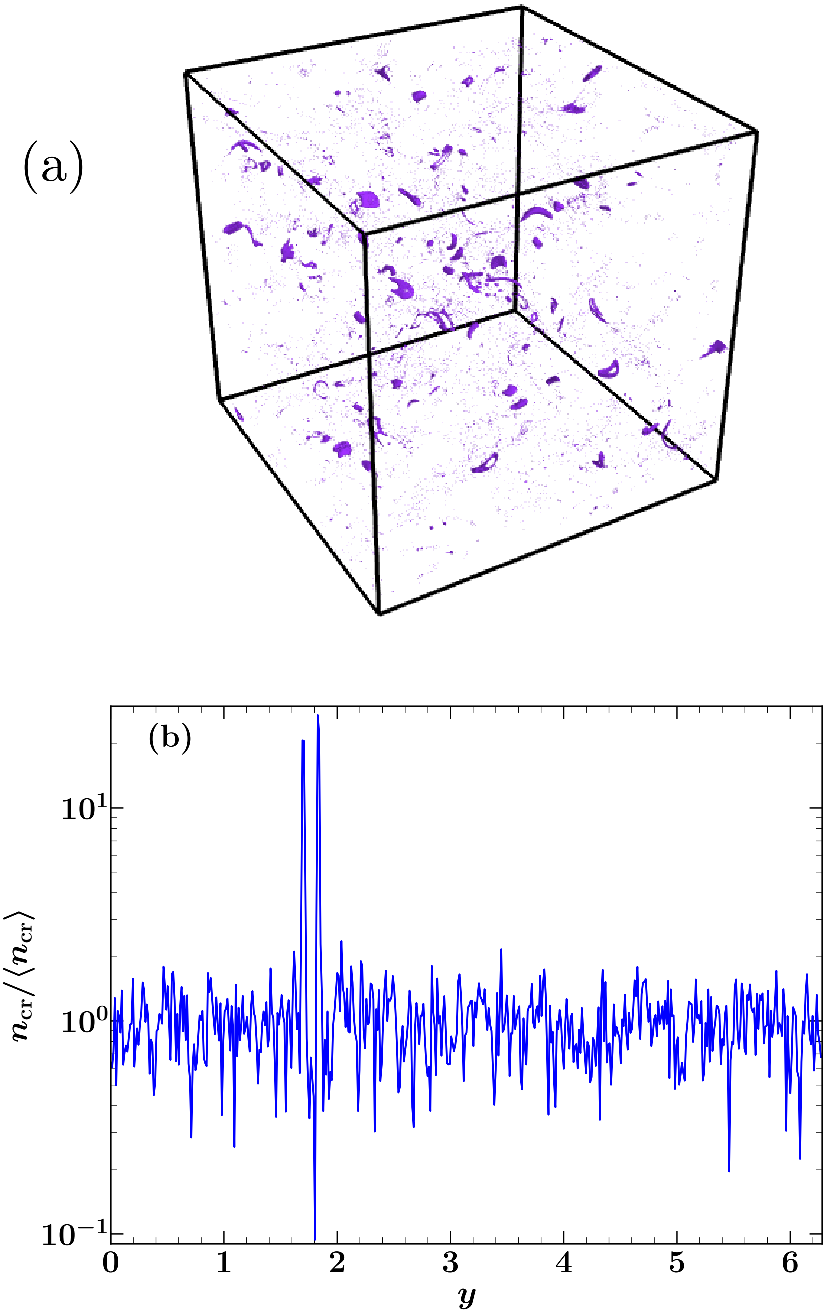

Figure 4.9: (a) Isosurfaces of the number density of cosmic rays in the intermittent magnetic field at $n_{\mathrm{cr}}/\langle n_{\mathrm{cr}}\rangle = 3.5$ for $r_{\mathrm{L}}/l_0 = 0.0016$. A number of small-scale cosmic ray structures are seen confirming an intermittent cosmic ray distribution. (b) The variation of the relative number density of the particles along the straight line $(x, z) = (\pi, 3.97)$, characterized by rare, strong maxima against a weakly fluctuating background.

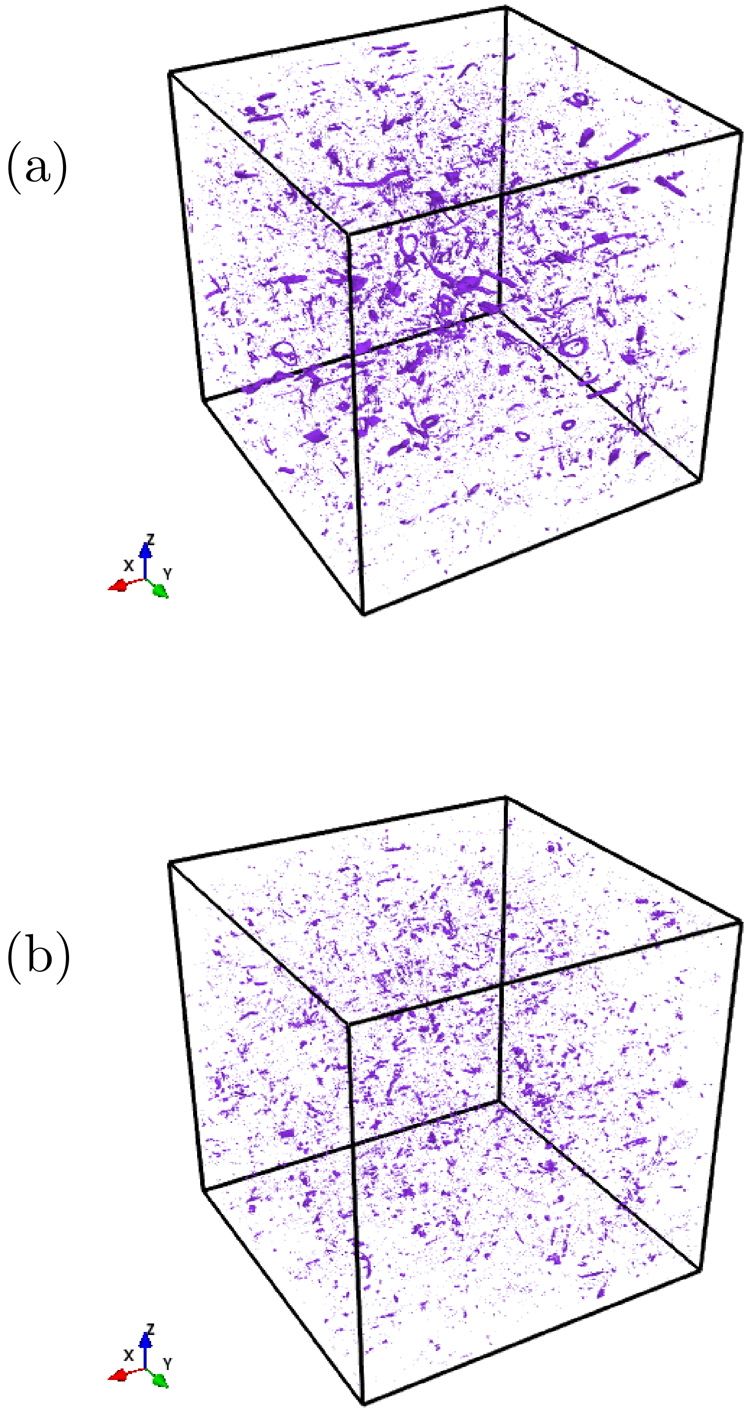

Figure 4.10: Isosurfaces of the number density of cosmic rays at $n_{\mathrm{cr}}/\langle n_{\mathrm{cr}}\rangle = 3.5$ for $r_{\mathrm{L}}/l_0 = 0.0016$ in an intermittent magnetic field with an imposed mean field of a strength $B_0/\,b_{\mathrm{rms}} = 1$ aligned with the x-axis (a) and with PAS further added (b).

Table 4.1: The volume filling factor $f = \langle n_{\rm cr}\rangle^2/\langle n_{\rm cr}^2\rangle$ in a representative selection of simulations, summarising the effects of particle energy, magnetic field structure and pitch angle scattering (PAS).

Model	$r_{\rm L}/l_0$	b	$B_0/\,b_{\rm rms}$	PAS	f
A	0.0016	Intermittent	0	no	0.81
B	0.0016	Intermittent	1	no	0.68
C	0.0016	Intermittent	1	yes	0.84
D	0.0016	Randomized	0	no	0.96
E	0.1592	Intermittent	0	no	0.99

structure of the magnetic field and the probability distribution of their number density is Gaussian. The dependence of the fractional volume, shown in Fig. 4.11, on the presence of the mean magnetic field and its change due to the pitch angle scattering confirms that the spatially intermittency increases on including mean field and decreases (but is not eliminated) on including pitch angle scattering.

Fig. 4.12 shows the PDF of magnetic field energy density and cosmic ray distribution for the tail region. Both distributions are power laws with exponent close to $-11/4$ for both the magnetic field and cosmic ray number density.

4.7 Statistical relation between magnetic fields and cosmic rays

The simplest measure of a relation between cosmic rays and magnetic field is their cross-correlation coefficient,

$$C(n_{\rm cr}, B^2) = \frac{\langle n_{\rm cr}B^2\rangle - \langle n_{\rm cr}\rangle\langle B^2\rangle}{\sigma_{n_{\rm cr}}\sigma_{B^2}}\,, \tag{4.19}$$

where $\langle\cdots\rangle$ denotes an average over the whole domain, and σ is the standard deviation of the quantity specified in the subscript. The value of C ranges from $C = 1$ for perfect correlation to $C = -1$ for perfect anti-correlation. In all cases considered, we find that the two distributions are uncorrelated, $C \approx 0$. This is true even for the lowest-energy cosmic rays considered ($r_{\rm L}/l_0 = 0.0016$) despite the fact that they are closely confined to magnetic field lines. The correlation does not emerge even when the cosmic ray density and magnetic field are smoothed to a coarser spatial grid. To confirm that this behaviour is not an artefact of the initial conditions used for the cosmic ray particles, we have also performed a simulation with their initial positions in the regions of the strongest magnetic field shown in Fig. 3.5a. The value of C in this case is very close to unity initially but vanishes quickly, within the time

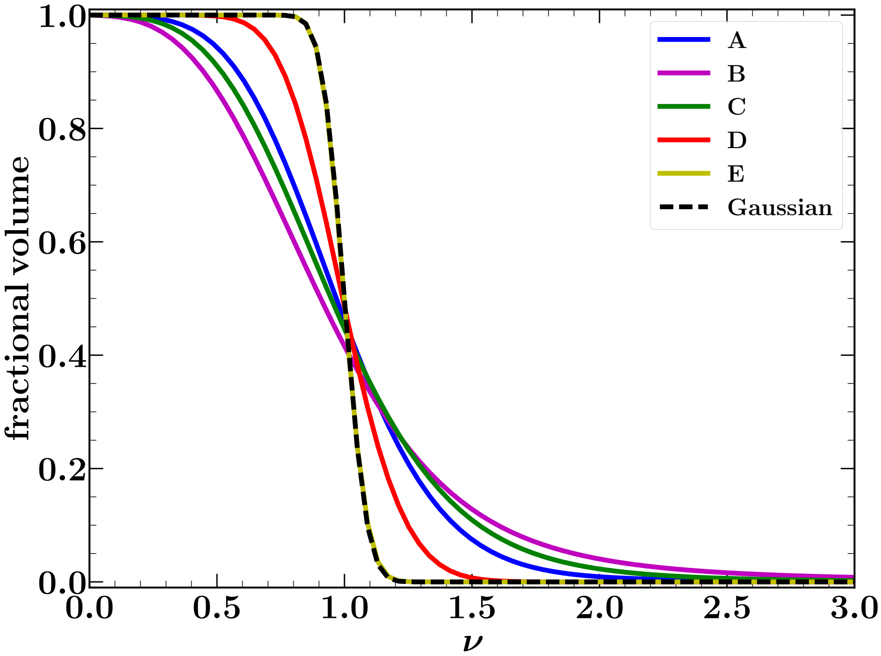

Figure 4.11: The fractional volume of cosmic ray structures with $n_{\rm cr}/\langle n_{\rm cr}\rangle \geq \nu$ for Models A–E of Table 4.1. A black dashed line shows the fractional volume for a random variable drawn from a Gaussian distribution with unit mean value and standard deviation of 0.07.

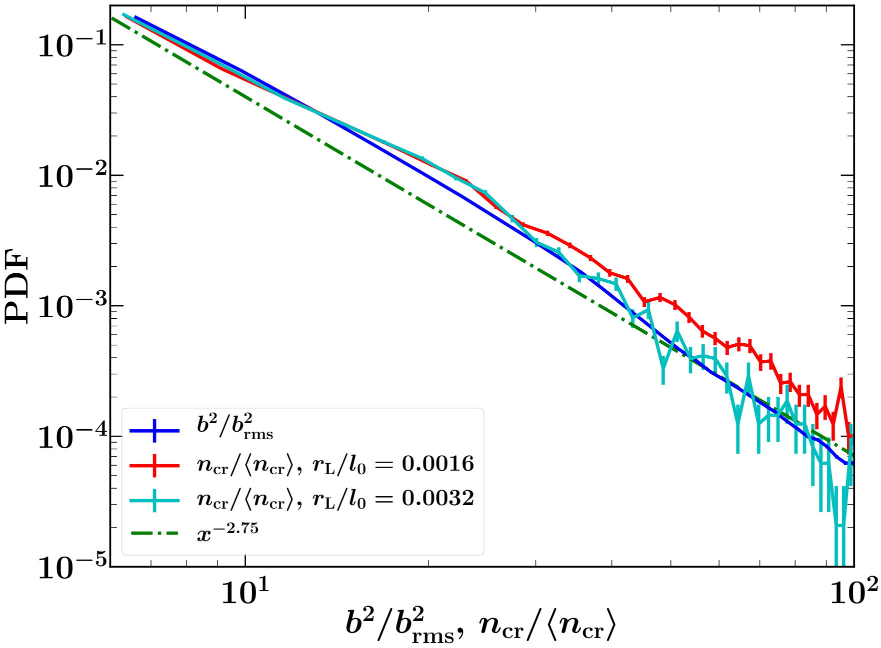

Figure 4.12: PDF of intermittent magnetic field energy density normalized to its rms value, $b^2/\,b^2_{\rm rms}$, and the number density of cosmic rays normalized to its mean, $n_{\rm cr}/\langle n_{\rm cr}\rangle$, for $r_{\rm L}/l_0 = 0.0016, 0.0032$. All three of them have power-law tails and the same exponent. Statistical errors are considerable at probability densities below about 5×10^{-5}.

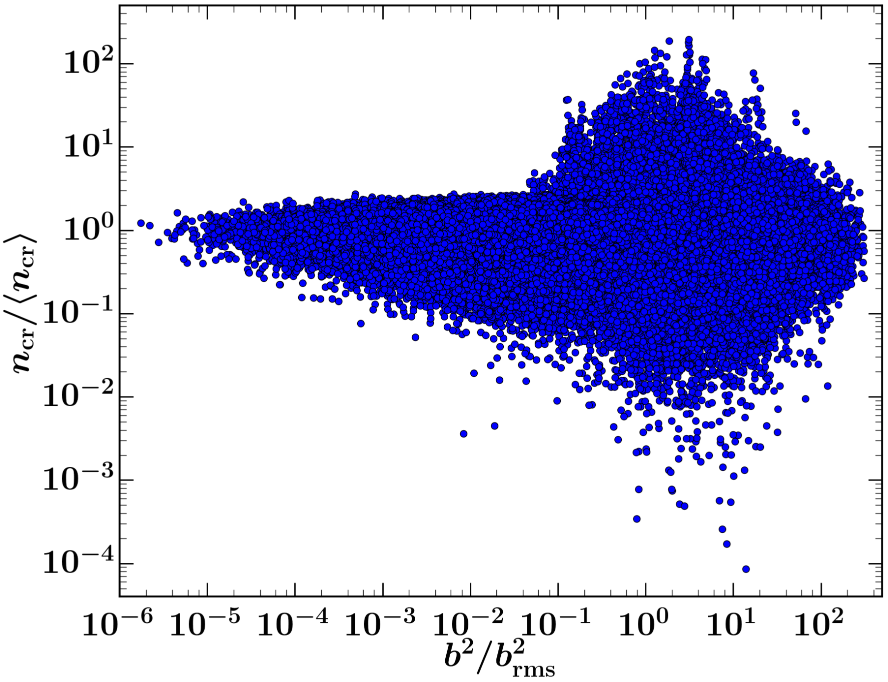

Figure 4.13: The scatter plot of cosmic ray number density, $n_{\rm cr}/\langle n_{\rm cr}\rangle$ and magnetic energy density, $b^2/\,b^2_{\rm rms}$, in an intermittent magnetic field for $r_{\rm L}/l_0 = 0.0016$. If they are correlated, we would expect a straight line with unit gradient but instead we see a cloud of points.

of order the diffusion time, $t_{\rm d}$. Fig. 4.13 shows the scatter plot of the cosmic ray number density and magnetic field energy density, whose form confirms that the two variables are uncorrelated.

We now check for their statistical independence, i.e., whether $p(n_{\rm cr}, b^2)$, the joint probability distribution function of the two variables is equal to $p(n_{\rm cr})p(b^2)$, the product of the probability distribution function of each component. To test for the statistical independence of b^2 and $n_{\rm cr}$, i.e. $p(n_{\rm cr}, b^2) = p(n_{\rm cr})p(b^2)$, we calculate the conditional probability distributions $p(b^2|n_{\rm cr})$ for a range of $n_{\rm cr}$ values and use the Kolmogorov-Smirnov (KS) test to prove that they are indistinguishable from each other. This is also done for $p(n_{\rm cr}|b^2)$ and a range of b^2. Fig. 4.14a and Fig. 4.16a show the joint probability densities of magnetic field strength and cosmic ray number densities in the intermittent and Gaussian (randomized) magnetic fields, respectively. We perform KS test on the conditional probability distributions, $p(b^2|n_{\rm cr})$ and $p(n_{\rm cr}|b^2)$ to check whether each of them is drawn from the same distribution. This is measured by the D statistic of the test, which is the absolute maximum difference between the cumulative distribution functions of the two samples. A value of D smaller than 0.087 provides 95% confidence that the two samples are drawn from the same distribution. For this we consider pairs of samples from the conditional probability distribution $p(b^2|n_{\rm cr})$ with consecutive $n_{\rm cr}$ (cuts along consecutive values of y-axis of Fig. 4.14a). We performed the KS test for all such pairs and found the mean value of D to be $\simeq 0.062$. A similar calculation for $p(n_{\rm cr}|b^2)$ gives $\simeq 0.072$. The mean D values for Gaussian (randomized) magnetic fields are $\simeq 0.054$ for $p(n_{\rm cr}|b^2)$ and $\simeq 0.114$ (higher than the critical value of $D = 0.087$ bit still quite low) for $p(b^2|n_{\rm cr})$ respectively. The small D values suggest that the cosmic ray number density and magnetic field distributions are independent of each other and the joint probability $p(n_{\rm cr}, b^2)$ can be factorized into $p(n_{\rm cr})$ and $p(b^2)$. We find the functional dependence of $p(n_{\rm cr})$ on $n_{\rm cr}$ and $p(b^2)$ on b^2 as follows. Cuts through the joint PDF in the intermittent magnetic field, shown in Fig. 4.14a, are well fitted with a Gaussian which, remarkably, has neither the mean value nor the standard deviation dependent on b^2 (as shown in Fig. 4.14b). The dependence of the maximum value of the conditional PDF $p_n(n_{\rm cr}|b^2)$ on b^2 is shown in Fig. 4.15a together with its fit with an exponential function. In the range $0 \leq b^2/\,b^2_{\rm rms} \leq 0.3$ and $0.25 \leq n_{\rm cr}/\langle n_{\rm cr}\rangle \leq 1.75$, the joint PDF of $n_{\rm cr}$ and b^2 has the form

$$p(n_{\rm cr}, b) \approx (1.6 + 9.9\mathrm{e}^{-10.5b^2/\,b^2_{\rm rms}})\mathrm{e}^{-(n_{\rm cr}/\langle n_{\rm cr}\rangle-1)^2/0.18}. \tag{4.20}$$

The relative accuracy of the fitted parameters is better than 5 per cent. This is confirmed by the scatter of the measured and fitted values of $p(n_{\rm cr}, b^2)$ shown in the lower left panel of Fig. 4.15b: for a perfect fit, the points would be all on the bisector of the quadrant angle. The scatter about that line, shown dashed (blue) provides a measure of the accuracy of the fit. A very small number of points systematically deviate from the main dependence. The joint PDF is thus factorizable emphasizing that both the distribution are independent.

Similar analysis for $p(n_{\rm cr}, b^2)$ in the randomized (Gaussian) magnetic field is illustrated in Fig. 4.16 and Fig. 4.17. As in the intermittent magnetic field, the joint PDF is factorizable in an approximate manner and thus $n_{\rm cr}$ and b^2 are statistically independent. The form of the conditional PDF of magnetic field strength is a lognormal distribution,

$$p(b|n_{\rm cr}) \approx 0.5(b^2/\,b^2_{\rm rms})^{-1}\mathrm{e}^{-0.3\ln(b^2/\,b^2_{\rm rms})^2} \tag{4.21}$$

for $0 \leq b^2/\,b^2_{\rm rms} \leq 3$. We find that

$$p(n_{\rm cr}, b) \approx 0.5(b^2/\,b^2_{\rm rms})^{-1}\mathrm{e}^{-0.3\ln(b^2/\,b^2_{\rm rms})^2}\,\mathrm{e}^{-(n_{\rm cr}/\langle n_{\rm cr}\rangle-0.9)^2/0.32}\,. \tag{4.22}$$

The scatter plot of the measured and fitted PDF values is shown (with the dashed blue line for the perfect match) in Fig. 4.17b.

To summarize, the distributions of cosmic ray number density and magnetic field strength

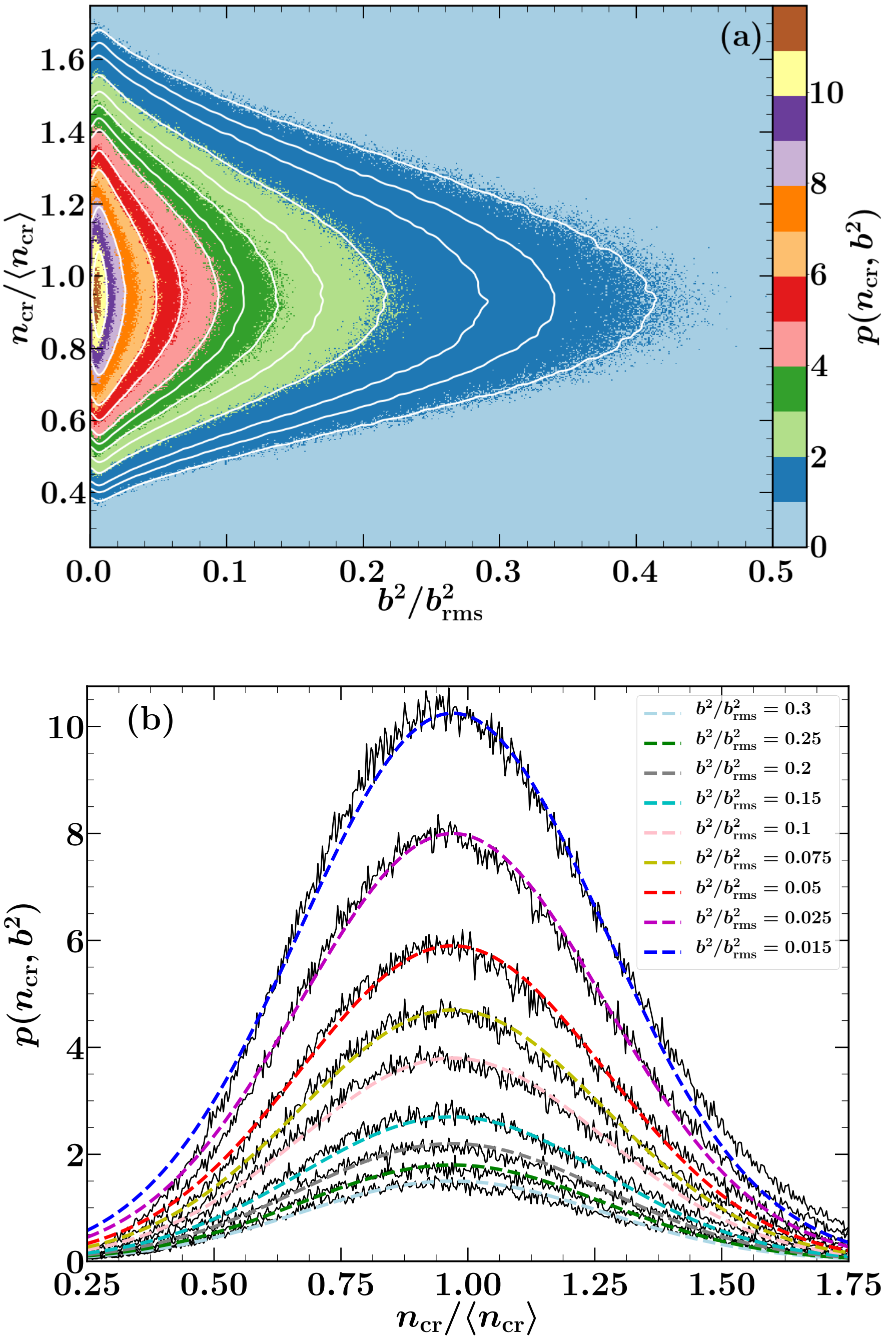

Figure 4.14: (a) The joint probability density function (PDF) $p(n_{\rm cr}, b^2)$ of $b^2/\,b^2_{\rm rms}$ and $n_{\rm cr}/\langle n_{\rm cr}\rangle$ in the intermittent magnetic field for $0 \leq b^2/\,b^2_{\rm rms} \leq 0.5$ and $0.25 \leq n_{\rm cr}/\langle n_{\rm cr}\rangle \leq 1.75$. (b) The joint PDF $p(n_{\rm cr}, b^2)$ as a function of $n_{\rm cr}/\langle n_{\rm cr}\rangle$ alone for various values of $b^2/\,b^2_{\rm rms}$ together with least-square fits of the form $p(n_{\rm cr}, b^2) = A(b^2){\rm e}^{-(n_{\rm cr}/\langle n_{\rm cr}\rangle - 1.0)^2/0.18}$ (smooth dashed curves).

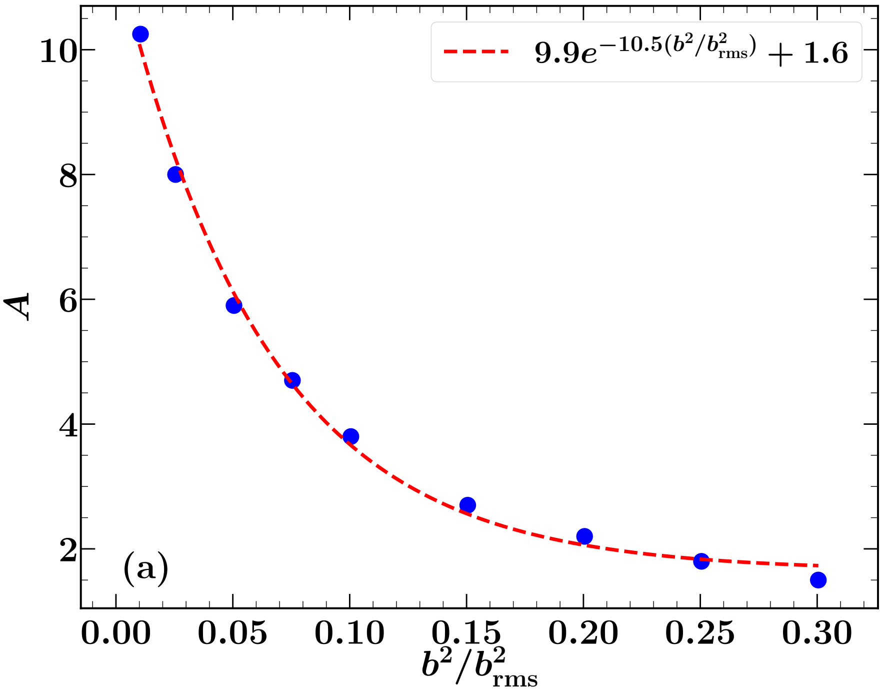

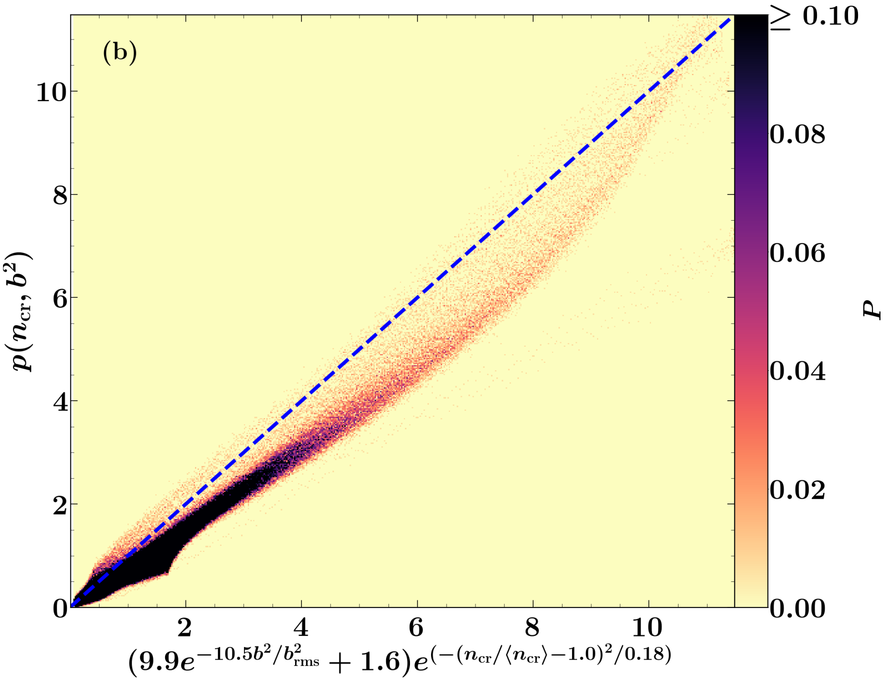

Figure 4.15: (a) The height of the curve's peak in Fig. 4.14b A as a function of $b^2/\,b^2_{\mathrm{rms}}$ fitted with an exponential (red, dashed). (b) Scatter plot of the computed and fitted values of $p(n_{\mathrm{cr}}, b^2)$, with a line corresponding to the perfect agreement shown (dashed, blue). Most points lie close to the dashed blue line confirming that the accuracy of the fit is reasonable.

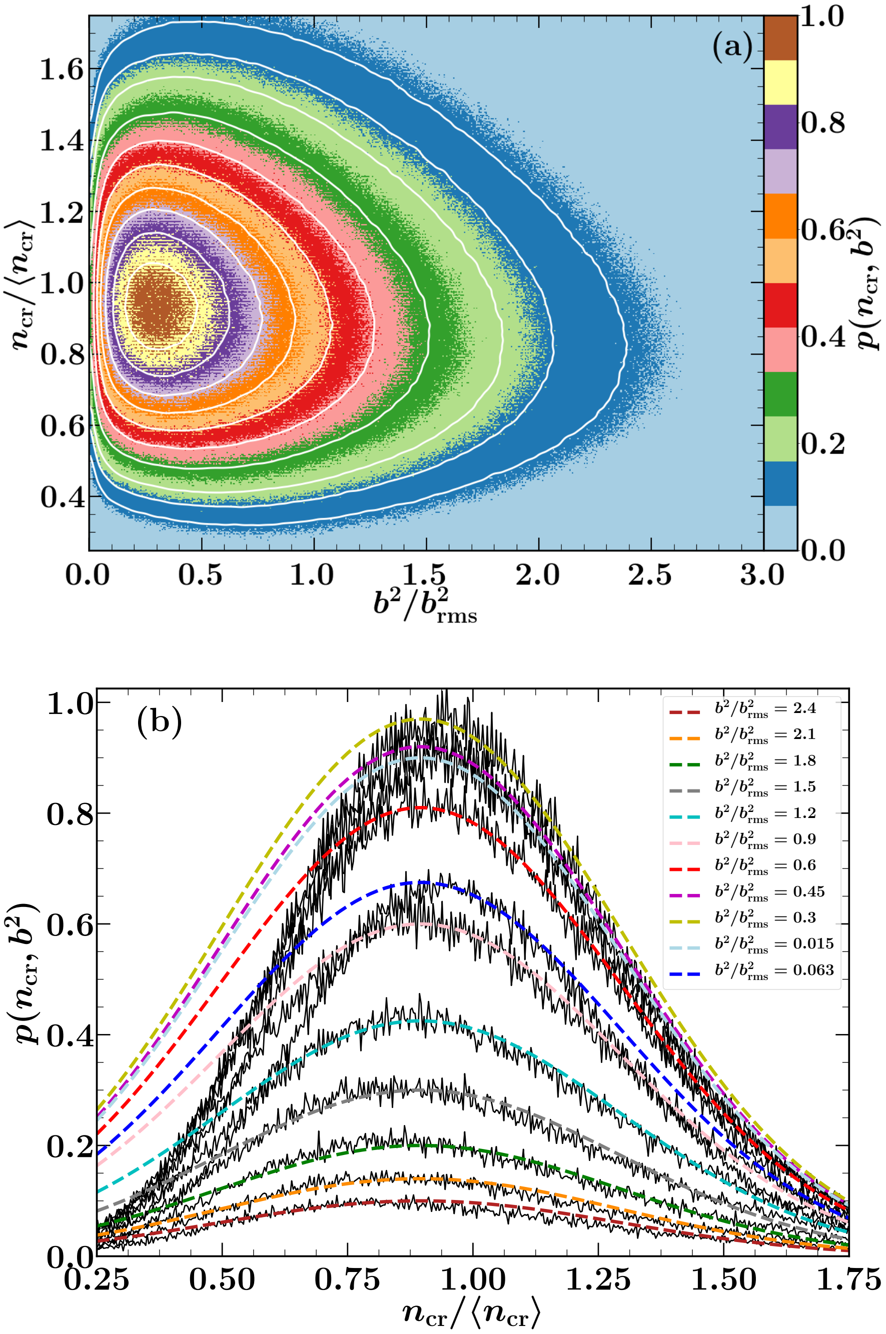

Figure 4.16: As in Fig. 4.14 but for the randomized (Gaussian) magnetic field for $0 \leq b^2/\, b^2_{\rm rms} \leq 3.0$ and $0.25 \leq n_{\rm cr}/\langle n_{\rm cr}\rangle \leq 1.75$.

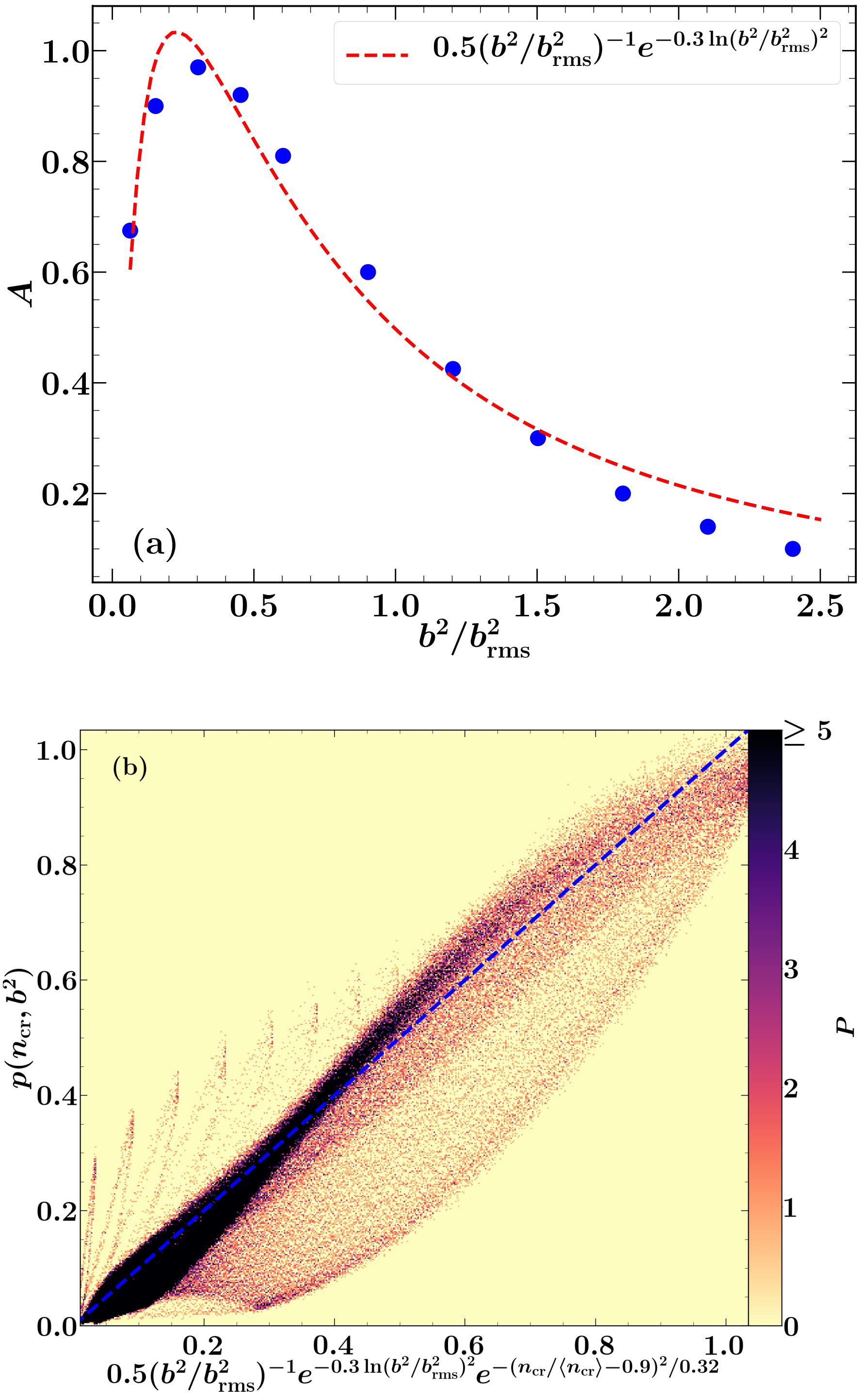

Figure 4.17: As in Fig. 4.15 but for the randomized (Gaussian) magnetic field for $0 \leq b^2/\,b^2_{\rm rms} \leq 3.0$ and $0.25 \leq n_{\rm cr}/\langle n_{\rm cr}\rangle \leq 1.75$.

are practically statistically independent in the diffusive regime of the cosmic rays. In the intermittent magnetic field, the joint PDF of $n_{\rm cr}$ and b is well approximated by a Gaussian in $n_{\rm cr}$ and a modified Gaussian in b. In randomized (Gaussian) field, the joint PDF is approximated by a Gaussian in $n_{\rm cr}$ and a lognormal distribution in b^2. The two variables remain statistically independent for cosmic rays of other energies too. The exact parameters of the joint PDF are likely to depend on details of the magnetic field structure and the energy of the particle. For both intermittent and non-intermittent magnetic fields, the joint PDF is separable which illustrates that the cosmic rays and magnetic field distributions are statistically independent. Assuming that this also applies to cosmic-ray electrons, Eq. (4.1) can also be written as

$$I = K \int_L n_{\rm cre}\, b_\perp^2 \, {\rm d}l = \frac{K}{L} \int_L n_{\rm cre}\, {\rm d}l \int_L b_\perp^2 \, {\rm d}l = KL \langle n_{\rm cre} \rangle \langle b_\perp^2 \rangle, \tag{4.23}$$

where $\langle \cdots \rangle$ denotes the average over the path length. Thus, one can use synchrotron intensity and the mean cosmic ray number density to obtain the average magnetic field strength.

4.8 Random magnetic traps

Since $n_{\rm cr}$ is not correlated with the magnetic field strength, the localized concentrations of cosmic rays must be caused by some geometrical property of the magnetic field lines. In fact, we find that these regions occur where cosmic rays are trapped between two magnetic mirrors, i.e., positions where magnetic lines converge.

Magnetic trapping of particles by long wavelength waves was studied analytically to explain the confinement of cosmic ray particles for which gyroresonant waves are damped quickly (Holman et al., 1979; Felice & Kulsrud, 2001). To test this numerically, we solve the equation of motion for a single particle in a uniform magnetic field along x axis, superimposed on a magnetic wave packet of the form Eq. (4.4) (same as Section 4.4) having a wavelength $2\pi/k \gg r_{\rm L}$. Fig. 4.18a shows the time evolution of the cosine of the particle pitch angle μ. The particle returns to follow its initial trajectory but in the opposite direction, after a reflection. The particles moves back and forth along x-axis and the trapped particles follow a closed curve in μ vs. kx plot. This is shown in Fig. 4.18b. The particles are trapped only if the pitch angle is less than a critical value.

Now we consider the particle distributions in random magnetic fields, in particular, regions (shown in Fig. 4.9 and Fig. 4.10) where cosmic ray density is higher than the mean cosmic ray density. These regions represent random magnetic traps, as confirmed by the form of individual particle trajectories and the magnetic field structure in locations of the

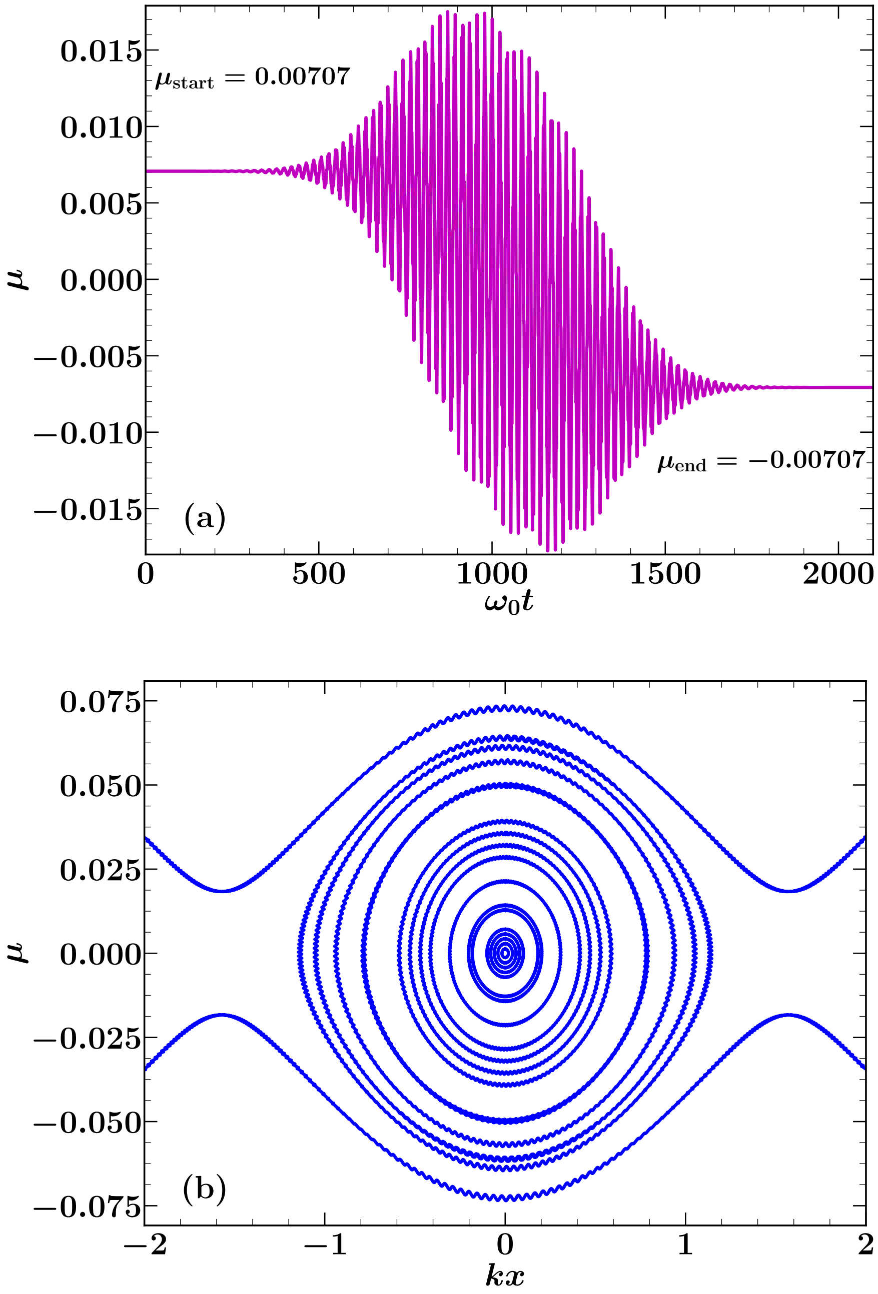

Figure 4.18: (a) The cosine of the particle pitch angle μ calculated from its trajectory as a function of normalized time $\omega_0 t$ for a single particle reflection. The fact that $\mu_{\rm final} = -\mu_{\rm initial}$ confirms that the particle is reflected back along the arrival direction, i.e. oscillates between the magnetic mirrors. (b) The cosine of the pitch angle μ as a function of kx, where k is the wavenumber of the wave and x is the displacement along the x-axis. For particles with the same energy but different initial pitch angles (before they enter the trap). When the initial pitch angle is less than a critical value, the particles are trapped.

high cosmic ray concentration. Fig. 4.19a shows a particle trajectory near a maximum of n_{cr} at $(x, y, z) = (3.15, 2.55, 5.975)$ in Fig. 4.9a. If a magnetic flux tube is pinched at both ends, then particles are repeatedly reflected at the magnetic mirrors (between the two ends), creating a magnetic trap. Because the field lines must be reasonably smooth in order to form a trap (otherwise the particle might get scattered), the regions of high cosmic ray density are typically smaller than the magnetic correlation length, l_b. The cosine of the particle's pitch angle, μ is shown in Fig. 4.19b as a function of position and magnetic field strength (similar to one of the closed curves in Fig. 4.18b). This quantity reverses sign along the trajectory whenever the particle is reflected at an end of the magnetic trap. This happens where the magnetic field is relatively strong. Magnetic trapping is associated with the conservation of $v_{\perp}^2/B$, an adiabatic invariant (Jackson, 1998), where $v_{\perp} = v \sin\theta$ is the particle speed perpendicular to the local magnetic field. We have verified that $v_{\perp}^2/B = \mathrm{const}$ with relative accuracy of order 10^{-5} along the trajectories of the trapped particles.

We estimate the enhancement of cosmic ray number density due to magnetic traps as follows. Consider a magnetic trap of a length l in a magnetic flux tube of radius d. The particle can escape the trap by scattering perpendicular to the field lines. For an ensemble of particles within the trap, the expected trapping time is estimated as $\tau_{\perp} \simeq d^2/\kappa_{\perp}$, where $\kappa_{\perp}$ is the local perpendicular diffusivity of cosmic rays. Defining $N_{\mathrm{m},\perp}$ to be the number of times that a particle travels along the trap before leaving it, we expect $N_{\mathrm{m},\perp} \simeq \tau_{\perp} v/l$. The resulting number density of particles within the trap is given by $n_{0,\perp} = N_{\mathrm{m},\perp}\langle n_{\mathrm{cr}}\rangle$ with $\langle n_{\mathrm{cr}}\rangle$ the mean number density of cosmic rays. The number density of the particles within the trap follows as

$$n_{0,\perp} \simeq \frac{vd^2}{l\kappa_{\perp}}\langle n_{\mathrm{cr}}\rangle. \tag{4.24}$$

According to this estimate, we expect that the number of trapped particles will depend inversely on the local perpendicular cosmic ray diffusivity and the length of the trap but directly on the velocity of the particle and the thickness of the trap.

Another escape route for the particles from the trap is via the loss cone due to parallel scattering events. The particles are then trapped for the time approximately equal to $\tau_{\parallel} \simeq l^2/\kappa_{\parallel}$, where $\kappa_{\parallel}$ is the local parallel diffusivity of cosmic rays. Again, defining $N_{\mathrm{m},\parallel}$ to be the number of times that a particle travels along the trap before leaving it via the loss cone, we expect $N_{\mathrm{m},\parallel} \simeq \tau_{\parallel} v/l$. The resulting number density within the trap $n_{0,\parallel} = N_{\mathrm{m},\parallel}\langle n_{\mathrm{cr}}\rangle$. Thus, the number density of particles following this process is

$$n_{0,\parallel} \simeq \frac{vl}{\kappa_{\parallel}}\langle n_{\mathrm{cr}}\rangle. \tag{4.25}$$

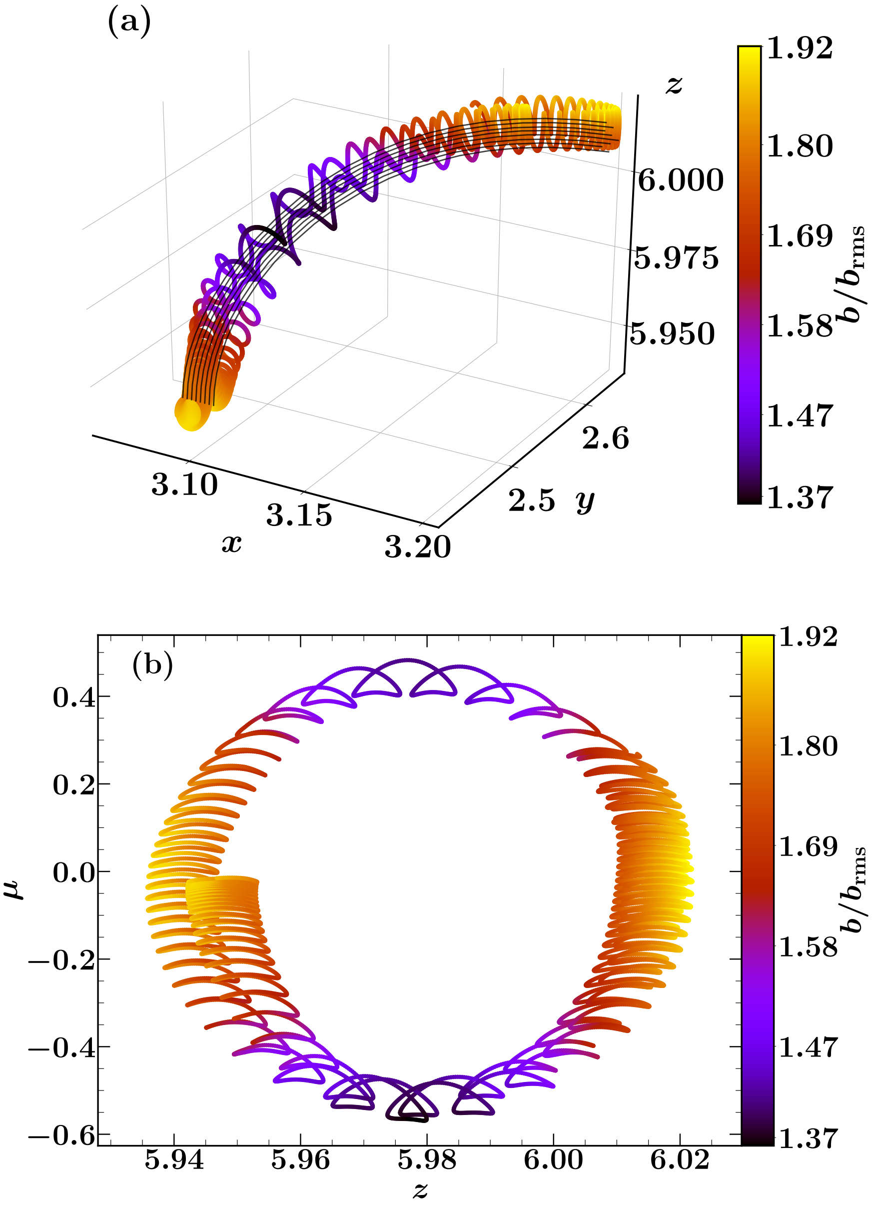

Figure 4.19: (a) A particle trajectory near a maximum of $n_{\rm cr}$ at $(3.15, 2.55, 5.975)$ with magnetic field strength along the trajectory shown with colour. The dark grey lines show magnetic field lines near the trajectory. The particle moves forward and backward between two magnetic mirrors. (b) The particle pitch angle μ as a function of z with magnetic field strength colour coded. The particle turns around (μ changes sign) at the magnetic mirrors, regions where magnetic field is stronger.

According to this estimate, we expect that the number of trapped particles will depend inversely on the local parallel cosmic ray diffusivity and directly on the velocity of the particle and the length of the trap. This number density $n_{0,\,\|}$ does not depend on the thickness of the trap, d.

In the ISM, $\kappa_\|$ is much greater than the $\kappa_\perp$ (for a $5\,\mathrm{GeV}$ particle in a $5\,\mu\mathrm{G}$ field, $\kappa_\| \sim 10^{28}\,\mathrm{cm}^2\,\mathrm{s}^{-1}$ and $\kappa_\perp \sim 10^{26}\,\mathrm{cm}^2\,\mathrm{s}^{-1}$). Thus, $\tau_\perp \gg \tau_\|$ (d and l are of similar magnitude as shown in Section 2.5). Thus, the parallel scattering is the more efficient escape mechanism. For a rough estimate of n_0, we assume that the local cosmic ray diffusivity $\kappa_\|$ is due to pitch angle scattering with a uniform background magnetic field (random magnetic fields on scales much smaller than the magnetic field correlation length can be considered uniform). We measure the dimensions of the trap from Fig. 4.19a and use the local cosmic ray diffusivity $\kappa_\|$ obtained in Fig. 4.5b. Using Eq. (4.25), we obtain $n_{0,\,\|} \approx 5\langle n_{\mathrm{cr}}\rangle$, which is of the same order of magnitude as the cosmic ray number density in traps obtained directly from the simulation (Fig. 4.9a and Fig. 4.9b).

To calculate n_0 throughout the entire volume using Eq. (4.24) or Eq. (4.25), the local cosmic ray diffusivites and the dimensions of the traps are required as a function of space. Even numerically, those are very difficult to calculate. It is hard to exactly calculate the local value of the cosmic ray diffusivity at the scales of such magnetic traps (results reported in Section 3.4 are for the global perpendicular diffusion coefficients when an uniform mean field is imposed). A simulation which involves defining diffusion coefficients perpendicular and parallel to local (turbulent) magnetic field lines is necessary to estimate the local values. It is even harder to calculate the dimensions of the trap since that depends on the subtle properties of magnetic field structure and the cosmic ray energy (different energies selects different traps from the same random magnetic field).

A mean magnetic field introduces a specific direction which particles follow and so increases the probability for a magnetic trap to occur, as shown in Fig. 4.10a. On the other hand, the pitch angle scattering due to self-generated waves decreases the level of intermittency in the cosmic ray number density, as shown in the Fig. 4.10b, because it facilitates the diffusion (the denominator increases in Eq. (4.24) or Eq. (4.25)). When the distribution in Fig. 4.10a is smoothed over a coarser scale, it does not correlate with the distribution in Fig. 4.10b. This further illustrates that the pitch angle scattering not only reduces the length of trapping region but also changes the propagation of particles significantly.

It is important to note that the spatial intermittency of cosmic rays does not require the intermittent structure of the random magnetic field. Even in the randomized magnetic field, which has almost perfect Gaussian statistics, and is free of intermittency, magnetic traps occur and lead to a spatial intermittency of cosmic rays.

4.9 Magnetic traps and cosmic ray diffusion

Cosmic ray intermittency at low energies in both non-Gaussian and Gaussian magnetic fields confirm the presence of magnetic traps in each type of field. From Fig. 4.7, we see that cosmic ray intermittency tends to be higher for the intermittent magnetic field as compared to randomized (Gaussian) magnetic field. This implies that either the number of magnetic traps is higher for the intermittent magnetic field or traps in the intermittent field are 'stronger' (keeping particles trapped for a long time). The cosmic ray intermittency is only seen for low energy cosmic rays, i.e., $r_\mathrm{L} \leq l_0$. As described in Section 3.4, this is also the energy range where magnetic field intermittency affects cosmic ray diffusion. Here, we describe how considering more magnetic traps for the intermittent magnetic field as compared to the Gaussian magnetic field might explain the enhancement of the cosmic ray diffusion coefficient when magnetic field intermittency is considered (results from Section 3.4 and Section 3.5).

Magnetic traps inhibit diffusion and an ensemble of trapped particles are non-diffusive in nature. If, for an intermittent magnetic field the number of traps is higher, the particles are trapped for a longer time as compared to the Gaussian field. If the magnetic traps are stronger, particles spend longer time in each trap. In both cases, since there is some additional trapping time for intermittent magnetic field, they require more scatterings for diffusion to set in and thus take longer to become diffusive (as can be confirmed by comparing t_d for $r_\mathrm{L}/l_0 = 0.016$ in Fig. 4.1a and Fig. 4.1b). It is difficult to confirm these arguments numerically since the statistical properties of the traps (such as their rate of occurrence and strength) are controlled by subtle properties of the random magnetic field and finding them is a non-trivial probabilistic problem.

4.10 Cosmic ray distribution and the Liouville's theorem

In an ideal situation, a perfectly isotropic and homogenous cosmic ray distribution would always remain isotropic and homogenous in a static magnetic field due to the Liouville's theorem (shown in Enßlin (2003)). However, we do obtain an inhomogeneous cosmic ray distribution. This is due to a finite number of particles in numerical simulations. The initial distribution in such simulations is not completely isotropic and homogeneous, this makes the final distribution inhomogeneous. We support this claim by showing PDFs of cosmic ray distribution in Fig. 4.20 for a different number of particles (Fig. 4.20a) and different time averaging (Fig. 4.20b) (different time integration for Eq. (4.2) to construct a cosmic ray number distribution from the ensemble of particle positions). The distribution becomes more Gaussian on increasing both the number of particles and the averaging time. However, spatially, the localized areas of high cosmic ray density are the regions with magnetic bottle traps and this is confirmed in numerical simulations by looking at particle trajectories in the vicinity of a trap (Section 4.8). The presence of such traps enhances cosmic ray number density at certain locations (or reduces at others) but those are not necessarily the strong magnetic field (or the weak magnetic field) regions. Thus, the cosmic rays and magnetic field distribution still remain uncorrelated.

4.11 Coupling of cosmic rays and thermal gas

To consider thermal gas-cosmic ray coupling, we solve the MHD equations using a two-fluid model: gas with adiabatic index $\gamma_{\mathrm{g}} = 5/3$ (a non-relativistic fluid) and cosmic rays with adiabatic index $\gamma_{\mathrm{cr}} = 4/3$ (a relativistic fluid). For an isothermal gas with equation of state $p_{\mathrm{g}} = c_s^2\rho$, where p_{g} is the gas pressure, c_s is the constant sound speed and ρ is the gas density, we solve equations for mass conservation (Eq. (4.26)), Navier-Stokes equation (Eq. (4.27)), magnetic induction (Eq. (4.28)) and cosmic ray advection-diffusion (Eq. (4.29) and Eq. (4.30)) in a box of dimensionless size $(2\pi)^3$ (periodic boundary condition for y and z, stress-free normal field boundary condition with energy density of cosmic rays $e_{\mathrm{cr}} = 0$ at boundaries $x = 0, 2\pi$) with 256^3 points.

The governing equations are

$$\frac{\partial \rho}{\partial t} + \nabla \cdot (\rho \mathbf{u}) = 0, \tag{4.26}$$

$$\frac{\partial \mathbf{u}}{\partial t} + \mathbf{u} \cdot \nabla \mathbf{u} = \frac{-\nabla(p_{\mathrm{g}} + p_{\mathrm{cr}})}{\rho} + \frac{\mathbf{j} \times \mathbf{b}}{c\rho} + \nu\left(\nabla^2 \mathbf{u} + \frac{1}{3}\nabla\nabla \cdot \mathbf{u} + 2\mathbf{S} \cdot \nabla \ln \rho\right) + \mathbf{F}, \tag{4.27}$$

$$\frac{\partial \mathbf{b}}{\partial t} = \nabla \times (\mathbf{u} \times \mathbf{b}) + \eta \nabla^2 \mathbf{b}. \tag{4.28}$$

where $\mathbf{u}$ is the gas velocity, $\mathbf{j}$ is the current density, $S_{ij} = 1/2\,(u_{i;j} + u_{j;i} - 2/3\delta_{ij}\nabla \cdot \mathbf{u})$ is the rate of the strain tensor, ν is the viscosity (assumed constant) and $\mathbf{F}$ is the forcing function driving turbulence at scale $2\pi/k_{\mathrm{F}}$, $\mathbf{b}$ is the magnetic field, c is the speed of light and η is the magnetic diffusivity (assumed constant). The forcing is mirror-symmetric, nearly incompressible and δ correlated in time (details described in Section 2.4.1 of Chapter 2).

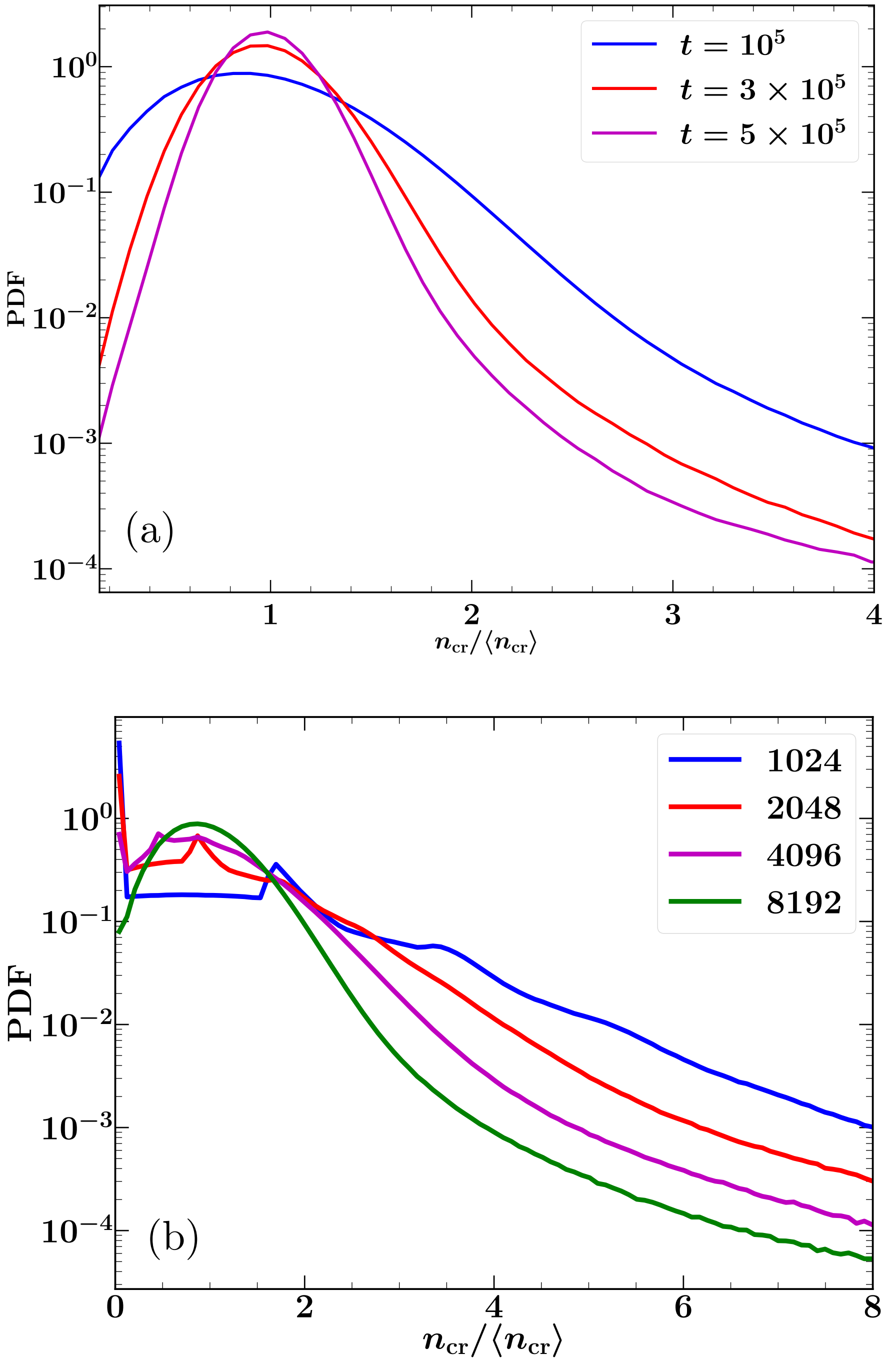

Figure 4.20: The PDFs of cosmic ray number density on increasing the averaging time (a) and decreasing number of particles from 8192 (Fig. 4.7a) to 1024 (b) for $r_{\rm L}/l_0 = 0.0016$ in the intermittent magnetic field. The distribution tends to be less intermittent (weaker tail in the distribution) as the averaging time increases or the number of particles increases. As the averaging time or number of particles increases even further, we expect that the distribution would tend to a Gaussian distribution and would eventually become a delta function at $n_{\rm cr} = \langle n_{\rm cr}\rangle$ for a very large averaging time or equivalently a large number of particles.

Table 4.2: Non-dimensional parameters used to solve the MHD and cosmic ray fluid equations (Eq. (4.26) - Eq. (4.30)) and their corresponding ISM values.

Parameter	Numerical value	ISM value
$\gamma_{\rm g}$	$5/3$	$5/3$
$\gamma_{\rm cr}$	$4/3$	$4/3$
$k_{\rm F}$	1 and 2	$100\,{\rm pc}$ and $50\,{\rm pc}$
ν	2×10^{-3}	$2\times10^{23}\,{\rm cm^2\,s^{-1}}$
η	1×10^{-3}	$1\times10^{23}\,{\rm cm^2\,s^{-1}}$
$\kappa_{\parallel}$	3×10^{-1}	$3\times10^{25}\,{\rm cm^2\,s^{-1}}$
$\kappa_{\perp}$	0	0
τ	3×10^{-1}	$0.3\,{\rm Myr}$
$Q_{\rm cr}$	$0.001, 0.005, 0.01$	$(0.001, 0.005, 0.01)\times10^{-26}\,{\rm erg\,cm^{-3}\,s^{-1}}$

Cosmic ray advection-diffusion equation [3] is

$$\frac{\partial e_{\rm cr}}{\partial t} + \nabla\cdot(e_{\rm cr}\mathbf{u}) + p_{\rm cr}\nabla\cdot u = -\nabla\cdot\mathbf{F}_{\rm cr} + Q_{\rm cr}. \tag{4.29}$$

where $e_{\rm cr}$ is the cosmic ray energy density, $p_{\rm cr} = e_{\rm cr}(\gamma_{\rm cr} - 1)$ is the cosmic ray pressure, $Q_{\rm cr}$ is the cosmic ray energy source by which cosmic rays are injected uniformly throughout the volume at a constant rate (note that the cosmic rays are lost via the boundaries in x direction), $\mathbf{F}_{\rm cr}$ is the cosmic ray flux defined via

$$\tau\frac{\partial F_{{\rm cr}i}}{\partial t} = -\kappa_{ij}\nabla_j e_{\rm cr} - F_{{\rm cr}i}, \tag{4.30}$$

where τ is the cosmic ray flux correlation time and κ_{ij} is the diffusion coefficient. $\kappa_{ij} = \kappa_{\perp}\delta_{ij} + (\kappa_{\parallel} - \kappa_{\perp})\hat{\mathbf{b}}_i\hat{\mathbf{b}}_j$ is written in terms of the parallel $\kappa_{\parallel}$ and perpendicular $\kappa_{\perp}$ diffusion coefficients ($\hat{\mathbf{b}}_i$ is the unit vector along i-axis). Here we solve the telegraph equation Eq. (4.30) to study cosmic ray diffusion (as justified in Section 3.7) instead of the usual diffusion equation.

We solve equations (Eq. (4.26) – Eq. (4.30)) using the Pencil code for parameters given in Table 4.2. All velocities are in units of the sound speed c_s, densities are in units of the initial gas density ρ_0, lengths are in units of the box size $L = 2\pi$ (so that the smallest wavenumber is $k_1 = 1$), time is in units of the eddy turn over time $t_0 = 1/u_{\rm rms}k_{\rm F}$, the magnetic field in units of $(4\pi\rho_0 c_s^2)^{1/2}$ and all the diffusivities are in units of c_s/k_1. All other units can be derived from these basic units. The unit of the cosmic ray source term is $Q_{\rm cr}$ is $\rho_0 c_s^3 k_1$. We

---

[3] Here it is assumed that cosmic rays in randomly generated magnetic fields are diffusing and choosing a diffusion coefficient κ_{ij} is equivalent to selecting an energy for particles in test particle simulations (Section 3.4)

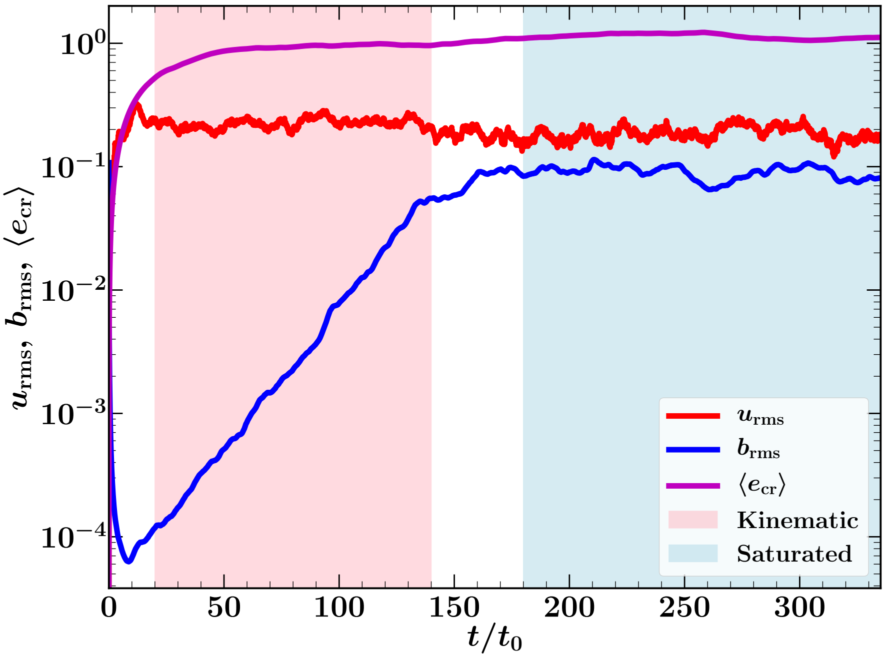

Figure 4.21: Time evolution of the rms velocity field $u_{\rm rms}$ (red) , rms magnetic field $b_{\rm rms}$ (blue) and mean cosmic ray energy density $\langle e_{\rm cr}\rangle$ (magenta) as a function of normalized time t/t_0, where t_0 is the eddy turnover time, for the case where $\langle e_{\rm cr}\rangle > b^2_{\rm rms}$. The magnetic field decreases till it becomes an eigenfunction of the induction equation and then it grows exponentially (kinematic stage, light pink). The magnetic field finally saturates (saturated stage, light blue) due to the back reaction on the velocity flow by Lorentz forces. The cosmic ray energy density saturates faster than the magnetic field.

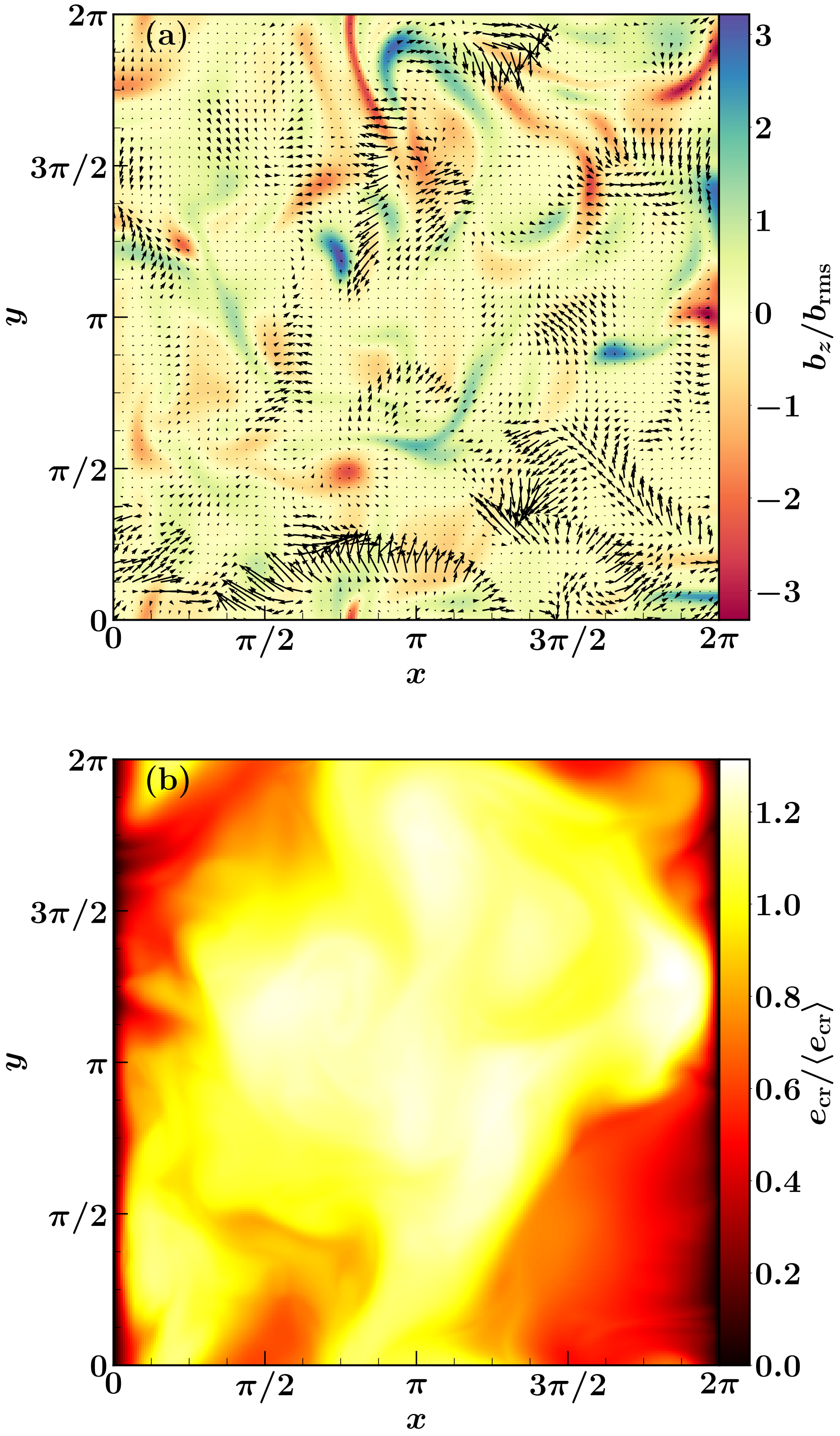

Figure 4.22: (a) 2D cut in the xy-plane through the middle of the domain with vectors for $(b_x/b_{\rm rms}, b_y/b_{\rm rms})$ and colours showing the magnitude of $b_z/b_{\rm rms}$ for magnetic field in the kinematic stage. (b) Similar 2D cut at the same time for the normalized energy density of cosmic rays $e_{\rm cr}/\langle e_{\rm cr}\rangle$ in the kinematic stage. This is for the case where $\langle e_{\rm cr}\rangle > b_{\rm rms}^2$.

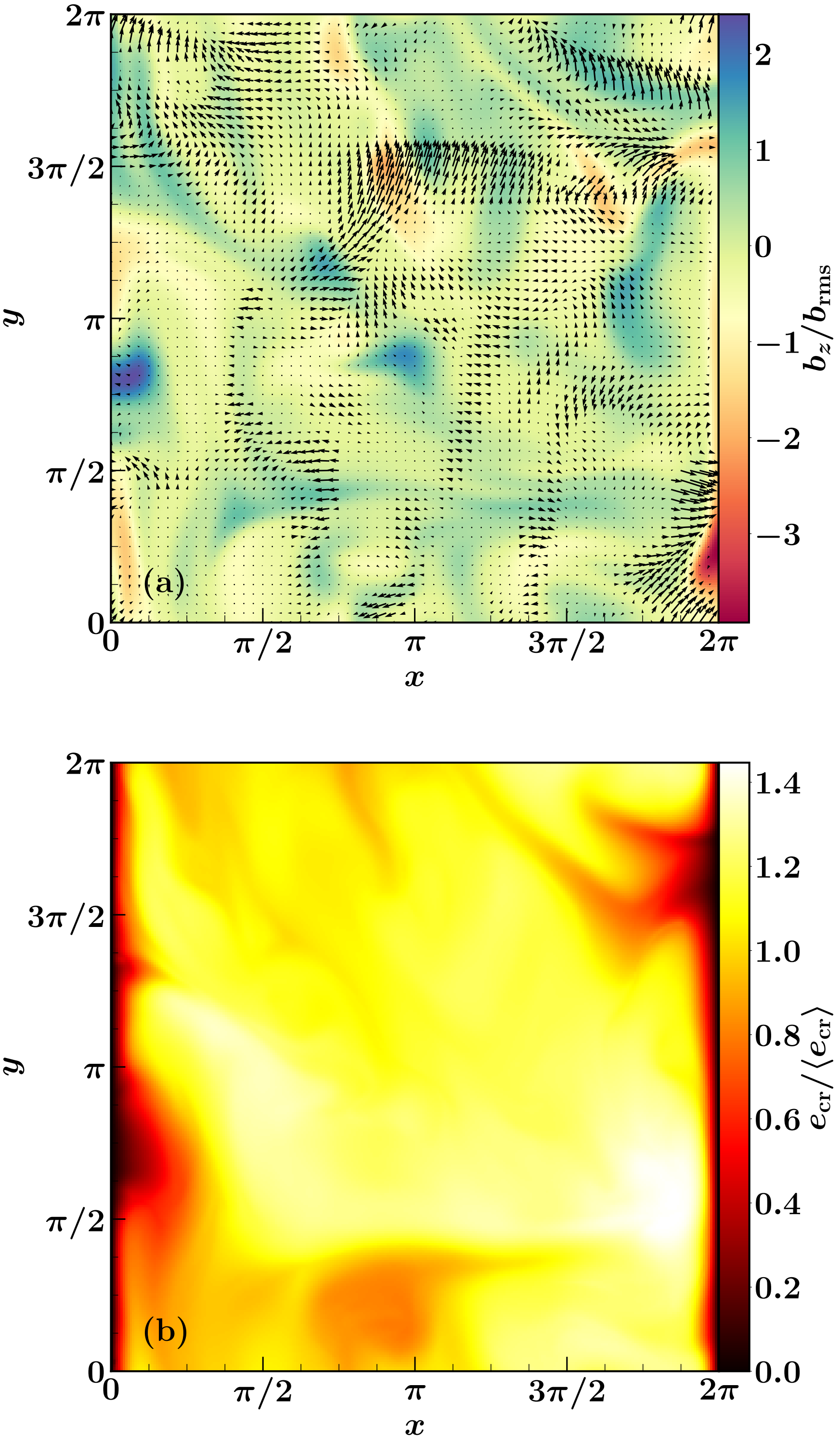

Figure 4.23: As in Fig. 4.22 but for the saturated stage.

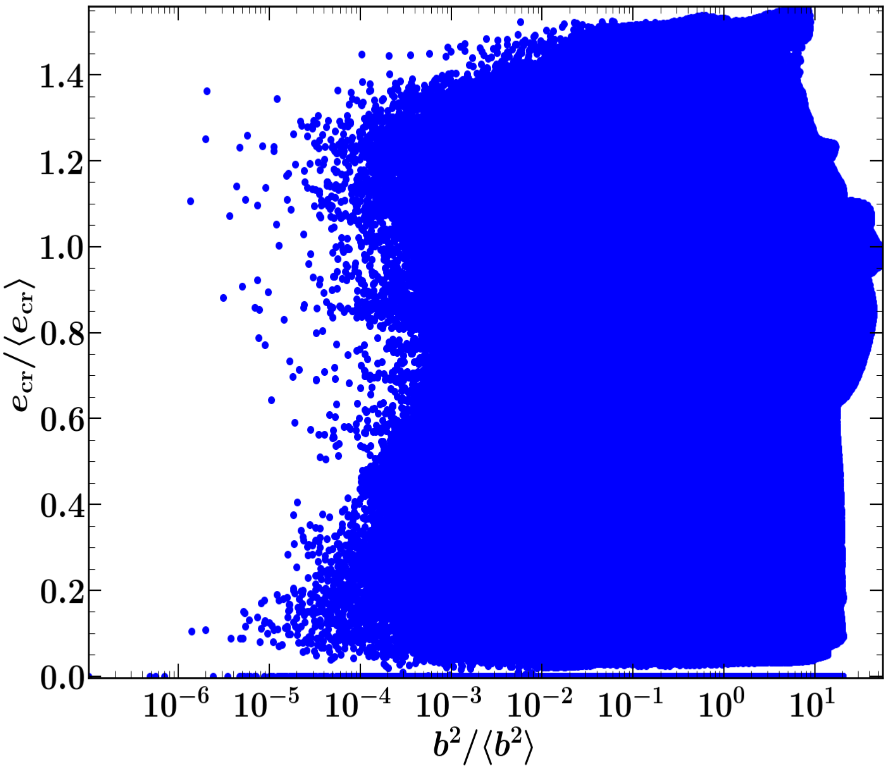

Figure 4.24: The scatter plot for the normalized energy densities of cosmic rays $e_{\mathrm{cr}}/\langle e_{\mathrm{cr}}\rangle$ and magnetic fields $b^2/\langle b^2\rangle$ for the case with $\langle e_{\mathrm{cr}}\rangle \approx \langle b^2\rangle$ at the box scale. Even though both energy densities are equal when averaged over the size of the domain, locally they are not correlated.

select $\kappa_\perp = 0$ for simplicity. We choose three different values for the cosmic ray source term $Q_{\rm cr}$ to have following three different cases in the saturated stage: $\langle e_{\rm cr} \rangle < b_{\rm rms}^2$, $\langle e_{\rm cr} \rangle \approx b_{\rm rms}^2$, $\langle e_{\rm cr} \rangle > b_{\rm rms}^2$. The gas density and magnetic field (of very small amplitude) are both initialized with a Gaussian random distribution in space. Fig. 4.21 shows the evolution of the root mean square (rms) velocity field, rms magnetic field and mean cosmic ray energy density. The magnetic field first decays till it latches on to an eigenfunction of the induction equation and then it grows exponentially (referred to as kinematic stage). Finally, the magnetic field becomes strong enough and the Lorentz force reacts back on the velocity flow saturating the magnetic field (referred to as saturated stage). Fig. 4.22 and Fig. 4.23 shows the magnetic field and cosmic ray distribution in a slice through middle of the numerical domain for the case $\langle e_{\rm cr} \rangle > b_{\rm rms}^2$. For all three cases, we find that the cross correlation between cosmic rays and magnetic fields (using Eq. (4.19)) is very close to zero. Thus, even including the effect of thermal gas, cosmic rays and magnetic fields remain uncorrelated. In Fig. 4.22 and Fig. 4.23, cosmic rays seems to follow the magnetic field vectors because we have considered only diffusion of cosmic ray fluid along the field line ($\kappa_\perp = 0$). Fig. 4.24 shows the scatter plot of the cosmic ray and magnetic field energy densities over the entire domain for the case where $\langle e_{\rm cr} \rangle \approx \langle b^2 \rangle$. The form of the plot confirms that the two quantities are not correlated. Thus, even when both energies are equal over the scale of the domain (by construction here), they are not correlated locally.

4.12 Discussion and conclusions

Using test-particle simulations of cosmic rays, we have demonstrated that the spatial distribution of cosmic rays is not correlated with magnetic field strength on scales that are less than (or comparable to) the outer scale, l_0, of a random flow that produces magnetic field. This implies that the local equipartition between cosmic ray and magnetic field energy densities does not occur on these scales. We have also shown the same using cosmic ray fluid equations, where the cosmic rays interact with both the thermal gas and the magnetic fields. In fact, in test-particle simulations we find that cosmic ray number density and magnetic field are approximately statistically independent. This allows us to express synchotron intensity as the product of the average cosmic ray number density and average magnetic field strength. However, energy equipartition between cosmic rays and magnetic fields may yet hold at scales much larger than the driving scale of turbulence, $l_0 \simeq 100\,\rm pc$ in spiral galaxies and $10\,\rm kpc$ in galaxy clusters.

At high energies, $r_{\rm L} > l_b$ with l_b the correlation length of the magnetic field, the cosmic ray distribution is uniform. At low energies, $r_\mathrm{L} < l_b$, the spatial distribution of cosmic rays is intermittent in both Gaussian and non-Gaussian (spatially intermittent) magnetic fields. This occurs because of the presence of magnetic traps in random magnetic fields where the local magnetic field has a specific structure but is not necessarily strong. As a result, the cosmic ray number density is not directly related to the local magnetic field strength. The trapping, and the ensuing intermittency in the cosmic ray distribution, are enhanced by a mean magnetic field and reduced by the pitch angle scattering of cosmic ray particles or any other additional diffusion.

The intermittency in the distribution of cosmic ray particles is a robust feature of their propagation in a random magnetic field that emerges in both Gaussian and non-Gaussian magnetic fields. The presence of small-scale cosmic ray structures due to random magnetic traps can enhance the synchrotron intensity locally. Such effects must be considered while analyzing high-resolution synchrotron observations of spiral galaxies. This extreme small-scale inhomogeneity may also affect the cosmic ray spectra or the interactions of cosmic rays with interstellar gas (Grenier et al., 2015), including spallation reactions and ionization, e.g., producing strong local variations in the ionization rate. The γ-ray emissivity can also be affected by the trapping of cosmic rays particles in random magnetic traps.

For cosmic rays to become trapped, their Larmor radius must be smaller than the correlation length of the magnetic field, i.e., $r_\mathrm{L} \leq l_b$. In spiral galaxies, where $l_b \lesssim 100\,\mathrm{pc}$, the proton energy in a $5\,\mu\mathrm{G}$ field with $r_\mathrm{L} = 100\,\mathrm{pc}$ is $10^8\,\mathrm{GeV}$. Thus, the trapping of cosmic rays described above should be effective and efficient for galactic cosmic rays. In galaxy clusters, with $l_b \lesssim 10\,\mathrm{kpc}$ and $b \simeq 1\,\mu\mathrm{G}$, protons of energy up to $10^9\,\mathrm{GeV}$ can be trapped and thus exhibit spatial intermittency. This particle trapping can effectively confine higher energy particles for which other confinement mechanisms (scattering by self-generated waves, scattering by extrinsic turbulence and field line random walk) are not very active (Chandran, 2000).

Chapter 5

Magnetic fields in elliptical galaxies

Fluctuation dynamo action is crucial for our understanding of the evolution of magnetic fields in galaxies. However, an unambiguous observational confirmation of the fluctuation dynamo action in galaxies is still missing. This is because, in spiral galaxies, it is difficult to differentiate between the small-scale magnetic field generated by a fluctuation dynamo and those due to the tangling of the mean field. We propose that observing magnetic fields in elliptical galaxies would serve as a probe of the fluctuation dynamo action in a galactic environment. In this chapter, we aim to explore this possibility via a grid of the Faraday rotation measures from background polarized sources seen through an elliptical galaxy. We estimate the properties of the rotation measure distribution in terms of the properties of the random magnetic field and thermal electron number density. We then confirm the estimates with numerical simulations, for which we use the magnetic field generated by a nonlinear fluctuation dynamo (Chapter 2) and three physically motivated thermal electron density distributions. Finally, we discuss the possibility of observing background radio sources through our nearest elliptical galaxy, Maffei 1. Such an observation would help us study the strength and structure of magnetic fields in an elliptical galaxy, which in turn would help us better understand the theory of fluctuation dynamos.

5.1 Motivation

Magnetic fields have been detected in many spiral galaxies (Beck, 2016) and are usually explained by the turbulent dynamo theory (Brandenburg & Subramanian, 2005). Based on the driving scale of turbulence, the observed magnetic field can be divided into large- and small-scale magnetic fields. The large-scale field is believed to be generated by a large-scale or mean-field dynamo (Beck et al., 1996; Brandenburg & Subramanian, 2005). As discussed in Section 2.1, the small-scale magnetic field in spiral galaxies can be generated by three mechanisms: tangling of the large-scale field, the fluctuation dynamo action and compression by shocks. The magnetic field generated by compression due to shocks is correlated with the gas density (Federrath et al., 2011). The small-scale magnetic field due to a fluctuation dynamo is spatially intermittent (Section 2.4.2), whereas that due to the tangling of the large-scale field is presumably Gaussian in nature. Considering the driving scale of turbulence within a range of $50–100\,\mathrm{pc}$[1](Ohno & Shibata, 1993; Gaensler et al., 2005; Fletcher et al., 2011; Houde et al., 2013), it would require a spatial resolution of $10\,\mathrm{pc}$ or less, to study the structure of the small-scale magnetic field in spiral galaxies. Such a resolution is extremely difficult to achieve with present day telescopes and thus it is difficult to observationally differentiate between the magnetic field generated by a fluctuation dynamo and that due to the tangling of the large-scale field. In a turbulent environment like the ISM of spiral galaxies, a fluctuation dynamo is physically the most plausible scenario for magnetic field amplification (Chapter 2) but we are yet to confirm this observationally. The existence of a fluctuation dynamo in galaxies is fundamental to the galactic dynamo theory. In the absence of a fluctuation dynamo, the magnetic field in protogalaxies would be seeded with a much weaker field and then the mean-field dynamo would take much longer to amplify the field up to the present day observed value (Ruzmaikin et al., 1988; Arshakian et al., 2009). Furthermore, the field generated by a fluctuation dynamo is important for low-energy cosmic ray propagation (Chapter 3) and for interpretations of radio observations. Thus, it is important to find a clear observational probe of the fluctuation dynamo action.

There is a similar question with respect to the solar magnetic field. The 11 year solar cycle is associated with the large-scale magnetic field of the Sun and a mean-field dynamo theory is used to explain the large-scale field. In the absence of a fluctuation dynamo in the Sun, the small-scale magnetic field would be correlated with the solar cycle since all the small-scale field would be due to the tangling of the large-scale field. The analysis of solar

---

[1] Even smaller values of $1–20\,\mathrm{pc}$ are also reported (Minter & Spangler, 1996; Haverkorn et al., 2008; Iacobelli et al., 2013)

magnetograms suggests that this is the case (Stenflo, 2012). However, there are also claims that the correlation is not that significant and a fluctuation dynamo is indeed active in the Sun (Jin & Wang, 2015a,b). Numerical simulations are consistent with the latter option (Karak & Brandenburg, 2016).

With a motivation to probe the fluctuation dynamo action in a galactic environment, we consider magnetic fields in elliptical galaxies (slow rotators as defined by the ATLAS$^{\rm 3D}$ Project[2]) . Unlike spirals, elliptical galaxies have a very small rotation rate (Emsellem et al., 2011; Cappellari et al., 2011) and so a mean-field dynamo action is unlikely. Moreover, these systems are not differentially rotating so an MRI generated large-scale field is also unlikely. However, the interstellar turbulence due to supernova explosions and random motion of stars can amplify a weak seed field (due to stellar mass ejecta) by fluctuation dynamo action (Moss & Shukurov, 1996). The magnetic field generated by a fluctuation dynamo can be further amplified by compression due to cooling flows [3] in elliptical galaxies (Mathews & Brighenti, 1997). This magnetic field is non-Gaussian and spatially intermittent (Section 2.4.2). The detection and characterization of magnetic field in an elliptical galaxy would be a direct observational confirmation of the fluctuation dynamo action. Moreover, the observations can be compared with the theories of fluctuation dynamos to further understand the physics of magnetic field saturation (Section 2.4.3). The structure of magnetic field generated by a fluctuation dynamo has been studied theoretically (Zeldovich et al., 1990) and numerically (Section 2.5) but lacks a concrete and convincing observational confirmation.

5.2 Magnetic fields in elliptical galaxies

Turbulence in the hot gas of elliptical galaxies

The source of hot gas in ellipticals can be internal or external to the galaxy. Internally, the hot gas can be due to outflows from evolved stars and Type Ia supernova explosions. Externally, some of the circumgalactic gas (expelled from the galaxy by winds driven by frequent Type II supernovae explosions at earlier stages of galactic evolution) can fall back into the galaxy, as well as the gas accreted from the galaxy group or cluster. The hot gas in elliptical galaxies is observed via its X-ray emission. The relationship between the X-ray luminosity L_X and optical luminosity (in B band) L_B of bright elliptical galaxies is observationally found to

---

[2] http://www-astro.physics.ox.ac.uk/atlas3d/

[3] The gas in the centres of elliptical galaxies quickly loses its energy via X-ray emission. Since the central core cools quickly, the weight of the outer region will cause the surrounding material to flow inwards. This is referred to as the cooling flow (Fabian, 1994).

be $L_X \propto L_B^{2.2}$ (O'Sullivan et al., 2001). This confirms the non-stellar origin of the X-ray emission, otherwise the relationship would have been linear. From X-ray observations, gas mass can be inferred. The total mass of the hot gas is about 1–2% of the total stellar mass. Generally, the hot gas is the dominant fraction of the interstellar medium of the elliptical galaxies.

The major and continuous sources of turbulent energy in elliptical galaxies are Type Ia supernovae explosions and random motions of stars (Moss & Shukurov, 1996). The length scales associated with random star motions would be much smaller than those due to supernova explosions, thus we consider Type Ia supernova explosions as the only source of turbulence in the ISM. Each explosion of a Type Ia supernova enriches the surrounding medium with roughly $0.7\,\mathrm{M}_\odot$ ($\mathrm{M}_\odot$ being the solar mass) of iron and thus the observed iron abundance can be used to estimate the supernova rate in ellipticals (Mathews & Brighenti, 2003). The supernova rate cannot be as high as in spiral galaxies. This is inferred from the following three observations. First, if the rate was very high there would be galactic outflows or winds from ellipticals, which are not observed. Second, the observed X-ray luminosity gives a rate which is much smaller than that in the spirals. Finally, the observed iron abundance also suggests that the rate is low.

We estimate the driving scale and velocity of the ISM turbulence driven by Type Ia supernova explosions in elliptical galaxies. First, we use the temperature of the hot gas inferred from X-ray observations to calculate the local sound speed. Then we calculate the size of largest supernova remnants assuming that a supernova explosion drives negligible turbulence once the shock front velocity is approximately equal to the local sound speed. The supernova radius at that time gives the driving scale of the turbulence l_0. Next, we consider that a fraction of the total supernova energy is converted to kinetic energy of the turbulence to calculate the turbulent velocity in the medium (very similar to Section 1.5 where this done for spiral galaxies).

X-ray observations suggest a temperature T of the order of $10^7\,\mathrm{K}$ for the diffuse interstellar gas in elliptical galaxies (Brighenti & Mathews, 1997). This implies a sound speed $c_s \approx \sqrt{k_B T/m_\mathrm{p}} \approx 300\,\mathrm{km\,s^{-1}}$, where $k_B = 1.38 \times 10^{-16}\,\mathrm{erg\,K^{-1}}$ is the Boltzmann constant and $m_\mathrm{p} = 1.67 \times 10^{-24}\,\mathrm{g}$ is the proton mass (assuming that most of the hot gas is made up of protons) . We now use the sound speed and Sedov–Taylor blastwave self-similarity solution (Ostriker & McKee, 1988) to calculate the driving scale of the turbulence. The radius of a supernova remnant R as a function of time t is then

$$R = \left(\kappa \frac{E_{\rm SN}}{\rho_0}\right)^{1/5} t^{2/5}, \tag{5.1}$$

where $E_{\rm SN}$ is the energy of a supernova explosion, ρ_0 is the average gas density of the ambient medium and κ is a parameter which is about 2 for a monoatomic ideal gas. Now, the radius R is roughly equal to the driving scale of the turbulence l_0, when the velocity of shock front is equal to c_s. So, then $t \approx R/c_s$. This gives

$$l_0 \simeq \left(\kappa \frac{E_{\rm SN}}{\rho_0}\right)^{1/3} \frac{1}{c_s^{2/3}}. \tag{5.2}$$

Using $E_{\rm SN} = 10^{51}\,{\rm erg}$, $\rho_0 = 10^{-3} m_{\rm p}\,{\rm cm}^{-3} = 1.67 \times 10^{-27}\,{\rm g\,cm}^{-3}$ and $c_s = 300\,{\rm km\,s}^{-1}$, we obtain $l_0 \simeq 300\,{\rm pc}$. This scale is slightly larger than that in spiral galaxies ($\simeq 100\,{\rm pc}$) because the ambient medium is less dense. The supernovae survive longer in the ellipticals as compared to the spirals but their frequency is much lower and so they inject less turbulent kinetic energy in the medium. To calculate the turbulent velocity, we assume that about 1% of the total supernovae energy is converted to the kinetic energy of the turbulence (Dyson & Williams, 1997). The rate at which supernovae inject energy into the medium can be balanced with the rate of gain of kinetic energy of the medium as

$$\frac{v_0^2}{l_0/v_0} \approx f \nu_{\rm SN} E_{\rm SN} M_{\rm gas}^{-1}, \tag{5.3}$$

where v_0 is the turbulent velocity, f is the fraction of energy that is injected into the medium, $\nu_{\rm SN}$ is the frequency of supernova explosions and $M_{\rm gas}$ is the mass of the hot gas. Using $l_0 = 300\,{\rm pc}$, $f = 0.01$, $\nu_{\rm SN} = 10^{-3}\,{\rm yr}^{-1}$(Cappellaro et al., 1999), $E_{\rm SN} = 10^{51}\,{\rm erg}$ and $M_{\rm gas} = 10^{10}\,{\rm M}_\odot$, we obtain $v_0 \simeq 2.5\,{\rm km\,s}^{-1}$. This is lower than that in spiral galaxies ($\simeq 10\,{\rm km\,s}^{-1}$ as derived in Section 1.5).

The driving scale of turbulence $l_0 \simeq 300\,{\rm pc}$ and velocity $v_0 \simeq 2.5\,{\rm km\,s}^{-1}$ are global values calculated from average quantities. The eddy turnover time can be calculated as $t_0 \approx l_0/v_0 \simeq 1.2 \times 10^8\,{\rm yr}$. The typical value of magnetic Reynolds numbers can also be calculated. Spitzer resistivity η for a plasma at a temperature T can be estimated from the following expression [4] (Brandenburg & Subramanian, 2005):

$$\eta \simeq 10^4 \left(\frac{T}{10^6\,\mathrm{K}}\right)^{-3/2} \mathrm{cm}^2\,\mathrm{s}^{-1}. \tag{5.4}$$

Using $T = 10^7\,\mathrm{K}$, we obtain $\eta \simeq 3 \times 10^2\,\mathrm{cm}^2\,\mathrm{s}^{-1}$. For $l_0 = 300\,\mathrm{pc}$ and $v_0 = 2.5\,\mathrm{km\,s}^{-1}$, we obtain $\mathrm{Re_M} = l_0 v_0/\eta \simeq 10^{22}$. The estimated $\mathrm{Re_M}$ is considerably greater than $\mathrm{Re}_\mathrm{M}^{(\mathrm{crit})}$ ($\simeq 10^2$–10^3), which is required for the fluctuation dynamo action. Thus, it is reasonable to expect fluctuation dynamo-generated magnetic fields in elliptical galaxies.

Since the gas and stellar densities in elliptical galaxies varies with the radius (usually the variation is described by the King profile $f = f(0)(1 + (r/a)^2)^{-\beta}$, where $f(0)$ is the density at radius $r = 0$, a is the radius of the central core and β is the exponent), the properties of the ISM turbulence would also change. We, however, are interested only in the core region of the elliptical galaxies where the density of the hot gas is high and thus the probability for an unambiguous detection of the magnetic field is higher.

Fluctuation dynamo action and further amplification by cooling flows

Any pre-existing magnetic field energy remaining from the galaxies which merge to form an elliptical galaxy will cascade down to smaller scales and will be eventually lost by resistive decay in a time of order $t_0 = 10^8\,\mathrm{yr}$. Thus, there must be a continuous generation of magnetic field within the galaxy, which we claim is via the fluctuation dynamo action due to the random turbulent velocity in the medium. The seed field from stellar ejecta or that remaining after galaxy merger events will be amplified by a fluctuation dynamo to produce intermittent magnetic fields (Chapter 2). The root mean square (rms) value of the amplified magnetic field b_rms in the core (where the density is higher) of the elliptical galaxy is related to the equipartition field b_eq (Table 2.1),

$$b_\mathrm{rms} \approx 0.5\, b_\mathrm{eq} = 0.5(4\pi\rho)^{1/2} v_0, \tag{5.5}$$

where ρ is the density of the medium and v_0 is the turbulent velocity. With $\rho = 0.1 m_\mathrm{p}\,\mathrm{cm}^{-3} = 1.67 \times 10^{-26}\,\mathrm{g\,cm}^{-3}$ (Forman et al., 1985) and $v_0 = 2.5\,\mathrm{km\,s}^{-1}$, we obtain $b_\mathrm{rms} \simeq 0.2\,\mu\mathrm{G}$.

The magnetic field would be further enhanced by the cooling flows due to compression. By flux conservation under spherically symmetric compression, the field strength b grows as $\rho^{2/3}$, where ρ is the gas density. In cooling flows, the density can be enhanced by a factor of 10 or more (Mathews & Brighenti, 1997). Thus, the magnetic field with magnitude

---

[4] Assuming the Coulomb logarithmic factor is of the order unity.

approximately equal to $0.2\,\mu$G can be further amplified to be around $1\,\mu$G. Mathews & Brighenti (1997), using a detailed spherical cooling flow model, suggest a radial dependence for the magnetic field of the form $b(r) \sim [1\text{–}10\,(r/10\,\mathrm{kpc})^{-1.2}]\ \mu$G.

Existing observations of magnetic fields in elliptical galaxies

The observational tracers of magnetic fields in spiral galaxies described in Section 1.9 are not very useful for ellipticals. Synchrotron emission from elliptical galaxies is not observed because of the lack of cosmic ray electrons. Polarized dust emission is also not observed because of a relative low level of dust. It is not possible to probe magnetic field via the Zeeman splitting because of the absence of dense cold gas. The most promising probe for studying magnetic fields in elliptical galaxies is Faraday rotation. The rotation measure RM in terms of convenient units is written as

$$\frac{\mathrm{RM}}{1\,\mathrm{rad\,m^{-2}}} = 0.81 \int_0^{L/1\,\mathrm{pc}} \frac{n_\mathrm{e}}{1\,\mathrm{cm^{-3}}}\frac{b_\parallel}{1\,\mu\mathrm{G}}\mathrm{d}\left(\frac{l}{1\,\mathrm{pc}}\right), \tag{5.6}$$

where n_e is the thermal electron number density, $b_\parallel$ is the magnetic field parallel to the line of sight and L is the path length. For a cosmologically distant source at a redshift z, the RM in the observer frame is further reduced by a factor of $(1+z)^2$ than that given by Eq. (5.6) (which is the RM in the rest frame).

Greenfield et al. (1985) studied the radio polarization signal from two gravitationally lensed images of the quasar 0957+561 ($z \approx 1.41$) at multiple wavelengths and found that the rotation measures of the two images differs by $100\,\mathrm{rad\,m^{-2}}$. This difference can be attributed to the magnetic field in the ISM of the lensing (cD) galaxy at $z \approx 0.36$. So, to estimate magnetic field in the galaxy using Eq. (5.6) for the quasar at a redshift z, we can write RM in terms of mean quantities as

$$\mathrm{RM} \approx \left(0.81 \frac{\langle n_\mathrm{e}\rangle}{\mathrm{cm^{-3}}}\frac{\langle b\rangle}{\mu\mathrm{G}}\frac{L}{\mathrm{pc}}\right) \Big/ (1+z)^2, \tag{5.7}$$

where $\langle\cdots\rangle$ denotes the average over the path length. Assuming $\langle n_\mathrm{e}\rangle \approx 0.01\,\mathrm{cm^{-3}}$ and $L \approx 30\,\mathrm{kpc}$, for $\mathrm{RM} = 100\,\mathrm{rad\,m^{-2}}$ and $z = 1.41$, we obtain $\langle b\rangle \simeq 2.5\,\mu$G. This is comparable in strength to magnetic fields observed in nearby spiral galaxies (Fletcher, 2010). However, mass modelling of the system suggest that the lens must also have some contribution from the cluster to explain the lensing observations (Greenfield et al., 1985). Thus, it then becomes difficult to differentiate between the contribution to the RM difference due to the galaxy's and cluster's magnetic fields.

Table 5.1: List of sources, their redshifts z, the depolarization fraction for jets $\mathrm{DP_j}$ and counter jets $\mathrm{DP_{cj}}$ (Garrington et al., 1991). The calculated standard deviation of the rotation measure in jets $\sigma_{\mathrm{RM_j}}(\,\mathrm{rad\,m^{-2}})$, counter jets $\sigma_{\mathrm{RM_{cj}}}(\,\mathrm{rad\,m^{-2}})$, elliptical hosts $\sigma_{\mathrm{RM_{ellip}}}(\,\mathrm{rad\,m^{-2}})$ and the rms magnetic field $b_{\mathrm{rms}}(\,\mu\mathrm{G}\,)$ in ellipticals are also given.

Name	z	$\mathrm{DP_j}$	$\sigma_{\mathrm{RM_j}}$	$\mathrm{DP_{cj}}$	$\sigma_{\mathrm{RM_{cj}}}$	$\sigma_{\mathrm{RM_{ellip}}}$	b_{rms}
0017+15	2.012	0.61	12.479	0.21	22.174	18.329	0.086
0123+32	0.794	0.96	3.586	0.89	6.059	4.884	0.065
0225-01	2.037	0.85	7.156	0.08	28.209	27.286	0.126
0232-04	1.436	0.81	8.148	0.16	24.028	22.604	0.163
0838+13	0.684	0.73	9.957	0.25	20.899	18.375	0.277
0850+58	1.322	0.57	13.308	0.15	24.448	20.509	0.162
1023+06	1.699	0.45	15.861	0.25	20.899	13.609	0.08
1115+53	1.235	0.86	6.893	0.18	23.243	22.197	0.19
1218+33	1.519	0.56	13.516	0.07	28.945	25.596	0.172
1226+10	2.296	0.69	10.812	0.04	31.845	29.953	0.118
1241+16	0.557	0.9	5.761	0.41	16.76	15.739	0.277
1258+40	1.659	0.84	7.412	0.11	26.371	25.308	0.153
1318+11	2.171	0.97	3.098	0.06	29.772	29.61	0.126
1323+65	1.618	0.73	9.957	0.18	23.243	21.002	0.131
1634+17	1.897	0.77	9.074	0.27	20.31	18.17	0.092
1634+58	0.985	0.84	7.412	0.25	20.899	19.54	0.212
1656+57	1.281	0.9	5.761	0.1	26.934	26.311	0.216
1709+46	0.806	0.56	13.516	0.15	24.448	20.372	0.267
1732+16	1.27	0.68	11.023	0.08	28.209	25.966	0.215
1816+47	2.225	0.82	7.907	0.06	29.772	28.703	0.118
0107+31	0.689	0.65	11.65	0.39	17.224	12.686	0.19
0712+53	0.064	0.34	18.436	0.28	20.026	7.82	0.295
0824+29	0.458	0.86	6.893	0.44	16.083	14.531	0.292
0903+16	0.411	0.65	11.65	0.38	17.46	13.005	0.279
0937+39	0.617	0.78	8.847	0.77	9.074	2.017	0.033
1001+22	0.974	0.5	14.778	0.36	17.941	10.173	0.112
1055+20	1.111	0.88	6.346	0.52	14.353	12.874	0.123
1354+19	0.72	0.59	12.893	0.23	21.518	17.228	0.249
1548+11	1.901	0.89	6.059	0.33	18.689	17.68	0.09
1618+17	0.555	0.84	7.412	0.62	12.272	9.781	0.173
1830+28	0.594	0.81	8.148	0.75	9.52	4.923	0.083
2325+29	1.015	0.83	7.662	0.6	12.686	10.111	0.106

Laing (1988) and Garrington et al. (1988) studied radio polarization from FRII radio sources and observed that the polarization signal strength was significantly higher on the jet side which is closer to us than that in the jet side which is further away from us (the counter jet). Assuming that both jets have similar intrinsic properties, the difference in the polarization can be attributed to the depolarization by a foreground screen (the radiation from the more distant side travels more through the screen and is thus more depolarized), which can be an X-ray emitting halo of the elliptical galaxy. Assuming that the depolarization is because of a halo of an elliptical galaxy, we can estimate its magnetic field. We consider that the elliptical galaxy acts as a Faraday screen, i.e., a medium with magnetic fields and thermal electrons but lacking relativistic electrons (this is a justified assumption since an elliptical galaxy has very few cosmic ray electrons). For a Faraday screen, assuming a Gaussian distribution of Faraday depths, the degree of polarization p at wavelength λ is given by (Burn, 1966; Sokoloff et al., 1998)

$$p = p_0 \exp(-2\sigma_{\mathrm{RM}}^2 \lambda^4), \tag{5.8}$$

where p_0 is the maximum degree of polarization and σ_{RM} is the standard deviation of the fluctuations in rotation measure due to the screen. The depolarization DP between the wavelengths λ_1 and λ_2 with $\lambda_1 > \lambda_2$ is given by

$$\mathrm{DP} = \exp(-2\sigma_{\mathrm{RM}}^2(\lambda_1^4 - \lambda_2^4)). \tag{5.9}$$

For the source 0225-01 at $z = 2.037$, DP at $\lambda_1 = 20\,\mathrm{cm}$ and $\lambda_2 = 6\,\mathrm{cm}$ for the jet $\mathrm{DP_j}$ and the counter jet $\mathrm{DP_{cj}}$ is observed to be 0.85 and 0.08, respectively (Garrington et al., 1991). Using Eq. (5.9), we obtain the standard deviation in the rotation measure distribution for the jet $\sigma_{\mathrm{RM_j}}$ and counter jet $\sigma_{\mathrm{RM_{cj}}}$ to be $7.156\,\mathrm{rad\,m^{-2}}$ and $28.209\,\mathrm{rad\,m^{-2}}$, respectively. Assuming that the difference is due to the halo of an elliptical galaxy and accounting for the factor $(1+z)^2$, we derive the the standard deviation in the rotation measure distribution for the galaxy $\sigma_{\mathrm{RM_{ellip}}}$ to be $\sqrt{28.20^2 - 7.15^2}/(1+2.037)^2 \approx 5.30\,\mathrm{rad\,m^{-2}}$. $\sigma_{\mathrm{RM_{ellip}}}$ in $\mathrm{rad\,m^{-2}}$ is given by (this assumes a uniform thermal electron number density, see Section 5.3.1)

$$\sigma_{\mathrm{RM_{ellip}}} = \frac{(2\pi)^{1/4}}{3^{1/2}} K \langle n_e \rangle\, b_{\mathrm{rms}} (L l_b)^{1/2}, \tag{5.10}$$

where $K = 0.81\,\mu\mathrm{G^{-1}\,cm^3\,pc^{-1}\,rad\,m^{-2}}$ is a constant, $\langle n_e \rangle$ is the mean thermal electron number density in $\mathrm{cm^{-3}}$, b_{rms} is the rms magnetic field strength in $\mu\mathrm{G}$, L is the path length in pc and l_b is the magnetic field correlation length in pc. Assuming $\langle n_\mathrm{e} \rangle \approx 0.01\,\mathrm{cm^{-3}}$, $L \approx 100\,\mathrm{kpc}$ (here the path length is larger because of the halo) and $l_b = 100\,\mathrm{pc}$, for $\sigma_{\mathrm{RM_{ellip}}} =$

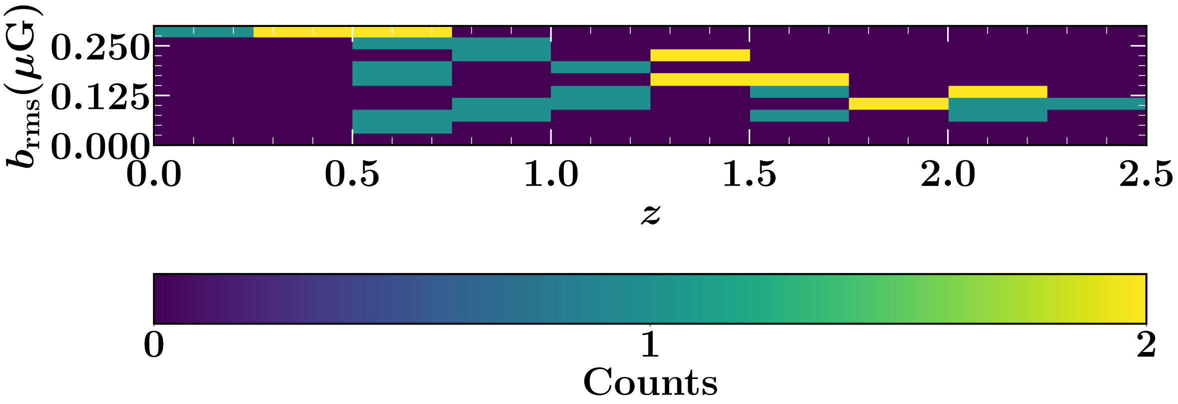

Figure 5.1: Two dimensional histogram of the redshift of the sources z and the calculated magnetic field of host galaxies $b_{\rm rms}(\,\mu\rm G\,)$. There is no clear trend of magnetic fields with redshift.

$5.30\,\rm rad\,m^{-2}$ and $z = 2.037$, we obtain $b_{\rm rms} \simeq 0.126\,\mu\rm G$. This estimate gives a slightly lower but still considerable magnetic field strength in the halo of an elliptical galaxy. In Table 5.1, we repeat this calculation for a number of sources. The rms magnetic field ranges from $0.03\,\mu\rm G$ to $0.3\,\mu\rm G$. Fig. 5.1 shows a two dimensional histogram of redshift of 32 sources listed in Table 5.1 and the calculated magnetic field in their host galaxies. We do not see any obvious relationship between the two quantities. However, the depolarization asymmetry can be due to an extended disk of magneto-ionic medium surrounding elliptical galaxies (Gopal-Krishna & Nath, 1997), anisotropic magnetic fields, absence of a spherically symmetric halo (Laing et al., 2008) or difference in Faraday rotation due to shocked and un-shocked medium (Guidetti et al., 2012).

Recently Nyland et al. (2017) found that cores of early-type galaxies are bright in synchrotron because stars are still being formed in the central regions of the galaxies. They find a deficiency in radio emission as compared to the infrared emission and one of the possible reasons for observation is a weak magnetic field in the medium[5]. These authors calculate magnetic field of the order of 1–$10\,\mu\rm G$ but to estimate that they assume that such early type galaxies are very similar in properties (such as energy equipartition between cosmic rays and magnetic fields, ratio of number density of cosmic ray electrons to cosmic ray protons to be 100 and disc-like or cylindrical geometry of the synchrotron emitting region with gas scale heights similar to a spiral galaxy) to the nearby spiral galaxies.

Our aim is to find observational evidence of magnetic fields in an elliptical galaxy which

---

[5] Another reason given is the quick escape of cosmic ray electrons. However, there is no sign of an outflow or wind in such galaxies. Thus, the cosmic rays transport must be dictated by magnetic fields. But it is extremely difficult to understand the cosmic ray propagation without knowing the structure and strength of magnetic fields in those galaxies.

is relatively isolated and does not have a central active nucleus. Considering the magnetic field amplification by a fluctuation dynamo and subsequent enhancement by a galactic cooling flow, Mathews & Brighenti (1997) suggest the radial dependence of magnetic field strength $b(r) \sim 1\text{–}10\, r^{-1.2}\,\mu\mathrm{G}$. The radial dependence of thermal electron number density is $n_\mathrm{e}(r) \sim 0.1r^{-1.5}\,\mathrm{cm}^{-3}$ (Mathews & Brighenti, 2003). Thus, we expect substantial fluctuations in Faraday rotation measure from at least the core (usually defined as the radius at which the slope of the surface brightness profile changes drastically from very low values) of an elliptical galaxy.

5.3 Simulated Faraday rotation measure in elliptical galaxies

5.3.1 Theoretical predictions of rotation measure fluctuations

The standard deviation of fluctuations in rotation measure σ_RM can be estimated from the two-point correlation function of RM, which in turn can be estimated from the two-point correlation of the magnetic field. For the simplest case, this can be done by assuming that the number density of thermal electrons is uniform. Assuming a constant n_e in Eq. (5.6), Shukurov & Sokoloff (2007) demonstrated that

$$\sigma_\mathrm{RM} = \frac{(2\pi)^{1/4}}{3^{1/2}} K n_e\, b_\mathrm{rms} L^{1/2} l_b^{1/2}, \tag{5.11}$$

where K is a constant, b_rms is the root mean square magnetic field strength in the region, L is the path length and l_b is the correlation length of the random magnetic field. In the central region, $n_\mathrm{e} = 0.1\,\mathrm{cm}^{-3}$ (Mathews & Brighenti, 2003), $b_\mathrm{rms} = 1\,\mu\mathrm{G}$, $l_b = 100\,\mathrm{pc}$ ($l_0/l_b \simeq 3-4$ in Table 2.1 and $l_0 \simeq 300\,\mathrm{pc}$), $L = 1.5\,\mathrm{kpc}$ (since the emission is considered from the central region only) and $K = 0.81$ (when rotation measure is in the units of $\mathrm{rad\,m^{-2}}$, number density is in the units of cm^{-3}, magnetic field is in the units of $\mu\mathrm{G}$ and lengths are in the units of pc), we obtain $\sigma_\mathrm{RM} \simeq 300\,\mathrm{rad\,m^{-2}}$. This is significant and we expect that this can be observable. However, the number density decreases with the radius and this might further decrease the σ_RM at larger radii.

The analysis can be extended to include the contribution from a varying thermal electron number density (see Appendix A in Bhat & Subramanian (2013)). Assuming the King profile for electrons in an elliptical galaxy $n_\mathrm{e} = n_\mathrm{e}(0)(1 + (r/a)^2)^{-3/4}$, where $n_\mathrm{e}(0)$ is the electron number density at $r = 0$, a is the core radius, and also assuming that $b_\mathrm{rms} \propto n_\mathrm{e}^\gamma$, σ_RM at $r = 0$

is

$$\sigma_{\mathrm{RM}}(0) = \frac{(2\pi)^{1/4}}{3^{1/2}} K n_{\mathrm{e}}(0)\, b_{\mathrm{rms}} a^{1/2} l_b^{1/2} \left(\frac{\Gamma(\frac{3}{2}(\gamma+1)-0.5)}{\Gamma(\frac{3}{2}(\gamma+1))}\right)^{1/2}. \tag{5.12}$$

Using $K = 0.81, n_{\mathrm{e}}(0) = 0.1\,\mathrm{cm}^{-3}$, $b_{\mathrm{rms}} = 1\,\mu\mathrm{G}, a = 400\,\mathrm{pc}, l_b = 100\,\mathrm{pc}$ and $\gamma = 2/3$ (motivated by the flux freezing condition, i.e., $b \propto \rho^{2/3}$), we obtain $\sigma_{\mathrm{RM}}(0) \simeq 125\,\mathrm{rad\,m}^{-2}$. The σ_{RM} as a function of the radial distance in the plane of the sky $r_\perp$ is

$$\sigma_{\mathrm{RM}}(r_\perp) = \sigma_{\mathrm{RM}}(0)\left[1 + (r_\perp/a)^2\right]^{-\left(\frac{1}{4}\Gamma\left(\frac{3}{2}(\gamma+1)-1\right)\right)}. \tag{5.13}$$

For $\sigma_{\mathrm{RM}}(0) = 125\,\mathrm{rad\,m}^{-2}$ and $\gamma = 2/3$, we obtain $\sigma_{\mathrm{RM}}(r_\perp) = 125\,\mathrm{rad\,m}^{-2}(1+(r_\perp/a)^2)^{-0.22}$.

5.3.2 Numerical simulations

We confirm our expectations for σ_{RM} (Section 5.3.1) using our numerical simulations of the nonlinear fluctuation dynamo (Section 2.4). We use the magnetic field from a nonlinear dynamo simulation with $k_{\mathrm{F}} = 5, \mathrm{Re} = 283, \mathrm{Re}_{\mathrm{M}} = 2261$ [6] and $\mathrm{Pr}_{\mathrm{M}} = 8$ (Table 2.4) in a box of non-dimensional size $L = 2\pi$ with 512^3 points. In terms of dimensional quantities, $2\pi/k_{\mathrm{F}} = 300\,\mathrm{pc}$ and $L = 1.5\,\mathrm{kpc}$. This means that there are 5 velocity correlation cells along each direction in the domain and a total of 125 cells in the whole cube. The simulations are for an isothermal and incompressible gas. Thus, the electron number density is roughly uniform within the domain. To consider the effect of thermal electron number density distribution on the rotation measure distribution, we consider the following physically motivated distributions:

- a uniform n_{e} as suggested by isothermal simulations,
- n_{e} following the King profile similar to the gas density, i.e., $n_{\mathrm{e}}(r) = n_{\mathrm{e}}(0)/(1 + (r/a)^2)^{3/4}$, where a is the core radius,
- n_{e} proportional to $b^{3/2}$ as suggested by the magnetic flux freezing.

We assume that the background polarized source density is uniform and the only effect the radiation has while passing through the simulation box is the rotation of its polarization angle,

---

[6] The typical value of Re_{M} estimated for an elliptical galaxy in Section 5.2 is not yet accessible by numerical simulations. However, based on Section 2.5.3 of Chapter 2, we expect that the magnetic field structure would approach an asymptotic state after a certain Re_{M}.

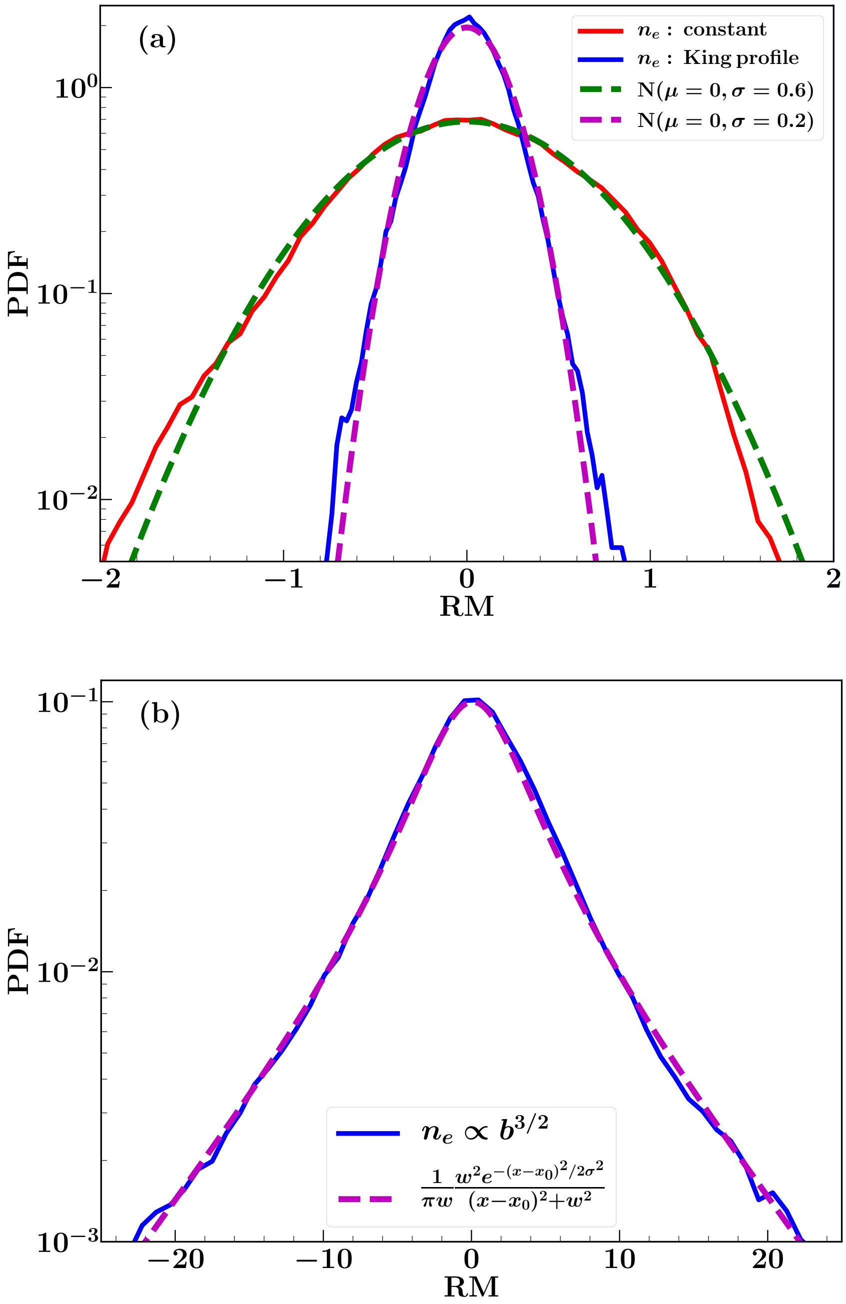

Figure 5.2: (a) PDFs of RM for the cases where the electron number density n_e is not correlated to the magnetic field strength: n_e constant (red) and n_e following the King distribution (blue) with $a = 1.25 l_0$, where l_0 is the driving scale of turbulence. Both distributions are roughly Gaussian with mean $\mu \approx 0$ (since a mean magnetic field is absent). The standard deviation σ is lower for the King profile. (b) PDF of RM for the case where n_e is related to magnetic field strength b via the flux freezing condition, i.e., $n_\mathrm{e} \propto b^{3/2}$. The distribution is non-Gaussian and can be approximated by a product of a Cauchy–Lorentz distribution and an exponential function. The parameters of the resulting function are as follows: the location parameter $x_0 = 0$, the width at half-maximum $w = 3.6$ and the standard deviation of the exponential function $\sigma = 15.81$.

which is quantified by RM. With the fluctuation dynamo generated magnetic field b for each n_e given above, we calculate the RM at each point within a face of the domain as

$$\mathrm{RM}(x_i, y_i) = K \sum_{i=1}^{512} n_\mathrm{e}(x_i, y_i, z_i)\, b(x_i, y_i, z_i)\, \mathrm{d}z, \tag{5.14}$$

where (x_i, y_i, z_i) is a coordinate on the grid and $\mathrm{d}z = 2\pi/512$ is the grid spacing. This involves looking along the sightlines through the core of an elliptical galaxy and gathering statistics from the periodic box of a physical length $1.5\,\mathrm{kpc}$, which is a good representation of the region of our interest. Fig. 5.2 shows the probability density function (PDF) of RM for the three electron number density distributions. In all cases, the mean RM ≈ 0. This is expected since there is no mean field in the domain. Fig. 5.2a shows the PDFs for the case when n_e is uniform and follows a King profile with $a = 1.25 l_0 = 375\,\mathrm{pc}$. Both distributions are Gaussian with different standard deviations σ_RM. The one with the King profile has a smaller standard deviation. The distributions agree well with the analytical expressions Eq. (5.11) and Eq. (5.12) respectively. Fig. 5.2b shows the RM distribution when $n_\mathrm{e} \propto b^{3/2}$. The distribution is clearly non-Gaussian and can be approximated by a product of a Cauchy–Lorentz distribution and an exponential function. The Gaussian or non-Gaussian nature of the RM distribution in these cases follows from Eq. (5.6) or Eq. (5.14). In an isotropic random magnetic field, the polarization angle performs a random walk as it rotates randomly along the path length. When n_e does not depend on b directly, RM depends on the first power of the magnetic field and the random walk is a Brownian motion which gives rise to a Gaussian distribution. For the case where $n_\mathrm{e} \propto b^{3/2}$, RM depends on a higher power of the magnetic field and since the underlying magnetic field is intermittent (Chapter 2), the resulting RM distribution is non-Gaussian. In the case of a non-Gaussian distribution, it is difficult to associate a single number (for example σ_RM) to the distribution but the calculated standard deviation for a non-Gaussian distribution would be far higher than that for a Gaussian distribution (compare the x-axis in Fig. 5.2a and Fig. 5.2b). The calculated standard deviation of the RM distribution shown in Fig. 5.2b is approximately equal to 8, whereas the deviation for both the Gaussian distributions in Fig. 5.2a is less than unity. Knowing the expected RM distribution in various cases, we aim to observationally explore the distribution of RM from background sources seen through an elliptical galaxy to probe its magnetic field.

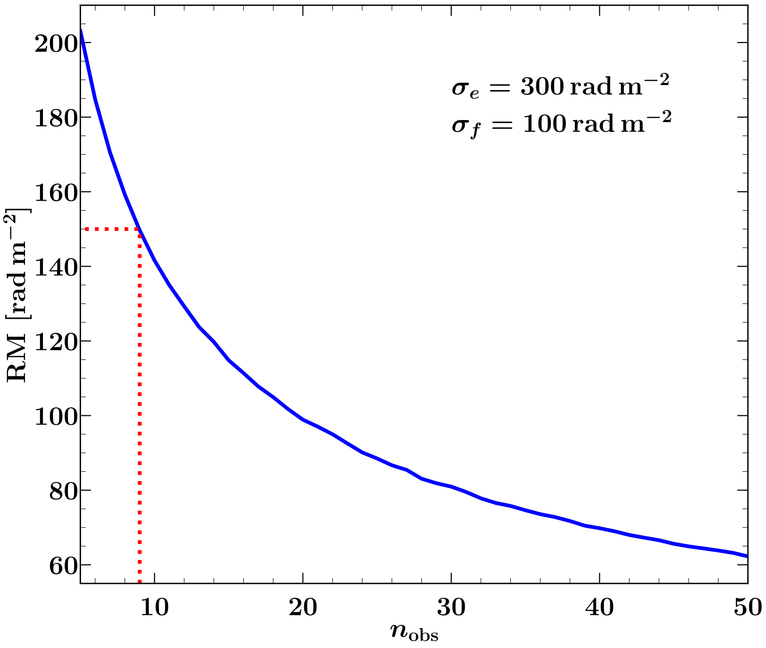

Figure 5.3: 95th percentile deviation from the combined σ of the elliptical galaxy and the Milky Way foreground versus the number of sources. We have assumed that the standard deviation of rotation measures due to the elliptical galaxy and foreground are $300\,\mathrm{rad\,m^{-2}}$ and $100\,\mathrm{rad\,m^{-2}}$ respectively. When the number of sources n_{obs} is greater than 9 (red dotted line), the error in the observed σ is less than half of σ_e in 95% of cases. Thus, we need at least 10 sources to differentiate between the elliptical galaxy and the Milky Way foreground.

5.4 Specific observational target: Maffei 1

To probe the magnetic field in elliptical galaxies via rotation measure from background sources, we choose the nearest elliptical galaxy, Maffei 1, to maximize the number of background sources. Maffei 1 is an E3 galaxy of an angular size $18.2'$ at a distance of $2.85 \pm 0.36\,\mathrm{Mpc}$ and is located at the galactic coordinates $(135.86^\circ, -0.55^\circ)$. Using arguments given in Section 5.3.1, we estimate the expected $\sigma_{\mathrm{RM}} \simeq 300\,\mathrm{rad\,m^{-2}}$ in the core of the galaxy. The elliptical galaxy lies in the Milky Way galactic plane and thus observations would suffer contamination due to the Milky Way foreground. σ_{RM} due to our galaxy in that region is around $100\,\mathrm{rad\,m^{-2}}$ (Schnitzeler, 2010). However, both RM distributions from the Milky Way and the Maffei 1 have a different standard deviations. The contribution from the elliptical galaxy can be isolated if a sufficient number of background sources is available. Moreover, any systematic large-scale trends should be removed since they can only be produced in the Milky Way.

To calculate the minimum number of background radio sources to be observed, we per-

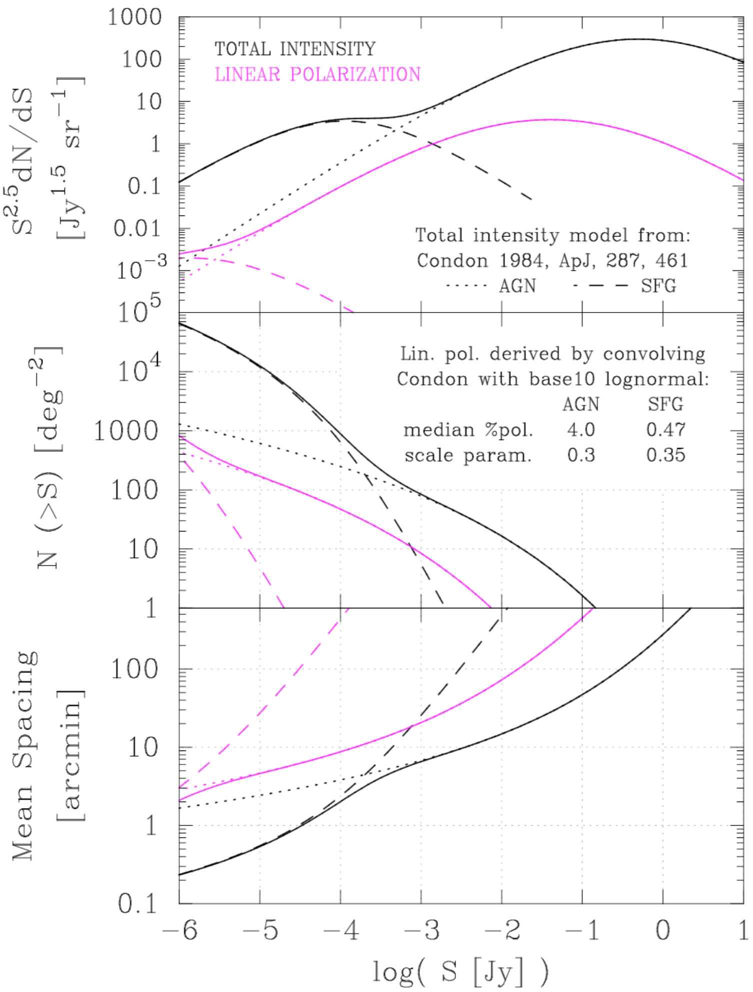

Figure 5.4: Properties of 1.4 GHz extragalactic sources of radio intensity up to 1 μJy (Hales, 2013). The total and linearly polarized intensity normalized by the differential source counts (top panel), the total number of source counts (middle panel) and the average spacing between the sources (bottom panel) are shown as functions of the intensity. The dotted lines shows the fitted models. Knowing the number of sources required per square degree, we can use the middle panel to obtain the minimum intensity we must achieve to observe that many sources.

form a Monte-Carlo simulation assuming RM fluctuations due to an elliptical galaxy with $\sigma_e = 300\,\mathrm{rad\,m^{-2}}$ and that due to the foreground with $\sigma_f = 100\,\mathrm{rad\,m^{-2}}$. We draw 10^5 random samples from a Gaussian distribution with the combined standard deviation $\sqrt{\sigma_e^2 + \sigma_f^2}$. From that sample, we select n_{obs} number of RM and calculate their standard deviation. Fig. 5.3 shows the plot of the 95th percentile deviation from the true standard deviation as a function of the number of sources n_{obs}. To distinguish the elliptical galaxy from the foreground, we at least need 10 sources because that will give an error of less than $150\,\mathrm{rad\,m^{-2}}$ (half of σ_e) in 95% of cases. To sample the core of Maffei 1, we need at least 10 or more sources within central core of size 2–3 arcmin (Buta & McCall, 1999; Davidge, 2002), which implies 300–200 sources per degree of the extragalactic sky. From the middle panel of Fig. 5.4, this implies a noise level of $10\,\mu\mathrm{Jy}$ or less. Using the exposure calculator [7] of the Very Large Array (VLA), we calculate that it requires 200 hours of observations in the L (low-frequency, 1–2 GHz) band to observe the background sources through the Maffei 1.

5.5 Discussion and conclusions

We suggest that observations of magnetic fields in elliptical galaxies would provide a direct confirmation of the operation of a fluctuation dynamo. We confirm that the supernova-driven turbulence in elliptical galaxies would generate magnetic fields of a sufficient strength to be observable. We then study the existing observations and show why they are not sufficient for this purpose. Finally, we propose to study the strength and structure of magnetic fields in the elliptical galaxy Maffei 1 by using a grid of Faraday rotation measures from background radio sources seen through it.

If the proposed observations suggest much lower fluctuations in rotation measure than our estimate, then the magnetic field generated by the fluctuation dynamo in the saturated stage is probably much weaker than that expected from the theoretical arguments and numerical simulations. This would further imply that the mean-field dynamo in spiral galaxies is probably seeded with a much weaker magnetic field. This in turn would require a much more efficient mean-field dynamo mechanism than presently known to explain the observed magnetic fields in a number of nearby spiral galaxies.

---

[7] https://science.nrao.edu/facilities/vla/docs/manuals/propvla/determining

Chapter 6

Final discussion and outlook

> “This work contains many things which are new and interesting. Unfortunately, everything that is new is not interesting, and everything which is interesting, is not new.”
>
> – Lev D. Landau

> “We can only see a short distance ahead, but we can see plenty there that needs to be done.”
>
> – Alan Turing

This thesis explores small-scale magnetic fields generated by a fluctuation dynamo and the propagation of cosmic rays in random magnetic fields. Here we discuss the questions raised and possible future directions for each chapter.

Chapter 2: Fluctuation dynamo and its nonlinear states

- **How does the non-linear fluctuation dynamo saturate?**
  After exploring the kinematic fluctuation dynamo, the main goal of this chapter was to study the mechanism for the saturation of the fluctuation dynamo. We discuss previous attempts to solve the problem and possible issues with them. Using numerical simulations, we studied the nonlinear fluctuation dynamos in driven turbulence at $\mathrm{Pr}_\mathrm{M} = 1$. It is confirmed that the statistically steady state of the magnetic field is maintained by a constant interaction between the velocity and magnetic fields. We have shown that both the amplification and diffusion of the magnetic field are affected by the back-reaction by the Lorentz force on the flow. The reduction in the amplification is due to the enhanced alignment between the velocity field and magnetic field (which reduces induction) and magnetic field and electric current density (which reduces the back-reaction itself, making the field more force-free). Moreover, the level of alignment between the velocity and magnetic field is higher where a larger reduction in amplification is required, i.e., the strong field regions. We further found that both aspects of the amplification, the local stretching and compression of magnetic field lines, are reduced. The increase in diffusion is confirmed by a decrease in the local magnetic Reynolds number $(\mathrm{Re}_\mathrm{M})_\mathrm{loc}$ and its mean value over the entire domain. However, this does not decrease to the critical magnetic Reynolds number $\mathrm{Re}_\mathrm{M}^{(\mathrm{crit})}$ as suggested by a few saturation mechanisms proposed earlier. $(\mathrm{Re}_\mathrm{M})_\mathrm{loc}$ varies from values much smaller to much larger than the $\mathrm{Re}_\mathrm{M}^{(\mathrm{crit})}$ and $\langle(\mathrm{Re}_\mathrm{M})_\mathrm{loc}\rangle \gg \mathrm{Re}_\mathrm{M}^{(\mathrm{crit})}$.

- **How does the intermittent structure of the fluctuation dynamo-generated magnetic fields depend upon its nonlinear state and on the magnetic Reynolds number?**
  Even though the turbulent velocity field is Gaussian, the fluctuation dynamo-generated magnetic field is spatially intermittent (with magnetic structures of various shapes and sizes) in both the kinematic and saturated stages. The magnetic field in the saturated stage is less intermittent than the kinematic magnetic field as confirmed by the shape of the PDF of the magnetic field strength, the calculated kurtosis and the correlation length of the magnetic field. The correlation length of the velocity field (still remaining

Gaussian in nature) also increases as the magnetic field saturates and this confirms the dynamical effect of the growing magnetic field on the velocity field. Magnetic structures are characterized by three scales, length, width and thickness, which are obtained using the Minkowski functionals. The length of the structures does not vary with Re_{M} but the width and thickness decrease as $\mathrm{Re}_{\mathrm{M}}^{-0.5}$ in nonlinear fluctuation dynamos. All three length scales increase in magnitude as the dynamo saturates but their Re_{M} dependences do not change. Thus, such a study of magnetic structures is not useful to probe the saturation mechanism of the fluctuation dynamo. The planarity and filamentarity (non-dimensional parameters to characterize the shape of magnetic structures) approach a near-asymptotic value as Re_{M} increases (with filamentarity always greater than planarity, suggesting that the structures are more like filaments). Thus, we can claim that even though the magnetic Reynolds number is high in most astrophysical systems ($\mathrm{Re}_{\mathrm{M}} \approx 10^{18}$ for galaxies and $\mathrm{Re}_{\mathrm{M}} \approx 10^{29}$ for galaxy clusters), the fluctuation-dynamo generated magnetic field occupies a significant fraction of the volume. Hence, such magnetic structures will therefore make a very significant contribution to the dynamics of the system (the simulations already show that the field strength is comparable to the equipartition value).

- **Future work**

  To completely explain the saturation mechanism, we first need to understand what exactly causes the alignment and why the magnetic field diffusion increases. Then the study can be extended to various other scenarios. We have explored the saturation mechanism of the nonlinear fluctuation dynamo and studied the morphology of magnetic structures for incompressible flows. An immediate extension would be to repeat the entire analysis for dynamos in a compressible medium (Haugen et al., 2004b; Federrath et al., 2011; Sur et al., 2018), which is more relevant for young galaxies and star-forming gas clouds. We expect that answers would qualitatively remain the same. Another extension would be to do the analysis for $\mathrm{Pr}_{\mathrm{M}} \gg 1$ (interstellar and intergalactic medium) and $\mathrm{Pr}_{\mathrm{M}} \ll 1$ (stars, planets and liquid metal experiments). In driven turbulence simulations like ours, the forcing is usually synthetic and thus it would be interesting to explore a fluctuation dynamo in a numerical setup with turbulence driven more naturally by convection (Cattaneo, 1999; Bushby et al., 2010). Also, this is more relevant for magnetic fields on the solar surface. Recent cosmological simulations with magnetic fields suggest the presence of fluctuation dynamo in galaxies (Pakmor et al., 2017) and the intracluster medium (Vazza et al., 2018). However, these claims are based on the power spectrum of the small-scale magnetic fields in simulations, which roughly agrees with the Kazantsev spectrum. A careful analysis of the small-scale velocity and magnetic fields is required to confirm convincingly that the fluctuation dynamo is indeed active in such simulations.

The fluctuation dynamo-generated magnetic field has filamentary structures. Such structures are also seen in a number of observations: neutral hydrogen (Heiles & Troland, 2005; Kalberla & Kerp, 2016; Kalberla et al., 2017), polarized synchrotron emission (Haverkorn et al., 2004; Jelić et al., 2015) and emission at submillimeter wavelengths (Planck Collaboration et al., 2016; Planck Collaboration et al., 2016). It is important to look for signatures of magnetic filaments in such observations. To address this, a systematic study (including both statistical and topological measures) can be performed to compare structures in simulations and observations.

We have adopted the MHD approximation but plasma effects might also play an important role. It would be interesting to compare our results with those of the plasma dynamo (St-Onge & Kunz, 2018) and see how the relationship between velocity and magnetic fields and the magnetic field structure change when plasma effects are considered. Plasma effects might be particularly important for the weakly collisional gas in galaxy clusters. We explored the fluctuation dynamo in an Eulerian setting and it can also be studied using Lagrangian properties of magnetic field lines. Eyink (2010) and Eyink et al. (2013) showed that, in the kinematic stage, the Lagrangian trajectories become stochastic due to the Richardson diffusion and this can lead to an additional 'anti-dynamo' effect. It would be interesting to extend such a study to the nonlinear stage and then compare both the Eulerian and Lagrangian scenarios.

Chapter 3: Cosmic ray diffusion in intermittent magnetic fields

- **Is the intermittent structure of magnetic field important for cosmic ray diffusion?** Cosmic ray diffusion is due to particles scattering in random magnetic fields. Using test-particle simulations, we calculated the diffusion coefficient of cosmic rays in intermittent and non-intermittent magnetic fields (with the same magnetic spectra). We showed that the diffusivity of low-energy particles (with a Larmor radius $r_{\rm L}$ less than the driving scale of the turbulence l_0) is higher for intermittent magnetic fields. For high-energy particles ($r_{\rm L} \geq l_0$), the intermittent structure of magnetic fields is not important for cosmic ray diffusion. For low-energy cosmic rays, the effect of intermittency is significant even when a mean field is present. For galaxies ($l_0 \simeq 100\,{\rm pc}$), the intermittency is important for cosmic ray particles with energy less than $10^9\,\mathrm{GeV}$, which is practically all of the confined cosmic rays.

- **How do magnetic structures alter cosmic ray propagation?**
  The increase in low-energy cosmic ray diffusivity is explained in terms of a correlated random walk of particles. The particles are not uniformly scattered but they have a preferred angle of deflection, which can be related to the typical width of the intermittent magnetic structures. This implies that the diffusivity depends not only on the step length and particle speed but also on the mean of the cosine of the deflection angles. We derive this dependence analytically and confirm it numerically. The diffusivity in both the intermittent and non-intermittent magnetic fields is better explained by a correlated random walk rather than a Brownian motion. Furthermore, in the continuum limit, the correlated random walk implies the telegraph equation. So, we propose that the cosmic ray fluid in random magnetic fields is better modelled by the telegraph equation rather than the diffusion equation.

- **Future work**
  We do consider the effect of a mean field on cosmic ray diffusion in random magnetic fields but this can be further explored. A spatially varying mean magnetic field can be considered and then the cosmic ray diffusivity may depend on the ratio of the correlation length and strength of the mean to random magnetic fields. Also, the expression for the parallel and perpendicular cosmic ray diffusivities must be derived from the correlated random walk model. This would involve performing the whole correlated random walk analysis in the direction parallel and perpendicular to the mean magnetic field.

  We can also extend numerical simulations to generate magnetic fields at a higher resolution, so particles of even smaller energies can be considered. Since high-energy particles are not affected by the intermittency, the dependence of cosmic ray diffusivity on energy ($\propto r_\mathrm{L}^2$) for them is the same in both intermittent and non-intermittent magnetic fields. We can test if the dependence changes for low-energy cosmic rays when magnetic field intermittency is considered. This requires a few more data points at lower energies.

Chapter 4: Correlation between cosmic rays and magnetic fields

- **Are cosmic rays and magnetic fields spatially correlated?**
  To extract magnetic field information from synchrotron intensity observations, a local

energy equipartition or correlation between cosmic rays and magnetic fields is usually assumed. Our test particle simulations have shown that at the scales less than the driving scale of the turbulence l_0, cosmic ray number density and magnetic field strength are not locally correlated. Furthermore, the correlation remains close to zero when both distributions are averaged over the size of magnetic structures. Even on including a uniform mean magnetic field, both the distributions remain uncorrelated. Furthermore, the magnetic field energy density and cosmic ray number density are statistically independent of each other. Thus, the synchrotron intensity can be expressed as the product of the average cosmic ray number density and average magnetic field strength (here 'average' refers to a spatial average over the path length). The conclusion remains valid for both intermittent and non-intermittent magnetic fields. However, the energy equipartition between cosmic rays and magnetic fields may hold at scales larger than l_0.

- **What is the reason for the presence of small-scale cosmic ray structures?**
  Even when the magnetic field and cosmic rays are uncorrelated, there are small-scale cosmic ray structures at low energies ($r_{\mathrm{L}} \leq l_b$, where l_b is the magnetic field correlation length). The resulting cosmic ray distribution is also intermittent with heavy tails at higher values of the number density in the probability distribution function. We show that this is due to magnetic mirror traps in random magnetic fields. The number of such cosmic ray structures increases when a uniform magnetic field is included and decreases when the pitch-angle scattering due to the unresolved magnetic fluctuations is added.

  We discuss that the inhomogeneity in the cosmic ray distribution is due the lack of perfectly isotropic and homogeneous in phase space of the initial cosmic ray distribution. However, the exact locations where cosmic ray number density is higher (or lower), which gives rise to the inhomogeneous cosmic ray distribution, is due to magnetic bottle traps as confirmed by the numerical trajectories. Furthermore, the cosmic ray and magnetic field distribution still remain uncorrelated at scales below the driving scale of turbulence.

- **Does the relation between magnetic fields and cosmic rays change when the pressure due to thermal gas is also included?**
  Cosmic rays exert pressure on the thermal gas which affects the magnetic field, which in turn controls the cosmic ray propagation. To include this nonlinear effect, we solved the MHD equations together with an advection-telegraph equation for the cosmic ray

fluid. We show that, even when cosmic rays are included as a dynamic component, the magnetic field and cosmic ray energy densities are not tightly correlated at scales less than the driving scale of the turbulence.

- **Future work**

  In addition to assuming local energy equipartition between cosmic ray and magnetic field energy densities for interpreting synchrotron observations, it is customary to make two additional assumptions. Firstly, it is assumed that that the cosmic ray protons (that carry most of the energy) are spatially distributed in same way as cosmic ray electrons (responsible for synchrotron radiation) and secondly, a constant ratio between the number of electrons to the number of protons is adopted. Both of these assertions need not be true, especially considering the fact that the electrons suffer significant energy losses during their propagation. The electron distribution is expected to be more intermittent than that of the protons (as electrons will spend a longer time in magnetic traps because of their smaller Larmor radii and energy losses). To test these assumptions, the next step would be to include energy loss for the particles. Once the energy loss is included, synthetic synchrotron maps can be generated from the spatial distribution of cosmic ray electrons and magnetic fields. Similar previous studies (Herron et al., 2016) assumed a uniform cosmic ray electron distribution but it is clear from our test-particle simulations that this cannot be true.

  Cosmic rays in our MHD simulations only exert pressure on the thermal gas. Another important effect is the cosmic ray streaming. Cosmic ray scatter off waves excited by the streaming instability (Kulsrud & Pearce, 1969; Skilling, 1971; Wentzel, 1974) and then stream at the Aflvén speed down their pressure gradient. The excited waves are damped and their energy is deposited into the medium. This could be modelled in our numerical simulations (a stable numerical scheme for the cosmic ray streaming is discussed in Sharma et al., 2010). The cosmic ray streaming is particularly important for launching of galactic winds (Ruszkowski et al., 2017b; Zweibel, 2017), the Parker instability (Heintz & Zweibel, 2018) and heating of galaxy clusters (Enßlin et al., 2011; Ruszkowski et al., 2017a). Another major extension would be to include cosmic rays in the multiphase ISM simulations where the turbulence is driven by supernova explosions (Gent et al., 2013a; Li et al., 2015; Kim & Ostriker, 2017). The cosmic rays would then accelerate in supernova shocks and diffuse away from their sources.

  The radio maps generated from such numerical simulations can be compared with observations. The comparative study will identify the relative importance of various physical processes and also constrain parameters of the simulations. Further, the results can be used to asses the efficiency of various data analysis techniques: gradient of polarization observations (Gaensler et al., 2011; Herron et al., 2017), gradient of synchrotron observations (Lazarian et al., 2017), analysis of synchrotron fluctuations in observations (Iacobelli et al., 2013; Stepanov et al., 2014) and topological analysis of the observational data (Makarenko et al., 2018a,b).

Chapter 5: Magnetic fields in elliptical galaxies

- **Can magnetic fields be detected in elliptical galaxies and used as a probe of the fluctuation dynamo theory?**
  Since any large-scale magnetic field is absent in elliptical galaxies, we propose that observing magnetic fields in those galaxies would be a direct probe for the fluctuation dynamo action. This is because the small-scale magnetic fields in ellipticals would not be contaminated by the tangling of the mean field as in the case of spiral galaxies. Also, since the spatial resolution with existing radio telescope is not capable of differentiating between the types of small-scale fields in spiral galaxies, observations of magnetic fields in ellipticals is required to study fluctuation dynamo action. Observations of magnetic fields in young galaxies can also probe fluctuation dynamo action but such measurements have only recently become possible. Furthermore, they mostly provide only the root mean square magnetic field strength of the galaxy.

- **What are the observational signatures of magnetic fields in elliptical galaxies?**
  We expect the core of the ellipticals to host strong magnetic fields. This can be probed by using Faraday rotation measures from background polarized radio sources seen through a large elliptical galaxy. The probability distribution of such rotation measure observations can be compared with that obtained from the theory to estimate the properties of the magnetic field. Based on the existing fluctuation dynamo theories, we would expect the rotation measure distribution to have a mean very close to zero and a non-zero standard deviation. The standard deviation can then be expressed in terms of the correlation length and strength of the random magnetic field (assuming the path length and thermal electron number density distribution are known to a reasonable degree of accuracy).

- **Future work**
  First we should actually conduct the observations for a grid of background sources

seen through the nearby elliptical galaxy, Maffei 1, and check whether what we propose can be done. Any large-scale trends in the data can be compared with the Milky Way magnetic field models in that region. This can benefit us in two ways. Firstly, it would help us to better probe magnetic fields in Maffei 1 and secondly, it would probably constrain the Milky Way magnetic fields. Also, a more realistic simulation of the fluctuation dynamo which includes heating at the core and the galactic gravitational potential to model cooling flows would provide a better picture. With upcoming telescopes (SKA and ngVLA), there would be numerous high resolution observations of magnetic fields in elliptical galaxies, spiral galaxies and young galaxies, which would help us to study the fluctuation dynamo action in much greater detail.

Appendix A

Shock Tube Test

The Sod shock tube problem (Sod, 1978) is a good test of code's capability to handle discontinuities, which are expected in the case of spatially intermittent random magnetic fields. We compare the results obtained using the Pencil code (fixed grid and uses finite difference numerical scheme) with the FLASH[1] code (adaptive mesh refinement and uses finite volume numerical scheme).

We solve the equations for conservation of mass, momentum and energy for a shock in one dimension (say x direction). The initial conditions (density ρ, pressure p and velocity v_x on the left and right hand side of the shock) for an ideal gas with $\gamma = 1.4$ in an interval $0 < x \leq 1$ are

$$(\rho, p, v_x)_{t=0} = \begin{cases} (1.0, 1.0, 0.0), & 0 < x \leq 0.5, \\ (0.125, 0.1, 0.0), & 0.5 < x \leq 1. \end{cases}$$

For the Pencil code, a very small explicit smoothing (tanh function with a smoothing parameter, which here is chosen to be 0.0005) is required across the shock since the code uses finite difference scheme. It also requires a small value of thermal conductivity (0.0001) and viscosity (0.00055). The FLASH solves the equations in a conservative form and such additional parameters are not required. Fig. A.1 shows profiles for the density, pressure, temperature and velocity on the left and right hand side of the shock as it evolves. Both codes give very similar solutions for the Sod shock tube test. The analytical solution (not shown) also agrees with it.

---

[1] http://flash.uchicago.edu/site/

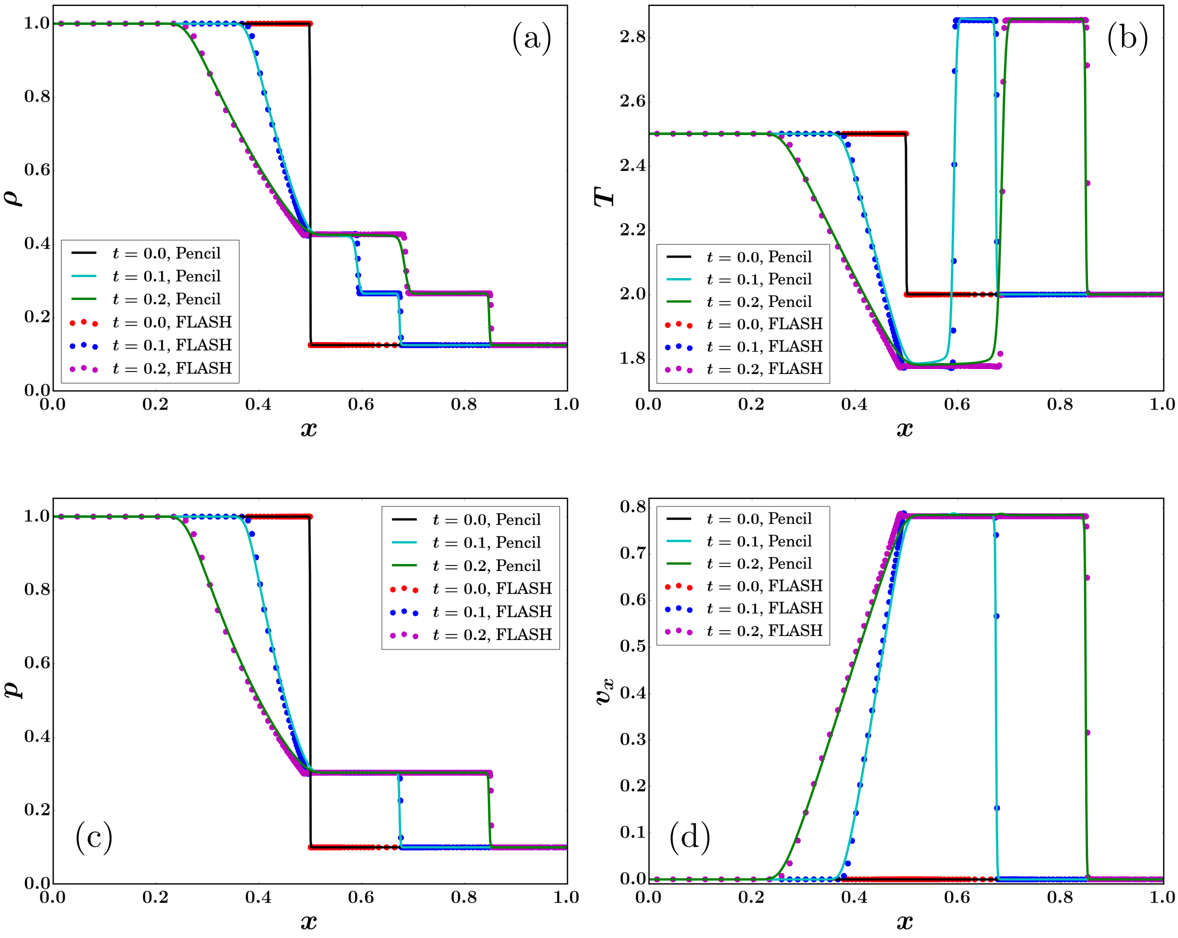

Figure A.1: Time evolution of the density ρ (a), pressure p (b), temperature T (c) and velocity in x direction v_x (d) for solution of Sod shock tube test using the Pencil (solid line) and FLASH (dotted line) codes. For profiles from FLASH, the number of dots increases closer to the shock since it use adaptive mesh refinement. The agreement between two solutions is quite good.

Bibliography

Ahlers, M., & Mertsch, P. 2017, Prog. Part. Nucl. Phys., 94, 184

Aloisio, R., & Berezinsky, V. 2004, Astrophys. J., 612, 900

Armstrong, J. W., Rickett, B. J., & Spangler, S. R. 1995, Astrophys. J., 443, 209

Arshakian, T. G., Beck, R., Krause, M., & Sokoloff, D. 2009, Astron. Astrophys., 494, 21

Arzoumanian, D., André, P., Didelon, P., et al. 2011, Astron. Astrophys., 529, L6

Balbus, S. A., & Hawley, J. F. 1991, Astrophys. J., 376, 214

Basu, A., & Roy, S. 2013, Mon. Not. R. Astron. Soc., 433, 1675

Beck, R. 2016, Ann. Rev. Astron. Astrophys., 24, 4

Beck, R., Brandenburg, A., Moss, D., Shukurov, A., & Sokoloff, D. 1996, Ann. Rev. Astron. Astrophys., 34, 155

Beck, R., & Krause, M. 2005, Astron. Nachr., 326, 414

Bell, A. R. 1978a, Mon. Not. R. Astron. Soc., 182, 147

—. 1978b, Mon. Not. R. Astron. Soc., 182, 443

Beresnyak, A. 2012, Phys. Rev. Lett., 108, 035002

Beresnyak, A., Yan, H., & Lazarian, A. 2011, Astrophys. J., 728, 60

Berezinskii, V. S., Bulanov, S. V., Dogiel, V. A., & Ptuskin, V. S. 1990, Astrophysics of Cosmic Rays (Amsterdam: North-Holland)

Berkhuijsen, E. M., Beck, R., & Hoernes, P. 2003, Astron. Astrophys., 398, 937

Berkhuijsen, E. M., Beck, R., & Tabatabaei, F. S. 2013, Mon. Not. R. Astron. Soc., 435, 1598

Bernet, M. L., Miniati, F., Lilly, S. J., Kronberg, P. P., & Dessauges-Zavadsky, M. 2008, Nature, 454, 302

Beskin, V. S. 2010, MHD Flows in Compact Astrophysical Objects, doi:10.1007/978-3-642-01290-7

Bharadwaj, S., Sahni, V., Sathyaprakash, B. S., Shandarin, S. F., & Yess, C. 2000, Astrophys. J., 528, 21

Bhat, P., & Subramanian, K. 2013, Mon. Not. R. Astron. Soc., 429, 2469

—. 2014, Astrophys. J., 791, L34

Bhat, P., Subramanian, K., & Brandenburg, A. 2016, Mon. Not. R. Astron. Soc., 461, 240

Bieber, J. W., & Matthaeus, W. H. 1997, Astrophys. J., 485, 655

Biskamp, D. 2003, Magnetohydrodynamic Turbulence (Cambridge University Press, Cambridge, UK), 310

Blandford, R. D., & Ostriker, J. P. 1978, Astrophys. J. Lett., 221, L29

Boldyrev, S., & Cattaneo, F. 2004, Phys. Rev. Lett., 92, 144501

Bouya, I., & Dormy, E. 2015, EPL (Europhysics Letters), 110, 14003

Braginskii, S. I. 1965, Reviews of Plasma Physics, 1, 205

Brandenburg, A. 2003, Computational aspects of astrophysical MHD and turbulence, ed. A. Ferriz-Mas & M. Núñez, Advances in Nonlinear Dynamics (Taylor and Francis Group, London), 269

Brandenburg, A., Jennings, R. L., Nordlund, Å., et al. 1996, Journal of Fluid Mechanics, 306, 325

Brandenburg, A., Nordlund, A., Stein, R. F., & Torkelsson, U. 1995, Astrophys. J., 446, 741

Brandenburg, A., Sokoloff, D., & Subramanian, K. 2012, SSRv, 169, 123

Brandenburg, A., & Subramanian, K. 2005, Phys. Rep., 417, 1

Brentjens, M. A., & de Bruyn, A. G. 2005, Astron. Astrophys., 441, 1217

Brighenti, F., & Mathews, W. G. 1997, Astrophys. J., 486, L83

Burbidge, G. R. 1956, Astrophys. J., 124, 416

Burn, B. J. 1966, Mon. Not. R. Astron. Soc., 133, 67

Bushby, P. J., Proctor, M. R. E., & Weiss, N. O. 2010, in Numerical Modeling of Space Plasma Flows, Astronum-2009, Vol. 429, 181

Buta, R. J., & McCall, M. L. 1999, ApJS, 124, 33

Bykov, A. M. 1988, Sov. Astron. Lett., 14, 60

Bykov, A. M., & Toptygin, I. N. 1985, Sov. Astron. Lett., 11, 75

—. 1987, Astrophys. Space Sci., 138, 341

Candia, J., & Roulet, E. 2004, J. Cosmol. Astropart. Phys., 10, 7

Cappellari, M., Emsellem, E., Krajnović, D., et al. 2011, Mon. Not. R. Astron. Soc., 416, 1680

Cappellaro, E., Evans, R., & Turatto, M. 1999, Astron. Astrophys., 351, 459

Casse, F., Lemoine, M., & Pelletier, G. 2002, Phys. Rev. D, 65, 023002

Cattaneo, F. 1999, Astrophys. J., 515, L39

Cattaneo, F., Hughes, D. W., & Kim, E.-J. 1996, Phys. Rev. Lett., 76, 2057

Cattaneo, F., & Tobias, S. M. 2009, Journal of Fluid Mechanics, 621, 205

Cesarsky, C. J. 1980, Ann. Rev. Astron. Astrophys., 18, 289

Cesarsky, C. J., & Kulsrud, R. M. 1981, in IAU Symposium, Vol. 94, Origin of Cosmic Rays, ed. G. Setti, G. Spada, & A. W. Wolfendale, 251

Chamandy, L., Shukurov, A., Subramanian, K., & Stoker, K. 2014, Mon. Not. R. Astron. Soc., 443, 1867

Chandran, B. D. G. 2000, Astrophys. J., 529, 513

Chen, A., & Renshaw, E. 1992, J. Appl. Probab., 29, 792

Chen, L. E., Bott, A. F. A., Tzeferacos, P., et al. 2018, ArXiv e-prints, arXiv:1808.04430

Chi, X., & Wolfendale, A. W. 1993, Nature, 362, 610

Childress, S., & Gilbert, A. D. 1995, Stretch, Twist, Fold

Cho, J., & Ryu, D. 2009, Astrophys. J., 705, L90

Codling, E., & Hill, N. 2005, J. Theor. Biol., 233, 573

Codling, E. A., Plank, M. J., & Benhamou, S. 2008, J. R. Soc. Interface, 5, 813

Cohet, R., & Marcowith, A. 2016, Astron. Astrophys., 588, A73

Cowling, T. G. 1933, Mon. Not. R. Astron. Soc., 94, 39

Cox, D. P. 2005, Annual Review of Astronomy and Astrophysics, 43, 337

Crofton, M. W. 1868, Philosophical Transactions of the Royal Society of London Series I, 158, 181

Crutcher, R. M. 2012, Annual Review of Astronomy and Astrophysics, 50, 29

Davidge, T. J. 2002, Astron. J., 124, 2012

Davidson, P. A. 2004, Turbulence : an introduction for scientists and engineers

Davis, Leverett, J., & Greenstein, J. L. 1951, Astrophys. J., 114, 206

DeMarco, D., Blasi, P., & Stanev, T. 2007, J. Cosmol. Astropart. Phys., 6, 027

Desiati, P., & Zweibel, E. G. 2014, Astrophys. J., 791, 51

Dmitruk, P., Matthaeus, W. H., & Seenu, N. 2004, Astrophys. J., 617, 667

Drury, L. O. 1983, Reports on Progress in Physics, 46, 973

Duric, N. 1990, in IAU Symposium, Vol. 140, Galactic and Intergalactic Magnetic Fields, ed. R. Beck, R. Wielebinski, & P. P. Kronberg, 235

Dyson, J. E., & Williams, D. A. 1997, The physics of the interstellar medium, doi:10.1201/9780585368115

Effenberger, F., & Litvinenko, Y. E. 2014, Astrophys. J., 783, 15

Emsellem, E., Cappellari, M., Krajnović, D., et al. 2011, Mon. Not. R. Astron. Soc., 414, 888

Enßlin, T., Pfrommer, C., Miniati, F., & Subramanian, K. 2011, Astron. Astrophys., 527, A99

Enßlin, T. A. 2003, Astron. Astrophys., 399, 409

Enßlin, T. A., Hutschenreuter, S., Vacca, V., & Oppermann, N. 2017, Phys. Rev. D, 96, 043021

Enßlin, T. A., & Vogt, C. 2006, Astron. Astrophys., 453, 447

Evirgen, C. C., Gent, F. A., Shukurov, A., Fletcher, A., & Bushby, P. 2017, Mon. Not. R. Astron. Soc., 464, L105

Eyink, G., Vishniac, E., Lalescu, C., et al. 2013, Nature, 497, 466

Eyink, G. L. 2010, Phys. Rev. E, 82, 046314

—. 2011, Phys. Rev. E, 83, 056405

Fabian, A. C. 1994, Annual Review of Astronomy and Astrophysics, 32, 277

Farmer, A. J., & Goldreich, P. 2004, Astrophys. J., 604, 671

Favier, B., & Bushby, P. J. 2012, Journal of Fluid Mechanics, 690, 262

Federrath, C. 2013, Mon. Not. R. Astron. Soc., 436, 1245

—. 2016, Journal of Plasma Physics, 82, 535820601

Federrath, C., Chabrier, G., Schober, J., et al. 2011, Phys. Rev. Lett., 107, 114504

Federrath, C., Roman-Duval, J., Klessen, R. S., Schmidt, W., & Mac Low, M.-M. 2010, Astron. Astrophys., 512, A81

Federrath, C., Schober, J., Bovino, S., & Schleicher, D. R. G. 2014, Astrophys. J., 797, L19

Felice, G. M., & Kulsrud, R. M. 2001, Astrophys. J., 553, 198

Fletcher, A. 2010, in The Dynamic Interstellar Medium: A Celebration of the Canadian Galactic Plane Survey, ed. R. Kothes, T. L. Landecker, & A. G. Willis, Vol. 438, 197

Fletcher, A., Beck, R., Shukurov, A., Berkhuijsen, E. M., & Horellou, C. 2011, Mon. Not. R. Astron. Soc., 412, 2396

Forman, M. A., & Gleeson, L. J. 1975, Astrophys. Space Sci., 32, 77

Forman, W., Jones, C., & Tucker, W. 1985, Astrophys. J., 293, 102

Fung, J. C. H., Hunt, J. C. R., Malik, N. A., & Perkins, R. J. 1992, J. Fluid Mech., 236, 281

Gaensler, B. M., Haverkorn, M., Staveley-Smith, L., et al. 2005, Science, 307, 1610

Gaensler, B. M., Haverkorn, M., Burkhart, B., et al. 2011, Nature, 478, 214

Galloway, D. J., & Proctor, M. R. E. 1992, Nature, 356, 691

Garcia-Munoz, M., Mason, G. M., & Simpson, J. A. 1977, Astrophys. J., 217, 859

Garrington, S. T., Conway, R. G., & Leahy, J. P. 1991, Mon. Not. R. Astron. Soc., 250, 171

Garrington, S. T., Leahy, J. P., Conway, R. G., & Laing, R. A. 1988, Nature, 331, 147

Gent, F. A., Shukurov, A., Fletcher, A., Sarson, G. R., & Mantere, M. J. 2013a, Mon. Not. R. Astron. Soc., 432, 1396

Gent, F. A., Shukurov, A., Sarson, G. R., Fletcher, A., & Mantere, M. J. 2013b, Mon. Not. R. Astron. Soc., 430, L40

Giacalone, J., & Jokipii, J. R. 1999, Astrophys. J., 520, 204

Gilbert, A. D., Mason, J., & Tobias, S. M. 2016, Journal of Fluid Mechanics, 791, 568

Gillis, J. 1955, Proc. Cambridge Philos. Soc., 51, 639

Ginzburg, V. L., & Syrovatskii, S. I. 1965, Annual Review of Astronomy and Astrophysics, 3, 297

Gleeson, L. J. 1969, P&SS, 17, 31

Globus, N., Allard, D., & Parizot, E. 2008, Astron. Astrophys., 479, 97

Goldreich, P., & Sridhar, S. 1995, Astrophys. J., 438, 763

—. 1997, Astrophys. J., 485, 680

Gopal-Krishna, & Nath, B. B. 1997, Astron. Astrophys., 326, 45

Gotoh, T., Fukayama, D., & Nakano, T. 2002, Physics of Fluids, 14, 1065

Govoni, F., & Feretti, L. 2004, International Journal of Modern Physics D, 13, 1549

Green, M. S. 1951, J. Chem. Phys., 19, 1036

Greenfield, P. D., Roberts, D. H., & Burke, B. F. 1985, Astrophys. J., 293, 370

Grenier, I. A., Black, J. H., & Strong, A. W. 2015, Ann. Rev. Astron. Astrophys., 53, 199

Gruber, D. E., Heindl, W. A., Rothschild, R. E., et al. 2001, Astrophys. J., 562, 499

Guidetti, D., Laing, R. A., Croston, J. H., Bridle, A. H., & Parma, P. 2012, Mon. Not. R. Astron. Soc., 423, 1335

Hales, C. A. 2013, ArXiv e-prints, arXiv:1312.4602

Hanasz, M., Kowal, G., Otmianowska-Mazur, K., & Lesch, H. 2004, Astrophys. J., 605, L33

Harari, D., Mollerach, S., & Roulet, E. 2014, Phys. Rev. D, 89, 123001

Haugen, N. E., Brandenburg, A., & Dobler, W. 2004a, Phys. Rev. E, 70, 016308

Haugen, N. E. L., Brandenburg, A., & Mee, A. J. 2004b, Mon. Not. R. Astron. Soc., 353, 947

Haverkorn, M., Brown, J. C., Gaensler, B. M., & McClure-Griffiths, N. M. 2008, Astrophys. J., 680, 362

Haverkorn, M., Katgert, P., & de Bruyn, A. G. 2004, Astron. Astrophys., 427, 549

Haverkorn, M., & Spangler, S. R. 2013, SSRv, 178, 483

Heald, G. 2009, in Cosmic Magnetic Fields: From Planets, to Stars and Galaxies, Vol. 259, 591–602

Heiles, C., & Troland, T. H. 2005, Astrophys. J., 624, 773

Heintz, E., & Zweibel, E. G. 2018, Astrophys. J., 860, 97

Herron, C. A., Burkhart, B., Lazarian, A., Gaensler, B. M., & McClure-Griffiths, N. M. 2016, Astrophys. J., 822, 13

Herron, C. A., Geisbuesch, J., Landecker, T. L., et al. 2017, Astrophys. J., 835, 210

Herron, C. A., Burkhart, B., Gaensler, B. M., et al. 2018, Astrophys. J., 855, 29

Hoernes, P., Berkhuijsen, E. M., & Xu, C. 1998, Astron. Astrophys., 334, 57

Holman, G. D., Ionson, J. A., & Scott, J. S. 1979, Astrophys. J., 228, 576

Houde, M., Fletcher, A., Beck, R., et al. 2013, Astrophys. J., 766, 49

Iacobelli, M., Haverkorn, M., Orrú, E., et al. 2013, Astron. Astrophys., 558, A72

Iskakov, A. B., Schekochihin, A. A., Cowley, S. C., McWilliams, J. C., & Proctor, M. R. E. 2007, Phys. Rev. Lett., 98, 208501

Jackson, J. D. 1998, Classical Electrodynamics, 3rd Edition (New York: Wiley), 832

Jelić, V., de Bruyn, A. G., Pandey, V. N., et al. 2015, Astron. Astrophys., 583, A137

Jin, C., & Wang, J. 2015a, Astrophys. J., 806, 174

Jin, C. L., & Wang, J. X. 2015b, Astrophys. J., 807, 70

Jokipii, J. R. 1966, Astrophys. J., 146, 480

Jokipii, J. R., & Parker, E. N. 1969, Astrophys. J., 155, 777

Kalberla, P. M. W., & Kerp, J. 2016, Astron. Astrophys., 595, A37

Kalberla, P. M. W., Kerp, J., Haud, U., & Haverkorn, M. 2017, Astron. Astrophys., 607, A15

Karak, B. B., & Brandenburg, A. 2016, Astrophys. J., 816, 28

Kareiva, P. M., & Shigesada, N. 1983, Oecologia, 56, 234

Kazantsev, A. P. 1968, Soviet Journal of Experimental and Theoretical Physics, 26, 1031

Kim, C.-G., & Ostriker, E. C. 2017, Astrophys. J., 846, 133

Kim, E.-j. 1999, Physics Letters A, 259, 232

Klein, U., & Fletcher, A. 2015, Galactic and Intergalactic Magnetic Fields (Springer Praxis Books, Springer International Publishing, Heidelberg, Germany)

Kolmogorov, A. 1941, Akademiia Nauk SSSR Doklady, 30, 301

Krause, F., & Rädler, K. H. 1980, Mean-field magnetohydrodynamics and dynamo theory

Krivova, N. A., & Solanki, S. K. 2004, Astron. Astrophys., 417, 1125

Kubo, R. 1957, Journal of the Physical Society of Japan, 12, 570

Kulsrud, R., & Pearce, W. P. 1969, Astrophys. J., 156, 445

Kulsrud, R. M. 1999, Annual Review of Astronomy and Astrophysics, 37, 37

—. 2005, Plasma Physics for Astrophysics (Princeton University Press, Princeton)

Kulsrud, R. M., & Anderson, S. W. 1992, Astrophys. J., 396, 606

Laing, R. A. 1988, Nature, 331, 149

Laing, R. A., Bridle, A. H., Parma, P., & Murgia, M. 2008, Mon. Not. R. Astron. Soc., 391, 521

Lazarian, A., Yuen, K. H., Lee, H., & Cho, J. 2017, Astrophys. J., 842, 30

Legland, D., Kiêu, K., & Devaux, M.-F. 2011, Image Analysis & Stereology, 2, 83

Leung, T., Swaminathan, N., & Davidson, P. A. 2012, Journal of Fluid Mechanics, 710, 453

Li, M., Ostriker, J. P., Cen, R., Bryan, G. L., & Naab, T. 2015, Astrophys. J., 814, 4

Longair, M. S. 1994, High energy astrophysics. Volume 2. Stars, the Galaxy and the interstellar medium.

Lynn, J. W., Parrish, I. J., Quataert, E., & Chandran, B. D. G. 2012, Astrophys. J., 758, 78

Makarenko, I., Bushby, P., Fletcher, A., et al. 2018a, Journal of Plasma Physics, 84, 735840403

Makarenko, I., Fletcher, A., & Shukurov, A. 2015, Mon. Not. R. Astron. Soc., 447, L55

Makarenko, I., Shukurov, A., Henderson, R., et al. 2018b, Mon. Not. R. Astron. Soc., 475, 1843

Malkov, M. A., & Sagdeev, R. Z. 2015, Astrophys. J., 808, 157

Malyshkin, L., & Kulsrud, R. M. 2002, Astrophys. J., 571, 619

Mao, S. A., Gaensler, B. M., Stanimirović, S., et al. 2008, Astrophys. J., 688, 1029

Mao, S. A., McClure-Griffiths, N. M., Gaensler, B. M., et al. 2012, Astrophys. J., 759, 25

Mao, S. A., Carilli, C., Gaensler, B. M., et al. 2017, Nature Astronomy, 1, 621

Mason, J., Cattaneo, F., & Boldyrev, S. 2006, Phys. Rev. Lett., 97, 255002

Mathews, W. G., & Brighenti, F. 1997, Astrophys. J., 488, 595

—. 2003, Annual Review of Astronomy and Astrophysics, 41, 191

Matthaeus, W. H., Qin, G., Bieber, J. W., & Zank, G. P. 2003, Astrophys. J. Lett., 590, L53

Meneguzzi, M., Frisch, U., & Pouquet, A. 1981, Physical Review Letters, 47, 1060

Michalek, G., & Ostrowski, M. 1997, Astron. Astrophys., 326, 793

Minkowski, H. 1903, Mathematische Annalen, 57, 447

Minter, A. H., & Spangler, S. R. 1996, Astrophys. J., 458, 194

Moffatt, H. K. 1978, Magnetic field generation in electrically conducting fluids. (Cambridge: Cambridge University Press)

Monin, A. S., & Yaglom, A. M. 1971, Statistical Fluid Mechanics (Cambridge, Massachusetts, USA: MIT Press)

Moss, D., & Shukurov, A. 1996, Mon. Not. R. Astron. Soc., 279, 229

Moss, D., Shukurov, A., & Sokoloff, D. 1999, Astron. Astrophys., 343, 120

Moss, D., Snodin, A. P., Englmaier, P., et al. 2007, Astron. Astrophys., 465, 157

Nyland, K., Young, L. M., Wrobel, J. M., et al. 2017, Mon. Not. R. Astron. Soc., 464, 1029

Ohno, H., & Shibata, S. 1993, Mon. Not. R. Astron. Soc., 262, 953

Ostriker, J. P., & McKee, C. F. 1988, Reviews of Modern Physics, 60, 1

O'Sullivan, E., Forbes, D. A., & Ponman, T. J. 2001, Mon. Not. R. Astron. Soc., 328, 461

Pakmor, R., Marinacci, F., & Springel, V. 2014, Astrophys. J. Lett., 783, L20

Pakmor, R., Gómez, F. A., Grand, R. J. J., et al. 2017, Mon. Not. R. Astron. Soc., 469, 3185

Parizot, E. 2004, Nucl. Phys. B, Proc. Suppl., 136, 169

Parker, E. N. 1965, P&SS, 13, 9

—. 1992, Astrophys. J., 401, 137

Pétrélis, F., Alexakis, A., & Gissinger, C. 2016, Phys. Rev. Lett., 116, 161102

Planck Collaboration, Ade, P. A. R., Aghanim, N., et al. 2016, Astron. Astrophys., 586, A141

Planck Collaboration, Ade, P. A. R., Aghanim, N., et al. 2016, Astron. Astrophys., 586, A136

Plotnikov, I., Pelletier, G., & Lemoine, M. 2011, Astron. Astrophys., 532, A68

Pope, S. B. 2000, Turbulent Flows

Rand, R. J., & Lyne, A. G. 1994, Mon. Not. R. Astron. Soc., 268, 497

Reville, B., O'Sullivan, S., Duffy, P., & Kirk, J. G. 2008, Mon. Not. R. Astron. Soc., 386, 509

Rincon, F., Califano, F., Schekochihin, A. A., & Valentini, F. 2016, Proceedings of the National Academy of Science, 113, 3950

Rodrigues, L. F. S., Sarson, G. R., Shukurov, A., Bushby, P. J., & Fletcher, A. 2016, Astrophys. J., 816, 2

Rodrigues, L. F. S., Shukurov, A., Fletcher, A., & Baugh, C. M. 2015, Mon. Not. R. Astron. Soc., 450, 3472

Rodrigues, L. F. S., Snodin, A. P., Sarson, G. R., & Shukurov, A. 2018, ArXiv e-prints, arXiv:1809.07194

Rogers, T. M., & McElwaine, J. N. 2017, Astrophys. J., 841, L26

Rohlfs, K., & Wilson, T. L. 2004, Tools of radio astronomy

Rosser, G., Fletcher, A. G., Maini, P. K., & Baker, R. E. 2013, J. R. Soc. Interface, 10, 20130273

Ruszkowski, M., Yang, H. Y. K., & Reynolds, C. S. 2017a, Astrophys. J., 844, 13

Ruszkowski, M., Yang, H.-Y. K., & Zweibel, E. 2017b, Astrophys. J., 834, 208

Ruzmaikin, A., Sokoloff, D., & Shukurov, A. 1989, Mon. Not. R. Astron. Soc., 241, 1

Ruzmaikin, A. A., & Sokoloff, D. D. 1979, Astron. Astrophys., 78, 1

Ruzmaikin, A. A., Sokoloff, D. D., & Shukurov, A. M., eds. 1988, Astrophysics and Space Science Library, Vol. 133, Magnetic fields of galaxies

Rybicki, G. B., & Lightman, A. P. 1979, Radiative processes in astrophysics

Sahni, V., Sathyaprakash, B. S., & Shandarin, S. F. 1998, Astrophys. J. Lett., 495, L5

Schekochihin, A. A., & Cowley, S. C. 2006, Physics of Plasmas, 13, 056501

—. 2007, Turbulence and Magnetic Fields in Astrophysical Plasmas, 85

Schekochihin, A. A., Cowley, S. C., Dorland, W., et al. 2009, ApJS, 182, 310

Schekochihin, A. A., Cowley, S. C., Hammett, G. W., Maron, J. L., & McWilliams, J. C. 2002, New Journal of Physics, 4, 84

Schekochihin, A. A., Cowley, S. C., Taylor, S. F., Maron, J. L., & McWilliams, J. C. 2004, Astrophys. J., 612, 276

Schekochihin, A. A., Haugen, N. E. L., Brandenburg, A., et al. 2005, Astrophys. J., 625, L115

Schekochihin, A. A., Iskakov, A. B., Cowley, S. C., et al. 2007, New Journal of Physics, 9, 300

Schlickeiser, R. 2002, Cosmic Ray Astrophysics (Berlin: Springer)

Schmalzing, J., Buchert, T., Melott, A. L., et al. 1999, Astrophys. J., 526, 568

Schmalzing, J., & Gorski, K. M. 1998, Mon. Not. R. Astron. Soc., 297, 355

Schnitzeler, D. H. F. M. 2010, Mon. Not. R. Astron. Soc., 409, L99

Servidio, S., Matthaeus, W. H., & Dmitruk, P. 2008, Phys. Rev. Lett., 100, 095005

Seta, A., & Beck, R. 2019, arXiv e-prints, arXiv:1903.11856

Seta, A., Bhat, P., & Subramanian, K. 2015, Journal of Plasma Physics, 81, 395810503

Seta, A., Shukurov, A., Wood, T. S., Bushby, P. J., & Snodin, A. P. 2018, Mon. Not. R. Astron. Soc., 473, 4544

Shalchi, A. 2009, Nonlinear Cosmic Ray Diffusion Theories, Vol. 362 (Berlin: Springer)

Sharma, P., Colella, P., & Martin, D. 2010, SIAM Journal on Scientific Computing, 32, 3564

Shukurov, A. 2004, ArXiv Astrophysics e-prints, astro-ph/0411739

Shukurov, A., Snodin, A. P., Seta, A., Bushby, P. J., & Wood, T. S. 2017, Astrophys. J. Lett., 839, L16

Shukurov, A., & Sokoloff, D. 2007, in Les Houches, Session LXXXVIII, Dynamos, ed. P. Cardin & L. F. Cugliandolo, Vol. 88 (Amsterdam: Elsevier), 251–299

Shukurov, A., Sokoloff, D., Subramanian, K., & Brand enburg, A. 2006, Astron. Astrophys., 448, L33

Skilling, J. 1971, Astrophys. J., 170, 265

—. 1975, Mon. Not. R. Astron. Soc., 172, 557

Snodin, A. P., Brandenburg, A., Mee, A. J., & Shukurov, A. 2006, Mon. Not. R. Astron. Soc., 373, 643

Snodin, A. P., Ruffolo, D., Oughton, S., Servidio, S., & Matthaeus, W. H. 2013, Astrophys. J., 779, 56

Snodin, A. P., Shukurov, A., Sarson, G. R., Bushby, P. J., & Rodrigues, L. F. S. 2016, Mon. Not. R. Astron. Soc., 457, 3975

Sod, G. A. 1978, Journal of Computational Physics, 27, 1

Sokoloff, D. D., Bykov, A. A., Shukurov, A., et al. 1998, Mon. Not. R. Astron. Soc., 299, 189

Soler, J. D., Alves, F., Boulanger, F., et al. 2016, Astron. Astrophys., 596, A93

Sonsrettee, W., Subedi, P., Ruffolo, D., et al. 2015, Astrophys. J., 798, 59

Sreenivasan, K. R. 1999, Reviews of Modern Physics Supplement, 71, S383

St-Onge, D. A., & Kunz, M. W. 2018, Astrophys. J., 863, L25

Stenflo, J. O. 2012, Astron. Astrophys., 547, A93

Stepanov, R., Fletcher, A., Shukurov, A., et al. 2009, in IAU Symposium, Vol. 259, Cosmic Magnetic Fields: From Planets, to Stars and Galaxies, ed. K. G. Strassmeier, A. G. Kosovichev, & J. E. Beckman, 93–94

Stepanov, R., Shukurov, A., Fletcher, A., et al. 2014, Mon. Not. R. Astron. Soc., 437, 2201

Stone, J. M., Hawley, J. F., Gammie, C. F., & Balbus, S. A. 1996, Astrophys. J., 463, 656

Strong, A. W., Moskalenko, I. V., & Ptuskin, V. S. 2007, Annual Review of Nuclear and Particle Science, 57, 285

Subedi, P., Sonsrettee, W., Blasi, P., et al. 2017, Astrophys. J., 837, 140

Subramanian, K. 1998, Mon. Not. R. Astron. Soc., 294, 718

—. 1999, Phys. Rev. Lett., 83, 2957

—. 2003, Phys. Rev. Lett., 90, 245003

Subramanian, K., & Brandenburg, A. 2014, Mon. Not. R. Astron. Soc., 445, 2930

Subramanian, K., Shukurov, A., & Haugen, N. E. L. 2006, Mon. Not. R. Astron. Soc., 366, 1437

Sur, S., Bhat, P., & Subramanian, K. 2018, Mon. Not. R. Astron. Soc., 475, L72

Sur, S., Federrath, C., Schleicher, D. R. G., Banerjee, R., & Klessen, R. S. 2012, Mon. Not. R. Astron. Soc., 423, 3148

Tautz, R. C., & Lerche, I. 2016, Research in Astronomy and Astrophysics, 16, 162

Taylor, G. I. 1922, Proceedings of the London Mathematical Society, s2-20, 196

Tilgner, A., & Brandenburg, A. 2008, Mon. Not. R. Astron. Soc., 391, 1477

Tobias, S. M., Cattaneo, F., & Boldyrev, S. 2011, ArXiv e-prints, arXiv:1103.3138

Vainshtein, S. I., & Zel'dovich, Y. B. 1972, Soviet Physics Uspekhi, 15, 159

van Dyke, M. 1982, An album of fluid motion (Parabolic Press, Stanford, CA)

Vazza, F., Brunetti, G., Brüggen, M., & Bonafede, A. 2018, Mon. Not. R. Astron. Soc., 474, 1672

Waelkens, A. H., Schekochihin, A. A., & Enßlin, T. A. 2009, Mon. Not. R. Astron. Soc., 398, 1970

Weidl, M. S., Jenko, F., Teaca, B., & Schlickeiser, R. 2015, Astrophys. J., 811, 8

Weiss, N. O. 1966, Proceedings of the Royal Society of London Series A, 293, 310

Wentzel, D. G. 1974, Ann. Rev. Astron. Astrophys., 12, 71

Wilkin, S. L., Barenghi, C. F., & Shukurov, A. 2007, Phys. Rev. Lett., 99, 134501

Willis, A. P. 2012, Phys. Rev. Lett., 109, 251101

Yan, H., & Lazarian, A. 2002, Phys. Rev. Lett., 89, 281102

Yoast-Hull, T. M., Gallagher, J. S., & Zweibel, E. G. 2016, Mon. Not. R. Astron. Soc., 457, L29

Zaroubi, S., Jelić, V., de Bruyn, A. G., et al. 2015, Mon. Not. R. Astron. Soc., 454, L46

Zel'dovich, Ya. B. 1957, Soviet Journal of Experimental and Theoretical Physics, 4, 460

Zel'dovich, Ya. B., Molchanov, S. A., Ruzmaikin, A. A., & Sokoloff, D. D. 1987, Soviet Physics Uspekhi, 30, 353

Zel'dovich, Ya. B., Ruzmaikin, A. A., Molchanov, S. A., & Sokoloff, D. D. 1984, Journal of Fluid Mechanics, 144, 1

Zeldovich, Ya. B., Ruzmaikin, A. A., & Sokoloff, D. D. 1990, The Almighty Chance (Singapore: World Scientific)

Zhdankin, V., Boldyrev, S., Perez, J. C., & Tobias, S. M. 2014, Astrophys. J., 795, 127

Zweibel, E. G. 2002, Astrophys. J., 567, 962

—. 2013, Physics of Plasmas, 20, 055501

—. 2017, Physics of Plasmas, 24, 055402